

Growth, fabrication, and investigation of light-emitting diodes based on GaN nanowires

DISSERTATION

zur Erlangung des akademischen Grades

Doctor rerum naturalium (Dr. rer. nat.)
im Fach Physik

eingereicht an der
Mathematisch-Naturwissenschaftlichen Fakultät
Humboldt-Universität zu Berlin

von
Dipl.-Phys. Mattia Musolino

Präsident der Humboldt-Universität zu Berlin:
Prof. Dr. Jan-Hendrik Olbertz

Dekan der Mathematisch-Naturwissenschaftlichen Fakultät:
Prof. Dr. Elmar Kulke

Gutachter:

- (i) Prof. Dr. Henning Riechert
- (ii) Prof. Dr. Ted W. Masselink
- (iii) Prof. Dr. Bruno Daudin

eingereicht am: 21. Juli 2015

Tag der mündlichen Prüfung: 15. Dezember 2015

*"...the only laws of matter are those which our minds must fabricate,
and the only laws of mind are fabricated for it by matter."*

James Clerk Maxwell
Analogies in Nature (1856)

Abstract

This PhD thesis provides an in-depth insight on various crucial aspects of light-emitting diodes (LEDs) based on (In,Ga)N/GaN heterostructures grown along the axis of nanowires (NWs) by molecular beam epitaxy on Si substrates.

In particular, the growth parameters are adjusted so as to suppress the coalescence of NWs; in this way the photoluminescence (PL) intensity emitted from the NW-LEDs can be increased by about ten times. The opto-electronic properties of the NW-LEDs can be further improved by exclusively employing indium tin oxide instead of Ni/Au as top contact. Furthermore, the compatibility of selective-area growth (SAG) of GaN NWs on AlN-buffered Si substrates with device operation is demonstrated, thus paving the way for a new generation of LEDs based on homogeneous NW ensembles on Si. Ordered arrays of ultrathin NWs are also successfully obtained by combining SAG and *in situ* post-growth thermal decomposition.

A double-line structure is observed in the electroluminescence (EL) spectra emitted by the NW-LEDs; it is likely caused by compressive strain introduced by the (Al,Ga)N electron blocking layer in the neighbouring (In,Ga)N quantum well. An in-depth analysis of temperature dependent PL and EL measurements indicates that carrier localization phenomena do not dominate the EL emission properties of the NW-LEDs. The forward bias current-voltage (I-V) characteristics of different NW-LEDs are analysed by means of an original model that takes into account the multi-element nature of LEDs based on NW ensembles by assuming a linear dependence of the ideality factor on applied bias. The transport mechanisms in reverse bias regime are carefully studied by means of deep level transient spectroscopy (DLTS) and temperature dependent I-V measurements. The physical origin of the detected deep states is discussed. Then, a physical model able to describe quantitatively the peculiar I-V-T characteristics of NW-LEDs is developed.

Keywords: gallium nitride, GaN, (In,Ga)N, nanowires, light-emitting diodes, MBE, ITO, top contact, electroluminescence, EQE, current-voltage, multi-element, deep states, DLTS.

Zusammenfassung

Diese Arbeit gibt einen tiefgehenden Einblick in verschiedene Aspekte von auf (In,Ga)N/GaN Heterostrukturen basierenden Leuchtdioden (LEDs), mittels Molekularstrahlepitaxie entlang der Achse von Nanodrähten (NWs) auf Si Substraten gewachsen.

Insbesondere wurden die Wachstumsparameter angepasst, um eine Koaleszierung der Nanodrähte zu vermindern. Auf diese Weise konnte die durch die NW-LEDs emittierte Intensität der Photolumineszenz (PL) um einen Faktor zehn erhöht werden. Die opto-elektronischen Eigenschaften von NW-LEDs konnten durch die Verwendung von Indiumzinoxid, anstatt von Ni/Au als Frontkontakt, verbessert werden. Zudem wurde demonstriert, dass auch selektives Wachstum (SAG) von GaN NWs auf AlN gepufferten Si Substraten mit einer guten Leistungsfähigkeit von Geräte vereinbar ist und somit als Wegbereiter für eine neue Generation von NW-LEDs auf Si dienen kann. Weiterhin war es möglich, strukturierte Felder von ultradünnen NWs durch SAG und thermische *in situ* Dekomposition herzustellen.

In den durch die NW-LEDs emittierten Elektrolumineszenzspektren (EL) wurde eine Doppellinienstruktur beobachtet, die höchstwahrscheinlich von den kompressiven Verspannungen im benachbarten Quantentopf, durch die Elektronensperrschicht verursacht, herrührt. Die Analyse von temperaturabhängigen PL- und EL-Messungen zeigt, dass Ladungsträgerlokalisierungen nicht ausschlaggebend für die EL-Emission von NW-LEDs sind. Die Strom-Spannungs-Charakteristiken (I-V) von NW-LEDs unter Vorwärtsspannung wurden mittels eines Modells beschrieben, in das die vielkomponentige Natur der LEDs berücksichtigt wird. Die unter Rückwärtsspannung aktiven Transportmechanismen wurden anhand von Kapazitätstransientenmessungen und temperaturabhängigen I-V-Messungen untersucht. Dann wurde ein physikalisches Modell zur quantitativen Beschreibung der besonderen I-V-T Charakteristik der untersuchten NW-LEDs entwickelt.

Stichwörter: Galliumnitrid, GaN, (In,Ga)N, Nanodrähten, Leuchtdioden, MBE, ITO, Top-Kontakt, Elektrolumineszenz, EQE, Strom-Spannung, Multi-Element, tiefen Störstellen, DLTS

Publications

Publications of parts of this work

M. Musolino, A. Tahraoui, F. Limbach, J. Lähnemann, U. Jahn, O. Brandt, L. Geelhaar, and H. Riechert, *Understanding peculiarities in the optoelectronic characteristics of light emitting diodes based on (In,Ga)N/GaN nanowires*, Appl. Phys. Lett. **105**, 083505 (2014).

M. Musolino, A. Tahraoui, S. Fernández-Garrido, O. Brandt, A. Trampert, L. Geelhaar, and H. Riechert, *Compatibility of the selective area growth of GaN nanowires on AlN-buffered Si substrates with the operation of light emitting diodes*, Nanotechnology **26**, 085605 (2015).

M. Musolino, M. Meneghini, L. Scarparo, C. De Santi, A. Tahraoui, L. Geelhaar, E. Zanoni, and H. Riechert, *Deep level transient spectroscopy on light-emitting diodes based on (In,Ga)N/GaN nanowire ensembles*, Proc. of SPIE **9363**, 936325 (2015).

F. Sacconi, F. Panetta, M. Auf der Maur, A. Di Carlo, A. Pecchia, M. Musolino, A. Tahraoui, L. Geelhaar, and H. Riechert, *Multiscale approach for the study of optoelectronic properties of InGaN/GaN nanowire light-emitting diodes*, Proc. of IEEE **978**, 8156 (2015).

J. K. Zettler, C. Hauswald, P. Corfdir, M. Musolino, L. Geelhaar, H. Riechert, O. Brandt, and S. Fernández-Garrido, *High-Temperature growth of GaN nanowires by molecular beam epitaxy: Toward the material quality of bulk GaN*, Crystal Growth & Design **15**, 4104 (2015).

M. Musolino, D. van Treeck, A. Tahraoui, M. Meneghini, L. Scarparo, C. De Santi, E. Zanoni, L. Geelhaar, and H. Riechert, *A physical model for the reverse leakage current in (In,Ga)N/GaN light-emitting diodes based on nanowires*, arXiv:1511.04044 [cond-mat.mes-hall] (2015).

Talks and conference presentations

M. Musolino, C. Hauswald, F. Limbach, M. Wölz, O. Brandt, R. Calarco, L. Geelhaar and H. Riechert, *Towards light-emitting diodes based on the selective-area growth of III-N nanowires on Si substrates* (poster presentation), Nanowires workshop, Berlin, Germany, September 2012.

M. Musolino, C. Hauswald, F. Limbach, M. Wölz, T. Gotschke, O. Brandt, L. Geelhaar and H. Riechert, *Toward light-emitting diodes based on homogenous III-N nanowire ensembles on Si substrates* (contributed talk), Frühjahrstagung der Deutschen Physikalischen Gesellschaft (DPG), Regensburg, Germany, March 2013.

M. Musolino, F. Limbach, A. Tahraoui, O. Brandt, L. Geelhaar and H. Riechert, *Significant improvement of the device characteristics of light-emitting diodes based on GaN nanowires* (contributed talk), European Material Research Society (E-MRS) Spring Meeting, Lille, France, May 2014.

M. Musolino, *Recent progress in light emitting diodes based on (In,Ga)N/GaN nanowire ensembles on Si* (seminar talk), Institute of Semiconductors (Chinese Academy of Sciences), Beijing, China, November 2014.

M. Musolino, M. Meneghini, L. Scarparo, C. De Santi, A. Tahraoui, L. Geelhaar, E. Zanoni and H. Riechert, *Deep level transient spectroscopy on light-emitting diodes based*

on *(In,Ga)N/GaN nanowire ensembles* (poster presentation), SPIE Photonics West, San Francisco (CA), USA, February 2015.

M. Musolino, A. Tahraoui, S. Fernández-Garrido, O. Brandt, A. Trampert, L. Geelhaar, G.-Z. Xu and H. Riechert (**presenter**), *Compatibility of the selective area growth of GaN nanowires on Si substrates with the operation of light emitting diodes* (contributed talk), Compound Semiconductor Week (CSW), Santa Barbara (CA), USA, June 2015.

M. Musolino, D. van Treeck, M. Meneghini, C. De Santi, E. Zanoni, A. Tahraoui, L. Geelhaar, and H. Riechert, *In-depth physical description of the current conduction in light-emitting diodes based on (In,Ga)N/GaN nanowire ensembles* (poster presentation), Nanowire workshop, Barcelona, Spain, October 2015.

Abbreviations

AFM	atomic force microscopy
BEP	beam equivalent pressure
C-AFM	conductive atomic force microscopy
CB	conduction band
CL	cathodoluminescence
EBIC	electron beam induced current
EBL	electron blocking layer
eBL	electron beam lithography
EDX	energy dispersive x-ray spectroscopy
EL	electroluminescence
EQE	external quantum efficiency
FWHM	full width at half maximum
HVPE	hydride vapor phase epitaxy
IQE	internal quantum efficiency
LD	laser diode
LED	light emitting diode
LO	longitudinal optical
MBE	molecular beam epitaxy
MOCVD	metalorganic chemical vapour deposition
NIL	nanoimprint lithography
NW	nanowire
PL	photoluminescence
QMS	quadrupole mass spectroscopy
RHEED	reflection high-energy electron diffraction
QCSE	quantum-confined Stark effect
QW	quantum well
QWR	quantum wire
RIE	reactive ion etching
RTA	rapid thermal annealing
SEM	scanning electron microscopy
TD	threading dislocation
TEM	transmission electron microscopy
VB	valence band
XRD	x-ray diffractometry

List of basic symbols

Symbol	Name	Unit
a	in-plane lattice parameter (along the $[11\bar{2}0]$ direction in α -GaN)	Å
a_0	Bohr radius (0.529×10^{-10})	m
c	out-of-plane lattice parameter (along the $[0001]$ direction in α -GaN)	Å
c_0	speed of light (299 792 458)	m s^{-1}
C_{ij}	elastic constants	GPa
q	elementary charge (1.602×10^{-19})	C
e_{ij}	piezoelectric tensor	C m^{-2}
E_F	Fermi energy	eV
E_g	band gap energy	eV
$E_{C,V}$	conduction band minimum / valence band maximum energy	eV
ΔE	energy difference	eV
$\Delta E_{C,V}$	conduction / valence band offset	eV
E_t	trap energy	eV
F	electric field strength	MV cm^{-1}
ϵ	dielectric constant	
ϵ_0	vacuum permittivity (8.854×10^{-12})	F m^{-1}
ϵ_r	relative permittivity	
h	Planck constant (6.626×10^{-34})	Js
\hbar	Planck constant divided by 2π (1.054×10^{-34})	Js
k_B	Boltzmann constant (1.381×10^{-23})	J K^{-1}
m_0	electron rest mass (9.109×10^{-31})	kg
$m_{e,h}^*$	effective mass of electrons / holes	m_0
$N_{D,A}$	donor / acceptor concentration	cm^{-3}
$P_{sp,pz}$	spontaneous / piezoelectric polarization	C m^{-2}
σ	capture cross-section	cm^2
$\tau_{r,nr}$	radiative / non-radiative lifetimes	s
T	temperature	K
u	internal cell parameter of the wurtzite structure	
ΔV	potential difference	eV
ω	angular frequency	rad/s

Contents

Introduction	1
1. The group-III-nitride material system for solid-state lighting	5
1.1. Crystal structure and band structure of group-III-nitrides	5
1.2. Light emitting diode basics	11
1.2.1. Operation principle of the LED	12
1.2.2. Electrical properties	14
1.2.3. Optical properties	16
1.3. Application of GaN nanowires as LEDs	18
2. Growth of group-III-N structures for NW-LEDs by molecular beam epitaxy	21
2.1. MBE basics and experimental apparatus	22
2.1.1. In-situ analytical tools	23
2.1.2. Calibration of the fluxes in growth rate units	26
2.2. Growth of self-induced GaN nanowires by MBE	27
2.2.1. Growth mechanisms of self-induced GaN NWs	28
2.2.2. Preparation of the Si substrates	31
2.2.3. Growth of self-induced (In,Ga)N/GaN NW-LEDs	33
2.3. Selective-area growth: Optimization of the AlN layer	39
2.3.1. A three-step approach for the growth of AlN layers on Si	40
2.3.2. Optimization of the AlN thickness	42
2.3.3. Microstructure of the AlN layer and current conduction	46
2.4. Selective-area growth of GaN NWs	50
2.4.1. Fabrication of a multi-purpose mask	50
2.4.2. Selective-area growth of GaN nanowires	53
2.4.3. Fabrication of ordered arrays of GaN quantum wires	55
3. Fabrication of (In,Ga)N/GaN NW-LEDs	61
3.1. Optimization of the fabrication process	62
3.1.1. Planarization of the NW ensemble	63
3.1.2. Spatial distribution of the current injected into the NW ensemble	65
3.1.3. Deposition and characterization of the p-type top contacts	68
3.2. Comparison of NW-LEDs with Ni/Au and ITO top contact	69
3.2.1. Characteristics of the contacts on the microscopic scale	70
3.2.2. Evolution of the density of EL spots with the applied bias	72
3.2.3. Comparison of the current-voltage characteristics	74

Contents

3.2.4. Effect of the top contact on the emission properties	76
3.3. Comparison of NW-LEDs on AlN-buffered and bare Si	78
4. Investigation of the opto-electronic characteristics of NW-LEDs	83
4.1. Emission properties of NW-LEDs	84
4.1.1. Evolution of the electroluminescence with the current	84
4.1.2. External quantum efficiency and ABC model	88
4.1.3. Colorimetric properties	92
4.1.4. Temperature dependence of PL and EL spectra	93
4.2. Effect of the multi-element nature of the NW-LEDs on the forward I-V characteristics	101
4.2.1. The limits of the Shockley model	101
4.2.2. Interpretation of the I-V curves	104
4.3. Deep level transient spectroscopy on NW-LEDs	107
4.3.1. Capacitance-voltage measurements	107
4.3.2. DLTS basics	109
4.3.3. Analysis of the DLTS measurements	110
4.3.4. The signature of the main deep level traps in NW-LEDs	112
4.4. A physical model for the reverse bias regime	115
4.4.1. Experimental data and introduction to conduction mechanisms . .	116
4.4.2. Temperature dependence of the reverse current	120
4.4.3. Fitting the I-V curves in the temperature range 83–403 K	122
4.4.4. Discussion of the fitting parameters	125
Conclusion and outlook	131
A. Sample list	135
Bibliography	139
Acknowledgements	159

Introduction

Worldwide demand for lighting grows hand in hand with technological development and world population, therefore it does not surprise that the energy consumption to illuminate our world dramatically increased in the last century. A conservative estimate made by the International Energy Agency forecasts that the global demand for artificial lighting will be 80 % higher by 2030^[1]. Worldwide, electric lighting consumed about 2650 TWh of electricity in 2005, that was 19 % of the total global electricity consumption. Taking all buildings together (residential, industrial, and commercial), lighting is the second cause of energy consumption in buildings. Consequently, lighting is one of the biggest causes of greenhouse gas emissions, roughly 1.9×10^{12} kg of CO₂ per year^[1].

Not only does lighting require a significant amount of energy, it is also extremely inefficient. Incandescent light bulbs convert only 5 % of the electricity they use into visible light, the rest is wasted as heat^[2]. Even energy-saving compact fluorescent lamps (a phosphor-coated gas discharge tube) have efficiencies of only about 20 %. Indeed, lighting is so inefficient, and it requires so much electricity, that there is probably more potential for large energy savings in this field than in any other area. A considerable reduction of energy consumption can be obtained by replacing conventional lighting sources by solid state lighting (SSL) technology, namely light-emitting diodes. SSL is evaluated as the most efficient lighting technology^[2]; it can emit light typically two times more efficiently than fluorescent lamps and ten times more efficiently than incandescent lamps, although current products have not yet reached a fully mature stage. Nowadays, light-emitting diodes (LEDs) are often used in traffic lights, vehicle lights, for street and home lighting, in smartphones, and in many other electronic devices.

In the last two decades the SSL technology was literally revolutionized by the introduction of GaN-based laser diodes (LDs) and LEDs into the market. Within few years, the efficiency of white-light sources obtained from GaN-based planar heterostructures has increased very quickly, outclassing many of the standard lighting technologies, such as incandescent bulbs, halogen lamps, mercury vapour tubes, and fluorescent lamps. In particular, white-light sources based on GaN LEDs have reached a similar luminescence efficiency as the sodium lamp, namely about 200 lmW^{-1} (lumens per watt)^[3]. Another advantage of the LED lamps is the possibility to combine in the same device emitters of different colours and independently tune their intensity. In this way chromaticity control, better light quality, and higher efficiency can be achieved.

Nowadays, the most common strategy to obtain white light from LEDs is to convert the blue or ultraviolet (UV) light emitted by (In,Ga)N/GaN heterostructures into white light by means of phosphor particles, which are embedded in the polymer material that

encapsulates the LED chip. This approach has several intrinsic limitations mainly related to the conversion efficiency of the phosphor and to the heat dissipation that degrades the performance of the device. Considering various aspects, a theoretical maximum luminescence efficacy of about 260 lmW^{-1} has been estimated for LEDs based on blue emitters and yellow phosphor^[3]. This means that, if the development proceeds as expected, the present GaN-LED technology will reach its ultimate limitations in the next years. For this reason a long term strategy to produce even more efficient light sources is required.

One of the most promising novel approaches for the development of a new generation of LEDs is the one based on GaN nanowires (also called nanorods or nanocolumns). Light emitting devices based on nanowires (NWs) are thought to produce a breakthrough development in solid state lighting in the near future^[4]. In general, NWs are three-dimensional (3D) structures with high aspect ratio, namely their height is several times more extended than their width, and nanoscopic sizes. Because of the very small dimensions and large surface-to-volume ratio the NWs are suitable for a wide range of different applications^[5]. Limiting the treatise to light emitting devices, NW-based LEDs have many potential advantages as compared to their planar counterparts, at present used in SSL. In fact, beyond the already mentioned limitations related to heat management and efficiency of phosphor, other important issues make the design of LEDs based on GaN planar heterostructures difficult. In particular, the lack of high-quality and low-cost GaN substrates inevitably leads to epitaxial growth on materials with large lattice mismatch. The LEDs based on thin films are also plagued by an efficiency droop at high injection currents and high In content^[6,7]. Furthermore, the realization of good red emitters based on III-nitride films, required to achieve white light without using phosphor, is inhibited by the presence of a high amount of strain in the (In,Ga)N/GaN heterostructure, when high In concentrations are used.

Nanowire based LEDs can respond to these challenges. In fact, the NW geometry enables the elastic relaxation of the strain induced by lattice mismatch at the free sidewalls^[8]. This peculiarity enables the growth of high quality (In,Ga)N/GaN heterostructures with high In content on several different substrates, including Si. Furthermore, the small footprint of the NWs on the substrate inhibits the vertical propagation of extended defects, which develop only at the interface with the substrate and bend towards the nearest sidewall^[9]. Moreover, light outcoupling from arrays of NWs can be enhanced compared to planar devices^[10]. In combination, these benefits could lead to cost-effective phosphorless monolithic white LEDs^[11]. The mentioned properties of NWs might even enable the integration of GaN-based devices in the standard silicon based technology. Indeed, GaN NWs can be grown with high crystalline quality on Si(111) and Si(100) substrates, as well as on SiO₂ layers^[12–14]. This field is so attractive that in the last few years several companies made significant investments to develop a new generation of LEDs based on NWs (sometimes called 3D-LED)^[15,16]. Despite the increasing interest and the many improvements obtained in the field of NW-based LEDs, many fundamental issues critical for the fabrication of efficient devices are still unresolved and require further investigations.

In this context, this PhD thesis aims at providing an in-depth insight on various crucial aspects of the NW-based LEDs. Different topics are covered in this work, from the epitaxial growth of the (In,Ga)N/GaN heterostructures to the technological processing steps required to fabricate working devices, ending with a careful investigation of the optoelectronic properties of NW-LEDs. In particular, the presented research deals with green NW-LEDs based on axial heterostructures grown by molecular beam epitaxy (MBE). Ax-

ial heterostructures obtained on top of thin NWs are very interesting for opto-electronic applications because they enable the elastic relaxation of the strain and the incorporation of a high amount of In in the (In,Ga)N quantum wells. For this reason NW-based axial heterostructures might help to solve the “green-gap” issue, which is a challenging aspect in the field of LEDs^[7].

This thesis can be in principle divided into two main logical lines: the discussion of new or optimized strategies to fabricate NW-LEDs with improved performance, and the in-depth characterization of the obtained devices to achieve a deeper understanding of their opto-electronic properties. The former topic is covered in chapter 2 and 3, whereas chapter 4 deals with the latter issue.

The first chapter introduces some general information on basic semiconductor physics and operating principles of GaN-based LEDs. The fundamental concepts needed to understand the different topics covered in the following parts of the thesis are presented and the work is further motivated. The second chapter is dedicated to the growth of the samples produced on purpose for this thesis; in particular, the Mg doping is optimized so as to obtain ensembles of well separated NWs with good opto-electronic properties. Furthermore, a new way to achieve functional LEDs based on ordered arrays of NWs grown on Si substrates is paved; in particular, the compatibility of selective-area growth via AlN buffer layers with the operation of LEDs is discussed. An innovative strategy to realize ordered arrays of ultrathin GaN NWs is also presented. The third chapter addresses several issues related to the realization of functional NW-LEDs. The optimization of various technological processing steps is presented, in particular the planarization of the NW ensembles and the formation of the p-type top contact is discussed. An astonishing improvement of the device performance is achieved by optimizing the p-type top contact. In the fourth chapter, the fabricated NW-LEDs are characterized by means of a wide spectrum of different techniques including: capacitance measurements (C-V), deep level transient spectroscopy (DLTS), temperature dependent current voltage measurements (I-V-T), as well as photoluminescence (PL) and electroluminescence (EL) acquired at different currents and temperatures. The opto-electronic properties of the NW-LEDs are carefully analysed. Furthermore, various models are developed to explain the peculiar transport characteristics of the investigated samples; they lead to a deeper understanding of the fundamental physics of this type of devices. A final chapter is dedicated to a summary of the obtained results and to further comments and conclusions.

The group-III-nitride material system for solid-state lighting

In this chapter general information on semiconductor physics and the operating principle of GaN-based light emitting diodes (LEDs) is summarized. The fundamental concepts needed for the understanding of the different topics covered in the thesis are presented. For a deeper treatise of fundamental properties of nitrides and the operation of GaN-based LEDs, the reader is directed to the text books by H. Morkoç^[17,18], E. F. Schubert^[19], and S. M. Sze^[20]. In addition to the general information provided in this chapter, specific aspects required for the understating of the presented measurements will be discussed in more detail throughout the thesis.

Section 1.1 focuses on the fundamental properties of the group-III-nitride (III-N) materials. Then, structure and operating principle of LEDs based on (In,Ga)N/GaN heterostructures are presented. Finally, general aspects of the nanowires and the advantages of three-dimensional structures for the fabrication of LEDs are discussed.

1.1. Crystal structure and band structure of group-III-nitrides

Crystal structure

In a single-crystalline solid the individual atoms are arranged in a highly ordered, periodic lattice extending in all directions. The type of bonds and the arrangement of the atoms in the lattice mainly depends on the size and on the electronic properties of the different elements. Group-III-N semiconductors such as GaN, AlN, and InN exhibit two different crystal phases: the thermodynamically meta-stable zincblende phase with a cubic symmetry and the stable wurtzite phase in which the atoms are arranged in a hexagonal close-packed lattice. The two structures and their characteristic parameters are depicted in figures 1.1 (a) and (b). The wurtzite structure (also known as α -phase) consists of alternating bi-atomic planes of metal (Ga, Al, or In) and N pairs stacked in the ABAB sequence along the [0001] direction, this means that the atoms in the first and third layer are directly aligned to each other. In contrast, the zincblende structure (or β -phase) is characterized by the ABCABC stacking sequence along the [111] direction. It is worth noting that since wurtzite and zincblende structures only differ in the stacking sequence of the atomic planes, the coexistence in the same crystal of the two phases can be caused by the formation of stacking fault defects.

1. The group-III-nitride material system for solid-state lighting

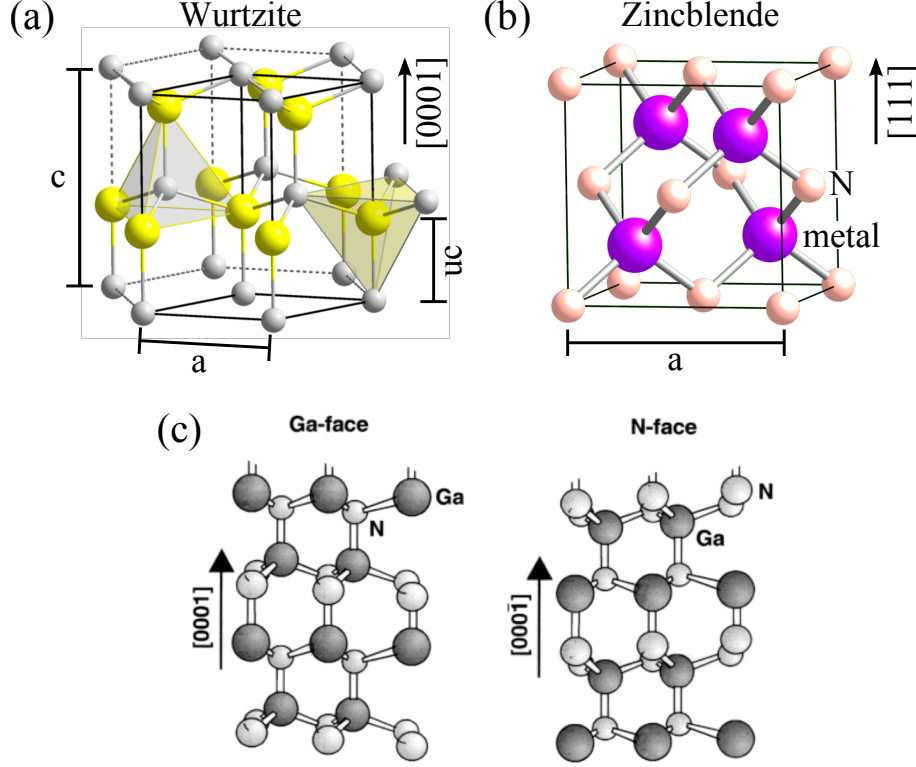


Figure 1.1: Crystal structures of the III-nitride semiconductors with (a) wurtzite phase and (b) zincblende phase. The metal atoms are depicted by the large balls, whereas the small ones represent the N atoms. (c) Illustrative scheme of the two possible crystalline polarities in wurtzite GaN as sketched in Ref. [21].

The wurtzite structure can be uniquely described by three parameters: the edge length of the basal hexagon (a), the height of the prism (c), and a third parameter (u) which defines the anion-cation bond length. Because of the different electronegativity of Ga, Al, and In atoms, the corresponding nitrides have different lattice constants, binding energies, and band gap. The fundamental parameters of GaN, AlN, InN*, and Si are summarized in table 1.1.

The technological relevance of the III-nitride semiconductors is given by their ability to form ternary and even quaternary compounds such as: $In_xGa_{1-x}N$, $Al_xGa_{1-x}N$, or $In_xAl_yGa_{1-x-y}N$. The equilibrium lattice parameters a and c of the alloy can be estimated by mean of Vegard's law, which expresses the final lattice constants of the compound as a linear combination of the lattice parameters of the original species. The weights of the linear combination are given by the relative concentration of the different species. For instance, in case of the out-of-plane lattice constant c of an $In_xGa_{1-x}N$ alloy Vegard's law is written as

$$c^{InGaN} = x c^{InN} + (1 - x) c^{GaN} \quad (1.1)$$

*Due to the difficulty of synthesizing high-quality InN crystals, the band structure of this semiconductor has been for long time subject of controversy. Nevertheless, it is nowadays widely accepted that InN has a direct band gap with $E_g = 0.68$ eV at 300 K [22].

1.1. Crystal structure and band structure of group-III-nitrides

Table 1.1: Fundamental parameters of the semiconductors of interest for this thesis. All the data are taken from Ref. [21–24].

Parameters (at 300 K)	α -GaN	α -AlN	α -InN	Si
In-plane lattice constant a (Å)	3.189	3.112	3.545	5.431
Out-of-plane lattice constant c (Å)	5.185	4.982	5.703	
Internal parameter u	0.376	0.380	0.377	
Energy gap E_g (eV)	3.51	6.25	0.78	1.12
Dielectric constant (static) ϵ_r	8.9	8.5	15.3	11.9
Electron effective mass (m_e^*/m_e)	0.22	0.32	0.07	0.91
Electron mobility μ ($\text{cm}^2\text{V}^{-1}\text{s}^{-1}$)	440	300	3200	1350
LO phonon energy (meV)	91.2	99	73	62.9
Spontaneous polarization (Cm^{-2})	-0.034	-0.09	-0.042	
Piezoelectric constant e_{31} (Cm^{-2})	-0.49	-0.60	-0.57	
Piezoelectric constant e_{33} (Cm^{-2})	+0.73	+1.46	+0.97	
Elastic constant C_{13} (GPa)	106	108	92	
Elastic constant C_{33} (GPa)	398	373	224	
Thermal conductivity ($\text{Wcm}^{-1}\text{K}^{-1}$)	1.3	2.9	0.45	1.48
Thermal expansion coeff. α (10^{-6}K^{-1})	5.59	4.2	3.8	2.59
Melting point T_m (K)	2791	3273	2146	1687

Symmetry and Polarization

Both wurtzite and zincblende structures have polar axes due to the lack of inversion symmetry of the crystal. This results in a stacking sequence always terminated either by metal or nitrogen atoms. The crystal is called metal-polar (or metal-face) when its last bi-atomic plane ends with Ga atoms, whereas it is called N-polar (or N-face) if characterized by bi-atomic planes terminated by N atoms. An illustrative scheme of the two structures in case of wurtzite GaN is shown in figure 1.1 (c). The chemophysical properties of both bulk and surface are significantly influenced by the polarity of the crystal; this issue will be addressed in more detail in section 2.2.

In the wurtzite crystal structure atoms of opposite electronegativity lie above each other along the [0001] direction, this causes a charge rearrangement that gives rise to a dipole along the same axis. This polarization dipole has non-zero values also in absence of external electric field, for this reason it is called spontaneous polarization. The magnitude of the spontaneous polarization in wurtzite group-III-nitrides has been calculated by Bernardini and co-authors [25], and experimentally determined by Lähnemann and co-authors [26]; the values obtained in case of metal-polar GaN, AlN and InN are listed in table 1.1. Note that the sign of the macroscopic polarization depends on the polarity of the crystal, and will thus be positive in case of N-polar material. In a ternary alloy, such as for example $\text{In}_x\text{Ga}_{1-x}\text{N}$, the dependence of the spontaneous polarization (P_{sp}) on the relative concentrations of the elements, can be estimated by means of the equation [27]

$$P_{sp}^{\text{InGa}} = x P_{sp}^{\text{InN}} + (1 - x) P_{sp}^{\text{GaN}} + x(1 - x) B_{sp} \quad (1.2)$$

where B_{sp} represents the so-called *bowing parameter*, which accounts for non linear effects; in case of (In,Ga)N alloys $B_{sp} \approx 0.038 \text{ Cm}^{-2}$.

1. The group-III-nitride material system for solid-state lighting

In contrast to the wurtzite case, the higher symmetry of the zincblende structure causes a compensation of the electric dipoles along the four [111] equivalent directions. Therefore, spontaneous polarization is negligible in zincblende crystals.

When the wurtzite structure is subjected to strain also a piezoelectric polarization is produced. From a microscopic point of view, the strain produces an internal displacement of the metal sub-lattice with respect to the nitrogen one, *i. e.*, a variation of the internal parameter u . This causes a spatial redistribution of the polarization charge in comparison with the unstrained state. In absence of external electric fields, the total macroscopic polarization of the crystal is given by the vector addition of spontaneous polarization in the equilibrium lattice and piezoelectric polarization induced by strain. The latter one can be described by means of a tensor (e_{ij}) with three independent non-vanishing components. The piezoelectric polarization along the [0001] direction, P_{pz3} , can be calculated by using the components e_{33} and e_{13} of the piezoelectric tensor

$$P_{pz3} = e_{33} \epsilon_3 + e_{31} (\epsilon_1 + \epsilon_2) \quad (1.3)$$

where $\epsilon_3 = (c_s - c)/c$ represents the strain along the [0001] direction, whereas $\epsilon_1 = \epsilon_2 = (a_s - a)/a$ is the in-plane strain, which is assumed to be isotropic. Here, c_s and a_s are the final out-of-plane and in-plane lattice parameters of the strain crystal. The third independent component of the piezoelectric tensor (e_{15}) is instead related to the polarization induced by shear strain, usually not considered in axial heterostructures in absence of external forces. In the wurtzite structure, out-of-plane and in-plane lattice parameters are linked by the relation

$$\frac{c_s - c}{c} = -2 \frac{C_{13}}{C_{33}} \frac{a_s - a}{a} \quad (1.4)$$

where C_{13} and C_{33} are the in-plane and out-of-plane elastic constants, respectively. Combining equations (1.3) and (1.4) the piezoelectric polarization along the [0001] direction can be calculated by means of the formula

$$P_{pz3} = 2 \frac{a_s - a}{a} \left(e_{31} - e_{33} \frac{C_{13}}{C_{33}} \right). \quad (1.5)$$

This equation is valid in the linear regime for small values of the strain. Piezoelectric constants of GaN, AlN, and InN semiconductors have been calculated by Bernardini *et al.* [25] and are listed, together with the interesting elastic constants, in table 1.1.

Typically, in (In,Ga)N/GaN heterostructures, the polarization effects result in high internal electric fields of the order of MV/cm. Such strong fields significantly influence the optical properties of the (In,Ga)N quantum wells (QWs), resulting in a red shift of the emission energy due to the Stark and Franz–Keldysh effects [17,21]. Furthermore, deformation of the band edges of the heterostructures causes a spatial separation of the electrons from the holes, thus decreasing the overlap of their wave functions and their recombination probability. This phenomenon is known as quantum confined stark effect (QCSE).

Band structure and electron-hole recombinations

The quantum mechanical behaviour of the electrons in an atom is described by the Schrödinger wavefunction. In a solid, the electrons are subjected to the electrostatic potential of the

1.1. Crystal structure and band structure of group-III-nitrides

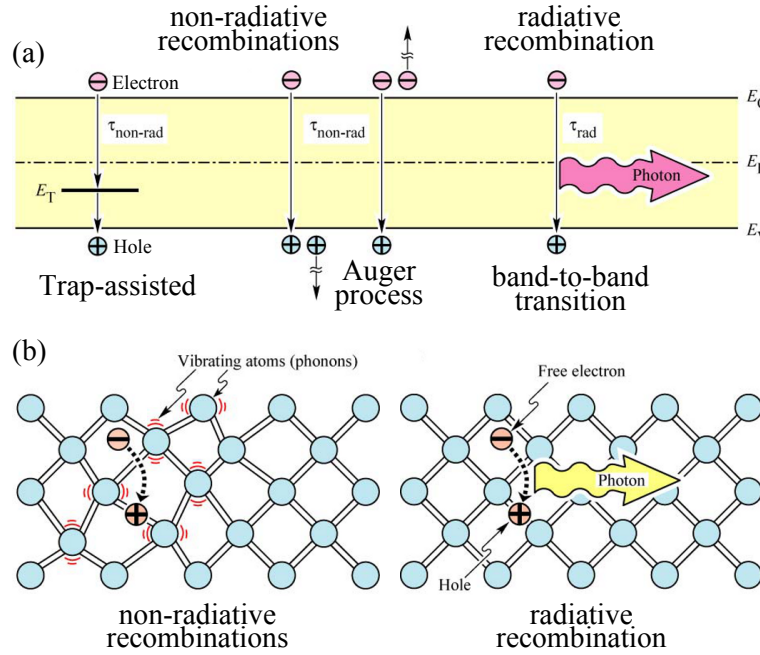


Figure 1.2: (a) Band diagram depicting the main recombination channels in a semiconductor: from left to right trap-assisted decay, recombination via Auger process, and band-to-band transition. (b) Illustration of the electron-hole pair recombination occurring non-radiatively with the emission of a phonon or radiatively with the emission of a photon. Images adapted from Ref. [19].

atoms, which are so close together that the electron wavefunctions overlap. In 1928 the Swiss physicist Felix Bloch demonstrated that a consequence of the interaction between electron wavefunction and crystal potential is the formation of continuous energy bands, which do not exist in case of free electrons with quantized energy states^[28]. In semiconductor materials, the allowed energy bands are separated by a forbidden region called band gap. An electron in a solid can change its quantum mechanical state from a higher to a lower energy level through different channels, the energy difference between the two quantum states is converted in other forms. Usually, a recombination process occurs when an electron in the conduction band (CB) of the semiconductor relaxes into an unoccupied state in the valence band (VB), commonly denoted as hole. The holes can move in the valence band as the electrons do in the conduction band, and can be described as positive charge particles with wave functions equivalent to the ones of the electrons.

Figure 1.2(a) shows the three main recombination channels present in an LED: trap assisted decay, Auger process, and band-to-band transition. In the first mechanism a electron is trapped by deformations of the potential due to defects in the ordered crystal lattice, such traps usually produce states with energy levels inside the band gap; after a certain time, the trapped electron will decay emitting a phonon (*i. e.*, a crystal vibration). The process is illustrated on the left side of figure 1.2(b), this recombination channel is usually non-radiative. An other type of transition without emission of photon is the one occurring via the Auger effect; this is a three-particle process in which the filling of a hole in the inner-shell of an atom by an electron is accompanied by the emission of an other electron from the same atom. The most important recombination channel, at the base of the LED operation, is the band-to-band transition, that occurs when an electron relaxes from the conduction band to the valence band of the semiconductor; this kind of

1. The group-III-nitride material system for solid-state lighting

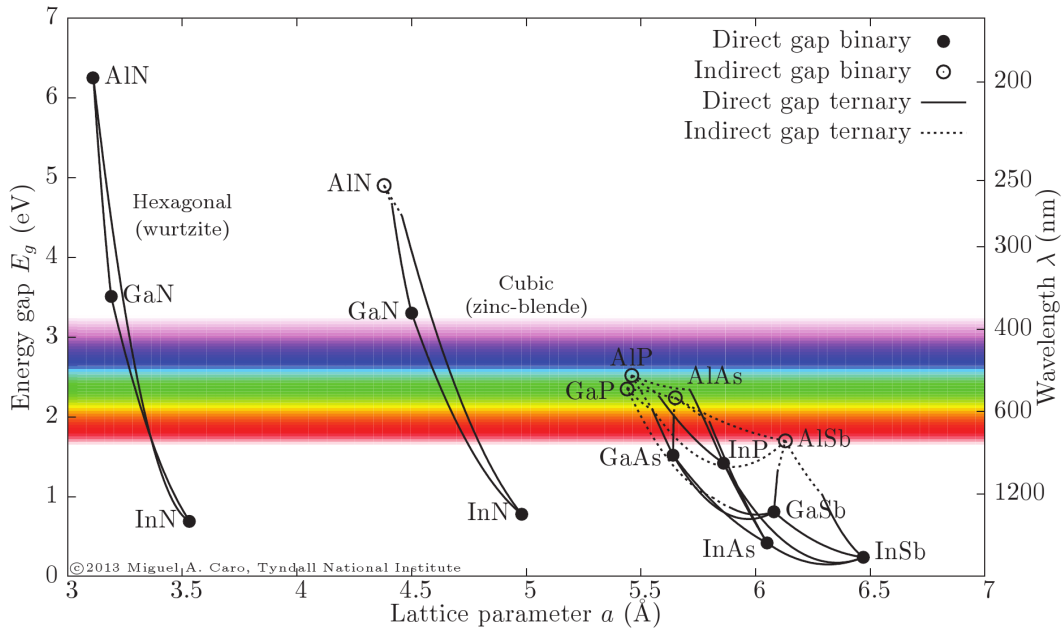


Figure 1.3: Energy band gap of various semiconductors used to fabricate LEDs as a function of the in-plane lattice parameter a , replotted from Ref. [29].

transition is usually radiative, *i. e.* a photon with energy close to the band gap is emitted ($h\nu \approx E_g$). This process is depicted on the right side of figure 1.2(b), in this case no energy is wasted with the emission of phonons. Note that electron-hole pairs can recombine only if their wavefunctions overlap spatially, thus the two particles must remain close to each other for a period of time longer than their characteristic life time.

Thanks to the extraordinary emission properties of III-nitride systems, many new optoelectronic devices were commercialized in the last 15 years, such as for instance blue and UV laser diodes, and white LEDs. In the last few years, the latter are gaining an increasingly importance on the market, and they are expected to replace the existing lighting sources in the near future. The reason for this huge success can be understood by looking at the graph in figure 1.3. In fact, the III-nitride semiconductors have direct band gaps characterized by energies ranging from 0.68 eV, for α -InN, up to 6.2 eV, for α -AlN. In this way, III-nitride alloys can be used to produce light sources with emission frequency spanning not only the entire visible spectrum but also the UV and infrared (IR) regions; thus paving the way to a number of different technological applications. As visible in figure 1.3, such a wide emission energy spectrum cannot be covered by the other material systems traditionally used to produce solid-state optical devices, namely III-arsenide, III-phosphide, and III-antimonide.

The wurtzite III-nitride semiconductors exhibit, in the vicinity of the Γ point, a split of the valence band into three different bands, commonly denoted as: heavy hole (HH), light hole (LH), and split-off (SO) or crystal hole (CH)^[23]. In particular, the latter one is due to spin-orbit and crystal-field interaction. In the case of ternary compounds, such as $In_xGa_{1-x}N$ or $Al_xGa_{1-x}N$, the band gap energy (E_g) changes gradually depending on the relative concentration of the different elements. The composition dependence of the band gap can be approximated by means of a quadratic relation^[23]; for example, in case

of $\text{In}_x\text{Ga}_{1-x}\text{N}$ alloy it is given by

$$E_g^{\text{InGa}} = x E_g^{\text{InN}} + (1 - x) E_g^{\text{GaN}} + x(1 - x) B_g \quad (1.6)$$

where B_g represents the so-called *bowing parameter*, which accounts for the deviation from a linear interpolation between the two constituent species; in case of (In,Ga)N alloys $B_g \approx 1.4 \text{ eV}$ ^[30]. Note that, the width of the band gap is also subjected to perturbations due to strain, alloy disorder, and potential fluctuations inside the crystal. These effects could cause discrepancies between the real band gap of the alloy and the one predicted by equation (1.6).

Substrates and related issues

Despite their technological importance, one of the main challenges of III-nitride semiconductors is still the lack of a lattice-matched substrates for epitaxial growth that are available at low cost and with large size. For this reason the manufacture of opto-electronic devices based on III-nitrides still relies on heteroepitaxy on various substrates with relatively large misfit of both lattice parameters and thermal expansion coefficients, such as Al_2O_3 , 6H-SiC, and Si. The heteroepitaxial growth on mismatched substrates inevitably produces strain and defects in the material, which are usually detrimental for the operation of the final device. Despite many growth expedients, such as use of heterostructures and patterned substrates, have been developed to compensate the strain and reduce the density of extended defects in the material^[31], the use of free-standing GaN substrates would be desirable to further improve the performances of the devices. Nowadays, the only company commercializing GaN-based LEDs homoepitaxially grown on free-standing GaN substrates is the American *Soraa Inc.* Recently, they have demonstrated that the higher cost of the free-standing GaN substrates are compensated by significant improvements of the device performances^[32].

The leading companies in the production of GaN-based optoelectronic devices (namely, *Osram*, *Cree*, *Nichia*, *Lumileds*, etc.) are following different strategy for the production of LEDs, employing various substrates for the GaN growth. It is hard to predict whether one of these approaches will dominate in the future, or they will simply be employed for different applications.

1.2. Light emitting diode basics

The first observation of luminescence induced by electrons injected into a semiconductor, namely electroluminescence (EL), was reported by H. J. Round in 1907^[33]. He observed EL from a SiC crystallite, he also noted that the colour of the emitted light changed with applied voltage, and that it was possible to inject current only when a positive bias was applied (rectifying behaviour). The investigation of the fascinating electroluminescence coming from artificial and natural crystals such as SiC, ZnS, and CdS proceeded in the following decades; doping and other optimizations were introduced to control the emission wavelength and improve the performance of the SiC LEDs^[34]. The SiC and ZnS LED prototypes were outclassed, in the 1950s, by the invention of a new class of artificial materials based on III-V semiconductors, namely GaAs, AlGaAs and GaAsP. These new material systems were found to be optically very efficient because of their direct band gap. First infrared LEDs and then laser diodes (LDs) based on GaAs and GaAsP

1. The group-III-nitride material system for solid-state lighting

were reported in 1962^[35]. In the mid 1960s the first infrared LED based on GaAsP was commercialized by *Texas Instruments Inc*[†].

Also during the 1960s research on GaN as a candidate for blue emitters was initiated. Although EL from GaN was reported already in the early 1970s^[36], the lack of an efficient p-type doping technique for GaN delayed the fabrication of the first functional LED until 1989. In this year Amano and co-authors demonstrated a method to obtain p-type doping of GaN by using activated Mg acceptors^[37]. Soon after the first p-n junction, LED and laser were demonstrated by Nakamura and co-authors^[38,39]. The Nobel prize in physics 2014 was awarded to Isamu Akasaki, Hiroshi Amano, and Shuji Nakamura for the invention of the GaN based blue LED[‡]. Over the last 20 years huge effort was spent to further improve the performance of GaN-based LEDs and LDs, to realize multicolour emitters and to develop white-light sources for solid-state lighting^[2].

1.2.1. Operation principle of the LED

LEDs combine the advantages of light sources and rectifying diodes; in fact, an LED emits light only if a bias higher than a certain threshold value is applied, otherwise it conducts only a negligible amount of current. This characteristic makes the LED not only a powerful light source but also a very useful element in many circuits, for instance as control light.

The p-n junction

In order to achieve a rectifying behaviour with a homojunction, the semiconductor must be doped so as to form a p-n junction. To this end, foreign atoms are introduced into the crystalline lattice of the intrinsic (pure) semiconductor. Impurity atoms can act either as donors or acceptors, changing the electron and hole concentrations in the host semiconductor. Donor impurity atoms have more valence electrons than the atoms they replace in the lattice of the host semiconductor. The surplus electron has usually a low ionization energy, and it is easily released into the conduction band, thus increasing the electron carrier concentration (n) of the semiconductor, making it n-type. In contrast, acceptor impurity atoms have less valence electrons than the atoms they replace; for this reason, they can trap electrons from the valence band, leaving excess holes. The hole concentration (p) in the host semiconductor is thus increased, and the material becomes p-type. It is worth noting that in binary or ternary alloys, impurity atoms might act both as donors and acceptors depending on which element of the host semiconductor they replace; this phenomenon is called amphoteric behaviour. For example, Si doping in GaN produces n-type material if the Si atoms substitute the Ga, but the material will exhibit p-type characteristic if the Si atoms replace the N^[17]. In doped semiconductor, the extrinsic electron (hole) concentration dominate over the intrinsic one; therefore, the Fermi level E_F of the semiconductor shifts, from the centre of the band gap, towards the conduction (valence) band edge.

A p-n junction is created by doping different regions of the same semiconductor either with donor or acceptor impurities. At the interface between the two regions excess electrons (in the n-side) and holes (in the p-side) are present. To re-establish an equilibrium in the crystal, charge carriers migrate between the p- and the n-side of the junction, thus producing a band bending and the alignment of the respective Fermi levels. The excess

[†]<http://www.datamath.org/Display/Monsanto.htm>

[‡]http://www.nobelprize.org/nobel_prizes/physics/laureates/2014/press.html

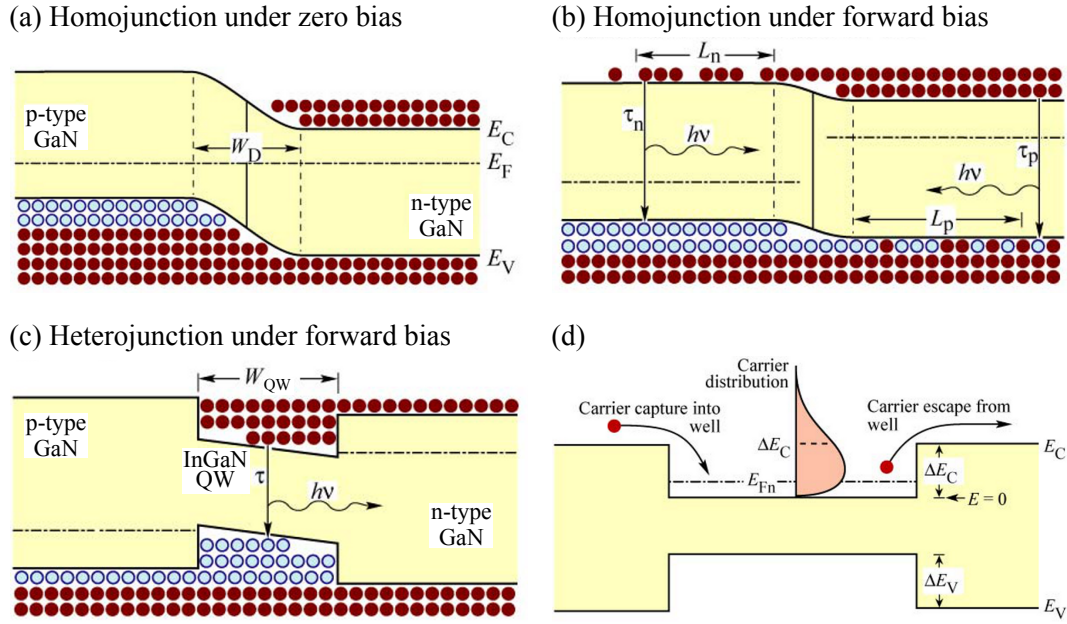


Figure 1.4: Illustration of the operation principle of an LED. (a) The p-n homojunction is depleted under zero bias, no recombination takes place. (b) Forward bias promotes diffusion of charge carriers, thus enabling recombination of electron-hole pairs and luminescence. (c) A double heterostructure with an (In,Ga)N QW embedded between the p-n junction. (d) Carrier distribution in the conduction band of a QW with barrier height ΔE_C . Adapted from Ref. [19].

electrons drift from the n-side to the p-side, leaving behind atoms with positive charge. A charge region (also called depletion region) of width W_D is thus formed at the interface. The fixed charge remaining after the electron migration produces an electric field inside the depletion region, which prevents further charges to drift. In this way an equilibrium condition is established and no current flows through the junction. The resulting band diagram and the occupation of the available states under zero bias are shown in figure 1.3(a).

If a positive bias is applied at the p-side of the junction (hereafter called forward bias), the strength of the electric field at the interface decreases, and the diffusion of charge carriers from both sides of the junction is promoted. Electroluminescence results from the recombination of electrons and holes, which are now spatially close, see figure 1.3(b).

Heterostructure-based LED

In the modern LED the EL emission is significantly enhanced by forcing electrons and holes to gather in a very small spatial region, called quantum well (QW), where high carrier concentrations are obtained. This is possible by means of heterostructures, obtained by combining materials with different band gaps; in GaN-based LEDs, the QW typically consists of an $\text{In}_x\text{Ga}_{1-x}\text{N}$ layer, see figure 1.3(c). The QW traps the charge carriers in a very small space equal to its width (W_{QW}), thus increasing the spatial overlap of electron and hole wave functions, and enhancing the recombination rate. An other important advantage of a heterostructure-based LED is the possibility to tune the energy of the emitted photons simply by changing the depth of the well. In case of (In,Ga)N/GaN heterostructures the emission energy can be tuned by varying either the In content or the thickness

1. The group-III-nitride material system for solid-state lighting

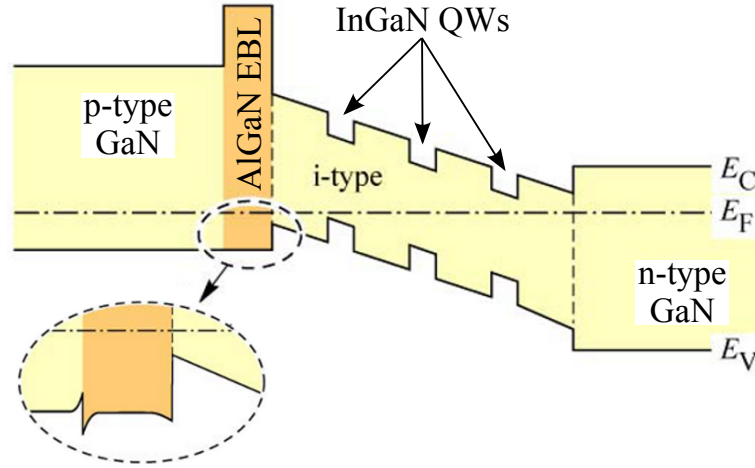


Figure 1.5: Band alignment in a heterostructure-based LED with multiple (In,Ga)N QWs and (Al,Ga)N EBL. Adapted from Ref. [19].

of the (In,Ga)N layer.

The efficiency of light creation in the QW depends on its capture cross section and on its ability to confine the carriers. The charge confinement usually improves with increasing depth of the QW. In any case, the energy of electrons in the conduction band varies accordingly to the Fermi-Dirac distribution, and thus some of the carriers can have energies high enough to escape from the well, which is usually few hundreds of meV deep. The carrier distribution in the conduction band of a QW with barrier height ΔE_C is depicted in figure 1.3(d). The electron leakage from the QW becomes even more important at high injected currents. In this case, the number of charge carriers injected into the QW might saturate all the available states; electrons would then overflow out from the well.

To counteract the carrier leakage, which is detrimental for the efficiency of the LED, two expedients are commonly adopted in modern LEDs. On the one hand, usually more QWs are piled up; hence, electrons escaping from a QW can be captured by the next one. On the other hand, an electron blocking layer (EBL) is deposited between the p-side and the active region of the LED. The EBL is a thin layer of a material characterized by band gap higher than that of the semiconductor constituting the QWs. In case of GaN-based devices, an (Al,Ga)N layer is usually employed; the resulting structure of a typical LED is shown in figure 1.5. The EBL creates an energy barrier for the electrons in the conduction band, thus stopping their drift into the p-type region of the junction. Note that the main contribution to the leakage current is caused by electrons, because they have a diffusion length longer than that of holes. To avoid the formation of a barrier also in the valence band, which would affect the injection of holes in the active region, the (Al,Ga)N EBL is p-type doped. In this way, the entire band discontinuity between (Al,Ga)N and GaN is shifted into the conduction band. The inset of figure 1.5 shows the detail of the valence band edge at the (Al,Ga)N/GaN interface, where a small potential spike and notch occur. Holes must tunnel through the thin potential spike to reach the active region and recombine.

1.2.2. Electrical properties

In this subsection, the electrical characteristics of an ideal p-n junction are described by using the standard diode model derived by William Shockley in the early 1950s^[40]. More

advanced models including different conduction mechanisms present in GaN-based NW-LEDs will be discussed in detail in sections 4.2 and 4.4.

The model considers an abrupt p-n junction with donor and acceptor concentrations equal to N_D and N_A , respectively. The dopants are assumed to be ionized, hence the free electron and hole concentrations are $n = N_D$ and $p = N_A$, respectively. Under this conditions, the potential present in the depletion region of the p-n junction, called diffusion voltage (V_D), can be written as

$$V_D = \frac{k_B T}{q} \ln \left(\frac{N_A N_D}{n_i^2} \right) \quad (1.7)$$

where n_i is the intrinsic carrier concentration of the semiconductor, k_B is the Boltzmann constant, whereas T and q represent the temperature and the elementary charge, respectively. The diffusion voltage defines the potential barrier that carriers must overcome to reach the opposite side of the junction. The diffusion voltage is related to the width of the depletion region by the formula

$$W_D = \sqrt{\frac{2\epsilon}{q} (V_D - V) \left(\frac{1}{N_A} + \frac{1}{N_D} \right)} \quad (1.8)$$

where $\epsilon = \epsilon_r \epsilon_0$ is the dielectric permittivity of the semiconductor and V is the applied bias. When a forward bias is applied, the injected electrons (holes) can migrate from the n-type (p-type) region to the opposite side of the p-n junction, where they recombine. The formula that describes the resulting current flow as a function of the applied bias is called Shockley equation

$$I = I_S \left(\exp \left(\frac{qV}{k_B T} \right) - 1 \right) \quad (1.9)$$

$$\text{with} \quad I_S = qA \left(\sqrt{\frac{D_p}{\tau_p}} \frac{n_i^2}{N_D} + \sqrt{\frac{D_n}{\tau_n}} \frac{n_i^2}{N_A} \right) \quad (1.10)$$

where the pre-exponential factor I_S is called saturation current and represents the drift of charge carriers occurring in an ideal rectifying diode under reverse (negative) bias. In the expression of I_S , A represents the area of the junction, whereas $D_{n,p}$ and $\tau_{n,p}$ are the electron and hole diffusion constants and carrier lifetimes, respectively. For forward biases much higher than $k_B T/q$, for instance $V \gg 0.025$ V at $T=300$ K, the exponential term of equation (1.9) dominates (namely, $\exp(qV/k_B T) \gg 1$). Therefore the Shockley formula can be rewritten using equation (1.7) as

$$I = qA \left(\sqrt{\frac{D_p}{\tau_p}} N_A + \sqrt{\frac{D_n}{\tau_n}} N_D \right) \exp \left(\frac{q(V - V_D)}{k_B T} \right). \quad (1.11)$$

The exponential term of this equation indicates that the diode current strongly increases as the applied bias approaches V_D . For this reason, V_D is also said threshold or knee voltage of the diode. For highly doped semiconductors the separation between the band edges and the Fermi level is much smaller than the band gap. In this case, the diffusion voltages can be approximated by the band gap energy divided by the elementary charge: $V_D \approx V_{th} \approx E_g/q$. This relationship holds true for many semiconductors; nevertheless,

1. The group-III-nitride material system for solid-state lighting

III-nitride LEDs exhibit often a threshold voltage slightly higher than the one predicted by this equation^[19]. This effect is mainly caused by large band gap discontinuities occurring in the nitride material system, relatively poor p-type conductivity, and difficulties in obtaining very good p-type contacts.

The Shockley equation describes the theoretically expected current-voltage characteristic of an ideal p-n junction. The measured I-V characteristics often deviate from the ideal behaviour. In particular, parasitic effects such as resistance of the contacts and of the neutral regions, and leakage currents due to conduction mechanisms not considered by the Shockley model might influence the current conduction in the diode. In order to fit the experimental data, three more empirical parameters are introduced in the Shockley model: the so called ideality factor η and two resistances R_S and R_P imagined as in series and in parallel to the diode, respectively. Hence, equation (1.9) becomes

$$I = I_S \left\{ \exp \left[\frac{q(V - IR_S)}{\eta k_B T} \right] - 1 \right\} + \frac{(V - IR_S)}{R_P} \quad (1.12)$$

An ideal diode would have $\eta = 1$, however ideality factors between 2 and 7 have been observed in III-nitride LEDs. The ideality factor of the GaN-based NW-LED will be discussed in section 3.2.3 and 4.2.

1.2.3. Optical properties

In this section the basic optical properties of the LEDs are introduced. Other aspects of the EL emission from the semiconductors interesting for this thesis are discussed in section 4.1.

The basic physical principle underlying the light emission from LEDs is the spontaneous recombination of electron-hole pairs and the simultaneous emission of photons. Figure 1.6 illustrates the recombination of an electron-hole pair in a semiconductor with direct band gap. Electrons and holes are assumed to have parabolic energy dispersion relations in the momentum space described by

$$E = E_{C,V} \pm \frac{\hbar^2 k^2}{2m_{e,h}^*} \quad (1.13)$$

where k is the wave vector, \hbar represents the Planck constant divided by 2π , and $m_{e,h}^*$ is the effective mass of electrons or holes. Electrons will thermalize to the conduction band minimum, whereas holes to the valence band maximum. Since the momentum of the emitted photon is negligible, energy conservation requires that the energy of the photon ($h\nu$) generated in the annihilation process equals the difference between the energies of the two particles: $h\nu = E_e - E_h \approx E_g$. In other words, the energy of the emitted photon is approximately equal to the band gap of the semiconductor; this approximation is particularly true for all the material with $E_g \gg k_B T$. Therefore the desired wavelength of light emitted by the LED can be tuned by choosing an appropriate semiconductor with the desired band gap.

A quantity able to describe the conversion efficiency of an LED, namely the ratio between the number of emitted photons and injected charge carriers, is required to assess the quality of the device. Typically, the internal quantum efficiency (IQE) is used to describe the efficiency with which photons are created in the active region. It is defined

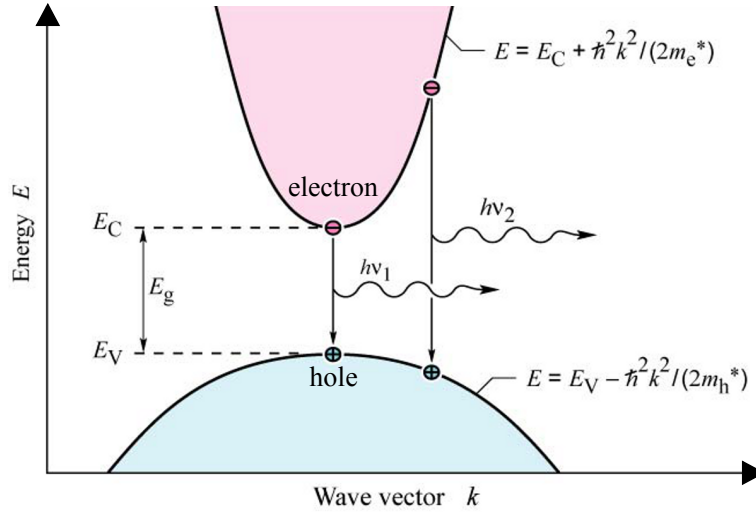


Figure 1.6: Illustration of electron and hole dispersion relations for a semiconductor with direct band gap, and recombination in momentum space. Adapted from Ref. [19].

as^[19]

$$IQE = \frac{\text{number of photons emitted per second}}{\text{number of electrons injected into the QW per second}} = \frac{P_{int}/(h\nu)}{I/(q)} \quad (1.14)$$

where P_{int} represents the emitted optical power, I is the current injected into the active region, $h\nu$ is the photon energy, whereas q represents the elementary charge. An ideal LED would have $IQE=1$; in other words for every injected electron-hole pair one photon would be emitted. In a real device, because of re-absorption or internal reflection of the light, not all photons created can escape out of the crystal. The extraction efficiency (η_{ext}) quantifies this effect:

$$\eta_{ext} = \frac{\text{number of photons emitted into free space per second}}{\text{number of photons produced per second}} = \frac{L/(h\nu)}{P_{int}/(h\nu)} \quad (1.15)$$

where L is the optical power emitted into free space. The product of internal and extraction efficiencies gives the so called external quantum efficiency (EQE)

$$EQE = IQE \eta_{ext} = \frac{L/(h\nu)}{I/(q)} \quad (1.16)$$

Practically, the most important figure of merit for the final LED is the power conversion efficiency η_{PC} , also known as *wallplug efficiency*, defined as the ratio of emitted optical power and consumed electrical power

$$\eta_{PC} = \frac{L}{IV} \quad (1.17)$$

State-of-the-art GaN-based LEDs exhibit impressive performance with power conversion efficiency in the ultraviolet range of about 70 % and IQE higher than 85 % at injected current density of 100 Acm^{-2} ^[32]. Nevertheless, their IQE significantly drops down to 50 % and 20 % at the same injected current density in case of blue and green LEDs, respectively^[7,41].

1.3. Application of GaN nanowires as LEDs

Shrinking the size of electronic components improves efficiency and operation speed of the devices, minimizing at the same time their power consumption and production cost. This idea was the main driving force behind the extraordinary development of microelectronics in the second half of the last century. At present, the structure size in silicon-based integrated circuits approaches physical limits, and fundamentally new device geometries must be explored. Also for this reason, the research field of nanotechnologies experienced a rapid expansion and gained much attention during the last decades. In this context, semiconductor nanowires are playing an important role.

Because of their very small dimensions and large surface-to-volume ratio, semiconductor NWs are suitable for a wide range of different applications^[5]. In electronics NW-based field-effect transistors, NOR-gates, and p-n junctions have been demonstrated. Because of their large surface NWs have been used as sensor devices with very high sensitivity. In photonics lasers, LEDs, single-photon emitters, and waveguides have been realized employing semiconductor NWs. These 3D structures have been found to be potentially very useful for the realization of efficient photovoltaic cells, and for the photosynthesis of various elements, for instance, hydrogen and oxygen from the electrolysis of water (called solar-water splitting). Furthermore, NW arrays have been used for the fabrication of lithium-ion battery prototypes employed for energy storage. In mechanics, NWs have found application as resonators and piezoelectric devices. Moreover, in bionics the small size of the NWs has been exploited to probe the interaction between nanostructures and cells. From the mentioned examples the great potential of semiconducting NWs for future technologies becomes clear.

Beyond the practical applications, nanostructures are also very interesting for the study of basic physical phenomena occurring once the size of the semiconductor becomes smaller than the wavelength of light or even comparable with the Bohr radius of the electrons. In these cases, plasmonic and quantum effects occur. Another example of basic physics investigations enabled by NWs is the study of Majorana fermions in semiconductor^[42].

An alternative to planar LED device geometry

In the framework of this thesis the application of GaN NWs as LEDs is addressed. In the previous sections we have already discussed the crucial role played by SSL to satisfy the increasing demand of efficient light sources. Nowadays, GaN-based white LEDs are playing a leading role in this field; they exploit various types of phosphors to convert the blue or UV light emitted by planar (In,Ga)N QWs into white light^[19]. Although very good performances have been obtained with this approach, some intrinsic issues of these systems set a maximum limit for the improvements that might not be easily overcome. For this reason, in the last few years many companies specialized in the fabrication of LEDs made significant investments to develop new approaches, among which the most promising seems to be that one based on NW-LEDs^[15,16][§].

Important challenges for the design of LEDs based on (In,Ga)N/GaN planar heterostructures are: the lack of high-quality and low-cost GaN substrates, which makes inevitable

[§]Further information can be found on the web pages of the companies:


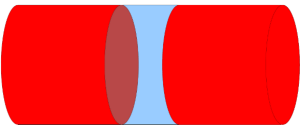
http://www.osram.de/osram_de/news-und-wissen/innovation

<http://www.aledia.com/en/technology>

<http://www.glo.se/technology.html>

<http://www.nordicgreen.net/startups/energy-efficiency/ecospark-ab>

Table 1.2: Various strategies for the design of (In,Ga)N/GaN heterostructures within the NW geometry. Adapted from Ref. [51].

(In,Ga)N/GaN heterostructure geometry	QW alignment	Main differences from C-plane planar device
<p>radial</p> 	M-plane (nonpolar)	<ul style="list-style-type: none"> • no QCSE • increased area of the active region
<p>axial</p> 	C-plane (polar)	<ul style="list-style-type: none"> • reduced QCSE • elastic strain relaxation enables incorporation of more In

the epitaxial growth on materials with large lattice mismatch; the poor efficiency of LEDs at high injection current^[6]; and the difficulty to incorporate high concentrations of In in the QWs caused by residual strain in the heterostructure. NW-based LEDs can respond to these challenges. In fact, the NW geometry enables the elastic relaxation of the strain induced by lattice mismatch at the free sidewalls^[8]. This peculiarity enables the growth of high quality (In,Ga)N/GaN heterostructures with high In content on several different substrates; particularly important are Si substrates due to their wide availability at low price and in large size. Light emission in the entire visible spectral range from blue to red, and even in the ultraviolet and infrared has successfully been demonstrated using (In,Ga)N/GaN heterostructures based on NWs^[43–47]. Moreover, QWs with different emission energies can be combined in the same device to achieve white LEDs without the need for phosphors^[48–50]. Furthermore, the small footprint of the NWs on the substrate inhibits the vertical propagation of extended defects up to the active region of the LEDs^[9]. In addition, light extraction from arrays of NWs can be enhanced compared to planar devices^[10]. This effect is based on the consideration that a light wave cannot be confined in a space smaller than its wavelength, and hence internal reflection is suppressed in comparison to planar films. In combination, these benefits could lead to cost-effective phosphorless monolithic white LEDs^[11].

The NW geometry enables various strategies for the design of (In,Ga)N/GaN heterostructures; the two main possibilities are shown in table 1.2. On the one hand, the active region of the LED can be grown radially on the M-plane side facets of the NWs; these facets are non-polar, and thus inhibit the presence of the QCSE. In addition, the shell geometry increases the surface area of the active region compared to a planar device, thus obtaining a larger emitting area and, at the same time, a lower current density in the QWs. On the other hand, the active region of the LED can be grown axially on the C-plane top facet of the NWs. In this case, if the diameter of the nanocolumn is small enough, interface strain at the heterostructure can elastically relax at the free sidewalls^[52]. In this thesis only axial heterostructures are treated.

Growth of group-III-N structures for NW-LEDs by molecular beam epitaxy

In the framework of this thesis various types of samples were grown: some of them are planar AlN layers, others self-induced or selective-area-grown GaN NW ensembles, and others again LED structures based on (In,Ga)N/GaN NWs. In any case they were produced by means of molecular beam epitaxy (MBE). Although the main topic of this work is the fabrication and characterization of functional NW-LEDs, some effort was also spent on the optimization of the growth parameters and on the development of new growth strategies to improve the performance of the final NW-LEDs.

In this chapter the growth of the samples produced on purpose for this thesis is presented; possible optimization of structure and growth parameters are discussed. Scanning electron microscopy (SEM) and atomic force microscopy (AFM) were used as standard characterization tools to analyse the morphology of the sample surface. When necessary, the crystallographic structure of the samples was further investigated by means of reflection high-energy electron diffraction (RHEED), X-ray diffraction (XRD) and transmission electron microscopy (TEM).

In the first section of the chapter the MBE technique is reviewed and the employed experimental equipment is presented. A brief overview on the *in-situ* characterization tools and on the standard calibration methods is provided. In the second section the current understanding on the formation processes of self-induced GaN NWs and (In,Ga)N/GaN axial heterostructures grown by MBE is summarized. Then, the LED samples grown in a self-assembled fashion on Si(111) are presented. In the last part of the chapter the selective-area growth (SAG) of GaN NWs for the fabrication of functional NW-LEDs with homogeneous emission properties on Si substrates is discussed. Our approach to SAG is based on AlN buffer layers, which thickness must be kept as thin as possible to obtain current conduction across the substrate. A new strategy for the growth of very thin AlN layers on Si is developed. Then, two different lithographic approaches, namely nanoimprint lithography and electron-beam lithography, for the patterning of the nano-features required for SAG are presented. Finally, the growth parameters and the morphology of the GaN SAG NWs samples are discussed. Furthermore, a novel strategy for the formation of ordered arrays of ultrathin quantum wires is described.

Extracts from these studies were presented at the Nanowires 2012 workshop held in Berlin (Germany), at the DPG spring meeting 2013 held in Regensburg (Germany), and at the CSW 2015 conference held in Santa Barbara (USA), and can be found in ref.^[53].

2.1. MBE basics and experimental apparatus

Molecular beam epitaxy is a versatile technique employed mainly for the epitaxial growth of thin films. The distinguishing characteristic of this technique is the ultra-high vacuum (UHV) ambient present inside the deposition chamber. The UHV condition has two main advantages: it suppresses the presence of impurities in the reactor, and thus their incorporation into the crystal, and minimizes the interaction between the impinging species so that they can reach the substrate as a molecular beam following a straight-line path^[54,55]. A third benefit of the UHV ambient is the feasibility of *in-situ* characterization techniques such as surface analysis by electron diffraction and desorption studied by line-of-sight quadrupole mass spectrometry (QMS). The molecular beams are usually provided by means of Knudsen thermal effusion cells. Mechanical shutters placed in front of the apertures of the cells enable a precise control of the molecular fluxes. The impinging atoms crystallize on the surface of the substrate which is maintained at elevated temperature. Because of the rather low fluxes employed, usually MBE has a slower growth rate than other fabrication methods, such as for example metalorganic vapour phase epitaxy (MOCVD). The slow growth rate has several advantages during the deposition of heterostructures: for instance, it provides a high degree of controllability of the stacking sequence and enables the formation of very smooth interfaces.

The experiments presented in this thesis were performed in three different MBE systems installed at the Paul-Drude-Institut (PDI) called MBE1, MBE8, and MBE9. The first one is a commercial P600 MBE apparatus fabricated by *DCA Instruments*, while MBE8 and MBE9 are custom designed systems manufactured by *Createc Fischer GmbH*. The growth chambers of all these machines are equipped with several Knudsen effusion cells used for the evaporation of metals (Ga, Al, and In) and dopant elements (Si and Mg). Figures 2.1(a) and (b) show the main features of the growth chambers employed in this work. Radio frequency (RF) plasma sources are used to dissociate the rather stable N_2 molecules into excited nitrogen species (neutral atoms, ions, and active molecules); the

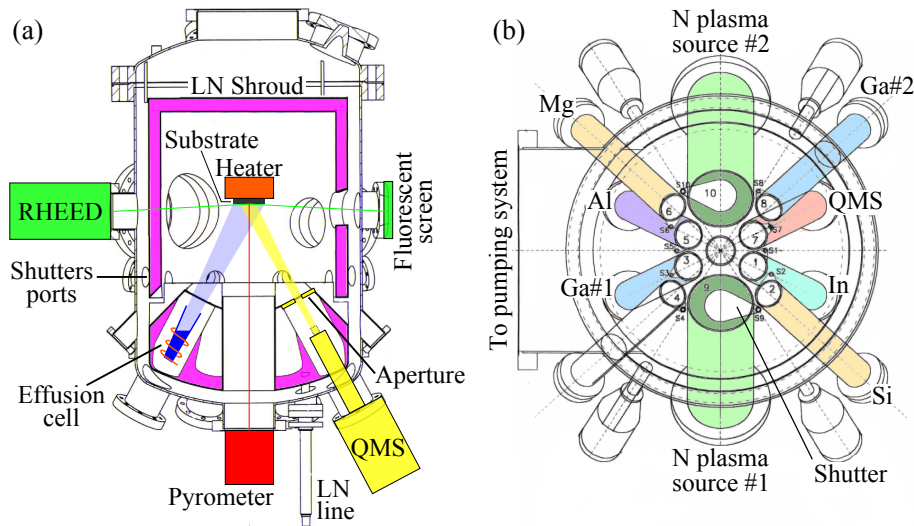


Figure 2.1: (a) Vertical cross-section of the growth chamber of MBE9. The main parts of the system and the installed components are shown. (b) Horizontal cross-section of the growth chamber of MBE8 in top-view; the position of effusion cells, shutters and of plasma sources is indicated.

dissociation efficiency of a common plasma source is about 10 %. The presence of a high density of ions in the nitrogen flow might affect the material quality by introducing point defects in the crystal lattice. However, it has been observed that the ion concentration can be reduced down to 0.1 % by optimizing the design of the plasma source^[56]. The obtained atomic nitrogen is chemically very active and bonds with many metals (Ga, Al, In, Hg, Zn, Cd, Mg etcetera), thus creating various types of nitrides. Each reactor is also equipped with useful tools for *in-situ* characterization of the samples during the growth. In particular a reflection high-energy electron diffraction (RHEED) system, a line-of-sight quadrupole mass spectrometer (QMS), and an optical pyrometer are mounted in the three growth chambers, see figure 2.1(a).

In MBE1 and MBE8 a stand-by base pressure in the growth reactor roughly equal to 1×10^{-10} mbar was obtained by means of a cryo pump, an ion getter pump and a cooling shroud filled with liquid nitrogen (LN). The same base pressure was obtained in MBE9 employing two turbo molecular pumps instead of a cryo pump. In all three machines, during the growth experiments the pressure in the reactor rose up to typically 2×10^{-5} mbar. The higher pressure during operation is due to the gaseous nitrogen flow coming from the plasma source. The substrate is heated by thermal radiation from above through a filament; the temperature is controlled by means of a thermocouple and can also be monitored through the calibrated optical pyrometer facing directly the centre of the substrate [see figure 2.1(a)]. The values of the substrate temperatures reported in this work were acquired by means of an optical pyrometer if higher than 400 °C and by a thermocouple in the case of lower values.

2.1.1. In-situ analytical tools

This subsection aims just at providing a brief overview on the operation principles of the two most used *in-situ* characterization tools present in our MBE systems: RHEED and QMS. A more detailed discussion on these instruments can be found in literature^[57–59].

RHEED

For long time RHEED is established as a powerful tool in MBE, and is routinely used to investigate growth rate, flatness, crystal structure, adlayer formation, and epitaxial relations of heterostructures^[57–60]. Furthermore, RHEED can be used to calibrate the substrate temperature by monitoring well-known temperature-dependent processes such as melting point, evaporation^[61], and surface reconstruction^[62].

In the RHEED technique an electron beam with high energy (5 – 40 keV) is focused onto the sample surface with a rather small angle ($1^\circ - 3^\circ$). The incident electrons are thus scattered by the atoms of the topmost atomic layers of the sample. Eventually, the scattered beam hits a fluorescent screen placed on the opposite side of the electron source and can thus be visualized [sketch shown in figure 2.1(a)]. The incident and scattered electrons can be described as planar waves with wave vectors equal to k_i and k_f , respectively. Constructive interference, and therefore high intensity of the scattered wave is obtained only when the difference between the wave vectors of incident and scattered electrons equals a translation of the lattice in the reciprocal space: $k_i - k_f = 2\pi n/a$, where a is the lattice parameter in the real space. In this way, the scattered electrons form specific pattern on the fluorescent screen.

In the framework of this thesis RHEED was mainly used to probe the morphology of the surface. The principal features of the RHEED patterns interesting for this purpose are

2. Growth of group-III-N structures for NW-LEDs by molecular beam epitaxy

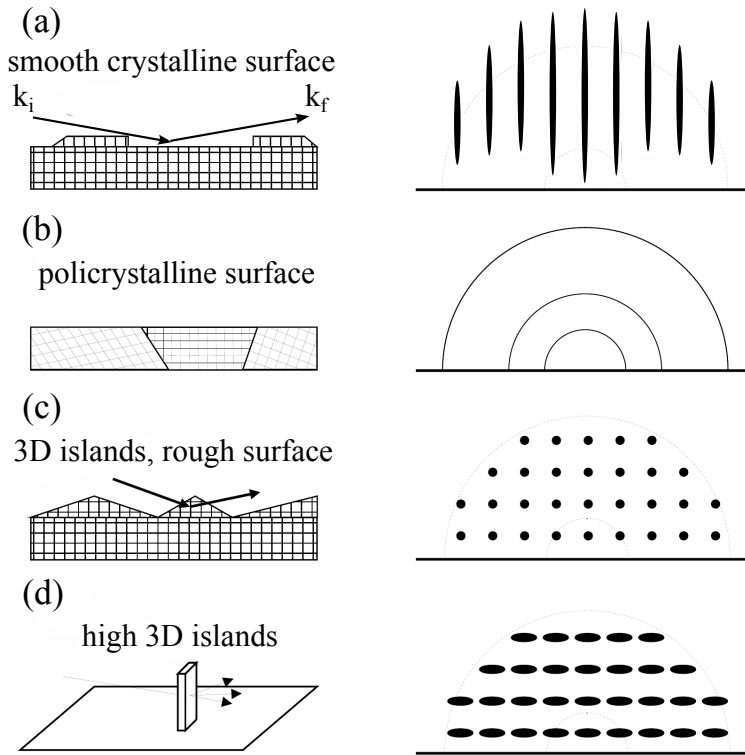


Figure 2.2: Correspondence between surface morphologies and RHEED patterns.

shown in figures 2.2(a)–(d).

Diffraction from an atomically smooth crystalline surface would produce a pattern of laterally equidistant reflections located on circles centred on the incident beam; because of the finite size of the e-beam and crystal imperfections a streaky pattern like the one shown in figure 2.2(a) is obtained in reality^[58]. Differently, a polycrystalline sample made of several grains with different orientations would create a ring pattern, as shown in figure 2.2(b); whereas, amorphous layers would correspond to a halo without any structure. If three-dimensional (3D) features or roughness are present on the sample surface, the electron beam can be scattered by several crystal planes, thus out-of-plane diffraction can be observed; this would result in a spotty RHEED pattern formed by reflections arranged in a grid, as shown in figure 2.2(c). If the 3D islands grow faster vertically than laterally (like in the case of nanowires), the RHEED reflections would broaden laterally, thus acquiring a slightly oval shape, as depicted in figure 2.2(d).

Line-of-sight QMS

Mass spectrometry is routinely used for the residual gas analysis in vacuum chambers. In the last decades, this tool was also used in the MBE systems to obtain quantitative information about the elements desorbing from the substrate. In this variant, the spectrometer is arranged in line-of-sight configuration to the substrate, and can thus detect only the atoms desorbing from the sample surface. The line-of-sight QMS technique has demonstrated to be very useful for studying *in situ* the growth and surface kinetic processes of different materials deposited by MBE. In particular, it helped to understand the growth mode diagram for GaN layers^[63,64] and enabled a quantitative analysis of the

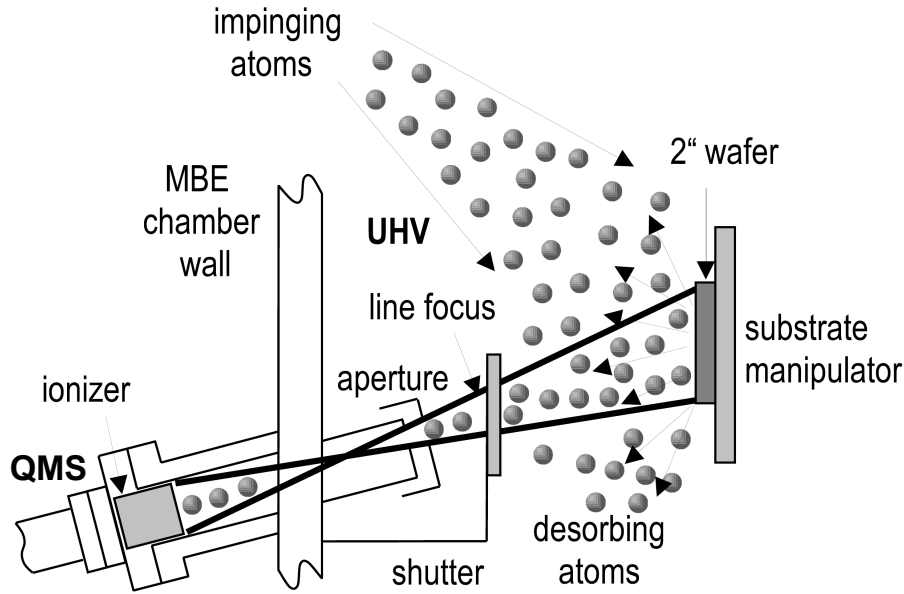


Figure 2.3: Schematic description of the operation of a line-of-sight QMS for the detection of desorbing atoms^[70]. An appropriate aperture plate limits the angle of acceptance to the size of the sample.

GaN decomposition processes^[65]. In addition, this technique is also very promising for studying the nucleation and growth of GaN NWs^[66–69].

Figure 2.3 illustrates the operation of a line-of-sight QMS employed for the detection of desorbing atoms. Because of the high substrate temperature, part of the impinging flux desorbs from the sample surface. A fraction of the desorbing atoms is detected by the QMS; the angle of acceptance can be adjusted by means of an appropriate aperture plate. In this way only the atoms coming from a specific part of the substrate can be collected; the aperture plate was designed so as to intercept only the flux desorbing from a roughly 1-inch-large area at the centre of the substrate. Therefore, the use of an aperture plate ensures that the measured signal is actually due to phenomena related to the growth processes; furthermore, it minimizes the background signal related to the desorption from the manipulator and/or the chamber walls.

The atoms that reach the QMS are ionized. The charged particles then travel through an electric field created by four electrodes to which a combination of direct and alternating voltages is applied^[59]. Depending on their mass to charge ratio various ions are deflected in different ways by the electric field. For a certain combination of applied voltages only the ions with a specific mass to charge ratio can thus be detected. The measured current is then amplified by means of an electron multiplier and converted into an equivalent partial pressure. The QMS devices installed in the MBE systems used for the experiments enable the detection of ions in a wide mass range, from 1 to 300 atomic mass units (amu). These devices can detect partial pressures roughly down to 1×10^{-13} mbar; nevertheless, the exact sensitivity of the QMS depends on several factors such as background pressure, ionization voltage, and integration time.

2. Growth of group-III-N structures for NW-LEDs by molecular beam epitaxy

2.1.2. Calibration of the fluxes in growth rate units

In this work the metal and nitrogen fluxes are given in equivalent growth rate units (*i. e.*, nm/min). On the one hand, this representation of the fluxes provides a direct and more intuitive relation between the employed amount of reagents and the actual growth rate of planar III-N layers. On the other hand, it differs both from the physical definition of flux (in units of atoms time⁻¹ area⁻¹) and from the commonly used beam equivalent pressure (BEP), usually given in Torr or mbar. Therefore, it is worth introducing the method used to express the fluxes in terms of equivalent growth rate unit. In this subsection only a brief overview of the topic is provided; a more detailed discussion can be found in literature^[70–72].

The flux of atoms emitted by a Knudsen effusion cells depends mainly on the shape of the crucible and on its filling level, which changes with the use. For this reason, a periodical calibration of the fluxes as a function of the effusion cell temperatures is necessary. Experimentally the temperatures of the crucibles containing the various metals are measured through W-Re thermocouples whereas the beam equivalent pressure (BEP) of the fluxes is determined by means of a retractable ion gauge, which can be placed in front of the substrate. The BEP measurements are acquired at different cell temperatures, starting from high values and then decreasing the temperature by 10 °C steps. In order to stabilize the fluxes a pause of 15 min between two consecutive measurements is taken. Then, the experimental data are fitted to the empirical formula

$$BEP = r \exp \left[\frac{1}{m_2} \left(m_1 - \frac{1}{T} \right) \right] \quad (2.1)$$

where r , m_1 and m_2 are fitting parameters which depend on the type of crucible and on its filling level. By way of example, the resulting fits of the BEP measurements carried out for a Ga and an In cell are shown in Figure 2.4. The agreement between BEP measurements and equation (2.1) is remarkable.

In order to correlate the measured BEP values of the metal fluxes with the actual amount of material that would be grown using a certain set of parameters (namely, cell

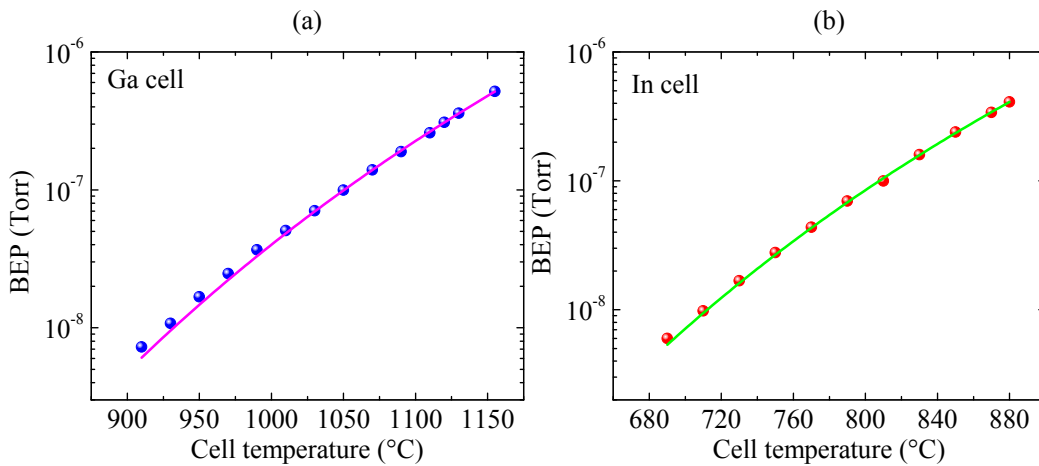


Figure 2.4: Semi-logarithmic plot of the BEP measurements carried out for (a) the Ga and (b) the In cell of one of the MBE systems used in this work. The solid lines depict the fits of the data to equation (2.1).

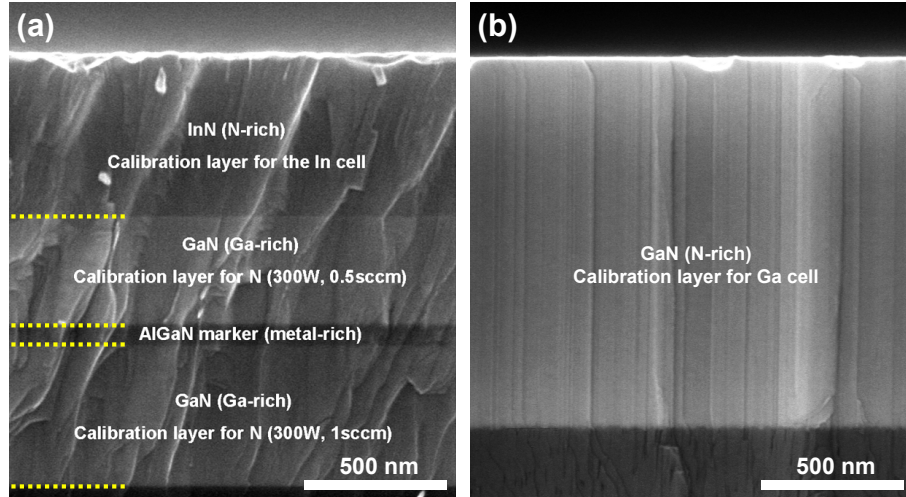


Figure 2.5: Cross-sectional SEM images of the planar layers grown to calibrate (a) the In and N fluxes and (b) Ga flux. Note that to improve the contrast between two layers of similar materials a thin (Al,Ga)N marker was deposited^[72].

temperature, N_2 flow and RF power of the plasma source), several thick planar layers of GaN, AlN, and InN were produced. To obtain a good crystal quality, the layers were deposited on commercial GaN templates grown on sapphire by hydride vapour phase epitaxy (HVPE) provided by *Kyma Technologies*. Figure 2.5 shows cross-sectional SEM images of the various GaN and InN layers used to calibrate (a) the In flux and the effective nitrogen flux for two different N_2 flows, and (b) the Ga flux. From these pictures the thickness of the various layers can be measured. For a given set of parameters, the equivalent growth rate (in nm/min) was estimated as the ratio of the thickness of the corresponding layer and the growth time.

To obtain calibrations with good accuracy, it is fundamental to minimize the amount of desorbing material during the growth. In an ideal case, all the impinging atoms of the element to be calibrated should be incorporated in the crystal. To this end, the samples were grown under specific conditions. To calibrate the metal fluxes (Ga, Al, and In) the layers were grown under slightly N-rich condition at temperatures for which the desorption of the considered metal is negligible. Under these conditions the growth rate is limited by the metal flux and all excess N desorbs, resulting in a stoichiometric GaN layer^[71]. Differently, to calibrate the N flux the GaN layers were grown under slightly Ga-rich condition at temperature lower than 740°C to avoid decomposition of the deposited GaN. Under these conditions the growth rate is limited by the active N flux and all excess Ga desorbs from the surface^[73].

2.2. Growth of self-induced GaN nanowires by MBE

This section aims at providing an overview on the current knowledge of the mechanisms involved in the self-induced growth of GaN NWs produced by MBE. Furthermore, structure, growth parameters, and morphology of the sample base of self-induced NW ensembles produced in this work are presented.

In general three-dimensional (3D) nanostructures with high aspect ratio (*i.e.*, with more prominent height than diameter) can be obtained by means of two opposite ap-

2. Growth of group-III-N structures for NW-LEDs by molecular beam epitaxy

proaches: the “Top-Down” and the “Bottom-Up” approach. In the former case a planar layer is selectively etched down to create the 3D nanostructures^[74,75]. In contrast, the latter approach implies that the nanostructures are grown *ab initio* on bare substrates by an epitaxial technique. The “Top-Down” fabrication employs as starting structure planar films, which may contain high density of extended defects in case of III-nitrides^[17]; the same defects will also be present in the final NWs. Moreover, additional defects could be produced by the etching process^[75]. Differently, the “Bottom-Up” method enables the growth of NWs in high crystalline quality on dissimilar substrates^[4]. In fact, the NW geometry does not favour the vertical propagation of extended defects like dislocations^[9]. Furthermore, the NW geometry allows the elastic relaxation of strain at the free sidewalls^[8,76], hence permitting the growth of (In,Ga)N/GaN heterostructures along the NW axis with higher In content than in the planar case. For all these reasons the “Bottom-Up” approach should be preferred for the fabrication of the final devices; it is worth mentioning that the two methods could also be combined^[77]. In this work only axial heterostructures grown by means of the “Bottom-Up” approach were produced.

The NWs can be grown through two main different processes: the “Vapor-Liquid-Solid” (VLS) and the “Vapor-Solid” (VS) growth method. In the former process the reagent materials in the gas phase are absorbed by liquid catalyst droplets and eventually precipitate forming the solid crystal^[78,79]. This technique has the principal disadvantage that the metal catalyst may contaminate the NW or react with the substrate^[80,81]. In contrast, the VS growth method does not require the use of any catalyst; the NWs form by self-organization phenomena from the gas phase. A direct comparison of the two approaches in case of GaN NWs grown by MBE can be found elsewhere^[82–84]. The NW samples presented in this thesis were grown by employing only the VS method.

Regardless the growth method, it is important to note that the self-induced NWs do not require any pre-patterning of the substrate. In contrast, this is necessary if one wants to exactly control the position and/or the shape of the nanostructure on the wafer. This technique is called selective-area growth (SAG) and is discussed in sections 2.3 and 2.4.

2.2.1. Growth mechanisms of self-induced GaN NWs

Although the first examples of GaN NWs grown by plasma-assisted MBE were reported already 18 years ago^[85,86], a complete growth diagram for such structures was published only in 2009^[87]. The Ga/N flux ratio and the substrate temperature define whether planar or columnar growth takes place. These regimes have been experimentally determined for a fixed nitrogen flux by Fernández-Garrido *et al.*; the resulting growth diagram is shown in figure 2.6. At very high substrate temperatures all the impinging Ga atoms desorb, and no growth occurs. The desorption of Ga atoms is thermally activated, and thus the Ga flux (Φ_{Ga}) required to compensate the desorption and obtain nucleation of GaN NWs exponentially increases with temperature. At low substrate temperatures, for which the Ga desorption is negligible, the NWs can be obtained only under N-rich growth conditions (*i.e.*, III/V flux ratio smaller than unity). In fact, for too low temperatures or too high Ga fluxes compact layers instead of NWs will form. Interestingly, nanocolumns can be obtained also in the nominally Ga-rich regime (III/V > 1) if the substrate temperature is high enough. However, because of desorption of Ga from the surface, also in this case the actual III/V flux ratio is smaller than unity.

In the following lines the growth mechanism of self-induced GaN NWs deposited by MBE on Si substrates is addressed. The growth process is commonly divided into two

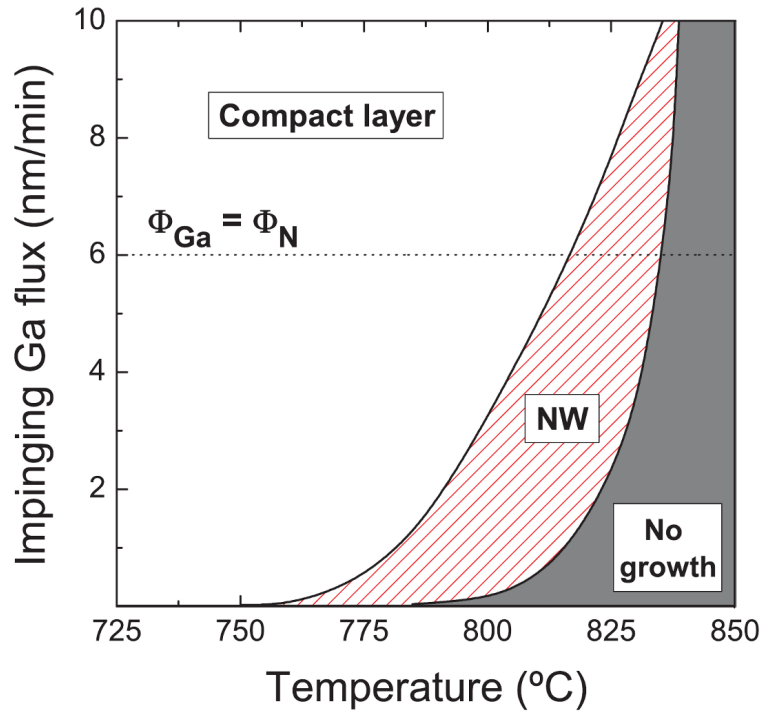


Figure 2.6: GaN growth diagram delimiting the compact and nanowire growth regimes as a function of Ga flux (Φ_{Ga}) and substrate temperature for a fixed nitrogen flux ($\Phi_N = 6 \text{ nm/min}$). Graph replotted from Ref. [87].

successive stages: the nucleation and the elongation phase. The nucleation phase of NWs can be described in terms of thermodynamic models^[88–91]. Figure 2.7(a) shows the early stage of the growth; the impinging atoms (Ga and N) can either desorb, diffuse on the surface, or adsorb by binding with other atoms. A cluster of several bonded atoms forms a nucleus; if its size is large enough (a diameter of few nanometres is sufficient^[90]), it will stabilize by acquiring a semi-spherical shape. The formation of such nuclei has been revealed by TEM studies of samples grown on Si substrates^[14,89]. In addition, an amorphous Si_xN_y layer roughly 2 nm thick was observed at the interface between the GaN NWs and the Si substrate; it forms from the reaction at high temperature of the impinging N atoms with the Si substrate. The stable nuclei will undergo a shape transition evolving into a nanowire with hexagonal horizontal cross-section (C-plane) bounded by M-plane side facets, as depicted in figure 2.7(b).

If the reagent fluxes continue to be supplied, the NWs will grow further both radially and axially (along the $[000\bar{1}]$ direction), but with different growth rates. In fact, it has been found that the axial growth rate is about 33 times higher than the radial one, under specific growth conditions^[92]. Differently from the nucleation stage, the elongation phase cannot be described by the thermodynamic growth models, instead, a kinetic description is required^[93,94]. As illustrated in figure 2.7(b), the impinging atoms (both Ga and N) can reach the top facet of the NWs through different paths. They can arrive directly from the incoming fluxes or diffuse along the sidewalls and eventually reach the C-plane top facet. This diffusion process is widely accepted to be a major contribution to the growth of GaN NWs^[83,88,93–98]. Because of diffusion from the side walls, the actual amount of Ga present on the top facet of the NWs can be significantly higher than the direct contribution of

2. Growth of group-III-N structures for NW-LEDs by molecular beam epitaxy

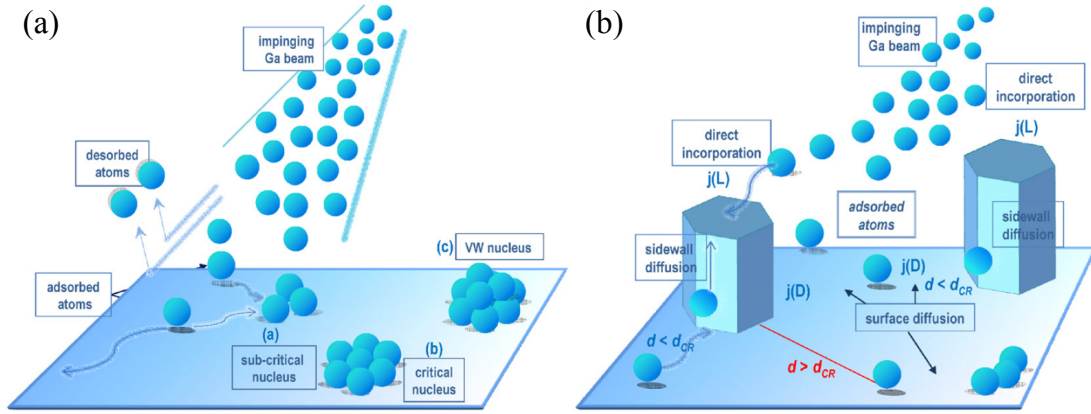


Figure 2.7: (a) Kinetics of the atoms on the substrate during the early stage of the NW growth. (b) Diffusion processes during the growth of GaN NWs. From Ref. [88].

the impinging atoms. This effect has various consequences; for instance, it has been experimentally found that, for a certain Ga flux, the axial growth rate of the NWs exceeds the one achievable for planar layers^[96]. This implies that the excess Ga atoms must come from diffusion from the side walls. Furthermore, it has been found that despite of the nominally N-rich growth condition employed, the finite amount of active N available on the top facet of the NWs may limit their axial growth rate^[94]. This effect is caused by the different diffusion lengths of Ga and N adatoms along the M-plane sidewalls. On the one hand the Ga adatoms are highly mobile and able to reach the NW tip; on the other hand, N adatoms are unstable against the formation of N₂ molecules, which are poorly reactive and very volatile. Consequently, the amount of Ga reaching the NW top facet can exceed the amount of active N available for the growth even for impinging III/V flux ratios lower than 1. A difference in sticking property of Ga and N adatoms on the M-plane sidewall was proposed to be the driving mechanism behind the NW formation also by Bertness and co-authors^[97]. Moreover, the diffusion enhanced incorporation process is diameter dependent; hence, NWs with various size will receive different amount of reactive material and thus will grow with different rates. Debnath *et al.* has found that the axial growth rate is proportional to the inverse of the NW diameter (d^{-1})^[98]. In other words, thick NWs grow slower than thin NWs.

Once the density of nanocolumns in the ensemble overcomes a certain limit (roughly $5 \times 10^8 \text{ cm}^{-2}$) the coalescence between adjacent NWs becomes important. Coalescence is an effect which takes place if two or more neighbouring NWs touch each other forming a single entity. It is mainly due to a not perfect epitaxial orientation of the various NWs to the substrate and to their later growth. Once several nanocolumns come into contact inhomogeneous strain on a microscopic scale is produced in the crystal^[99]. As result dislocations and basal-plane stacking faults are formed at the coalescence joints if the strain cannot be accommodated elastically^[100]. This results in a degradation of the optical properties and is therefore in most cases not desirable^[100,101].

As already introduced in section 1.1, the lack of a centre of inversion symmetry in wurtzite III-nitrides implies the existence of polar axes. Polarity plays an important role in the formation mechanisms of the NWs^[102] as well as in many other chemophysical properties such as: direction of both spontaneous and piezoelectric polarization^[25], incorporation of dopants^[103] and impurities^[104], formation of native point defects^[105], and

also incorporation of In^[106,107]. Self-induced GaN NWs have been found to form with N-polarity when grown on various non-polar substrates such as Si and Si_xN_y^[108–110], or on N-polar AlN layers^[102]. In contrast, on metal-polar AlN films a compact Ga-polar GaN layer and sporadic N-polar NWs instead of the expected dense ensemble have been observed.

2.2.2. Preparation of the Si substrates

The samples presented in this work were grown on 2-inch n-type Si(111) substrates delivered by *CrysTec GmbH*. The Si wafers were loaded into the MBE system as-received, without any chemical treatment; after an outgassing procedure, the substrates were then transferred into the growth chamber. In order to remove the native oxide present on the surface of the Si, the so called “Ga-polishing” or “Ga flash-off” method was employed. It consists in the *in situ* deposition of 100 monolayers (ML) of Ga on the substrate heated up to 550 °C, which are subsequently desorbed by increasing the substrate temperature up to 800 °C. The Ga desorption is monitored by means of line-of-sight QMS; the substrate is kept at high temperature until the QMS signal due to the Ga desorption reaches the zero level. The entire process is repeated until the RHEED pattern characteristic for the 7×7 surface reconstruction is clearly observed, usually two repetitions are enough. This procedure effectively removes the native oxide from the Si surface; in fact, at high temperature the Ga reacts with the oxygen atoms forming volatile Ga_xO_y, which is flashed off when the liquid Ga film is desorbed^[111].

Figure 2.8(a) shows the RHEED pattern of the 7×7 reconstructed Si surface obtained at the end of the “Ga-polishing”. The observation of the surface reconstruction with the Kikuchi lines in the RHEED pattern should guarantee flatness and good atomic order of the surface. Nevertheless, a careful inspection of a substrate carried out after the “Ga-polishing” treatment by means of AFM reveals that the surface is not as smooth as expected. Figure 2.8(d) shows the topography of the surface measured by AFM, a huge number of circular islands with density equal to about $1.4 \times 10^{10} \text{ cm}^{-2}$ is observed. They exhibit a relatively high aspect ratio with heights and diameters in the range 1 – 5 nm and 10 – 40 nm, respectively. We believe that these protrusions are Ga droplets that remain on the surface even after the Ga desorption at high temperature. At least two different causes could inhibit the complete evaporation of the residual Ga. On the one hand, once the droplets shrink to nanoscopic sizes with high aspect ratio, the high surface tension can stabilize the cluster of atoms preventing further evaporation. On the other hand, the Ga could react with the Si or the oxygen present on the surface forming alloys that might be much more stable than the pure liquid Ga. Whatever the explanation, we will show that the presence of these islands plays an important role in the subsequent stages of the NW growth.

It is well known that during the nucleation stage of GaN NWs grown on Si by MBE a Si_xN_y layer is formed on the surface^[14,88,89]. The epitaxial alignment of the NWs has been found to depend on the quality of this layer^[112]. In order to obtain reproducible NW ensembles, we controlled the formation of Si_xN_y by exposing in a standardized manner the Si surface only to active N. In particular, the substrate was always nitridized for 5 min, at a temperature $T_S = 780^\circ$ and with a nitrogen flux $\Phi_N \approx 10 \text{ nm/min}$ (RF power and N₂ flow equal to 500 W and 2 sccm, respectively). Immediately after the exposure to the active N, the atoms on the Si surface rearrange themselves. After only 5 s of nitridation, the RHEED pattern evolves from the original 7×7 reconstruction into the one shown

2. Growth of group-III-N structures for NW-LEDs by molecular beam epitaxy

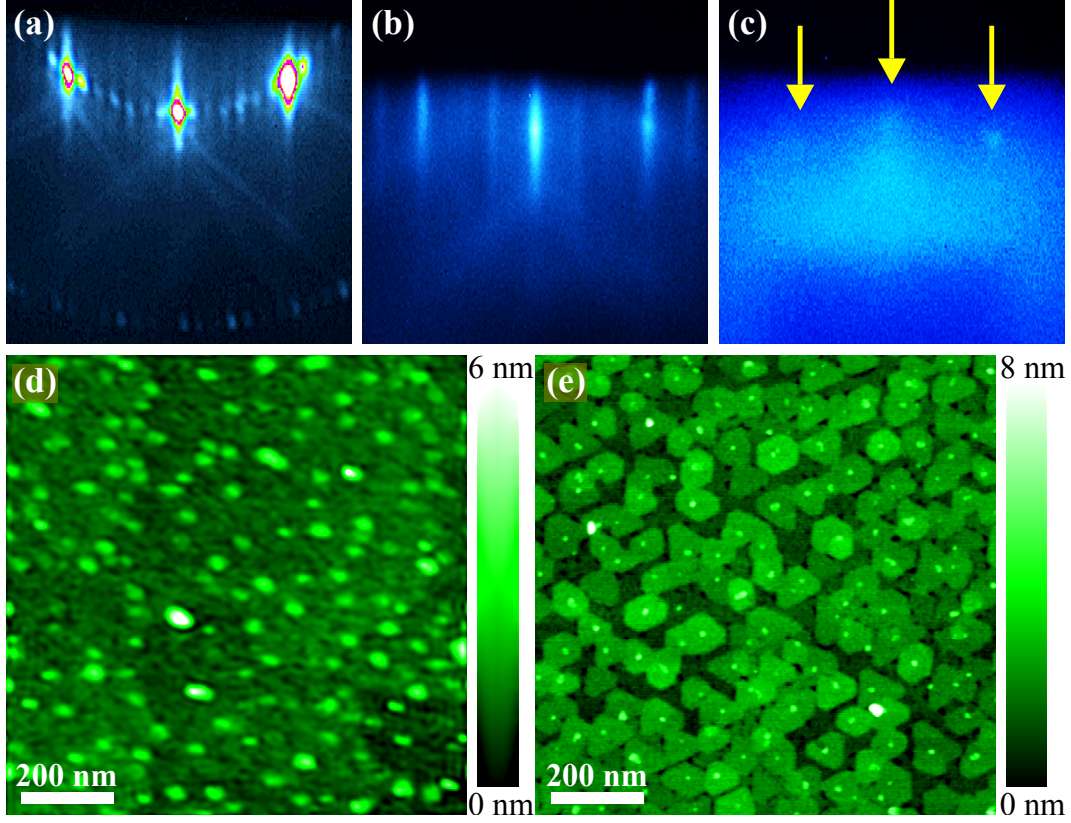


Figure 2.8: (a)–(c) RHEED patterns of the Si surface acquired along the $[11\bar{2}0]$ azimuth (a) at the end of the “Ga-polishing”, after (b) 5 s and (c) 5 min of nitridation. The yellow arrows indicate the weak pattern under the diffuse halo. (d)–(e) AFM images of the Si surface (d) directly after the “Ga-polishing”, and (e) after the nitridation; samples prepared by Sergio Fernández-Garrido.

in figure 2.8(b). Although not all the streaks are well identifiable, this pattern should correspond to the 8×8 reconstruction related to the formation of crystalline Si_3N_4 ^[113]. After 5 min of nitridation, the RHEED image consists of a bright diffuse halo and a rather weak pattern [see figure 2.8(c)], thus indicating the presence on the surface of a mixture of crystalline and amorphous Si_xN_y .

Figure 2.8(e) shows the surface of the sample after “Ga-polishing” and nitridation measured by AFM. Flat islands with a typical size of 60 – 90 nm, separated by 1-nm-deep grooves were observed. These patches exhibit well developed hexagonal or triangular shapes that suggest their crystalline microstructure. Similar features have been observed also after the nitridation of Si(111) surfaces *not* treated with “Ga-polishing”^[112,114]; in these cases the Si_xN_y islands nucleate at the step edges of Si(111) or within terrace areas by forming nucleation pits^[114]. In contrast, the islands observed in our samples treated with “Ga-polishing” seem to develop around the small protrusions almost always observed at the centre of the patches in figure 2.8(e). These hillocks are roughly 3 nm high and have a density of about $1.4 \times 10^{10} \text{ cm}^{-2}$, which coincides with the density of islands observed on the Si surface directly after the “Ga-polishing”, see figure 2.8(d). Therefore, it seems natural to imagine that the Si_xN_y islands nucleate around the residual Ga droplets produced by the “Ga-polishing” treatment. The consequences of the observed microstructures on both NW nucleation and current conduction across thin AlN layers

grown on Si will be further discussed in section 2.3.3. Note that the unexpected consequences of the “Ga-polishing” treatment has been identified at the PDI only recently, and at that time all the samples discussed in this thesis had already been grown.

2.2.3. Growth of self-induced (In,Ga)N/GaN NW-LEDs

In the following lines, the steps required for the fabrication of a NW-based LED are presented. The sequence of the growth steps and the optimal parameters needed to obtain a successful doping of the p-i-n structure and an efficient (In,Ga)N/GaN active region were developed at the PDI by Friederich Limbach and Martin Wölz in the framework of their PhD theses^[51,115]. In this work, the already existing growth protocol was followed, but introducing few important optimizations, such as the adjustment of the Mg flux to avoid the coalescence of NWs.

Si doped GaN base

In order to produce a functional NW-LED, (In,Ga)N/GaN heterostructures were embedded in a n-i-p diode. Figure 2.9(a) depicts a schematic of the employed LED structure; by way of example, a cross-sectional SEM micrograph of the as grown NW-LED is shown in figure 2.9(b). The bottom part of the NWs consists of a Si doped n-type GaN segment, roughly 500 nm long. The Si concentration was estimated by means of secondary ion mass spectrometry (SIMS) measurements performed only on reference planar layers^[115]. Because of their 3D morphology, similar characterization techniques are very difficult to apply to NW ensembles^[116]. For the Si cell temperature used in this work (1100 °C) a Si concentration of about $3 \times 10^{19} \text{ cm}^{-3}$ was estimated. It is worth noting that this is also the highest Si flux that preserves a good NW morphology. In fact, higher fluxes cause coalescence of the nanocolumns, due to an enhanced radial growth, and loss of the perpendicular orientation of the NWs with respect to the Si substrate^[115].

To verify the morphological and electrical properties of the Si doped NW ensemble used as base for the LED structure, a dedicated sample was prepared (refer to NW:Si in table A.1 of the appendix A). After the Si nitridation process, the NWs were grown at a substrate temperature of 780 °C for 90 min with a III/V flux ratio of about 0.31: the Ga and N fluxes were respectively set to $\Phi_{\text{Ga}} = 3 \text{ nm/min}$ and $\Phi_{\text{N}} \approx 9.6 \text{ nm/min}$ (obtained by combining a RF power of 500 W with a N_2 flow equal to 2 sccm). Figures 2.10(a) and (b) show the morphology of the obtained NW ensemble. We note that the degree of

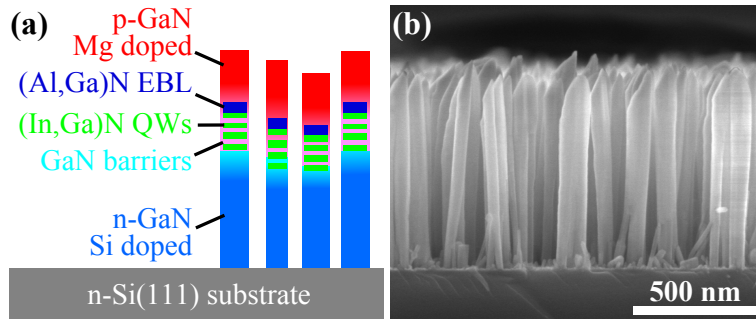


Figure 2.9: (a) Schematic of the employed LED structure; the different parts are labelled. Note that the various dimensions are not to scale. (b) Cross-sectional SEM micrograph of a NW-LED grown on Si (LED1) shown by way of example.

2. Growth of group-III-N structures for NW-LEDs by molecular beam epitaxy

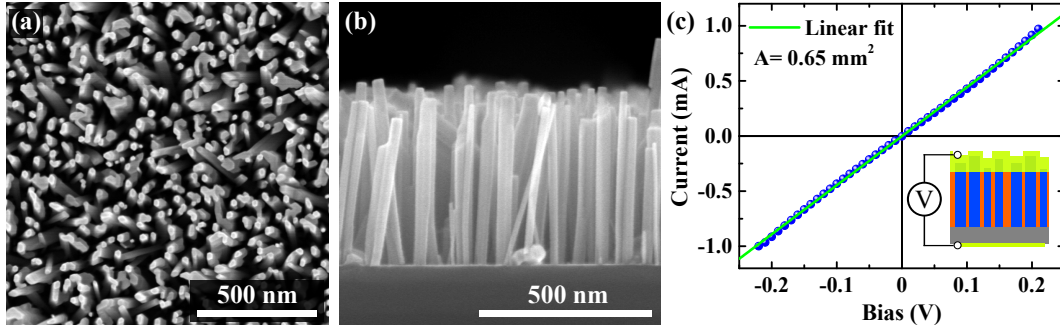


Figure 2.10: (a) Top-view and (b) cross-sectional SEM micrograph of the as grown Si doped NWs. (c) Current-voltage measurements performed on the same NW ensemble. The green solid line represent the linear fit of the data, while the inset in the bottom right corner depicts a schematic of the employed device.

coalescence of the NWs is relatively low and the nanocolumns are roughly 500 nm high. The homogeneity of the height could be further improved by growing the NWs for longer time^[117]; nevertheless longer NWs would also imply higher resistance of the final LED and higher degree of coalescence.

In order to study the electrical properties of the Si doped NW ensemble, a piece of the sample was cut and planarized by following the procedure described in section 3.1. Subsequently, n-type contacts were produced by evaporating various metals on top of the NWs and on the backside of the Si substrate. An illustrative sketch of the final device is shown in the inset of figure 2.10(c). As top-contact to the n-type NWs the Ti(20 nm)/Al(80 nm)/Ni(40 nm)/Au(50 nm) metallization scheme was used; whereas the n-type contact on the backside of the Si substrate was achieved through an Al(50 nm)/Au(50 nm) bilayer. To improve the conductivity of the contacts, the sample was annealed by means of rapid thermal annealing (RTA) at 800 °C for 30 s in N_2 atmosphere. Then, the current-voltage (I-V) characteristics of the device were measured through a probe station connected to a *Keithley* parameter analyser (model 4200-SCS). The resulted I-V curve acquired through a contact with surface area equal to 0.65 mm² is plotted in figure 2.10(c). An Ohmic-like behaviour was observed in the entire current range analysed. The resistance of the device was estimated from the slope of a linear fit of the data: $R=1/\text{slope}=224 \Omega$. The linearity of the I-V characteristics and the relatively low resistance of the NW ensemble proves that a good Si doping of the GaN NWs was achieved, and also confirms that the base of the LED can effectively conduct current.

(In,Ga)N/GaN active region

Directly on top of the n-type NW base the active region of the LED is grown, that is the part of the device where the recombination of holes and electrons takes place. The active region of the investigated NW-LEDs consists of four (In,Ga)N quantum wells (QWs), separated by three GaN barriers. This part is nominally undoped and is embedded between the n-type and the p-type GaN segments, so that an n-i-p diode is created. The (In,Ga)N alloy cannot be grown at the same temperature used for the GaN base, *i.e.*, 780 °C. In fact, this value is well above the decomposition temperature of MBE grown InN, which is about 470 °C^[118,119]. At the same time good quality (In,Ga)N NWs can be grown only at temperatures higher than 500 °C^[120]. For this reason, the decomposition of the (In,Ga)N crystal necessarily plays a significant role during the growth of the quantum wells, and a

2.2. Growth of self-induced GaN nanowires by MBE

dynamic process of formation and breaking of the bonds between In and Ga and N atoms takes places.

The challenging issue of the axial growth of (In,Ga)N QWs on GaN NWs has been addressed at the PDI by Martin Wölz, an in-depth discussion on this topic can be found in his PhD thesis^[51]. In the present work, the active region of the LEDs was produced following the growth protocol developed by Wölz. After the deposition of the Si doped NW base, the substrate temperature is gently decreased down to the desired value, 603 °C in case of the NW-LEDs presented in this thesis, and it is let stabilized. Meanwhile, the Ga cell temperature is also decreased to obtain a flux equal to about 0.95 nm/min, whereas the In flux is set to 0.8 nm/min. The active N flux remains the same used for the growth of the NW base, namely 9.6 nm/min. Once all the parameters are stable, the first (In,Ga)N QW is grown for 2 min, then the In shutter is closed and only Ga and N are supplied for 8 min to form the first GaN barrier. The process is repeated until the four QWs and the three barrier are ready.

The desorption of In during the growth of the active region is monitored by line-of-sight QMS. Figure 2.11 shows the partial pressure of the isotope ¹¹⁵In due to the atoms desorbing from the substrate. The four peaks observable at about 20, 30, 40, and 50 min are related to the deposition of the four different QWs. The dashed black line depicts the In shutter opening and closing times. Note that, although the QMS signal starts to rise immediately after the opening of the In shutter, it reaches its peak value only after a delay of about 50 s. This effect would suggest the progressive accumulation of metallic In on the NW top facet; the effect saturates when an equilibrium between impinging and desorbing fluxes is reached. In other words, immediately after the opening of the shutter there is a shortage of In on the surface and all the impinging atoms are incorporated. Progressively, the supplied In adds to the one coming from the decomposition of (In,Ga)N and some metal starts to accumulate on the surface. The excess indium will continue to desorb also when the shutter of the source is closed, as it is actually visible in figure 2.11. A careful look at the QMS peaks related to the desorption from different QWs seems to suggest that slightly less In desorbs during the formation of the first QW, and thus slightly more material would be incorporated. This effect is illustrated in the inset of figure 2.11, which shows the integrated ¹¹⁵In QMS signal in case of the four different QWs. Although the observation is confirmed, the amplitude of the experimental error bars would question the relevance of the observed effect.

By means of a simple calibration technique, the QMS can be used to obtain a rough estimation of the average In content inside the QWs^[121]. In fact, the QMS signal tells us the amount of In desorbing from the surface, the difference between the impinging and the desorbing flux coincides with the amount of material incorporated in the crystal. The total impinging In flux can be easily measured by QMS when all the supply material desorbs. This condition is satisfied at high substrate temperatures ($T_S \gtrsim 650$ °C), at which both solid InN and liquid In are not stable and desorb. We routinely carried out such a calibration prior to the growth of the active region. It can be seen in the graph of figure 2.11 for times shorter than 4 min. The substrate temperature as high as 720 °C ensures that all impinging In (0.8 nm/min) desorbs. From the ratio between the maximum intensity of the QMS signal measured at $T_S = 720$ °C and at $T_S = 603$ °C the amount of desorbing In can be calculated. The In concentration (x_{QMS}) in the QWs grown under

2. Growth of group-III-N structures for NW-LEDs by molecular beam epitaxy

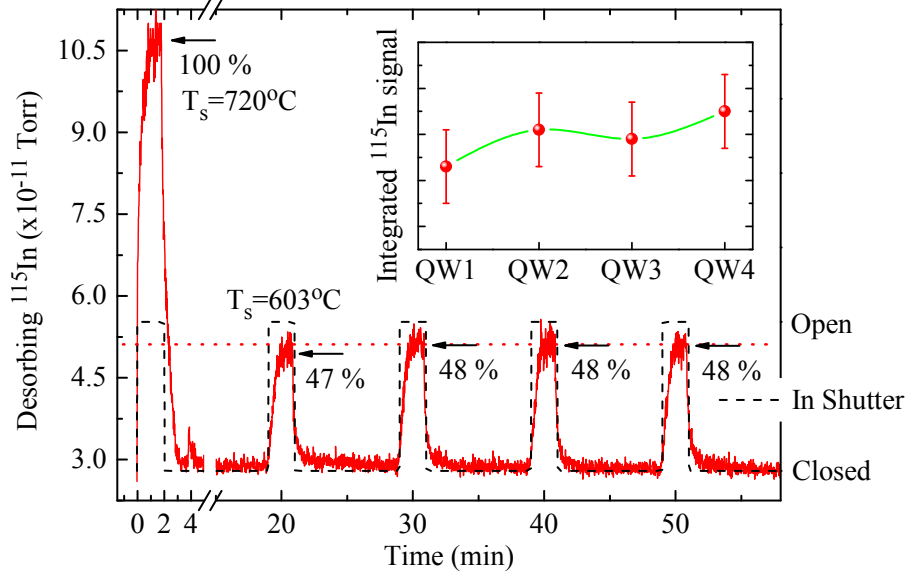


Figure 2.11: In-situ QMS monitoring of the ^{115}In desorption during the growth of the active region; the dashed black line depicts the In shutter opening and closing times. The inset shows the QMS signal integrated over 6 min from the opening of the In shutter in case of the four different QWs.

N-rich growth conditions, can thus be estimated by the formula^[121]

$$x_{\text{QMS}} = \frac{\Phi_{\text{In}} - \Phi_{\text{In}}^{\text{des}}}{\Phi_{\text{Ga}} + \Phi_{\text{In}} - \Phi_{\text{In}}^{\text{des}}} \quad (2.2)$$

where $\Phi_{\text{In}}^{\text{des}}$ represents the flux of desorbing In. In the case of the sample under discussion $\Phi_{\text{Ga}} = 0.95 \text{ nm/min}$, $\Phi_{\text{In}} = 0.8 \text{ nm/min}$, and $\Phi_{\text{In}}^{\text{des}} \approx 48\% \Phi_{\text{In}}$; hence, an average In content of 30% was obtained.

To cross check the average In incorporation in the QWs, a different technique was applied. We performed X-ray diffraction (XRD) measurements with $\text{Cu K}\alpha_1$ radiation using a $\text{Ge}(220)$ hybrid monochromator and a $\text{Ge}(220)$ analyser crystal. The amount of $(\text{In,Ga})\text{N}$ present in the LED samples with four QWs is not enough to produce a decent signal in the XRD profile. For this reason a dedicated sample with eight QWs and without doping (called QWref in table A.1) was fabricated. Despite the use of nominal growth parameters identical to those employed for the presented LED device, fluctuations both in In flux and substrate temperature led to an In incorporation slightly lower than that obtained in the LED sample. In particular, the analysis of the QMS signal indicates that in the reference sample about 25 % more In desorbed. Such variation is not unusual in growth runs performed at different times; also, more than one month passed between the growth of the two samples.

Figure 2.12 shows the symmetric $\omega - 2\theta$ scan performed on the reference sample. The main peak is related to the $\text{GaN}(0002)$ reflection; the shoulder visible on the left side represents the zero order reflection (ω_0) coming from the $(\text{In,Ga})\text{N}$ QWs. Note that the lower value of ω of the $(\text{In,Ga})\text{N}$ peak indicates an increased lattice spacing in the QWs region due to In incorporation. The zero order $(\text{In,Ga})\text{N}$ peak is surrounded by regularly spaced satellites marked by arrows in figure 2.12. These satellites arise from thickness interference at the periodic $(\text{In,Ga})\text{N}/\text{GaN}$ heterostructure; their positions can be used

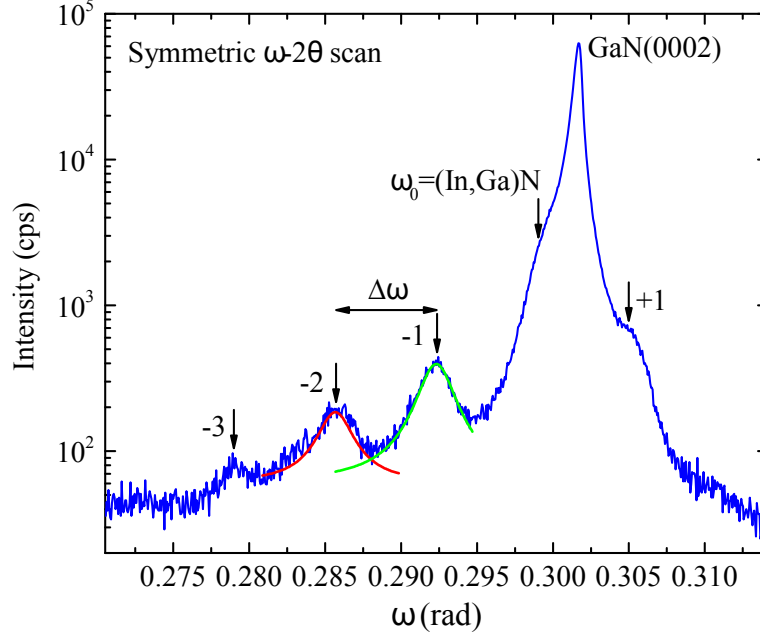


Figure 2.12: Measured $\omega - 2\theta$ scan across the GaN(0002) reflection of the reference sample with eight QWs (QWref). The periodic (In,Ga)N/GaN heterostructure gives rise to the satellite peaks as indicated by the arrows. The red and green solid curves represent the fit of the data to a Lorentzian peak. The data are plotted on a semi-logarithmic scale.

to determine the average lattice spacing (c_{avg}) via Bragg's law^[122]. The positions of the first and second order satellites were obtained by fitting the data to a Lorentzian peak function. Then, c_{avg} was calculated through the formula $c_{avg} = \lambda_{CuK\alpha} / \sin(\omega_0)$, where $\lambda_{CuK\alpha}$ is the wavelength of the X-ray radiation (1.5406 Å). Hence, the average In content of the QWs can be estimated by means of the Vegard's law

$$x_{XRD} = \frac{c_{avg} - c_{GaN}}{c_{InN} - c_{GaN}} \frac{t_{QW} + t_{bar}}{t_{QW}} \quad (2.3)$$

where $c_{GaN} = 5.185 \text{ Å}$ and $c_{InN} = 5.705 \text{ Å}$ are the lattice parameters of GaN and InN, respectively, whereas t_{QW} and t_{bar} represent the growth times used for QWs and barriers. Note that in equation(2.3) we assumed that the growth rates of QWs and barrier are equal; because of the very low growth rates employed for the deposition of the active region, the relative error introduced by this approximation is small^[121]. The In concentration in the reference sample estimated by XRD is about 22 %. This value is lower than the one obtained from the analysis of the QMS data of the LED sample. Nevertheless, it has to be considered that the In desorption observed during the growth was higher in the reference sample than in the LED, and thus a higher In content is expected in the latter case. Taking into account the different results obtained from various methods and also considering sample-to-sample fluctuations, it seems fair to conclude that our current best estimate for the average In content in the NW-LEDs is $(25 \pm 10) \%$.

From the analysis of the XRD data also the average thickness of QWs (d_{QW}) and barriers

2. Growth of group-III-N structures for NW-LEDs by molecular beam epitaxy

(d_{bar}) can be estimated. The former one is given by the formula

$$d_{QW} = d_{SL} \frac{t_{QW}}{t_{QW} + t_{bar}} = \frac{160000}{\Delta\omega} \frac{t_{QW}}{t_{QW} + t_{bar}} \quad (2.4)$$

where $d_{SL} = d_{QW} + d_{bar}$ is the period of the (In,Ga)N/GaN superlattice and $\Delta\omega$ represents the spacing between two consecutive satellites in arcsec. Thicknesses of 2.3 nm and 9 nm were obtained for QW and barrier, respectively.

Mg doped GaN cap

The last QW is immediately followed by a p-type (Al,Ga)N electron blocking layer (EBL), see figure 2.9(a). The aim of this segment is to create a potential barrier for the electron so as to confine them inside the active region and enhance the radiative electron-hole recombinations^[19]. A comparison of similar NW-LEDs grown by Friederich Limbach with and without EBL reveals the crucial role of this segment. In fact, the NW-LED without EBL was much less bright than the one with EBL. The crucial role played by this layer in NW-based LEDs has also been discussed by Brubaker *et. al.*^[123]. In the NW-LEDs presented in this work a Mg doped EBL was always deposited, its nominally thickness and Al content are 15 nm and 30 %, respectively. The (Al,Ga)N EBL is immediately followed by a Mg doped GaN segment used as p-type part of the junction. The p-GaN was grown for 120 min employing the same Ga and N fluxes used for the growth of the active region ($\Phi_{Ga} = 0.95$ nm/min and $\Phi_N = 9.6$ nm/min), a nominal thickness of about 120 nm is expected. In order to improve the crystalline quality of the material, the substrate temperature was gently increased by 150 °C up to 750 °C with a ramp rate of 2 °C/min.

Particular attention was paid to the choice of the Mg flux used to dope the crystal. In fact, it was found that high Mg fluxes promote the lateral growth of the NWs and thus their coalescence^[67,115]. As already mentioned, a high degree of coalescence of the NW ensemble is not desirable because it degrades the optical properties of the NWs^[100,101]. For this reason the Mg flux was optimized by growing different NW-LED structures with various temperatures of the Mg cell; then the morphology of the NWs was checked by means of SEM. The optimal value of the Mg flux used in this work corresponds to a BEP of about 3×10^{-10} mbar obtained by setting the temperature of the Mg cell to 250 °C. The resulting morphology of the as grown NW-LED structure is shown in figure 2.13(a); it is clearly visible that the degree of coalescence is relatively low. In contrast, a NW-LED structure (labelled LEDref) grown with comparable parameters but higher Mg flux exhibits much more coalesced NWs, see figure 2.13(b). The Mg cell temperature was set to 280 °C in this case, which correspond to a BEP of about 1×10^{-8} mbar. The optical properties of the two samples were investigated by means of room temperature (T=303 K) photoluminescence (PL) spectroscopy. The NWs were excited by a HeCd laser emitting at 325 nm; the resulting PL signal was collected by an optical microscope and analysed through a grating spectrometer (groove density equal to 600 mm^{-1}) connected to a cooled CCD camera. The measurements were acquired by Christian Hauswald at PDI. The PL intensity coming from the (In,Ga)N QWs, that is the broad band centre around 2.3 eV, is about ten times higher in LED1 than in LEDref. This result highlights the strong detrimental effect produced by a too high Mg doping in the LED structure. In fact, point defects introduced by the Mg atoms in the bulk crystal and boundary dislocations at the edge of coalescing NWs can act as effective non-radiative recombination centres^[100,101].

As already mentioned, the polarity of the crystal plays a crucial role in many different

2.3. Selective-area growth: Optimization of the AlN layer

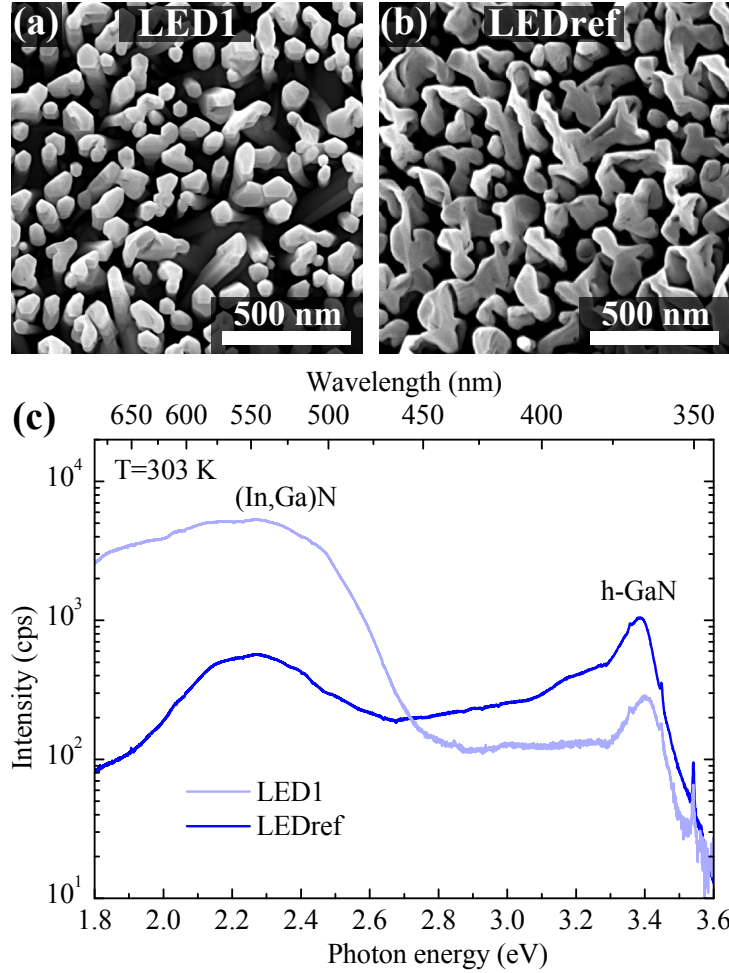


Figure 2.13: (a)–(b) Top-view SEM micrographs of NW-LEDs grown with two different Mg fluxes corresponding to BEP of about (a) 3×10^{-10} mbar and (b) 1×10^{-8} mbar. (c) Comparison of the room temperature PL spectra of the two NW-LEDs. The measurements were acquired by Christian Hauswald at PDI.

aspects of an LED device^[103–107]. Although self-induced GaN NWs have been found to form with N-polarity when grown on Si substrates^[108–110] or on N-polar AlN layers^[102], a flip of GaN polarity has been reported for MBE grown layers doped with Mg^[124]. Therefore, it is worth checking the polarity of the NW-LEDs at different positions along the p-i-n structure. To this end, Friederich Limbach and Xiang Kong performed a careful transmission electron microscopy (TEM) investigation of the NW-LED samples^[115]. The polarity of the wires was determined via electron energy loss spectroscopy (EELS); several wires were investigated at various positions along the wire axis and in each case a nitrogen polarity was found.

2.3. Selective-area growth: Optimization of the AlN layer

Several groups have already demonstrated the possibility to fabricate LEDs based on (In,Ga)N/GaN NWs grown on Si(111) with the help of self-assembly processes^[48,68,125–132]. In fact, Si substrates are very attractive for their low cost, availability on large sizes, and

2. Growth of group-III-N structures for NW-LEDs by molecular beam epitaxy

well developed processing technologies. However, the NW ensembles grown in such a way inevitably exhibit fluctuations in length and diameter of the NWs, that in turn cause differences in In incorporation. As a consequence, LEDs fabricated from such NW ensembles suffer from multicolour emission^[48,133] and strong inhomogeneities in the current path^[131].

More homogeneous properties might be achieved by controlling the diameter and spacing of the NWs by selective-area growth (SAG)^[44]. Another benefit of this approach is that nano-LEDs emitting at different colours may be fabricated on the same substrate in a single growth run^[44,134]. The SAG of III-N nanowires has been achieved by a few groups, both by plasma-assisted MBE and by MOVPE, on GaN templates grown on sapphire^[47,135–140]. Recently, the approach involving MBE was extended to GaN buffers on Si^[47]. Prior to this development, the SAG of GaN nanowires on Si substrates was demonstrated in an alternative way employing AlN buffers^[141–143]. For a comparison of these two approaches on Si, we recall that when planar III-N layers are grown on Si substrates, the first step is typically the growth of an AlN buffer layer, because the mismatch in thermal expansion coefficient is much smaller than for GaN and because interfacial reactions can be suppressed more efficiently (during the direct growth of GaN on Si, the formation of Si_xN_y and/or the melt back etching of Si by Ga are likely)^[24]. At the same time, the large band gap of AlN presents a drawback for the overall series resistance of any electronic device fabricated on such structures. For the *self-organized* growth of GaN NWs on Si by MOVPE, AlN buffers have been employed to induce NW nucleation. LEDs based on such NWs exhibited high threshold voltages exceeding 10 V, but the origin of this high value was not analyzed further^[130]. For either of the approaches to the SAG of III-N NWs on Si substrates it is, therefore, at present not clear whether functional LEDs can be obtained.

Our approach to SAG via AlN buffer layers^[143,144] is based on the observation that the spontaneous growth of GaN nanowires is preceded by a nucleation time during which there is no appreciable incorporation of Ga, indicating that nucleation of GaN does not occur^[92,145]. For SAG we exploit the fact that the nucleation time depends sensitively on the substrate material. In particular, for appropriate growth conditions the nucleation time can be extended to several hours on bare Si or on Si_xO_y , while it is much shorter on AlN. Good growth selectivity is achieved if the difference between the nucleation time of the GaN NWs on the mask (Si_xO_y in our case) is much longer than that on the underlying AlN buffer layer. Hence, the shorter the nucleation time on the AlN layer, the better is the selectivity.

In this work, we have demonstrated the suitability of the approach involving AlN buffers. In order to minimize the resistance of the AlN buffer on the current flow through the LED, we reduced the thickness of this layer while maintaining its effectiveness for SAG. Then, we fabricated LEDs based on spontaneously formed NWs grown on such an AlN buffer layer to demonstrate that electrical conduction is possible (see section 3.3).

2.3.1. A three-step approach for the growth of AlN layers on Si

In order to obtain thin, uniform, and crystalline AlN buffer layers with a smooth surface directly on Si, we developed a three-step growth procedure that avoids the undesirable formation of Si_xN_y and produces a closed and continuous AlN layer without any droplets. We point out that the use of an AlN buffer with smooth and uniform morphology over the entire wafer is fundamental to obtain SAG NWs with similar properties everywhere on the substrate.

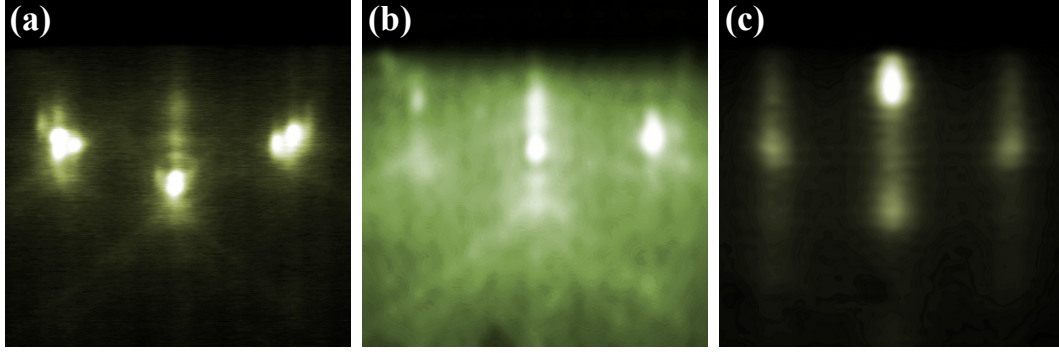


Figure 2.14: (a)–(c) RHEED patterns of the sample surface acquired along the $[11\bar{2}0]$ azimuth after (a) the deposition of the Al, (b) the nitridation at low temperature, (c) the growth of the AlN layer at high temperature.

The growth procedure developed in the framework of this thesis to obtain thin AlN layers without voids consists of three main steps. After the “Ga-polishing” procedure, the temperature of the substrate was lowered down to about 50°C and 1.2 ML of Al were deposited on the 7×7 reconstructed Si surface at the relatively low rate of 1.5 nm/min ($\text{BEP} = 2.65 \times 10^{-8}$ mbar). Figure 2.13(a) shows the RHEED pattern of the sample surface after the deposition of 1.2 ML of Al; the presence of spotty features different than the ones related to the Si substrate indicates that the Al forms crystalline islands on the surface. Note that the unusually low deposition temperature was required to decrease the mobility of the Al atoms and thus to prevent the formation of big droplets. It is worth mentioning that for the growth of relatively thick AlN films ($\gtrsim 50$ nm) the Al is commonly deposited at higher temperatures^[146]; in this case, the voids present between the Al droplets are filled once the various AlN islands coalesced. However, a complete coalescence will not occur if the AlN layer is very thin, and voids will be present on the surface. This conclusion was reached by growing many thin AlN layers with different III/V flux ratios, substrate temperatures, and deposition procedures. As long as high substrate temperatures were employed, voids in the layers were always observed.

After the deposition of the Al, which protects the Si surface, the plasma source was ignited and the sample was nitridized for 1 min at the same low temperature employing a N flux of about 5 nm/min (RF power of 400 W, N_2 flow equal to 3 sccm). Figure 2.13(b) shows the RHEED pattern of the nitridized surface, the presence of a streaky pattern with bright background suggests that the nitridation of the Al at low temperature leads to the formation of a very thin partially crystalline AlN film. Subsequently, the substrate temperature was raised up to 680°C , and AlN was grown up to the desired total layer thickness by supplying simultaneously Al and N. During growth the III/V flux ratio was kept close to unity to avoid the formation of Al droplets; in particular an AlN flux of 5.8 nm/min ($\text{BEP} \approx 1.01 \times 10^{-7}$ mbar) and a N flux of about 6 nm/min (RF power of 500 W, N_2 flow equal to 2 sccm) was used. Figure 2.13(c) shows the RHEED image at the end of the growth of a 14-nm-thick AlN layer; the streaky pattern indicates that the AlN is crystalline.

In the next section we show that, this procedure allows the fabrication of smooth, uniform and closed AlN layers on Si(111) even for thicknesses of only few nanometres.

2. Growth of group-III-N structures for NW-LEDs by molecular beam epitaxy

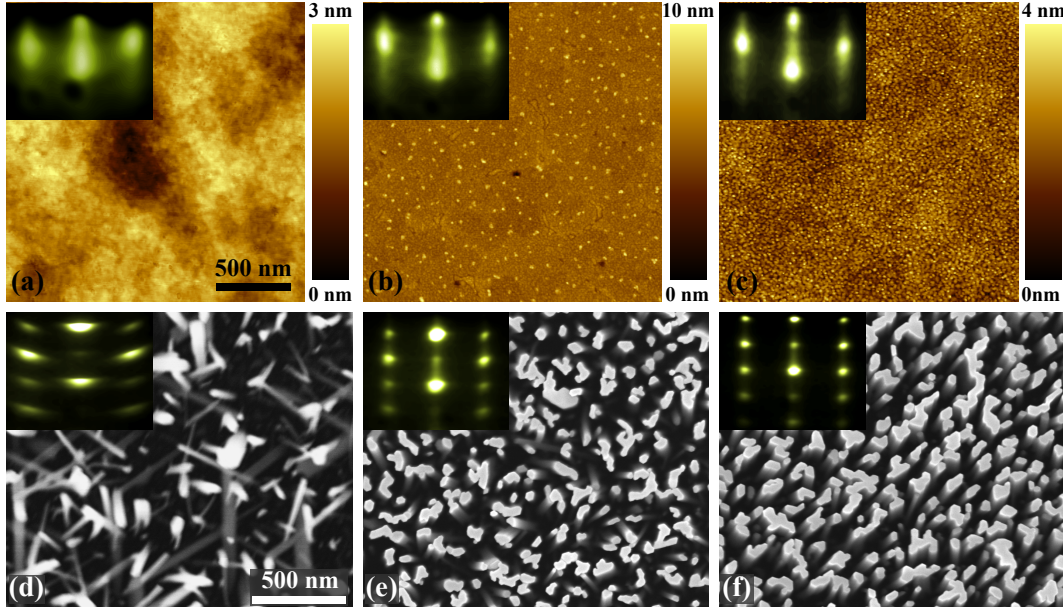


Figure 2.15: (a)–(c) AFM images of three AlN layers with different thicknesses: (a) 2 nm, (b) 4 nm, and (c) 8 nm. (d)–(f) Top-view SEM images of the GaN NWs grown on these AlN layers. The insets of the figures (a)–(c) and (d)–(f) depict the corresponding RHEED patterns acquired at the end of the growth along the $[11\bar{2}0]$ azimuth, respectively.

2.3.2. Optimization of the AlN thickness

In order to minimize the series resistance of a NW-LED device grown on the AlN buffer, the thickness of this layer must be kept as thin as possible. At the same time, the GaN NWs grown on it must exhibit a good morphology and have to be well aligned perpendicular to the substrate surface, because it would otherwise not be possible to achieve the vertical contacting of the NW ensemble, and the controlled growth of an n-i-p junction and heterostructure that are well-stacked along the NW length would be seriously compromised. In order to find the thinnest AlN layer that meets these requirements, a series of samples was prepared by growing GaN NWs on AlN layers of different thickness (refer to NW1–5 in table A.1 of the appendix A). In addition, to investigate the properties of the AlN surface as a function of the thickness, the same series of samples was reproduced without GaN NWs (refer to AlN1–4 in table A.1). The growth parameters of both the AlN layer and the GaN NWs were kept constant for all samples, which differ only in the growth time of the AlN layer. AlN layers with thicknesses between 2 and 14 nm were produced using the procedure described before, whereas the GaN NWs were grown at a substrate temperature of 805 °C using a Ga flux equal to 4 nm/min ($\text{BEP} \approx 9.2 \times 10^{-8}$ mbar) and a N flux of about 10.5 nm/min obtained by means of two plasma sources operated in parallel (RF power of 500 and 400 W and N_2 flow equal to 2.5 and 3 sccm). The thickness of the AlN layers was determined by X-ray reflectivity measurements (data not shown here), while the crystalline structure and the morphology of its surface was analysed by RHEED and AFM, respectively.

Figures 2.15(a)–(c) show the AFM images of the surfaces of three AlN layers with different thicknesses (2, 4, and 8 nm), while the insets depict the corresponding RHEED patterns. All the three samples exhibit a very smooth surface with a root-mean-square (RMS)

2.3. Selective-area growth: Optimization of the AlN layer

value of the roughness of about 0.5 nm. Nevertheless, the surface morphology depends strongly on the thickness of the layer. In particular, the surface of the 2-nm-thick layer [figure 2.15(a)] is not completely flat, but modulated on the scale of a few hundreds of square nanometres by depressions, which in some points likely reach the substrate. The corresponding RHEED pattern shows broad and diffuse reflections, suggesting a poor crystalline quality. In contrast, the 4-nm-thick layer [figure 2.15(b)] is almost completely closed, and sporadic pits with average diameter of about 40 nm are visible. However, many small islands are observed, their origin will be further discussed in section 2.3.3. In this case, the RHEED pattern is brighter and better defined. Finally, the 8-nm-thick layer [figure 2.15(c)] shows a completely closed surface characterized by a very dense distribution of small islands. The corresponding RHEED pattern shown in the inset is more streaky than the ones related with the thinner layers, suggesting a better crystalline quality.

The alignment of the NWs with respect to the substrate was investigated *in situ* by RHEED and *ex situ* by SEM and XRD. Figures 2.15(d)–(f) show the SEM top view images of the GaN NWs grown on the three AlN layers described before, while the insets depict the corresponding RHEED patterns. As visible in figure 2.15(d), the NWs grown on the 2-nm-thick AlN layer are completely misaligned; and this result is also revealed by the RHEED pattern composed of reflections of oval shape arranged on circles, which indicates diffraction from crystallites oriented in different directions. Obviously, this AlN layer is not suitable for our purpose. The alignment of the NWs improved drastically when the thickness of the AlN layer was increased by only 1 nm, and further improvements were obtained by increasing the thickness to 4 nm, as visible in figure 2.15(e). In this case, the RHEED pattern exhibits reflections of circular shape arranged on a rectangular grid and the SEM top view image reveals that the NWs are well-oriented perpendicular to the substrate surface, with only a small amount of inclined NWs. The shape and arrangement of these NWs is suitable for the realization of NW-based LEDs. With further increasing thickness of the AlN layer, the alignment of NWs improved more and more, as is visible in particular from the RHEED pattern with sharp reflections in figure 2.15(f) for the NWs grown on a 8-nm-thick AlN layer.

The improved alignment of the GaN NWs with increasing thickness of the AlN layer is also confirmed by XRD measurements. Figure 2.16(a) shows the $\omega - 2\theta$ scans performed on the NW samples grown on AlN layers of different thickness; for comparison also the profile of a sample grown on bare Si is plotted (grey profile). The main peak is due to the GaN NWs while the vertical dashed line indicates the Bragg angle related to unstrained GaN material (0.30165 rad). The perfect overlap between theoretical and measured position of the diffraction peaks for all the analysed samples indicates that the GaN NWs are free of macro-strain, regardless of the substrate. Nevertheless, micro-strain due to structural defects might be present^[99]. The higher intensity of the GaN related peak in case of samples with thicker AlN indicates that more NWs have the same crystallographic orientation, in other words they are better aligned on thick AlN layers than on thin ones. The peak at higher angle, about 0.314 rad, is given by the diffraction of the AlN layer; it is visible only in the sample where a 14-nm-thick film is deposited, in the other cases the amount of material is too little to be detected by the used XRD diffractometer.

Figure 2.16(b) shows the symmetric ω -scans performed around the GaN(0002) reflection. In this configuration, the width of the Bragg peaks depends on the epitaxial alignment of the NWs; the broader the peak, the worse the alignment of NWs in the ensemble. The peak width related to GaN NWs grown on 8- or 14-nm-thick AlN layers is signifi-

2. Growth of group-III-N structures for NW-LEDs by molecular beam epitaxy

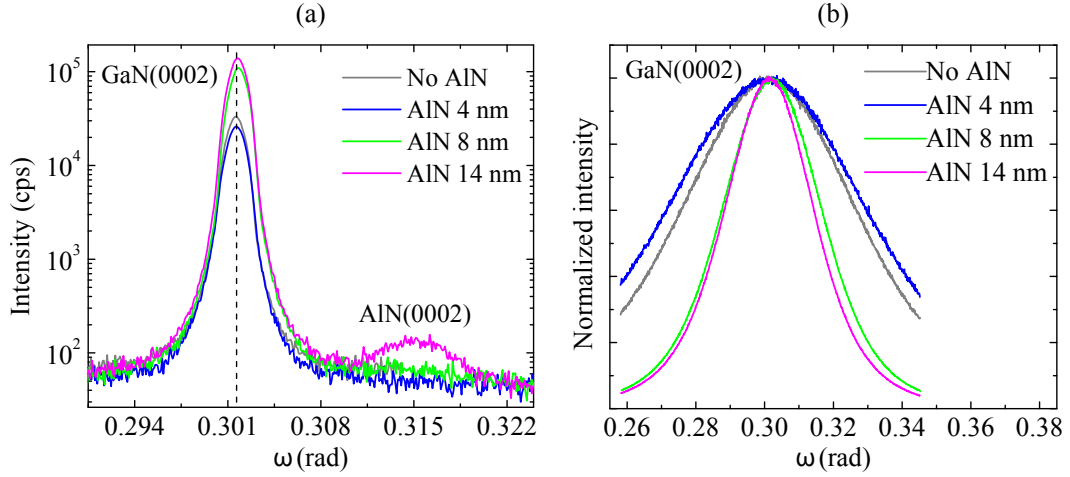


Figure 2.16: XRD measurements in (a) $\omega - 2\theta$ and (b) ω geometry around the GaN(0002) reflection of the NW samples grown on AlN layers of different thickness. For comparison also the profile of a sample grown on bare Si (No AlN) is plotted.

cantly lower than that of NWs grown on 4-nm-thick AlN or on bare Si: the FWHM of the peaks is roughly 0.031 rad and 0.048 rad in the former and latter case, respectively. This result agrees with what was suggested by SEM and RHEED images, *i. e.*, the alignment of the NWs improves with increasing AlN thickness.

Next, we investigate the suitability of these very thin AlN layers for SAG. The same series of samples described above was used to study the nucleation time of the GaN NWs. To this end, we monitored *in situ* the flux of Ga desorbing from the substrate (Φ_{QMS}) by line-of-sight QMS. The QMS data acquired during the growth of GaN NWs on bare Si (grey curve) and on various AlN layers are plotted in figure 2.17: the red, blue, and green profiles correspond to layer thicknesses of 3, 4, and 8 nm, respectively. The evolution of the QMS signals shown in figure 2.17 is similar to the one already reported in previous studies carried out on Si substrates^[66,67,94]. Three main regions are noticeable: i) an initial stage where Φ_{QMS} is nearly constant, associated with the incubation of the NWs; ii) a second stage where Φ_{QMS} decreases because of the formation of GaN NWs; iii) a final stage where Φ_{QMS} reaches steady-state conditions, related to the continuous elongation of the NWs. We observe that the elongation stage is not completely evident in the case of NWs grown on the 3-nm-thick AlN layer (red curve). In fact, in this case the NWs are completely misaligned and do not form a homogeneous ensemble [see figure 2.17(d)], which could obviously affect the transition between the different stages of NW nucleation and growth. More interesting, it is clearly visible that the GaN NWs grown on AlN layers exhibit incubation stages much shorter than the one observed on Si, reflecting the fact that the nucleation of GaN NWs takes place faster on AlN than on Si. Moreover, this first stage becomes shorter and shorter with increasing AlN thickness. For instance, the incubation stage ends after only few tens of seconds in the case of the 8-nm-thick layer. Interestingly, immediately after the beginning of the deposition the samples on AlN show a lower desorption of Ga, although all the samples were grown under the same conditions. This observation might be explained by a higher sticking coefficient of the Ga atoms on the AlN surface due to its higher roughness which might offer nucleation centres for the formation of GaN islands.

Using the QMS data, we define the average nucleation time of the NWs as the time

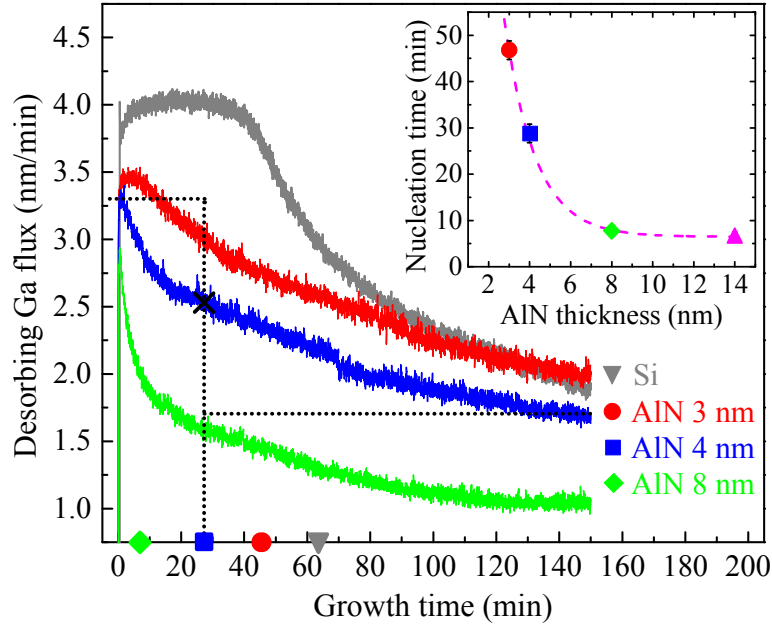


Figure 2.17: Desorbing Ga flux measured by QMS as a function of growth time for different starting surfaces: Si (grey profile) and AlN buffer layers with thickness equal to 3 nm (red profile), 4 nm (blue profile), and 8 nm thick (green profile). The nucleation times plotted in the inset were obtained from the QMS profiles as schematically sketched by the black dotted lines in the case of the blue profile. The dashed line in the inset is a guide to the eye. The magenta upward-facing triangle in the inset depicts the nucleation time of GaN NWs grown on a 14-nm-thick AlN buffer layer.

from the beginning of the deposition to the moment when the desorbing Ga flux decreases by half the difference between the values that it has during the incubation and the elongation stages, respectively^[94]. This method is sketched by the dotted line in figure 2.17 for the QMS profile in blue. Applying the same procedure also to the QMS profiles of the other samples, we extracted the data plotted in the inset of figure 2.17, which shows the nucleation time of the GaN NWs as a function of the thickness of the AlN layer. It is clear that the nucleation time strongly depends on the AlN thickness. In particular, the nucleation time decreases very fast with increasing thickness from 3 to 8 nm, whereas a further increase in AlN thickness does not lead to further significant changes in the nucleation time. In fact, the difference between the nucleation time on the 8 and 14-nm-thick AlN layers is only 1 min. However, in all the considered cases the nucleation time of the NWs grown on AlN is shorter than the one observed for NWs on bare Si, which was as long as 62 min. The decrease of the nucleation time with increasing thickness of the AlN layers might be correlated with the higher density of surface irregularities observed in figure 2.15(a)–(c) for thicker AlN layers.

In conclusion of this subsection, the thinnest AlN layer that leads to the growth of well-aligned GaN NWs characterized by a relatively short nucleation time is the one with a thickness of 4 nm. Therefore, this is the most promising buffer layer to achieve selective-area grown NW-LEDs. In the following subsection the morphological and electrical properties of the 4-nm-thick AlN layer are further investigated.

2. Growth of group-III-N structures for NW-LEDs by molecular beam epitaxy

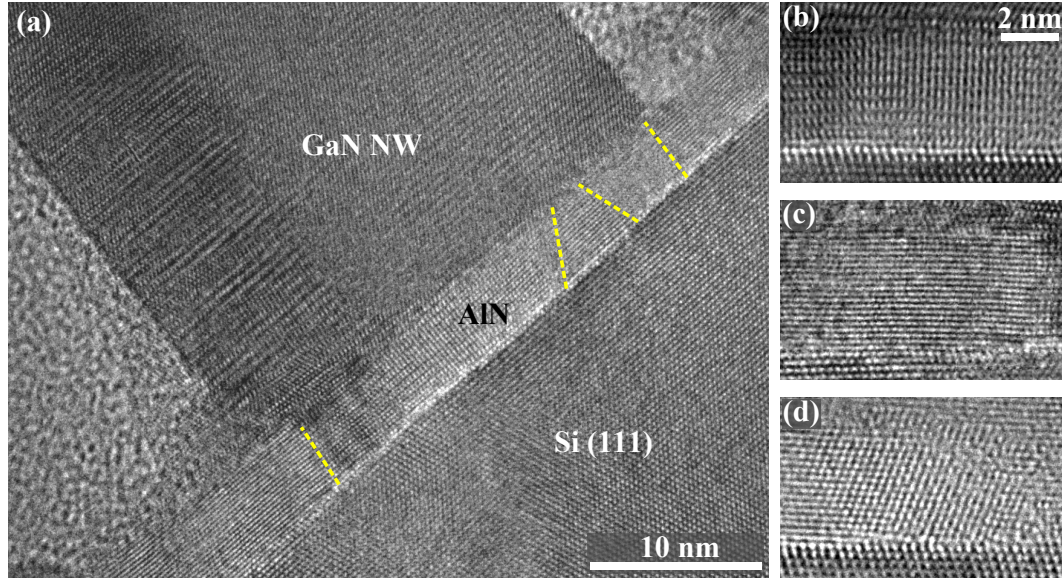


Figure 2.18: (a) HR-TEM image of a GaN NW grown on the 4-nm-thick AlN layer. The yellow dashed lines highlight the boundaries of different grains in the AlN layer. (b)–(d) Magnification of three different grains with (b) hexagonal, (c) twisted hexagonal, and (d) cubic phase. Images acquired by Achim Trampert and Javier Grandal-Quintana at PDI.

2.3.3. Microstructure of the AlN layer and current conduction

Since the AlN buffer layer is expected to influence the current flow through the envisioned NW-LED, it is important to investigate its microstructure and its conduction properties. To this end, the 4-nm-thick AlN was characterized by means of transmission electron microscopy (TEM) and conductive AFM (C-AFM).

TEM analysis

The interface region between the base of the NWs, the AlN buffer, and the Si substrate was analysed by high-resolution TEM (HR-TEM). The micrograph in figure 2.18(a) shows a representative GaN NW grown on the 4-nm-thick AlN layer. Besides confirming the nominal thickness of the buffer layer, this image shows a fairly smooth interface between the Si substrate and the AlN, free of amorphous Si_xN_y . In addition, it becomes clear that the AlN layer is not a single crystal; on the contrary, it is composed of several grains with different crystallographic orientations, as highlighted by the yellow dashed lines in figure 2.18(a). A more detailed analysis of the grains reveals that the majority of them exhibits the hexagonal phase [see figure 2.18(b)], with some tilted and twisted domains [see figure 2.18(c)]. We found also a few inclusions of the cubic phase [see figure 2.18(d)]; cubic inclusions are likely to form during the growth of thin AlN layers at low temperature (lower than 700 °C)^[147–149]. Underneath the base of a NW, even if the NW is as thin as the one in figure 2.18(a) with a diameter of about 30 nm, typically several grains are visible. At this point it is worth emphasizing that reasonable current conduction across a closed and single crystalline AlN layer would indeed not be possible. In fact, in that case charge transport could take place only by tunnelling that could only enable the conduction of a negligible amount of electrons through a 4-nm-thick AlN layer. For the envisioned NW-LED it is desirable that the AlN buffer layer exhibits a high density of conductive paths

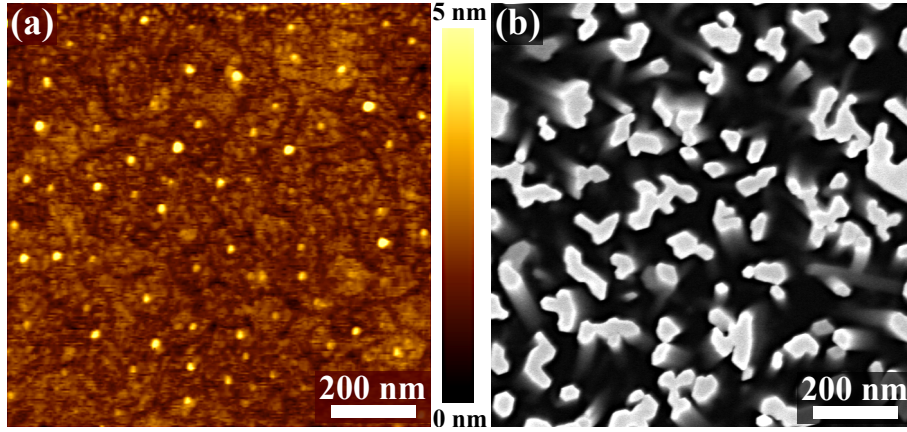


Figure 2.19: (a) AFM images of a 4-nm-thick AlN layer acquired in tapping mode. (b) Top-view SEM micrograph of GaN NWs grown on the same type of AlN. The two images have the same scale.

for electrons. Therefore, in our case the formation of grain boundaries in the AlN layer is actually favourable; in fact, such defects are known to facilitate charge transfer across insulating layers^[150].

AFM analysis

The surface microstructure of the 4-nm-thick AlN layer was also analysed by means of AFM measurements. Figure 2.19(a) shows the topography; small protrusions about 2–4 nm high with a density equal to $7 \times 10^9 \text{ cm}^{-2}$ are visible. They are almost always located at the centre of flat islands separated by 1-nm-deep grooves. This morphology is rather similar to the one observed in figure 2.8(e), thus suggesting that the small protrusions might be due to the “Ga-polishing” procedure used to remove the native oxide from the Si substrate. The density of hillocks observed in figure 2.8(e) is about two times higher than that counted after the deposition of the thin AlN film. This outcome might be explained by imaging that the shortest protrusions are covered by the AlN layer, or by taking into account sample-to-sample fluctuations of the growth parameters.

Figure 2.19(b) shows a top-view SEM micrograph of GaN NWs grown on the 4-nm-thick AlN layer. The density of coalesced nanostructures is about $6.5 \times 10^9 \text{ cm}^{-2}$, this value clearly increases if the coalesced NWs are counted separately. Interestingly, density and distribution of NWs are very similar to those of the protrusions observed on the AlN buffer. This fact might indicate that the hillocks, likely due to the “Ga-polishing” procedure, could act as nucleation centres for the NWs. Dedicated experiments on the nucleation of GaN NWs performed by Sergio Fernández-Garrido at the PDI seem to support this hypothesis. In any case, the comparison of figures 2.19(a) and (b) suggests that almost every NW or cluster of coalesced NWs is likely in contact with the protrusions present on the AlN. An example of such a contact might be visible in the HR-TEM micrograph of figure 2.18(a), where the base of the GaN NW seems to touch a protrusion emerging from the AlN with sizes comparable to the one measured by AFM (see bottom left corner of the NW). The contact of the two structures seem to produce strain and/or stacking faults inside the NW, as indicated by the dark contrast in the HR-TEM image.

The current conduction across thin AlN layers was investigated by means of C-AFM. This technique enables the direct correlation of morphological and electrical properties of

2. Growth of group-III-N structures for NW-LEDs by molecular beam epitaxy

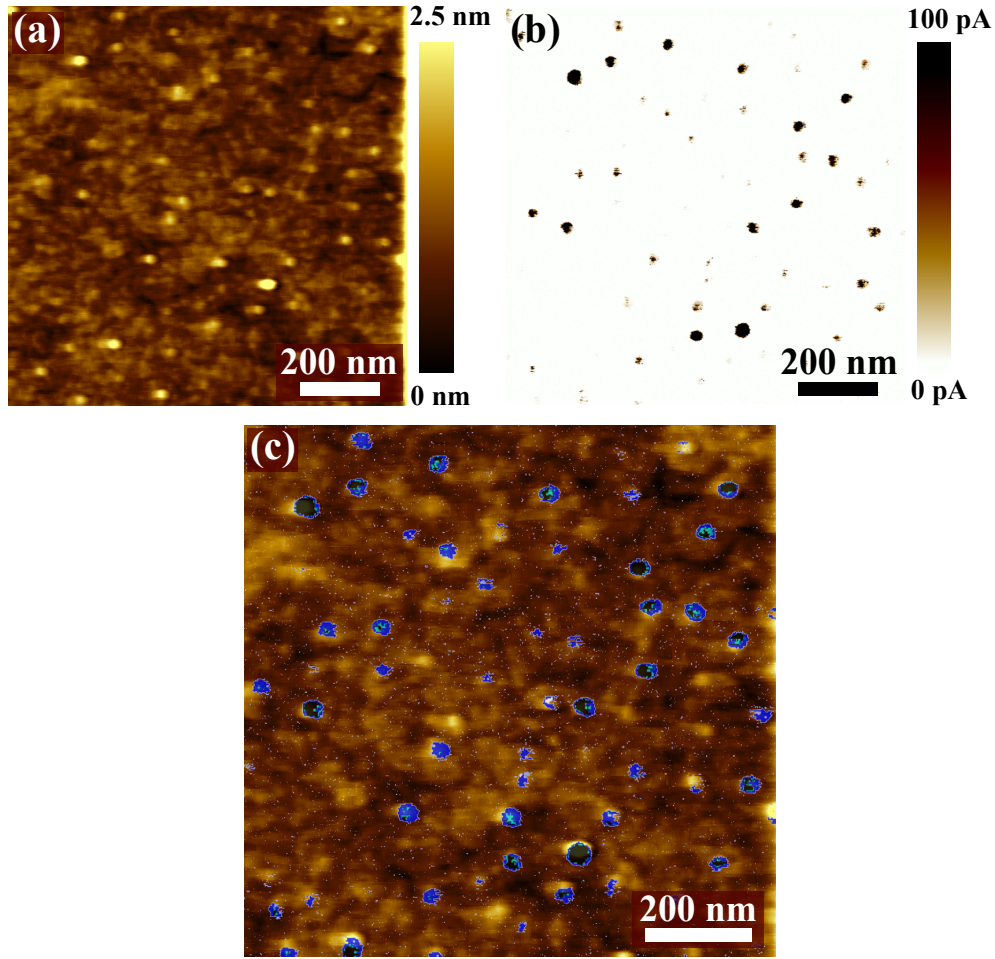


Figure 2.20: C-AFM measurements performed on a 4-nm-thick AlN layer: (a) topography of the surface acquired in contact mode, (b) corresponding current map normalized to the noise level, and (c) superimposed topography and current images. During the measurements, the tip was grounded whereas a negative bias of -5 V was applied at the back side of the Si substrate. The data were acquired under the supervision of Dr. Xu Gengzhao and Dr. Haijian Zhong at SINANO.

the sample. The C-AFM measurements were performed at the Suzhou Institute of Nano-Tech and Nano-Bionics (SINANO) in China under the supervision of Dr. Xu Gengzhao and Dr. Haijian Zhong. The data were acquired at room temperature ($T=303$ K) by means of a Veeco Multimode AFM system equipped with a 20-nm-wide conductive Si tip coated with Pt. During the C-AFM measurements, the tip was grounded whereas a negative bias of -5 V was applied at the back side of the Si substrate.

Figure 2.20(a) shows the AFM topography of the sample surface measured in contact mode. The same features observed in figure 2.19(a) are recognizable; the blurred aspect of figure 2.20(a) in comparison with 2.19(a) is due to the different conditions used for the measurements, namely kind of tip and scanning mode. Figure 2.20(b) shows the corresponding current map, that represents the charges flowing from the AFM tip into the sample during the scan; the dark spots identify more conductive areas. Note that current of the order of magnitude of 100 pA flows through each spot at the applied bias of -5 V; this is a relatively high current for a so small area, we estimated a current density

2.3. Selective-area growth: Optimization of the AlN layer

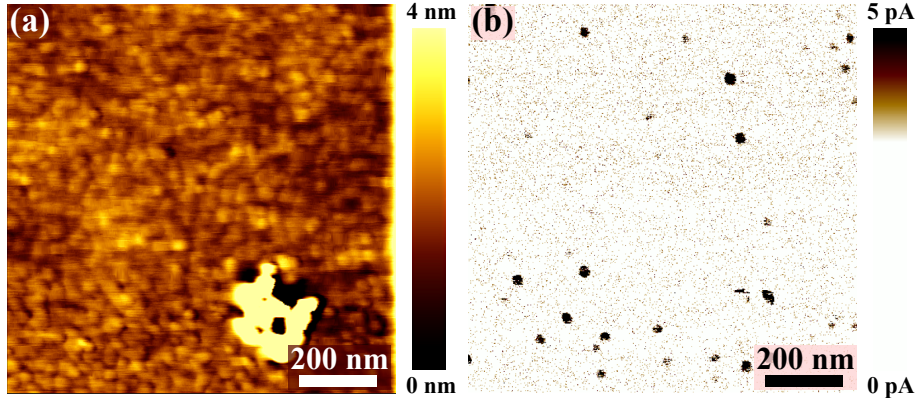


Figure 2.21: C-AFM measurements performed on a 10-nm-thick AlN layer: (a) topography of the surface acquired in contact mode, (b) corresponding current map normalized to the noise level. During the measurements, the tip was grounded whereas a negative bias of -5 V was applied at the back side of the Si substrate. The data were acquire under the supervision of Dr. Xu Gengzhao and Dr. Haijian Zhong at SINANO.

roughly equal to 15 Acm^{-2} . To better visualize the correlation between current conduction and spatial features of the surface, the measured current and topography images were superimposed, see figure 2.20(c). It is clearly visible that the majority of the current flows through the protrusions present on the surface, almost every hillock conducts current. In contrast, the rest of the surface is much more resistive and only a relatively small current is measured.

Since better alignment and shorter nucleation times can be achieved by increasing the thickness of the AlN buffer layer (see subsection 2.3.2), it is worth checking the electrical properties of a thicker layer too. To this end, the C-AFM measurements were repeated also on a 10-nm-thick AlN layer. Figure 2.21(a) shows the AFM topography of the sample surface measured in contact mode. In this case the protrusions observed in the thin AlN are not visible; on the contrary, the whole surface is covered by a very dense distribution of small islands. The protruding feature on the bottom right side of the image is due to one of the sporadic Al droplets present on the surface. It was scanned on purpose to check whether it exhibits peculiar conduction properties, but no particular behaviour was observed. Figure 2.20(b) depicts the corresponding current map; although also in this case some conductive spots were observed, their density and intensity is much lower than the one measured in case of the thinner AlN. In particular, the amount of current that can cross the 10-nm-thick AlN film is about 20 times lower than that achievable in case of a 4-nm-thick layer. We believe that this big difference is due to the absence of the conductive protrusions on the surface. Consequently, NW-LEDs grown on such a 10-nm-thick AlN buffer will most likely not work.

In conclusion, we have demonstrated that a relatively good current conduction across a 4-nm-thick AlN layer is possible. The conductive paths are mainly given by small protrusions emerging from the thin AlN layer, their origin is likely due to the “Ga-polishing” procedure, and thus they might be composed by a mixture of Ga, Si, and N atoms. In addition, grain boundaries present in the thin AlN film might also provide further conductive paths. The electrical properties of a NW-LED grown on such an AlN buffer will be discussed in section 3.3.

2.4. Selective-area growth of GaN NWs

So far the SAG of GaN NWs has been achieved at PDI by means of AlN buffer layers with thickness of about 12 nm^[143,144]. Since the nucleation time of the NWs strongly depends on the properties of the AlN buffer, it is at present unclear whether similar results can be also obtained with the 4-nm-thick AlN identified in section 2.3.2 as a possible candidate for the fabrication of LEDs based on ensembles of ordered NWs. Therefore, as the next step we have to prove that SAG of GaN NWs with good selectivity and morphology is actually possible on this type of AlN buffer. The fabrication of the patterned substrates and the subsequent growth of ordered GaN NW ensemble is discussed in this section.

2.4.1. Fabrication of a multi-purpose mask

As already mentioned, SAG of GaN nanocolumns on Si substrates requires a buffer layer and a mask; in our case, the latter one is given by a 10-nm-thick Si_xO_y film deposited by magnetron sputtering on the AlN layer. A schematic representation of this approach to SAG of GaN NWs on Si is depicted in figure 2.22(a). Holes in the mask were produced by means of two different nano-lithographic techniques.

As first step towards the final patterned substrate, a multi-purpose mask was designed. The mask consists of many different fields with arrays of nano-holes, see figure 2.22(b). All the holes in the fields have circular shape and are arranged in a hexagonal pattern. Four equivalent sectors separated by 1-mm-large spacers [(red cross in figure 2.22(b))] are present on the mask. The spacers enable the cut of the 2 inch wafer into four quarters, which can be used for different growth runs or for various characterizations. Each sector contains nine fields of area equal to 2 × 2 mm²; the arrangement of the fields is different in the four parts. In this way the various arrays of nano-holes are present on different

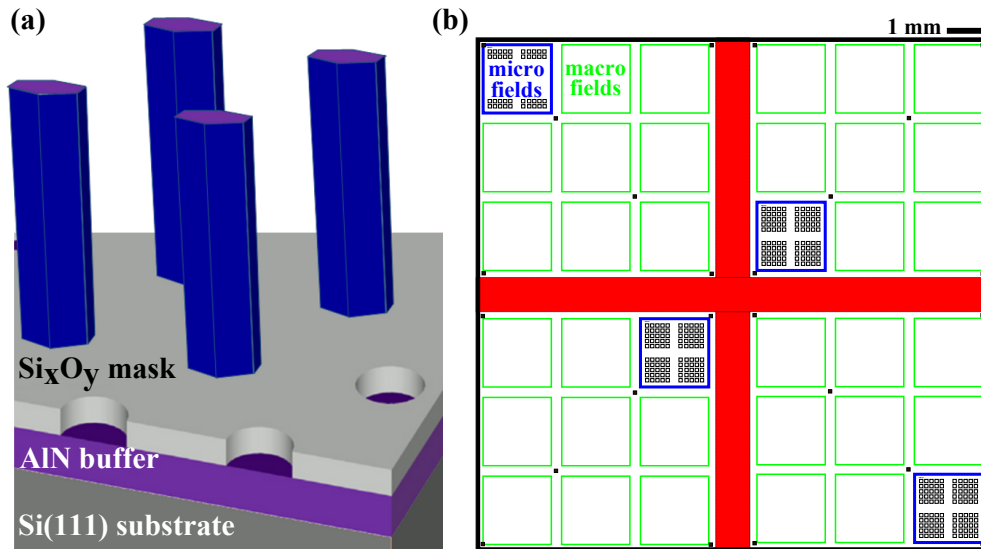


Figure 2.22: (a) Schematic representation of the approach to SAG of GaN NWs on Si based on AlN buffer layer and Si_xO_y mask. Note that the various dimensions are not to scale. (b) Overview of the multi-purpose mask designed in the framework of this thesis. The micro- and macro-fields are highlighted in blue and green, respectively. The red cross represents the spacers that divide the different parts of the mask.

parts of the wafer, which are likely exposed to slightly different temperatures and fluxes. In each sector, eight macro-fields [highlighted by green frames in figure 2.22(b)] are completely filled by holes with a fixed geometrical combination of diameters and pitches (*i. e.*, distance between the centres of the holes). These macro-fields are suitable for XRD measurements and for LED processing that require samples of relatively large area. Each of the remaining parts contains 100 different micro-fields of area equal to $100 \times 100 \mu\text{m}^2$, as highlighted by blue frames in figure 2.22(b). The micro-fields are characterized by different combinations of diameters and pitches, ranging from 30 to 230 nm and from 0.1 to $10 \mu\text{m}$, respectively. Such a big variety of geometrical features on the same sample enables the study of different properties of the SAG NWs as a function of both diameter of the holes and distance between their centres. Furthermore, the micro-fields with large spacing between the holes might make easier the characterization of single NWs, whereas the more dense arrays might be best suitable for fabrication of devices.

Once designed the mask has to be transferred into the Si_xO_y layer. The substrates used in this work were patterned by means of two different lithographic techniques: soft UV-nanoimprint lithography (NIL) and e-beam lithography (eBL). The main three technological steps involved during NIL and eBL process are illustrated in figures 2.23(a)

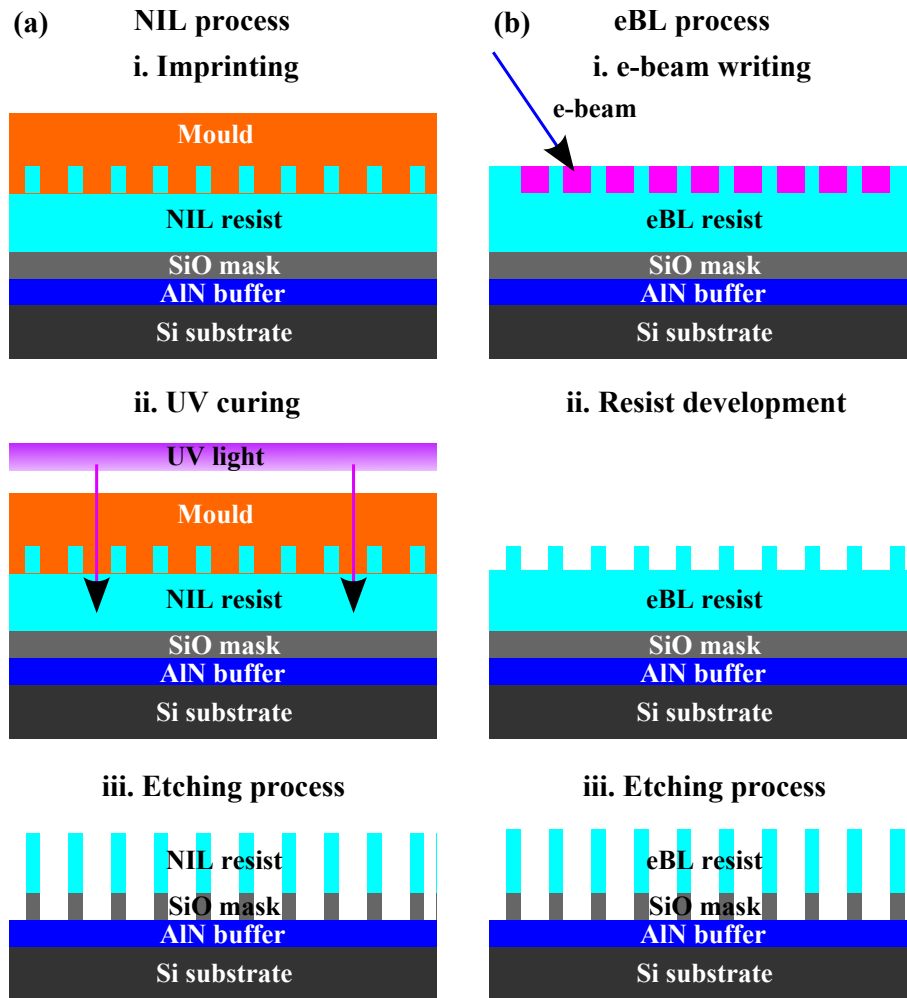


Figure 2.23: Schematic representation of the main three steps involved during (a) NIL and (b) eBL process. Note that the various dimensions are not to scale.

2. Growth of group-III-N structures for NW-LEDs by molecular beam epitaxy

Table 2.1: List of the optimized parameters used to transfer the pattern defined by NIL into the mask.

Process	Gas flow	RF power	Pressure	Time	Etching rate
ICP-RIE of the residual resist	O ₂ =8 sccm	RF _{RIE} =40 W RF _{ICP} =100 W	0.5 Pa	85 s	23 nm/min
RIE of the Si _x O _y mask	CHF ₃ =25 sccm	RF _{RIE} =100 W	1 Pa	90 s	18 nm/min
Surface cleaning	O ₂ =10 sccm	RF _{RIE} =50 W	1 Pa	180 s	

and (b), respectively. The NIL process employed in this thesis was developed by Namil Koo and Jungwuk Kim at the *AMO GmbH* in Aachen. As first step, a special photoresist sensitive to UV light (called AMONIL) is spun on the surface of the Si_xO_y mask; the parameters employed during the spin-coating process produce a layer about 90 nm thick. A flexible mould is then pressed on the sample surface and the pattern is thus transferred into the NIL resist; eventually, the AMONIL is made harder by UV curing. At this point the residual NIL resist present inside the holes (roughly 20 nm thick) has to be removed, and then the Si_xO_y mask has to be etched down to the AlN buffer. The holes in the mask were produced via reactive ion etching (RIE) with CHF₃ gas, whereas the residual resist inside the holes was removed through inductively coupled plasma RIE (ICP-RIE) with O₂. The etching process is a crucial step and its optimization required many efforts. In fact, the AlN layer was found to react very easily with the CHF₃ gas used to etch the mask, and even few seconds of extra exposure can affect the surface properties of the AlN buffer, thus impeding the nucleation of NWs. The optimized parameters of the dry etching processes used in case of substrates patterned via NIL are listed in table 2.1. By way of example, the surface of the final patterned mask obtained through NIL is shown in figure 2.24(a). The sample looks clean and the holes with average diameter of about 150 nm are well formed in the mask.

The second technique used to pattern the substrate was e-beam lithography; the samples were processed in collaboration with Mathias Matalla at the Ferdinand-Braun-Institut in Berlin, and with Abbes Tahraoui and Bernd Drescher at the PDI. As shown in fig-

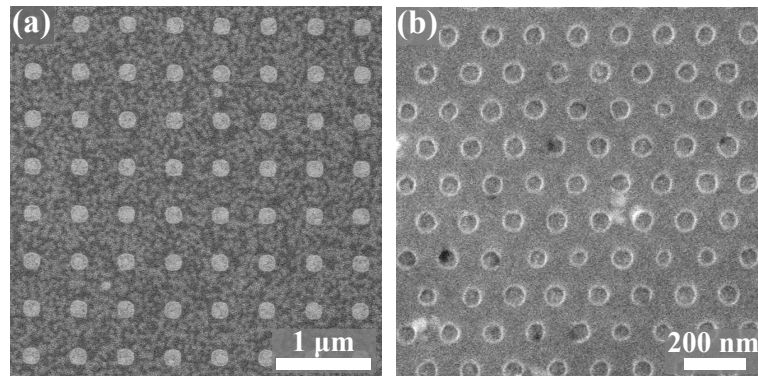


Figure 2.24: SEM top-view micrograph of two different fields patterned into the Si_xO_y mask by means of (a) NIL and (b) eBL. Note the different scale of the two images.

Table 2.2: List of the optimized parameters used to transfer the pattern defined by eBL into the mask.

Process	Gas flow	RF power	Pressure	Time	Etching rate
ICP-RIE of the residual resist	O ₂ =8 sccm	RF _{RIE} =40 W RF _{ICP} =100 W	0.5 Pa	5 s	≈20 nm/min
RIE of the Si _x O _y mask	CHF ₃ =20 sccm	RF _{RIE} =100 W	1 Pa	1 min	17 nm/min

ure 2.23(b), a special e-beam resist (called ZIT 520a) is spun on the surface of the Si_xO_y mask, so as to produce a layer about 100 nm thick. The various arrangements of holes are then written into the resist by means of a *Vistec SB251* eBL system. The special resist used is very sensitive to the e-beam and enables the writing of a huge number of very small features in a relatively short time; for instance, our complex mask pattern required about 1 hour to be prepared. Then the sample is developed; this process removes the resist exposed to the e-beam, thus leaving the written pattern in the resist. Like in the case of NIL, to transfer the pattern into the Si_xO_y mask the residual resist inside the holes has to be removed and then the Si_xO_y has to be etched down. ICP-RIE with O₂ and RIE with CHF₃ were employed to etch the residual resist and the Si_xO_y, respectively. The optimized parameter used for the preparation of the substrates patterned via eBL are listed in table 2.2. After the dry etching, the wafers were cleaned by means of an appropriate resist stripper, and then rinsed in deionized water. The surface of the final patterned mask obtained through eBL is shown in figure 2.24(b). Well ordered arrangements of holes with diameter as small as 50 nm were obtained.

In both the cases, the final patterned substrates were further cleaned with acetone and isopropanol in ultrasonic bath just before their insertion into the MBE chamber.

2.4.2. Selective-area growth of GaN nanowires

As already mentioned, the selective-area growth of GaN NWs is based on the different nucleation time of the nanocolumns on various materials. For instance, in section 2.3.2 we have seen that the NWs nucleate faster on an AlN layer than on bare Si. This concept was studied in detail by Tobias Gotschke in his PhD thesis^[144]. He grew a series of GaN NW samples both on bare Si and on 10-nm-thick AlN layers using different Ga fluxes while keeping the N flux constant (about 10 nm/min). For a given Ga flux the substrate temperature was varied until the nucleation of NWs was observed via line-of-sight QMS (namely, until a significant drop of the desorbing Ga occurred); in this way he obtained the nucleation temperature as a function of the impinging Ga flux. Figure 2.25 shows the growth diagram of the GaN NWs obtained from this study. The blue and grey solid lines indicate the border of the growth region for GaN NWs deposited on AlN and Si, respectively. Above these lines no growth takes place, below the NWs can nucleate within 50 min. In the window between the two lines the nanocolumns can grow on AlN but not on Si. Therefore, if a Si (or Si_xO_y) mask partially covered an AlN buffer layer the GaN NWs could form only where the AlN is exposed, thus enabling the selective-area growth. It is worth noting that the nucleation temperature of GaN NWs is very similar on bare Si and on Si_xO_y^[144]; therefore, the experimental points of figure 2.25 obtained using Si substrates can be assumed to be valid also in case of Si_xO_y.

2. Growth of group-III-N structures for NW-LEDs by molecular beam epitaxy

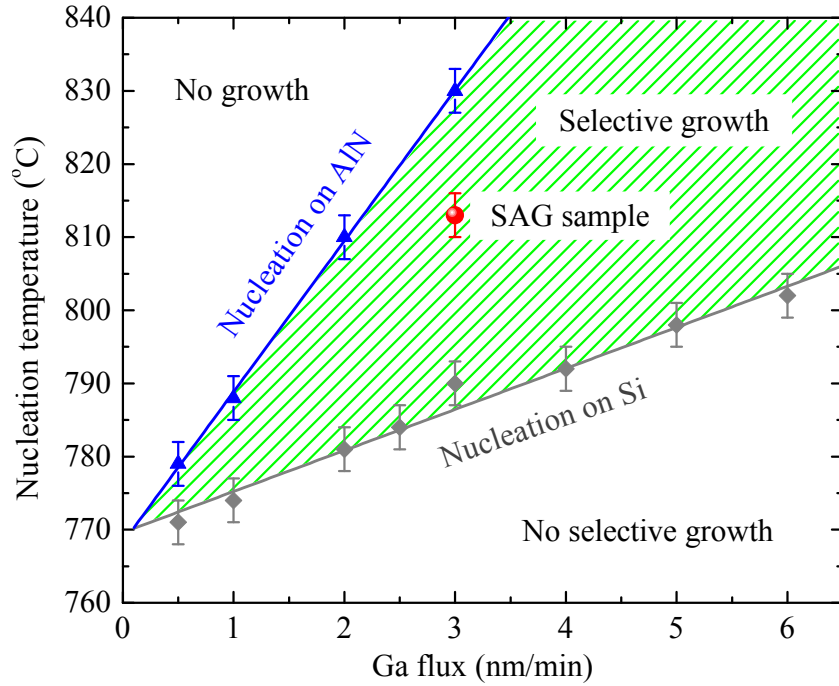


Figure 2.25: Nucleation temperature obtained by monitoring the desorbing Ga atoms via line-of-sight QMS. The experiments were carried out by Tobias Gotschke both on bare and AlN-buffered Si substrate^[144]. The region between the solid lines define the growth window where SAG of GaN NWs can take place. The red data point indicates the growth parameters used for the SAG sample presented in this work.

Making use of the diagram plotted in figure 2.25, we chose the growth parameters suitable for the SAG of GaN NWs. The employed conditions are indicated by the red data point in figure 2.25, they are: $\Phi_{Ga}=3$ nm/min, $\Phi_N=10$ nm/min (obtained using a RF power of 500 W and a N_2 flow of 2 sccm), and substrate temperature equal to 813 °C. The SAG sample presented in this subsection was grown for 3 hours in the reactor of MBE8, refer to SAG1 in table A.1. The patterned substrate was obtained by means of soft UV-nanoimprint lithography. Further details about the optimization of the growth

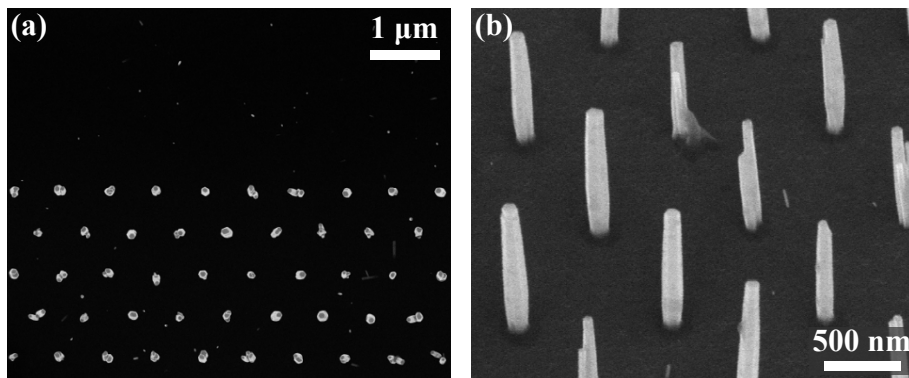


Figure 2.26: (a) Top-view and (b) bird's-eye view SEM images of selectively grown GaN NWs with different arrangements. The diameter of the holes is 60 nm while the distance between their centres is 0.7 and 1 μ m for (a) and (b), respectively.

parameters for the SAG of GaN NWs using a Si_xO_y mask and AlN buffer layers can be found elsewhere^[143]. After growth the sample was analysed by SEM; figure 2.26 presents a top view (a) and a bird's-eye view (b) of different arrays of SAG NWs. Figure 2.26(a) shows that the selectivity is good even outside the patterned area; only very few and thin NWs spontaneously formed on the mask. In between the regular array of NWs the parasitic nucleation of GaN on the mask is suppressed even better, also when the distance between the NWs is as large as $1\text{ }\mu\text{m}$, as shown in figure 2.26(b). In almost all of the holes with diameters in the range of $40\text{--}70\text{ nm}$, one single NW is formed. In larger holes, multiple nucleation took place leading to the formation of separated NWs that are expected to coalesce into single NWs with continued growth. In this respect, it is worth noting that only in thin NWs, for which the elastic relaxation of strain at the free sidewall surfaces is efficient, a high crystal quality and high In content of axial (In,Ga)N/GaN heterostructure is possible^[8,76]. Almost all of the NWs are oriented perpendicular to the substrate, have a hexagonal C-plane top facet, and exhibit rather homogeneous heights and diameters. Therefore, the SAG of GaN NWs is possible on Si substrates even with an AlN buffer layer that is only 4 nm thick.

2.4.3. Fabrication of ordered arrays of GaN quantum wires

As already mentioned, one of the most important benefits of nanowires is the elastic relaxation of strain at the free sidewall surfaces. However, for heterostructures with considerable lattice mismatch, this conceptual advantage requires NW diameters that are much smaller than what can typically be achieved^[8,76]. In particular, self-induced GaN NWs usually are several tens of nanometres thick, but diameters significantly smaller than 20 nm are required to achieved elastic relaxation of strain in case of high lattice mismatch. In this part of the thesis, we present an innovative approach developed at the PDI to overcome this limitation. It enables the production of ordered arrays of ultrathin GaN NWs with diameters below 10 nm , which can be used as base for the growth of axial heterostructures. For such extreme diameters, even the considerable lattice mismatch of 10% between InN and GaN can be relieved elastically. In addition, diameters below 10 nm result in strong lateral dielectric confinement. Therefore, an InN insertion grown on top of the ultrathin NWs would act as an electronic quantum dot (QD) with a zero-dimensional density of states formed on a one-dimensional (1D) GaN quantum wire (QWR). Such a system might be used as a tunable single photon emitter with high performance.

The experimental procedure to obtain the ultrathin QWR was developed at the PDI by Johannes K. Zettler. Continuing the idea proposed by Brockway and co-authors^[151], the *self-induced* GaN NWs were thermally decomposed in the MBE reactor under high vacuum condition directly after the growth. A dense ensemble of QWRs with diameters lower than 10 nm can be obtained in this way, but because of their high density and the mutual electrostatic attraction the ultrathin QWRs bend. This undesired effect might be avoided by growing NW ensembles with low density, for instance via SAG. The feasibility of this approach is tested here.

In this subsection two SAG samples are presented, in both cases the GaN NWs were prepared under identical conditions; after the growth one of the samples was thermally decomposed, whereas the other one not (refer to SAG2 and SAG3 in table A.1, respectively). The samples were produced in the reactor of MBE9; the substrate was not rotated during the deposition because of a technical failure. A $10\text{-nm-thick Si}_x\text{O}_y$ mask patterned by means of eBL and deposited on a 10-nm-thick AlN buffer layer was used

2. Growth of group-III-N structures for NW-LEDs by molecular beam epitaxy

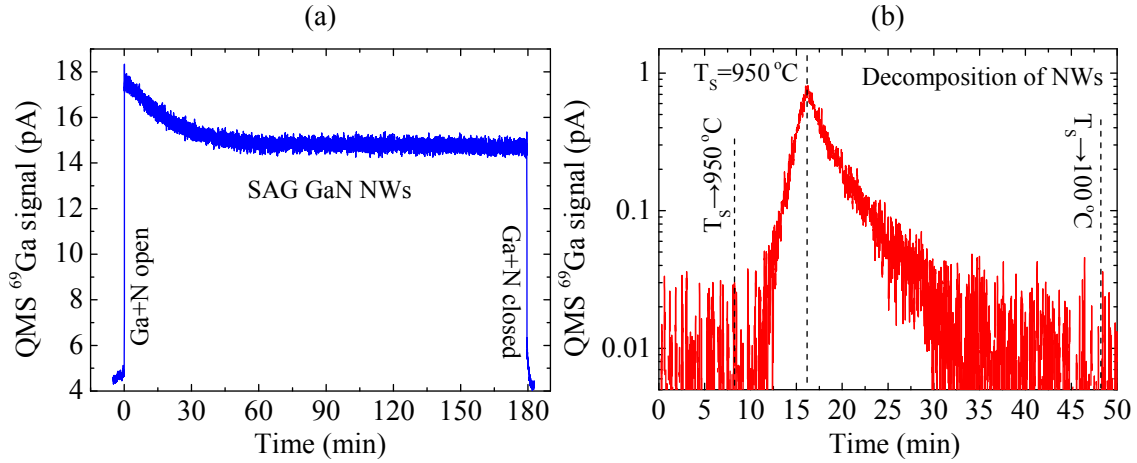


Figure 2.27: QMS signal related to the desorbing ^{69}Ga atoms acquired during (a) the SAG of GaN NWs and (b) the thermal decomposition of the NWs. In the latter case the data are plotted on logarithmic scale.

as substrate for SAG. To find the optimal growth parameters experiments similar to the one presented in the previous subsection were carried out. The resulting growth parameters are: $\Phi_{\text{Ga}}=3 \text{ nm/min}$ ($\text{BEP}=1.85 \times 10^{-7} \text{ mbar}$), $\Phi_{\text{N}} \approx 8 \text{ nm/min}$ (obtained using a RF power of 500 W and a N_2 flow of 3.5 sccm), and substrate temperature equal to 846°C . The NWs were grown for 3 hours. The QMS signal related to the desorbing ^{69}Ga atoms acquired during the selective-area growth of the NWs is shown in figure 2.27(a). The QMS profile characteristic of SAG differs from that observed during the growth of self-induced NWs, see for example the curves in figure 2.17. In fact, in the former case no nucleation delay is visible, and after a relatively small drop the QMS signal stabilizes remaining constant during the entire growth. The different QMS profiles are mainly due to the dissimilar surface area available for the nucleation of NWs in the two cases. In fact, when a patterned mask is present the NWs preferentially nucleate inside the holes that cover a relatively tiny area compared to the total surface of the wafer. Therefore, the total amount of Ga incorporated on the surface during SAG is much smaller than in the case of self-induced NWs.

At the end of the NW growth, the substrate temperature (T_s) was lowered down to about 600°C , the Ga cell and the plasma source were set to stand-by conditions, and the pressure of the chamber was let recover. Once the high vacuum condition ($\approx 1 \times 10^{-7} \text{ mbar}$) was reached, the substrate temperature was increased again up to 950°C with a rate equal to 40°C/min . As soon as the T_s is risen above 840°C , the GaN NWs started to decompose and the QMS signal related to the desorbing ^{69}Ga atoms increased. In figure 2.27(b) the QMS signal as a function of the time is plotted on logarithmic scale. The linearity of the profile between 11 and 17 min (*i.e.*, when T_s was ramped up) indicates that the GaN decomposition rises exponentially with temperature. The sample was let decompose at $T_s = 950^\circ\text{C}$ for 30 min. As visible in figure 2.27(b), in this time interval the QMS ^{69}Ga signal drops quickly, reflecting the fact that the amount of GaN present on the sample decreases. About 25 min after the beginning of the decomposition, the QMS signal reached the background level, meaning that the amount of desorbing Ga atoms was too small to be detected by the QMS. After 30 min at $T_s = 950^\circ\text{C}$ the sample was cooled down to 100°C .

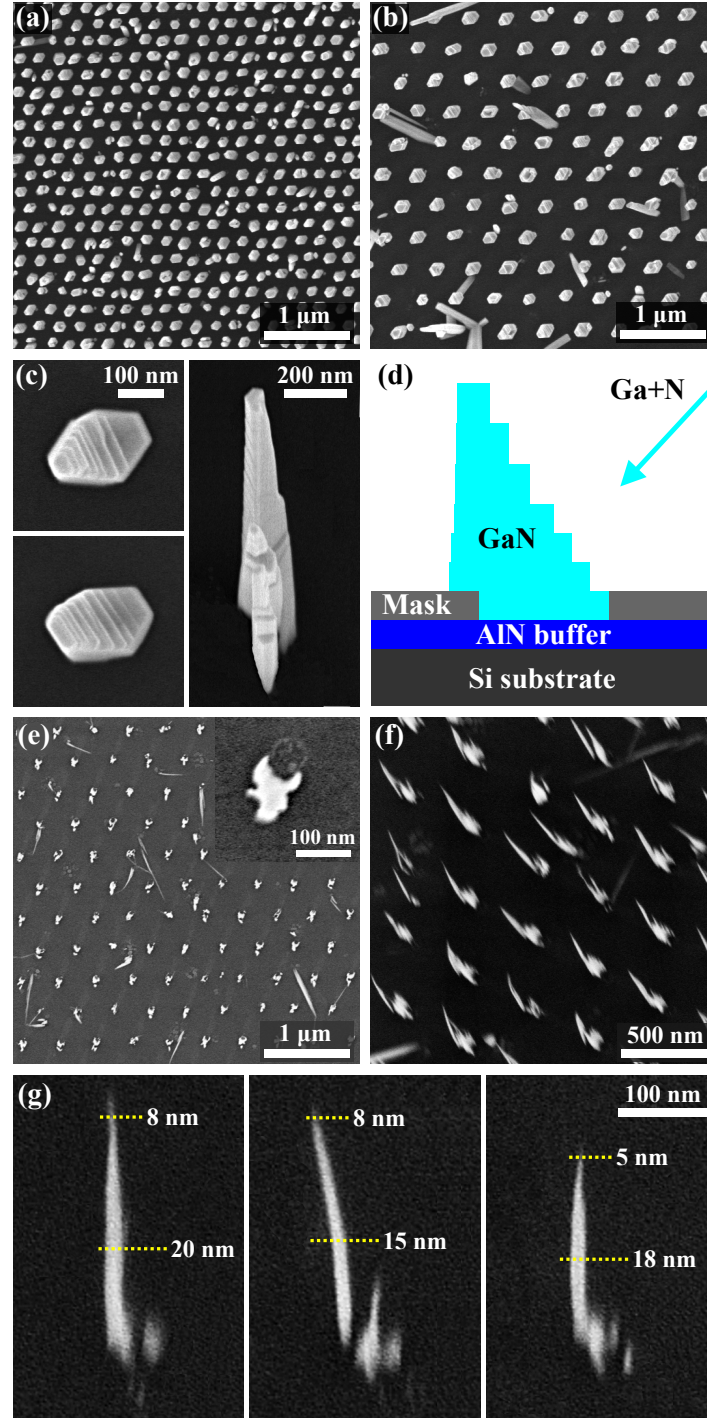


Figure 2.28: (a)–(b) Top-view SEM micrographs of GaN NWs grown in arrays of holes with diameter of about 60 nm and pitches equal to (a) 200 and (b) 400 nm. (c) Highly magnified images of representative NWs, the step-like structure due to the lack of substrate rotation is schematically illustrated in (d), note that the various sizes are not to scale. (e)–(f) Top- and tilted-view SEM micrographs of the SAG NWs after the thermal decomposition, the same field as in (b) is shown. (g) High magnification of three different NWs after the decomposition. The diameter of the ultrathin wires at the tip and at the middle is indicated.

2. Growth of group-III-N structures for NW-LEDs by molecular beam epitaxy

Figures 2.28(a) and (b) show the top-view SEM images of the SAG NWs before the decomposition; two different fields characterized by holes with diameter of about 60 nm separated by 200 and 400 nm are presented. Good selectivity is achieved in both cases, although more parasitic NWs were observed once the distance between the holes increases. Figure 2.28(c) shows highly magnified images of three representative NWs. Interestingly, the SAG NWs exhibit a step-like structure with a large hexagonal pedestal, which tapers with increasing height of the nanocolumns. For this reason the NWs have different diameters at the base and at the tip; the size shrinks from about 140 nm on the bottom part to roughly 40 nm at the tip. We associate this effect to the lack of substrate rotation during the growth. The sketch in figure 2.28(d) illustrates the formation of a selectively-grown NW under the used conditions, the Ga and N fluxes arrive from different directions on the substrate. Without rotation the impinging atoms will accumulate on one edge of the holes, thus the nucleation will be promoted on this side and the NWs will growth earlier and faster. As long as the height of the nanostructures is shorter than the diffusion length of the impinging atoms, the material on the mask can move onto the NWs and be incorporated^[152]. This effect can partially compensate the asymmetry of the system due to the lack of rotation and explain the presence of pedestals with well developed hexagonal shape at the base of the NWs. However, once the height increases, the contribution of the atoms impinging directly on the top facet becomes more important, and thus the growth on the side that receives more atoms is promoted. This phenomenon would produce the observed structures. It is worth noting that for our purpose, the shrinking of the NW diameter is actually desired; in fact, it may help to obtain even thinner NWs after the decomposition.

The array of ordered nanostructures after the thermal decomposition is shown in figures 2.28(e) and (f). From the comparison of the SEM images in figure 2.28(e) and (b), which depict the same field, it is possible to note that most of the GaN decomposed. In fact, in the final sample only tiny structures remained; note that they are located always on the same side of the original hole, as visible in the magnified images in the inset of figure 2.28(e). The lack of rotation and the consequent formation of asymmetrical structures can explain this observation. The actual morphology of the decomposed NWs is visible in figure 2.28(f). Typically, single high and very thin NWs arise from a forest of short and very small objects. Again the peculiar shape can be understood by taking into account the original asymmetric nanostructure. Figure 2.28(g) shows three highly magnified SEM images of different NWs. Their height is roughly 300 nm shorter than the original one [see figure 2.28(c)]. More interestingly, they exhibit very small diameters, which are thinner than 20 nm at the middle and shrink further to less than 8 nm at the tip. These measurements are limited by the resolution of the SEM system, TEM analysis would be more adequate for a better characterization of these ultrathin NWs. In any case, the presented images already proved that the employed method can produce ordered arrays of well aligned and ultrathin NWs with diameters smaller than 10 nm.

The optical properties of the ordered array of NWs before and after the thermal decomposition were investigated by means of low temperature ($T=10$ K) PL spectroscopy; the measurements were performed by Pierre Corfdir at PDI. The NWs were excited by a HeCd laser emitting at 325 nm; the resulting PL signal was collected by an optical microscope and analysed through a grating spectrometer (groove density equal to 600 nm^{-1}) connected to a cooled CCD camera. The resulting spectra are plotted in figure 2.29. The blue profile is the spectrum acquired from SAG NWs formed inside holes with diameter of 60 nm and pitch of 400 nm, whereas the red profile refers to the NWs on the same field

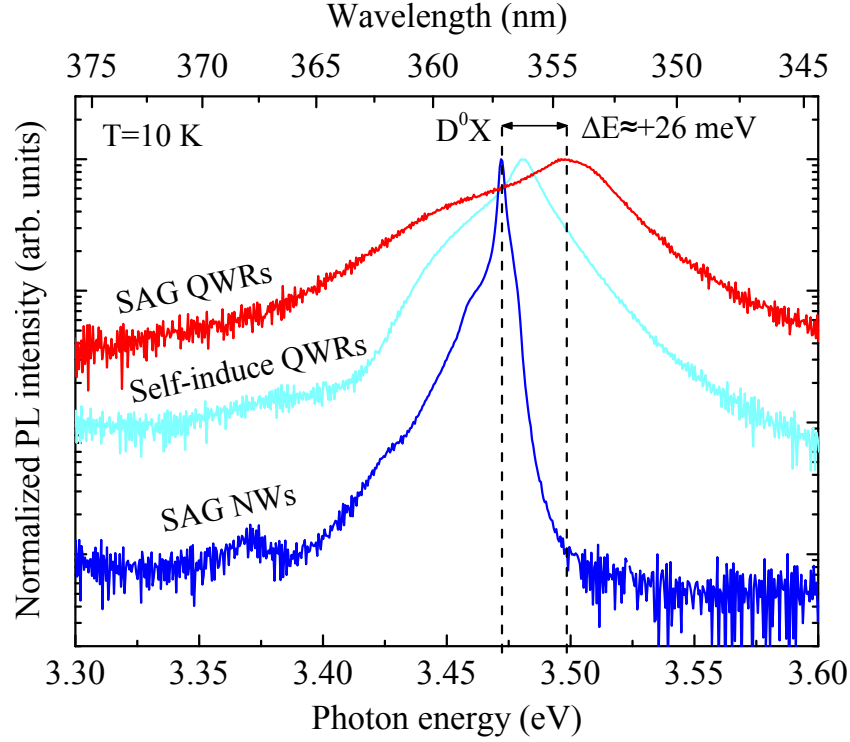


Figure 2.29: Comparison of the low temperature ($T=10$ K) normalized PL spectra of the ordered array of NWs before (blue profile) and after (red profile) the thermal decomposition. For sake of completeness, the spectrum of self-assembled quantum wires (QWRs) is also shown (cyan profile). The measurements were acquired by Pierre Corfdir at PDI.

after the thermal decomposition; the morphology of the NWs is shown in figures 2.28(b) and (e), respectively. The PL spectra are dominated by the donor bound exciton peak (D^0X), but the energy position of this transition significantly differs in the two cases. Before the decomposition the position of the D^0X peak corresponds to the one of relaxed GaN (3.472 eV). In contrast, the ultrathin NWs obtained via thermal decomposition have a D^0X peak blue-shifted by about 26 meV. This shift towards higher energy is due to the dielectric confinement of the exciton occurring in very thin semiconductor structures when a dielectric contrast between the excited material and its surrounding environment is present^[153–155]. This is the case for GaN QWR that have a dielectric constant 9.5 times higher than that of vacuum. The broad peak is likely due to the variation of the confinement energy induced by the tapering of the QWR, from the large base to the extremely thin tip, and to QWR-to-QWR shape fluctuations. In addition, residual micro-strain in the thin wires could make the PL peaks broader.

For comparison, the spectrum of ultrathin self-induced NWs obtained also via thermal decomposition by Johannes K. Zettler is shown in figure 2.29 (cyan profile). As already mentioned, the NWs grown by self-assembled processes suffer from a pronounced bending caused by electrostatic attraction between the NWs when their density is too high. The bending causes inhomogeneous strain inside the NWs that might produce a shift of the exciton energy line towards lower values^[156]. Such a red-shift could compensate the blue-shift due to dielectric confinement and explain the peak position of the self-induced QWRs. Therefore, the larger energy shift observed in the ordered array of NWs indicates

2. Growth of group-III-N structures for NW-LEDs by molecular beam epitaxy

that the bending caused by electrostatic interaction between QWRs is negligible when the distance between the structures is controlled by SAG. The success of this study paves the way to exciting new applications of ultrathin NWs.

Summary

In this chapter various optimizations of the growth protocol used to produce NW-LEDs based on (In,Ga)N/GaN heterostructures have been presented. In particular, we have found that the coalescence of the nanostructures can be suppressed adjusting the Mg flux, and the PL intensity emitted from the QWs can be increased by about ten times. The average In content in the QWs has been estimated by two different methods: the analysis of the In desorption measured *in situ* by means of line-of-sight QMS, and the study of the XRD spectrum. Furthermore, a three-step growth procedure for the deposition of very thin (10 nm and below), smooth, and closed AlN layers on Si substrate has been developed. On this basis, we have demonstrated that an AlN buffer layer that is only 4 nm thick both enables the SAG of GaN NWs on Si substrates and permits the current conduction required for the operation of NW-LEDs. A detailed study of micro-structure and conduction properties of the AlN has been carried out via TEM, AFM, and C-AFM measurements. In particular, the latter ones have revealed that the electron flow across the thin AlN layer is facilitated by the presence of small conductive protrusions likely formed during the “Ga-polishing” process used to remove the native Si_xO_y from the Si substrates. In addition, we have produced ordered arrays of ultrathin NWs by combining SAG and *in situ* post-growth thermal decomposition.

These results represent a fundamental step towards many other interesting experiments, such as fabrication and characterization of NW-LEDs on Si and AlN, growth of ordered arrays of nano-LEDs with different emission colours on Si substrates, integration of III-nitride systems with Si-based electronics, and realization of vertically aligned ultrathin GaN NWs. The former topic will be presented in the next two chapters.

Fabrication of (In,Ga)N/GaN NW-LEDs

One of the goals of this PhD work has been to improve the fabrication process of the NW-LEDs, with the aim of obtaining a new generation of devices with superior performance. In fact, the first generation of LEDs based on GaN NW ensembles^[10,48,125,131,133,157] had significant limitations in device performance. In particular, careful investigations showed that only about 1 % of the NWs in the ensemble may emit electroluminescence^[48,131,133]. Furthermore, in many cases high turn-on voltages in the range of 4.5–8 V were measured^[129,131,133,158]. Clearly, the processing of such LEDs is rather complex because of the three-dimensional morphology of NW ensembles. Our work aims to understand whether the reported limitations are due to peculiarities of the NW-LEDs grown on Si substrates, such as the formation of insulating Si_xN_y at the GaN/Si interface^[159] and the inhomogeneity of the current path in the NW ensemble^[131], or such devices simply need further advances in processing technology.

In this chapter all the technological optimizations achieved during this PhD work are presented. In the first section of the chapter the different steps required to fabricate a functional NW-LED starting from the as-grown sample are explained. More specifically, the issues related to the planarization process and to the deposition of the contacts are discussed; particular attention is paid to the optimization of the p-type top contact. The electrical properties of the NW ensemble before the deposition of the top contact are probed by means of conductive AFM maps; moreover, the optical transmittance of the semi-transparent p-type contact is measured. In the second section a direct comparison of two NW-LEDs with Ni/Au and ITO top contacts is presented. The analysis of the opto-electronic properties (I-V and EL characteristics) of the two samples proves that the ITO contact can significantly improve the performance of the devices. In the third section the effect of a 4-nm-thick AlN layer on the opto-electronic properties of the NW-LEDs is investigated. This is exactly the same buffer layer employed for the selective-area growth (SAG) of GaN NWs, as discussed in chapter 2. The EL and the I-V characteristics of two devices grown on bare and AlN-buffered Si are compared. This study provides surprising and unexpected outcomes and turns out to be fundamental to verify the compatibility of SAG on AlN-buffered Si substrates with the operation of LED devices, which could pave the way to the integration of III-nitride systems with the Si-base technology.

Extracts from this study were presented at the European-MRS 2014 conference held in Lille (France) and at the CSW 2015 conference held in Santa Barbara (USA), and can be

3. Fabrication of (In,Ga)N/GaN NW-LEDs

found in ref. [53,68].

3.1. Optimization of the fabrication process

In order to obtain functional devices, the as-grown NW-LED samples need to be processed by means of several nanotechnology techniques; this fabrication process enables the macroscopic contacting of the NW ensemble. The processing steps were developed initially at PDI by Friederich Limbach^[115]; part of the present PhD work was to revise and optimize each single processing step. In particular, the planarization process and the p-type top contact were significantly improved.

Figures 3.1(a)–(f) show the main processing steps required to fabricate a functional NW-LED starting from the as-grown sample. As first step, a piece with size equal or larger than $1.5 \times 1.5 \text{ cm}^2$ is obtained from the wafer on which the NW-LED was grown. In order to keep the surface of the sample as clean as possible, it is recommended to cover the entire wafer with a resist (a lithography resist removable in acetone is suitable) before proceeding with the dicing. In this way, any particles produced during the cutting process will stick on the surface and will thus be flushed away with the resist. Subsequently, the NW ensemble is planarized so as to fill up the space between the NWs and then the top contact is deposited [see figures 3.1(b), (e), and (c)]; these two steps are discussed in more detail in section 3.1.1 and 3.1.3, respectively. After the deposition of the semi-transparent top contact, the pattern of the bonding pads is defined by UV optical lithography, and then 20 nm of Ti followed by 150 nm of Au are evaporated on the surface. After the lift off in acetone, the Ti/Au layer will work as both bonding pad and current spreading layer; in fact, it creates a ring around the perimeter of the device and a cross that divides the emitting area of the LED into four quarters, as visible in figure 3.1(f).

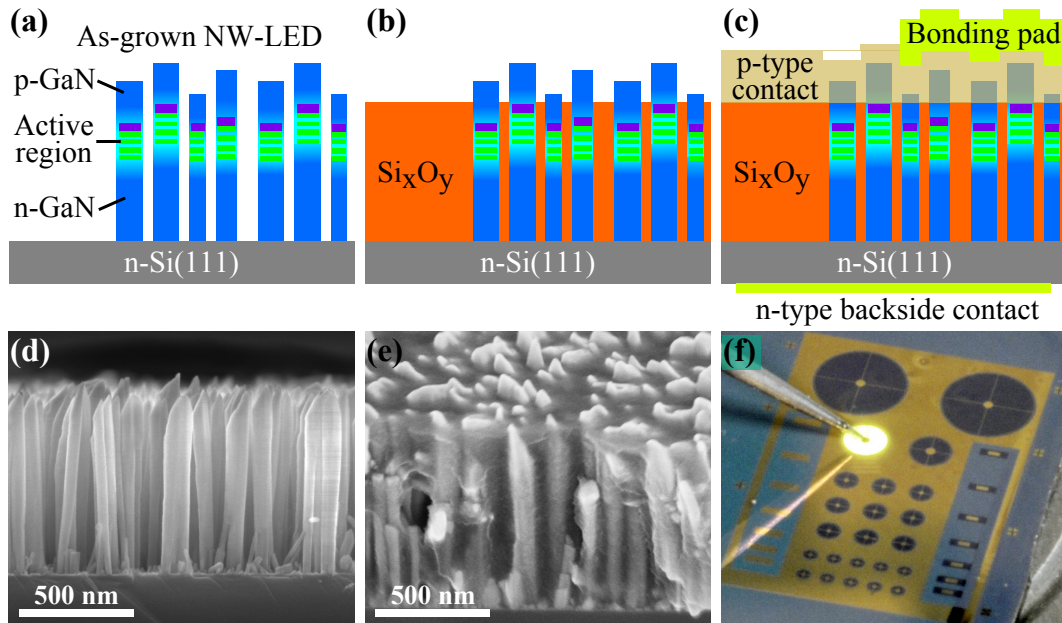


Figure 3.1: Illustrative sketch and SEM or photo camera images of the main processing steps required to fabricate a functional NW-LED: (a) and (d) as-grown NW ensemble, (b) and (e) planarization of the NW ensemble, (c) and (f) final device with contacts. Note that the different dimensions in the sketches are not to scale.

Then, the top side is covered again by a protective resist and the sample is dipped in a 3 % solution of HF for approximately 60 s in order to remove any oxides from the backside of the silicon substrate. Immediately after the etching, 50 nm of Al followed by 50 nm of Au are evaporated on the back side to create the n-type contact. The protective resist is then flushed away by rinsing the sample in acetone and isopropyl alcohol. A photograph of the final sample with several devices of different sizes, one of which in operation, is shown in figure 3.1(f).

At this point, the sample is ready to be glued, by means of a silver paste, onto a chip carrier suitable for the various experimental setups employed for the measurements. The silver paste has the dual purpose of fixing the sample and creating good thermal and electrical contact with the chip carrier. In case the piece has to be further diced to fit into the chip carrier, it is recommended to cover its surface with a protective resist before proceeding with the dicing. The final step is the gold wire bonding between chip carrier and the bonding pads of the single device.

3.1.1. Planarization of the NW ensemble

In order to create a contact with uniform properties over the entire surface of the device, the ensemble of NWs, which has an intrinsic three-dimensional morphology, must be planarized. In addition to creating an even surface for the contact, the planarization of the ensemble prevents detrimental short-circuits between the p-type top contact and the n-type base of the NW-LEDs by filling the voids between the NWs with an insulating material. The dielectric material chosen to planarize the ensemble should have a refractive index close to the one of GaN, so as to enhance the light extraction from the active region of the NW-LEDs; moreover, it should be transparent for all the wavelengths emitted by the LED and it must be a good electrical insulator. Various materials satisfy the properties listed above and can effectively planarize an ensemble of NWs^[160]; in this work we have employed the hydrogen silsesquioxane (HSQ) resin commercialized by the Dow Corning Corporation^[161]. This is an inorganic polymer ($\text{H}_8\text{Si}_8\text{O}_{12}$) diluted in a carrier solvent (methylisobutylketone) that can be transformed into amorphous Si_xO_y by thermal annealing in air. This material can be prepared with various viscosities, so as to change the penetration properties of the solution into the ensemble of NWs and obtain films of different thicknesses. We tested two different solutions called FOx14 and FOx25^[162], the former is more diluted and thus produces thinner films, whereas the latter can create thicker layers. The results obtained with the two types of solutions are discussed in the following lines.

Few drops of the FOx14 solution were dispersed on the surface of the sample, which was then spun at 1800 rpm for 50 s. This process uniformly distributes the resist over the surface; the excess material is expelled away by the centrifugal force. One single application of FOx14 produces a film with a thickness of about 250 nm; therefore, it cannot fill completely the ensemble of NW-LEDs, which are roughly 700 nm high. Several runs (usually 3–4) are thus required to planarize the ensemble with this resist. After each run of spin coating, the sample was annealed at a temperature of about 300 °C for 30 min. Figure 3.2(a)–(c) show the NW ensemble after (a) the first, (b) the second, and (c) the third run of spin coating. The SEM micrograph in figure 3.2(a) clearly proves that the solution FOx14 is not able to fill completely the space between the NWs in one single run. On the contrary, a compact layer is observed only at the bottom part of the NWs; the remaining part of the sample is almost completely empty. After the second run, see figure 3.2(b), the first 500 nm of the ensemble are filled but in the upper part still large voids

3. Fabrication of (In,Ga)N/GaN NW-LEDs

are present. Eventually, after the third spin coating run the entire ensemble is planarized. Nevertheless, some voids, probably due to trapped air bobbles, are visible between the NWs, as indicated by the yellow arrows in figure 3.2(c).

A similar spin coating procedure was repeated using the less diluted FOx25 solution. In this case one single run was more than sufficient to planarize the ensemble of NWs, and actually an over-layer of about 400 nm was created above the tips of the NWs, see figure 3.3(a). The layer produced by the FOx25 solution is compact without any voids between the NWs. It seems thus more convenient to use the less diluted FOx25 solution rather than the FOx14.

In order to contact the NW-LEDs, the excess Si_xO_y on top of the NW tips must be removed. This is one of the most critical parts of the entire fabrication process. In fact, this step will define the actual number of contacted NWs and the quality of the p-type contact; it is not an overstatement to say that the final performance of the NW-LED is strongly influenced by the way in which the excess Si_xO_y is etched. For this reason we paid particularly attention to this process step. In order to etch down the planarization resist in a controllable and accurate way we employed the reactive-ion etching (RIE) technique with CHF_3 . In addition to a good reproducibility, this dry etching method has also an excellent etching selectivity; in other words, the CHF_3 ions etch well the Si_xO_y but cannot harm the GaN NWs.

We kept the parameters of the plasma always constant: 25 sccm of CHF_3 , a RF power of 100 W, and a pressure in the chamber equal to 1 Pa. Instead, we varied the annealing procedure of the HSQ. On the one hand, we used the conventional annealing process, that heats the sample directly up to 300 °C for 30 min. The long exposure to high temperature turns the HSQ into hard Si_xO_y . On the other hand, we employed a two-step annealing process. Before the etching the sample is progressively heated from 100 °C to 200 °C increasing the temperature by 50 °C every 2 min. This 6-min-long heating is enough to evaporate the solvent but will not transform completely the HSQ into hard Si_xO_y . Then the sample is etched by RIE until the desired amount of superfluous material is removed. Finally, the NW ensemble is annealed again at 300 °C for 30 min to transform all the HSQ into Si_xO_y . We found that the etching rate of HSQ annealed with the first procedure significantly fluctuates over time. Hence, it was impossible to estimate with certainty an etching time and process the sample in only one run; instead, several iterations were required to achieve the desired result. In contrast, the etching rate of HSQ annealed with

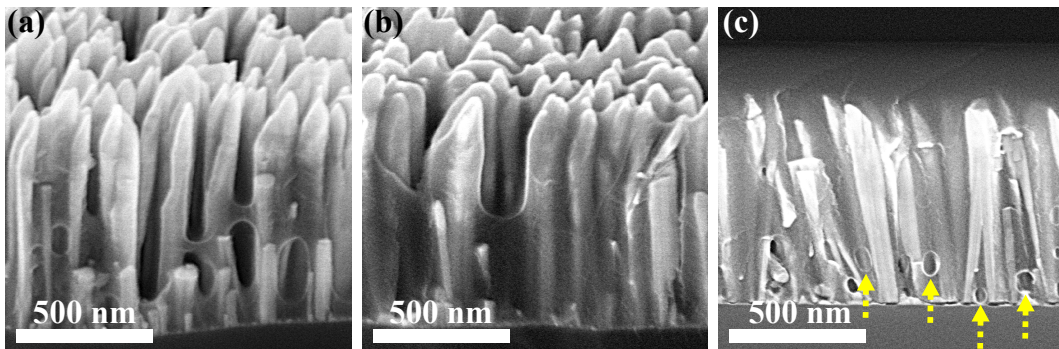


Figure 3.2: Planarization of the NW ensemble by spin coating using the more diluted solution of HSQ (FOx14). (a)–(c) Bird’s eye view SEM images of the NW ensemble after (a) the first, (b) the second, and (c) the third run of spin coating. The yellow arrows indicate the presence of voids in the planarization layer.

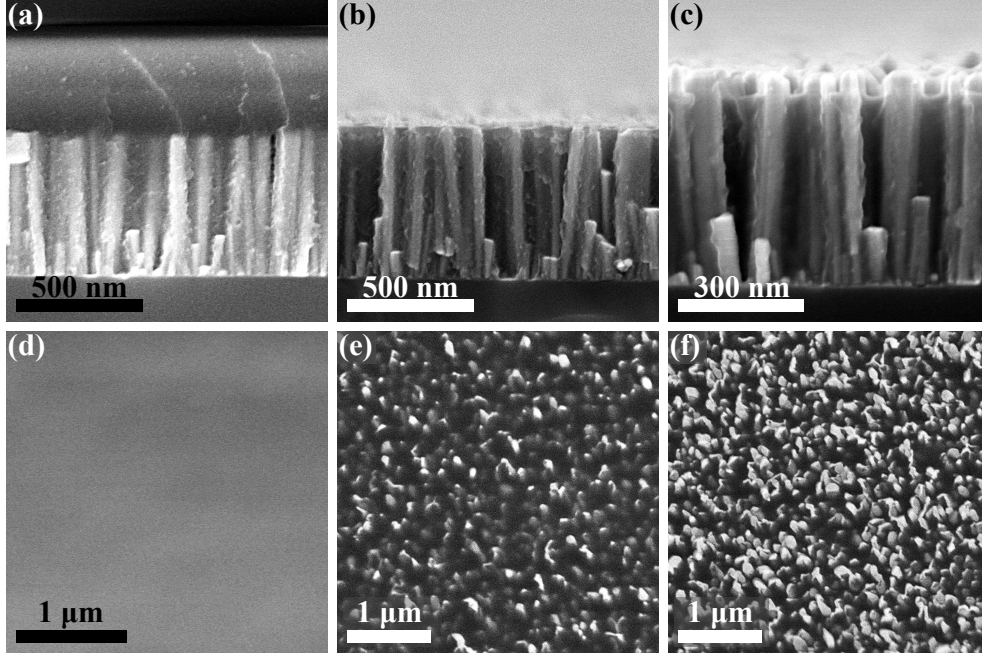


Figure 3.3: Optimization of the etching of the excess Si_xO_y . (a)–(c) Cross-sectional SEM images of the NW ensemble (a) directly after the planarization with FOx25 and after (b) 23 min and (c) 27 min of dry etching; (d)–(f) corresponding top-view micrographs.

the second procedure is very stable (about 17 nm/min), thus enabling an accurate control of the etching depth and consequently the use of few etching iterations.

Figures 3.3(a)–(c) show a NW ensemble at various stages of the etching process: (a) directly after the planarization with FOx25 and the short annealing, and after (b) 23 min and (c) 27 min of dry etching. Figures 3.3(d)–(f) depict the corresponding morphology of the top surface, the presence of bright spots indicates that the tips of the NWs are uncovered. Comparing the SEM images in figures 3.3(b) and (e) with the ones in (c) and (f), it is possible to appreciate the precision with which one can control the number of NWs set free from Si_xO_y . We aimed at removing about 70 nm of Si_xO_y down from the tips of the highest NWs, but because of fluctuations in the height of both NWs and Si_xO_y layer, the actually etched thickness fluctuates on a local scale as well.

3.1.2. Spatial distribution of the current injected into the NW ensemble

In order to check the electrical properties of the NW ensemble directly after the dry etching, conductive AFM (C-AFM) measurements were performed before the deposition of the top contact. In particular we aimed at checking the number of NWs actually able to conduct current and possibly also the spatial distribution of the current flow on the surface of a single NW. For this purpose, a NW-LED sample (refer to LED1 in table A.1, appendix A) was planarized and the Si_xO_y was etched down until a considerable number of NWs was exposed. The morphology of the surface after the etching is similar to the one shown in figure 3.3(f).

The C-AFM measurements were performed at the Suzhou Institute of Nano-Tech and Nano-Bionics (SINANO) in China under the supervision of Dr. Xu Gengzhao and Dr. Haijian Zhong. The data were acquired at room temperature ($T=303\text{ K}$) by means of

3. Fabrication of (In,Ga)N/GaN NW-LEDs

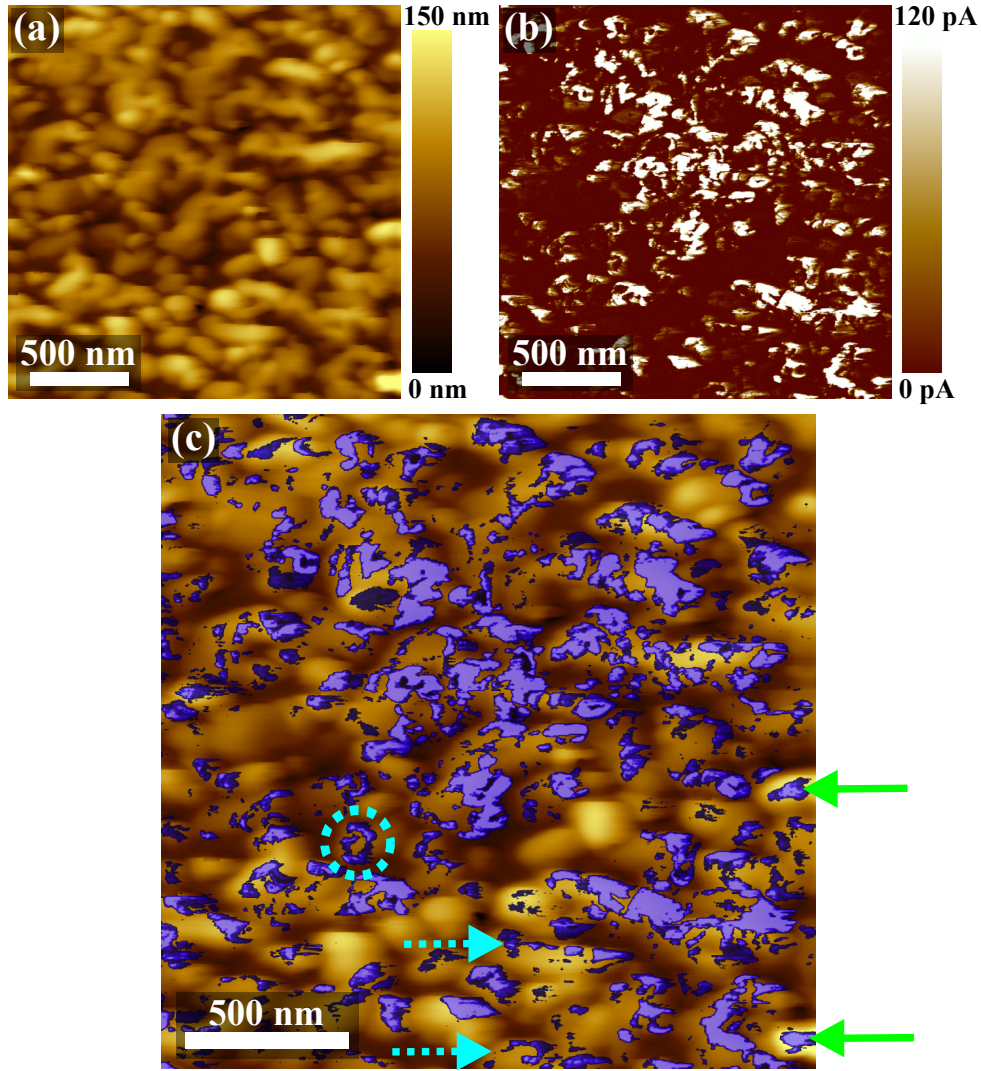


Figure 3.4: C-AFM measurements performed before the deposition of the top contact: (a) topography of the surface of the NW ensemble; (b) corresponding current map normalized to the noise level; (c) superimposed topography and current images. During the measurements, the tip was grounded whereas a positive bias of +2 V was applied at the back side of the Si substrate. The data were acquire under the supervision of Dr. Xu Gengzhao and Dr. Haijian Zhong at SINANO. Green arrows and cyan arrows and ring indicate NWs that conduct current mostly through the inner part and the sidewalls, respectively.

a Veeco Multimode AFM system equipped with a 20-nm-wide conductive Si tip coated with Pt. The Pt/p-GaN junction can be imagined as a rectifying Schottky diode connected in back-to-back configuration with the LED. To get a current flow the Pt/p-GaN Schottky junction must be under forward polarization; because of the back-to-back configuration, this results in a reverse polarization for the LED. Therefore, with the employed setup, it is possible to measure only the reverse leakage current of the LED. During the C-AFM measurements, the tip was grounded whereas a positive bias of +2 V was applied at the back side of the Si substrate.

Figure 3.4(a) shows the AFM topography of the sample surface measured in contact mode. The protrusions correspond to the tips of single or coalesced NWs that come out

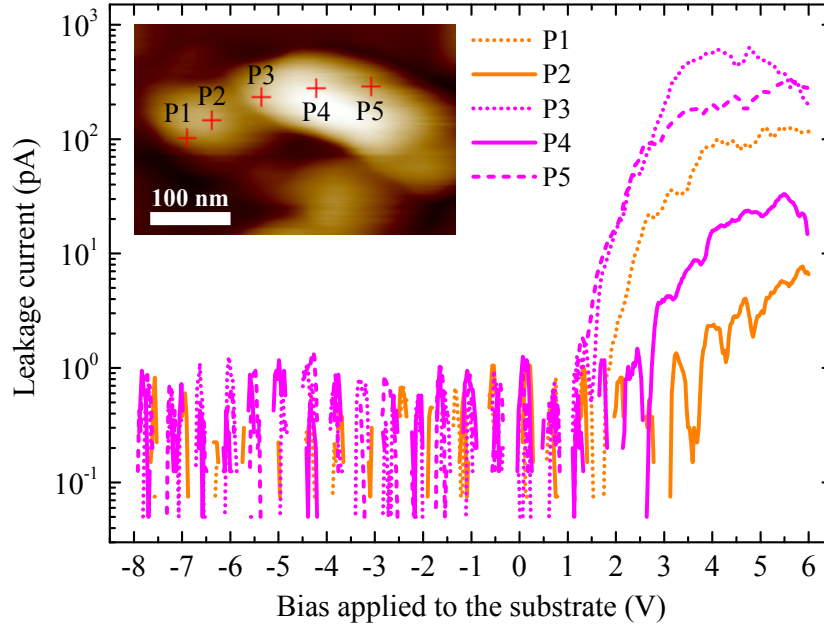


Figure 3.5: I-V characteristics acquired on five different positions (labelled P1–5) across the top surface of a cluster of few NWs, as depicted in the inset on the upper left side of the graph. The orange and magenta curves refer to two different NWs. The data are plotted on semi-logarithmic scale.

from the Si_xO_y layer. Because of the finite size of the AFM tip, the shape of the protrusions does not coincide with the actual shape of the NWs, but is rather due to the convolution of the structures of NWs and AFM tip. Few small dark and flat areas are visible, these correspond to the space between the NWs planarized by Si_xO_y . Figure 3.4(b) shows the corresponding current image, that represents the charge flowing from the AFM tip into the sample during the scan. The dark and bright regions identify less and more conductive areas, respectively; in this way, the C-AFM enables to characterize the electrical properties of each single NW. To better visualize the correlation between current conduction and spatial features of the sample, the measured current and topography maps were superimposed, see figure 3.4(c). It is clearly visible that the majority of the NWs conduct current, whereas no charge flow is measured in the areas surrounding the NWs filled by Si_xO_y . The absence of current conduction across some of the NWs might be due to the presence of oxides on their surface or to a less leaky behaviour (we remind that the C-AFM can measure only the reverse leakage current of the LED). More interestingly, the spatial distribution of the leakage current differs from NW to NW; some of them conduct current mostly through the inner part [see green arrows in figure 3.4(c)], whereas others are more conductive close to the sidewalls [see cyan arrows and ring in figure 3.4(c)]. Furthermore, many NWs have a mixed behaviour.

In order to further elucidate the spatial distribution of the current on nanometre scale single-point measurements were performed. In fact, beyond the scanning mode at constant bias, the C-AFM can also be used in single-point mode. In this mode, the tip contacts only a specific position on the surface of the sample, and the I-V characteristics of that particular point can be measured by varying the applied bias. Figure 3.5 shows the I-V characteristics measured on five different positions (labelled P1–5) across the top surface of a cluster of few NWs, see inset on the upper left side of the graph. In particular, P1 and

3. Fabrication of (In,Ga)N/GaN NW-LEDs

P2 are acquired close to the edge and to the centre of a thin single NW, respectively; P3 and P5 refer to points located on the opposite edges of a large NW (likely formed by two coalesced NWs), while P4 is measured close to the centre of this NW. Comparing the I-V curves related to P1–2 and P3–5 (orange and magenta lines in the graph of figure 3.5, respectively), one can note that the leakage current measured close to the edge of the NW (P1, P3 and P5) is more than ten times higher than the one acquired at the centre (P2 and P4). This observation would support the idea that the leakage current is partially conducted through surface states on the sidewalls of the NWs. A detail discussion on the leakage current in NW-LEDs is presented in chapter 4.

3.1.3. Deposition and characterization of the p-type top contacts

In this work two different types of p-type contact were tested: a Ni/Au semi-transparent bilayer and an indium tin oxide (ITO) single-layer. The former was commonly used for a long time in planar^[163,164] and NW based LEDs^[10,48,125,127,128,131,165]. The Ni/Au contact was improved by adding an ITO layer onto the top of the metallic film^[126,129,133]; the ITO is used to enhance the current spreading without affecting the extraction of the light significantly. In planar LEDs the metal based multi-layer contacts were slowly replaced by a single-layer ITO contact, in fact the latter has shown better performance^[166]. Nevertheless, very rarely single-layer ITO was employed in NW-based LEDs^[167].

Regardless of the chosen top contact, before the deposition, it is recommended to clean the surface of the samples by means of either Ar sputtering for 40 s or a dip into a 20 % solution of HCl for 20 s. Both methods effectively remove any residual oxide, but while the HCl etching does not harm the GaN, the Ar sputtering could also etch the NWs. The former method is thus preferable. Immediately after the surface cleaning, the samples were transferred into the vacuum for the deposition of the top contact. When the metal contact was employed, 5 nm of Ni and consecutively 5 nm of Au were deposited by thermal evaporation. Differently, the transparent oxide was sputtered by bombarding an ITO target with Ar ions, to improve the quality of the material the substrate was heated up to 250 °C during this process; usually 120 nm of ITO were deposited. We found that the opto-electronic properties of the ITO improve if the material is further annealed at 300 °C in N₂ atmosphere for 30 min. In particular, after the annealing the resistivity of the ITO decreases, whereas its optical transmittance increases.

In order to compare their optical properties, the Ni/Au (5 nm/5 nm) and the ITO (120 nm) contacts were deposited on transparent glass substrates, then their transmittance was measured. The solid red and dashed blue lines in figure 3.6 represent the absolute transmittance of the Ni/Au and ITO layer, respectively. The latter exhibits superior optical transmittance over the entire visible spectral range. Particularly, in the spectral range interesting for green LEDs (the investigated NW-LEDs emit roughly at 540 nm), the 120-nm-thick ITO has a transmittance equal to about 90 %, which is roughly two times higher than the one of the 10-nm-thick Ni/Au (roughly 44 %). We note that the transmittance of ITO increases after the thermal annealing, especially for wavelengths shorter than 500 nm, see dotted magenta line in figure 3.6.

The shape of the semi-transparent contacts is defined by UV optical lithography. In case of the Ni/Au contact the lithographic pattern is impressed before the evaporation of the metals, whereas when the ITO is used the surface is patterned after the sputtering of the transparent oxide. In fact, the photolithography resist cannot be heated up to the temperature used during the sputtering (250 °C). For this reason, the ITO is deposited everywhere on the surface and the excess material must be etched away. We

3.2. Comparison of NW-LEDs with Ni/Au and ITO top contact

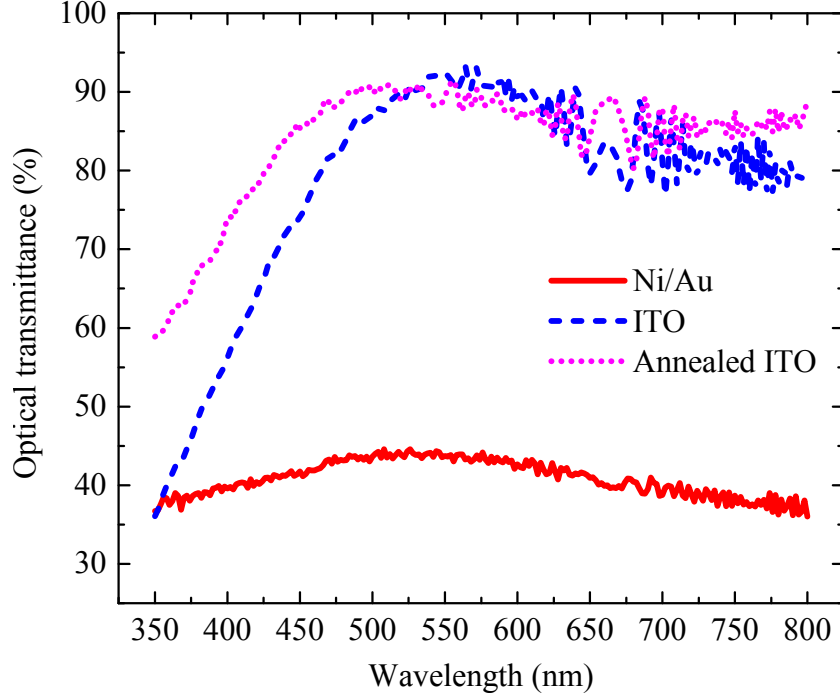


Figure 3.6: Optical transmittance as a function of the wavelength for a 10-nm-thick Ni/Au layer and a 120-nm-thick ITO layer before and after the annealing: see solid red, dashed blue and dotted magenta lines, respectively.

tested two different approaches to remove the unnecessary ITO: dry etching by means of RIE with BCl_3 gas, and wet etching in a solution of hydrochloric and nitric acid, namely $\text{HCl}:\text{HNO}_3:\text{H}_2\text{O}$ (with the stoichiometric ratio 4:1:5). We found that the dry etching is rather aggressive (etching rate of about 50 nm/min) and has a poor selectivity between ITO and GaN, whereas a 30-min-long wet etching can effectively remove the ITO without harming the NWs. For this reason, the investigated devices were processed by means of wet etching.

3.2. Comparison of NW-LEDs with Ni/Au and ITO top contact

In this section we study the effect of the Ni/Au and ITO top contact on the performance of NW-LEDs. To this end, two NW-LEDs were fabricated from two adjacent pieces of the same wafer; for further details about structure and growth parameters of the sample refer to LED1 in table A.1, appendix A. The two pieces were processed following similar steps, but eventually one sample was contacted with Ni/Au and the other one with ITO. The opto-electronic properties of the final devices were then characterized by means of different techniques. The goal of this comparison is to check whether the significant limitations in device performance (low density of NWs emitting EL and high turn-on voltages) reported for NW-LEDs contacted with Ni/Au^[48,131] and Ni/Au/ITO^[133] can be improved simply using a better p-type contact. In this case, the peculiarities of the NW-LEDs grown on Si substrates, such as the formation of Si_xN_y at the GaN/Si interface or the inhomogeneity of the current path in the NW ensemble^[131], would not be the bottleneck for the development of the NW-LED technology. To the best of our knowledge, the analysis carried out in this thesis has been the first direct comparison of these two

3. Fabrication of (In,Ga)N/GaN NW-LEDs

types of contacts applied to NW-LEDs^[68].

3.2.1. Characteristics of the contacts on the microscopic scale

As the first step to investigate the properties of the two different contacts, we checked the morphology of the deposited layers on microscopic the scale. To this end, dices of the two samples were cut by means of an ion beam milling process; in fact, this method can produces cross-sections with very even sidewalls. Figures 3.7(a) and (b) show bird's eye view SEM images of the NW-LED samples processed with Ni/Au and ITO contacts, respectively. We note that the NW density, estimated by means of top-view SEM images, is exactly the same in the two devices under investigation. The different amount of dark areas (corresponding to Si_xO_y) in the micrographs of figure 3.7(a) and (b) is just due to the different cross-sections obtain after the ion beam milling process. More interestingly, the SEM images clearly show that because of the different film thicknesses the contact area between the tips of the NWs and the contacting layers is very different in the two cases. As sketched in figures 3.7(c) and (d), the 10-nm-thick Ni/Au layer can contact either the top facet or a small portion of the side walls of the NW tips, depending on their height. If a long NW segment protrudes from the Si_xO_y , as indicated in figure 3.7(d), the amount of deposited Ni/Au is too small to form a continuous film in touch with both the top facet and the sidewalls. Moreover, the poor wetting behavior of Ni and Au on Si_xO_y may produce voids and cracks in the metal film, thus reducing the contact area at the metal/NW interface^[168]. In contrast, the transparent ITO layer can be made much thicker (120 nm in our case) without affecting the extraction of light significantly, and is hence able to fill any gaps between the NW tips so that the p-type top segments are completely embedded as depicted in figure 3.7(e). Therefore, a larger contact area both with the top facet and the side walls of the NWs is produced.

It is important to note that a larger contact area can reduce the contact resistance, which is inversely proportional to this parameter. To quantify the extent of this effect we esti-

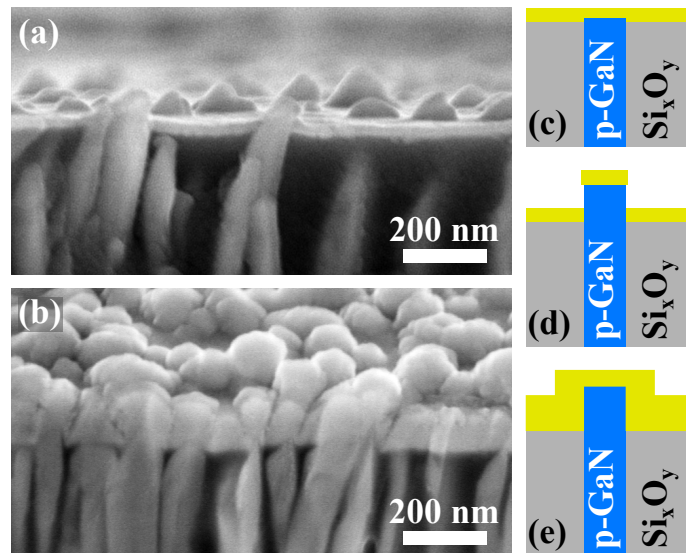


Figure 3.7: Bird's eye view SEM images of NW-LEDs processed with (a) Ni/Au and (b) ITO top contact, respectively. (c)–(e) Schematics of three possible configurations of the top contact.

3.2. Comparison of NW-LEDs with Ni/Au and ITO top contact

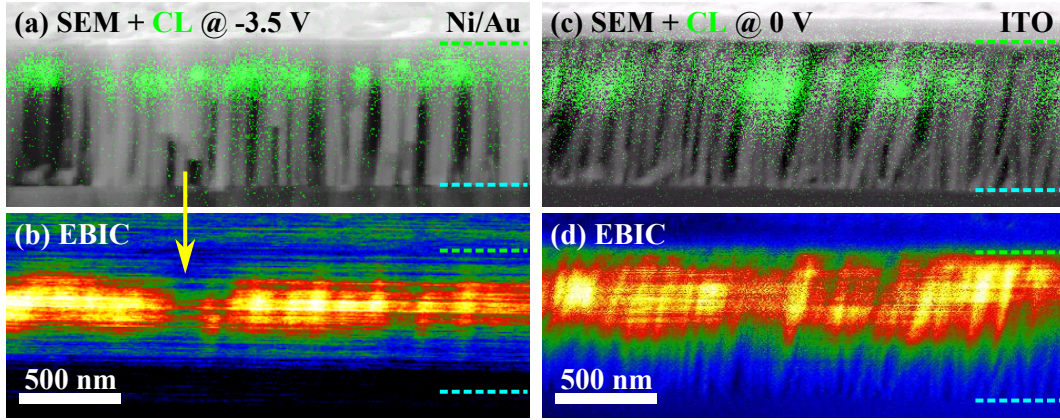


Figure 3.8: (a,c) Monochromatic false-colour CL images superimposed on cross-sectional SEM micrographs and (b,d) corresponding EBIC maps with color-coded intensity (temperature scale) from the samples with Ni/Au (a,b) and ITO (c,d) contacts. A negative bias equal to -3.5 V was applied during the measurements of the NW-LED with Ni/Au contact, whereas no bias ($V=0$ V) was applied in case of the device with ITO. The dashed lines indicate the substrate/NW (cyan) and NW/top-contact (green) interface. The yellow arrow highlights the position of broken NWs that do not contribute to the EBIC signal. The data were acquired by Jonas Lähnemann.

mated the contact area in the three possible cases depicted in figures 3.7(c)–(e). Using the typical dimensions of the NW-LED structure (radius NW equal to about 50 nm and etching depth of 100 nm), we found that the contact area sketched in figure 3.7(e), *i. e.* when the NW tips are completely surrounded by the contact material, is 4 and 12 times larger than in the cases depicted in figures 3.7(c) and (d), respectively.

In order to verify whether an electric contact was actually established between the NW-LEDs and the top layers, cross-sectional electron beam induced current (EBIC) measurements were performed on NW-LED samples processed with the two different contact schemes. The data were acquired by Jonas Lähnemann; our set-up enables the simultaneous acquisition of secondary-electron (SE), CL and EBIC signals. Such a set of measurements is depicted in figure 3.8 for samples with Ni/Au [(a,b)] and ITO [(c,d)] contacts. In figures 3.8(a) and (c), the monochromatic CL from the (In,Ga)N QWs is superimposed on the corresponding SE image; the CL was recorded in a spectral window of 30 nm centred around 560 and 520 nm in (a) and (c), respectively. The use of two different spectral windows is mainly due to fluctuations of the emission energy in the NW ensemble. The CL intensity visualizes the approximate position of the QWs along the nanostructures; almost all the NWs emit CL, although the intensity varies significantly from NW to NW.

Figures 3.8(b) and (d) show the corresponding EBIC maps with color-coded (temperature scale) intensity. In EBIC, electron-hole pairs created by the incident e-beam are separated by the electric field present in the depletion region of the p-n junction. The resulting short-circuit current can be detected through an external current amplifier while the e-beam is scanned across the sample. The NWs need to be contacted electrically in order to contribute to the EBIC signal. In figures 3.8(b) and (d) the bright stripes in the middle of the images indicate the approximate positions of the p-n junctions. With the employed acceleration voltage of the e-beam (8 kV) almost only the first row of NWs can be excited and contribute to the CL and EBIC signals. Therefore, the strong EBIC signal measured in the cross-sectional maps directly proves that the majority of NWs is con-

3. Fabrication of (In,Ga)N/GaN NW-LEDs

tacted by both the Ni/Au and ITO contact. The few NWs not contributing to the EBIC signal are broken and thus not connected to the substrate, as highlighted by the yellow arrow in figure 3.8(b).

It is worth noting that while the application of a reverse bias equal to -3.5 V was required to obtain a decent EBIC signal in the sample contacted with Ni/Au, in the one with ITO a strong current was measured even without an additional reverse bias ($V=0$ V). The reverse bias increases the electric field in the depletion region of the p-n junction, thus enhancing the separation of electron-hole pairs; therefore, the application of a reverse bias increases the EBIC signal and reduces the amount of carriers recombining in the QWs. Consequently, when a negative bias is applied, only carriers excited close to the QWs can recombine and emit light, and the spatial resolution of the CL is thus enhanced; this effect is visible by comparing of the CL images in figures 3.8(b) and (c), which were acquired with a bias of -3.5 V and 0 V, respectively. More interestingly, the zero bias EBIC signal being much stronger in the sample with ITO than in the one with Ni/Au suggests that the current can flow easier in the former case than in the latter. Thus, these results are consistent with the idea that the ITO produces a smaller contact resistance than the Ni/Au.

3.2.2. Evolution of the density of EL spots with the applied bias

To investigate the influence of the two types of top contacts on a macroscopic scale, the electroluminescence maps of the samples with ITO and Ni/Au were recorded. Figures 3.9(a) and (b) show the resulting images acquired through an optical microscope on a device with an area of 0.19 mm^2 when a forward bias of +6 V was applied. Both samples exhibit a spotty emission pattern but the number density of EL spots is very different in the two cases. In particular, the sample with ITO exhibits a number density of emitting spots which is roughly one order of magnitude higher than for the sample with Ni/Au. In agreement with previous findings^[48,131,133], the EL map of the sample with Ni/Au contact is characterized by EL spots separated by large portions of surface area that are much darker, essentially without any emission of light. In contrast, the emitting NWs in the sample with ITO cover the whole surface without any dark areas in between.

We acquired EL maps of the two samples for various forward biases; the extracted number densities of EL spots are summarized in figure 3.9(c). Several important differences between the two samples are remarkable. In particular, the turn-on of the first EL spots occurs at lower forward bias in the device with ITO than in the one with Ni/Au. This result clearly proves that the ITO contact provides a lower series resistance. For sake of clarity, we remind that a NW-LED can be seen as a multi-element device composed by millions of nano-LEDs contacted in parallel. Because of fluctuations of the NW sizes (diameter and height) in the ensemble, each individual nano-LED could have slightly different In content, doping level, and resistance. When a small bias is applied, the current will preferentially flow through the NWs that offer lower resistance^[131], and thus the NW-LEDs will not light up all together. Understanding the multi-element nature of the NW-LEDs is fundamental to correctly interpret the opto-electronic characteristics of the devices. This topic is further discussed in section 4.2.

In the sample with ITO the number density of emitting NWs rises very quickly with the bias, and almost saturates beyond +5 V. In contrast, in the sample contacted with Ni/Au the density of EL spots increases with the forward bias much more slowly than in the sample with ITO. Also compared to previous reports for similar types of NW-LEDs^[48,131,133], the highest density of EL spots counted at +10 V in the sample contacted

3.2. Comparison of NW-LEDs with Ni/Au and ITO top contact

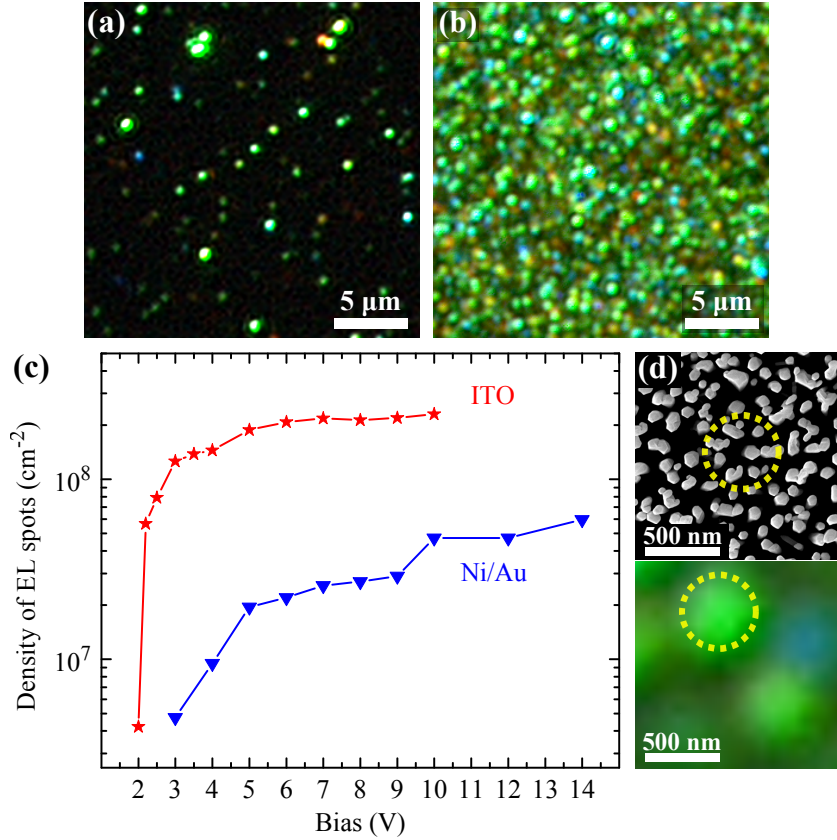


Figure 3.9: Top-view EL maps acquired at 6 V forward bias through an optical microscope for two NW-LEDs processed with (a) Ni/Au and (b) ITO, respectively. (c) Dependence of the number density of EL spots on the forward bias for the two different types of NW-LED. (d) Top-view SEM micrograph of an unprocessed sample (upper part) and a highly magnified top-view EL map of a NW-LED under operation (bottom part). The yellow dashed circles represent the area of a diffraction limited EL spot, about $0.2 \mu\text{m}^2$.

with ITO is about one order of magnitude higher. It is important to note that resolving the size of the EL spots is limited by the diffraction at the optical lens of the microscope to an area of approximately $0.2 \mu\text{m}^2$. Therefore, roughly eight NWs might contribute to the formation of one single spot, and the density of spots is likely underestimated. This issue is depicted in figure 3.9(d), that shows a top-view SEM micrograph of the unprocessed sample (upper part) and a highly magnified EL map of a NW-LED under operation (bottom part). The yellow dashed circles roughly coincide with the area of a diffraction limited EL spot ($0.2 \mu\text{m}^2$); as visible in the SEM image, this area contains about eight single NWs. Taking this effect into account, the actual density of NW-LEDs that emit EL could turn out to be of the same order of magnitude as the total density of NW tips free from Si_xO_y (which is about $5 \times 10^9 \text{ cm}^{-2}$).

From the analysis of the EBIC measurements we concluded that the majority of NWs is contacted both in the sample processed with Ni/Au and ITO. Therefore, the causes of the drastic difference in number density of emitting spots must be sought in the different electrical properties of the two types of contacts. For instance, a lower contact resistance between the tips of the individual NWs and the contacting layer might be responsible for the observed effect. In section 3.2.1 we have already discussed that a larger contact

3. Fabrication of (In,Ga)N/GaN NW-LEDs

area can reduce the contact resistance. In addition, the larger thickness of the ITO layer can create a more uniform contact, allowing in this way the current to reach every part of the surface with equal ease. This helps to mitigate the inhomogeneity of the current path in the NW ensemble due to the fluctuations of the resistance of different individual NWs^[131].

It is worth saying that when the ITO contact has been employed to fabricate many different devices obtained from several wafers, despite of device-to-device fluctuations, good device performance have always been observed. Nevertheless, an amorphous Si_xN_y layer is present in all of these samples, in fact it inevitably forms on the silicon surface during the first stage of the GaN NWs growth by MBE^[159]. Also the size distribution typical of self-induced NWs is obviously present in all the considered devices^[169]. Therefore, it is clear that the severe limitations in device performance reported for NW-LEDs cannot be due to these intrinsic features of the GaN NWs grown on Si, but have to be attributed to a not optimum top contact.

3.2.3. Comparison of the current-voltage characteristics

Next, we present the analysis of the electrical characteristics of the two types of NW-LEDs. Figure 3.10 shows the current-voltage (I-V) curves of NW-LEDs with ITO and Ni/Au contact on linear scale. Five different devices, processed at the same time, were measured for each type of contact, and the presented data are typical ones. The current rises at much smaller biases in the NW-LED contacted with ITO than in the one employing Ni/Au, see red and blue solid curve, respectively. In particular, the former LED reaches the current of 5 mA for a forward bias of 3.3 V, while the latter LED requires 8.7 V to reach the same value. The value of the turn-on voltage found for the NW-LED contacted with ITO is lower than the ones previously reported for similar NW-LEDs employing either Ni/Au/ITO^[158] or Ni/ITO^[133] as p-type contact, although for more complex NW structures low turn-on voltages were obtained also employing Ni/ITO as top contact^[129,167,170].

It is important to highlight that this result does not imply that the actual turn-on voltages of the individual NW-LEDs contacted with ITO are much smaller than the ones contacted with Ni/Au. In fact, as visible in the graph of figure 3.9(c), the first individual NW-LEDs start to emit EL at very similar applied biases: +2 and +3 V in the devices with ITO and Ni/Au, respectively. What causes the large difference in the two I-V curves is mainly the different number of individual NW-LEDs in operation, and the actual amount of current that each NW conducts. As discussed before, in the devices contacted with ITO, the number of individual NW-LEDs in operation might be several tens of times greater than in the one with Ni/Au. At the same time, the lower contact resistance produced by the larger contact area in the sample with ITO can significantly increase the current injected into each individual NW-LED.

To better visualize this peculiar issue of NW-LEDs, we performed a “*Gedankenexperiment*”. We supposed that, similarly to the ITO, also the Ni/Au contact was able to effectively inject current into a high number of NWs. Under this assumption, the total current obtained in the devices contacted with Ni/Au would be higher than the measured one. To simulate this effect the experimental data (blue solid curve in figure 3.10) should be multiplied with a positive factor greater than one. The blue dotted line in figure 3.10 shows that a multiplicative factor equal to about 200 would produce an I-V characteristic of the device contacted with Ni/Au very similar to the one of the NW-LED employing ITO. This outcome clearly proves that a NW-LED cannot be treated simply like a planar

3.2. Comparison of NW-LEDs with Ni/Au and ITO top contact

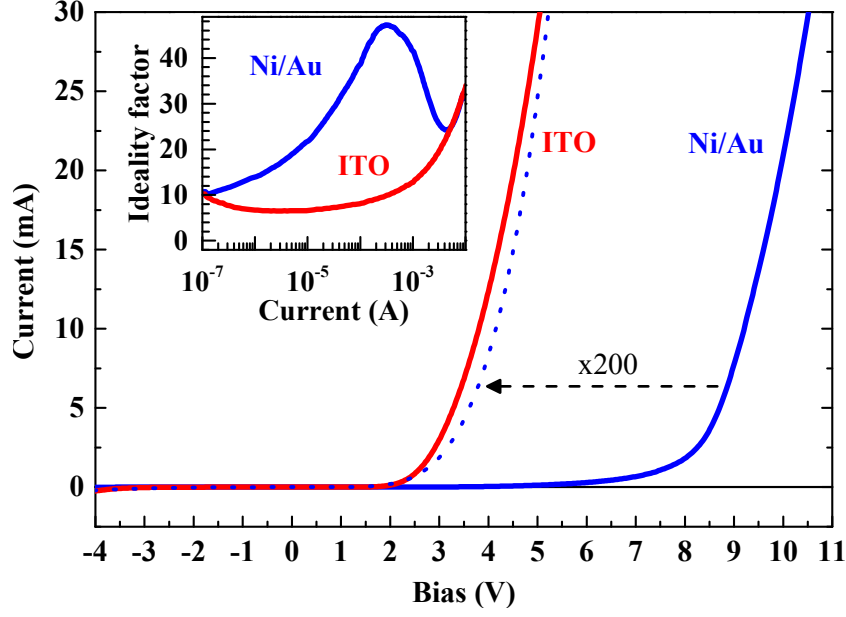


Figure 3.10: Current-voltage characteristics on a linear scale of NW-LEDs with area of 0.19 mm^2 contacted with either Ni/Au or ITO. The blue dotted curve is obtained by multiplying the I-V characteristic of the device with Ni/Au contact by 200. The inset shows the ideality factor derived from the I-V curves of the two samples versus the current.

LED. In fact, the multi-element nature of the NW-LED makes the analysis of this device more complex than for a common planar LED. In particular, to achieve an in-depth understanding of the opto-electronic properties of a NW-LED, one has to consider this device as an ensemble of millions of nano-devices contacted in parallel. In this new vision of the system, the analysis of the EL maps as a function of the applied bias and the estimation of the number of working NWs (see section 3.2.2) become fundamental tools to interpret all the other data. This novel interpretation of the I-V characteristics of NW-based LEDs will be discussed in more details in section 4.2. In fact, the main scope of the present chapter is to describe the technological optimizations showing only basic characterizations, whereas an in-depth investigation of the opto-electronic characteristics is provided in chapter 4.

The series resistance (R_S) of the overall device was extracted from a linear fit to the I-V curve in the high bias range. The R_S of the sample with ITO is approximately 30 % lower than that of the sample with Ni/Au: the absolute values are 30 and 43Ω , respectively. The series resistance of NW-LEDs contacted with Ni/Au and Ni/Au/ITO contact has been reported to be equal to $50^{[171]}$ and $30 \Omega^{[172]}$, respectively. In addition, we calculated the ideality factor (η) of the NW-LEDs from the I-V curves using the formula

$$\eta = \frac{q}{k_B T} \left[\frac{\partial \ln(I)}{\partial V} \right]^{-1} \quad (3.1)$$

where q , k_B , and T are the elementary charge, the Boltzmann constant and the temperature, respectively. The result is depicted in the inset of figure 3.10 in blue and red for the device contacted with Ni/Au and ITO, respectively. In the sample with Ni/Au contact, the ideality factor varies continuously over the entire range of currents, with values

3. Fabrication of (In,Ga)N/GaN NW-LEDs

always higher than 10. In contrast, the sample with ITO exhibits an ideality factor approximately constant over the low-to-moderate current range ($10^{-6} - 10^{-3}$ A), with an average value of about 9. This value is lower than the ones previously reported both for this kind of device and for NW-LEDs obtained through top-down methods from planar GaN templates^[173,174]. Values of η much higher than 2 have also been reported for GaN-based planar LEDs, and as one possible origin poor quality of the p-type contact has been identified^[175], which could explain the observed difference in η between the two types of devices considered here. A more comprehensive discussion on the I-V characteristics and on the causes of high ideality factors is given in section 4.2.

3.2.4. Effect of the top contact on the emission properties

In the following section the opto-electronic properties of the two samples are compared. The spectra were acquired at room temperature ($T=303$ K) applying a direct current (DC), the light was collected by means of an optical microscope and analysed through a grating spectrometer (groove density equal to 600 mm^{-1}) connected to a cooled CCD camera.

Figures 3.11(a) and (b) depict the EL spectra acquired for the samples with Ni/Au and ITO contacts, respectively; the various curves, from the bottom to the top, refer to increasing total current densities (J) injected into the devices. The EL spectra of the two samples are composed of several peaks among which the main two are centred around 520 and 570 nm. The relative intensity of these two peaks is different in the samples with Ni/Au and ITO and varies also with the injected current. In particular, the relative intensity of the EL line at lower wavelength increases at higher current. This effect might be mainly explained by different current densities in the individual NWs emitting EL. In the device with Ni/Au contact, where less NWs are conducting the current and thus the charge carrier density per individual NW is higher, the EL line at lower wavelength dominates the spectra. A detailed discussion on the effect of different injected currents on the EL spectra is presented in section 4.1.1. In addition, In content inhomogeneity over the wafer might explain the slightly different position of the two main EL lines in the investigated devices.

In order to estimate the average current densities in the single NW (J_{NW}) we used the formula

$$J_{NW} = \frac{J}{D_{on}A_{NW}} \quad (3.2)$$

where A_{NW} is the mean area of the NW top facets while D_{on} is the density of NWs emitting EL extrapolated from the number of EL spots. From top-view SEM images of the sample under study (see LED1 in table A.1, appendix A), we estimated $A_{NW} \approx 1.38 \times 10^{-10} \text{ cm}^2$, whereas D_{on} was evaluated for each injected current using the data points in the graph of figure 3.9(c). We found that the ranges of total current densities considered in figures 3.11(a) and (b) roughly correspond to the following ranges of J_{NW} : $440-5600 \text{ A/cm}^2$ and $120-1300 \text{ A/cm}^2$ for the samples contacted with Ni/Au and ITO, respectively. The obtained values of the current densities flowing in the single NW are quite high, but if the limitation in optical resolution of the EL mapping is taken into account, these values might be lower by about a factor of eight. I-V measurements performed on single NWs would indicate that the low current range is most likely closer to the actual one^[176].

As shown in figure 3.11(c), the behaviour of the spectrally integrated EL intensity as

3.2. Comparison of NW-LEDs with Ni/Au and ITO top contact

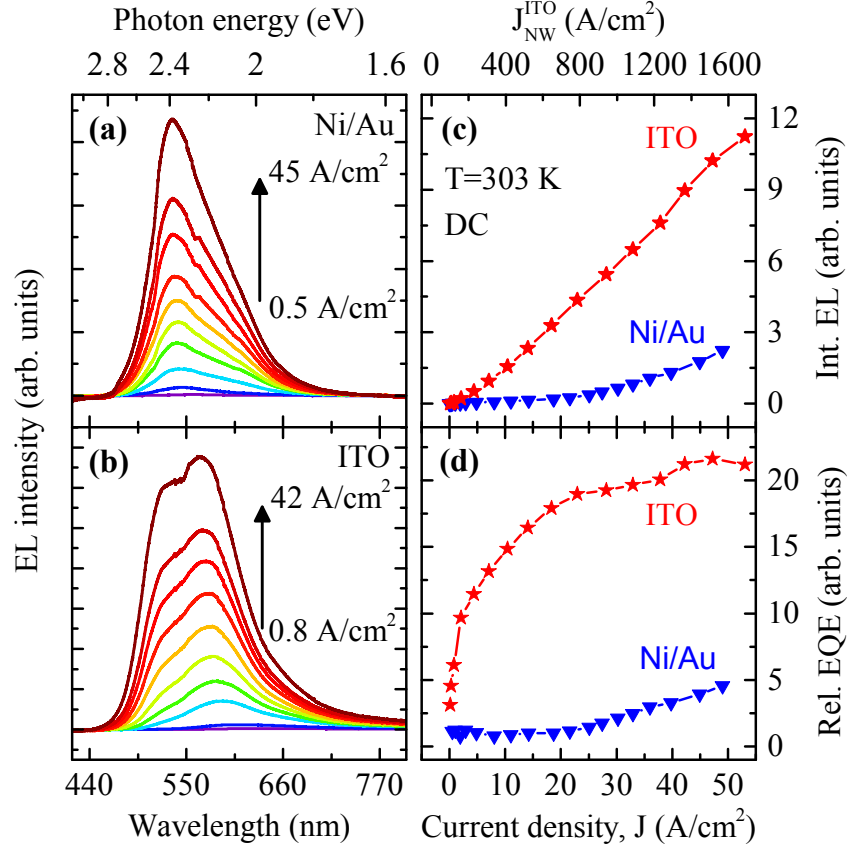


Figure 3.11: Room temperature EL spectra acquired at different current densities (J) for the NW-LEDs with (a) Ni/Au and (b) ITO top contact (same devices as in Fig. 3.10). (c) Integrated EL and (d) relative EQE plotted versus the injected current density. The top axis shows the average current density per NW estimated in the case of the device contacted with ITO.

a function of the current density strongly differs between the two samples. The integrated EL intensity of the LED with ITO rises faster and more linearly than that of the sample with Ni/Au top contact. The employed experimental setup is not able to integrate the EL intensity over the solid angle; for this reason, only relative intensities are discussed. Nevertheless, the performance of the devices can be compared by using the relative external quantum efficiency (EQE). This quantity was calculated by dividing the spectrally integrated EL intensity by the corresponding total current density, the result is depicted in figure 3.11(d). Again, it is possible to identify several differences between the two samples. In particular, the relative EQE of the LED with ITO increases quickly with the current, and then almost saturates for current densities higher than 30 A/cm². In contrast, the relative EQE of the sample with Ni/Au contact increases slowly, and does not saturate in the studied range of currents. The latter trend is similar to the one reported by other groups for comparable devices contacted with Ni/Au/ITO^[129,158]; in these cases, the relative EQEs saturate for much higher current densities (in the range 100–300 A/cm²). The comparison with published data seems thus to suggest that the presence of compact metal layers between the ITO and the p-GaN NW tips does not improve the overall characteristics of the contact. More importantly, our measurements also show that the LED with ITO exhibits a relative EQE about an order of magnitude higher

3. Fabrication of (In,Ga)N/GaN NW-LEDs

than the sample with Ni/Au. This significant improvement may be explained by a better injection of holes together with a higher number of individual emitters and an enhanced extraction efficiency.

In conclusion, exclusively employing ITO instead of Ni/Au as the top contact for NW-LEDs significantly improves many of the factors that have so far limited device performance; such as low number density of emitting NWs, poor hole injection efficiency, and high turn-on voltage. Furthermore, the low density of emitting NWs reported so far can be explained by a poor p-type top contact and is thus not caused by limitations intrinsic to (In,Ga)N/GaN NWs grown on Si, such as the presence of Si_xN_y at the interface to the Si substrate or fluctuations in NW sizes.

3.3. Comparison of NW-LEDs on AlN-buffered and bare Si

In section 2.3 of the previous chapter we demonstrated that the 4-nm-thick AlN layer is suitable for the selective-area growth of GaN NWs. This is the first step needed to realize LEDs based on homogeneous NW ensembles on Si substrates. At this point still a fundamental requirement must be verified to demonstrate the compatibility of the AlN buffer with both SAG and LED operation: the electrical conductivity of the buffer layer. In other words, if the cathode of the LED is placed on the backside of the Si substrate, the current has to pass across the thin AlN layer to reach it. Since the AlN has a wide band gap, it is *a priori* not easy to predict its effect on the charge carrier transport.

To better investigate this point, two LEDs based on NWs spontaneously formed on the 4-nm-thick AlN buffer layer (LED2) and directly on bare Si (LED1) were fabricated, and then the performance of the two devices were compared. The two samples were grown using nominally identical conditions (the growth parameters are listed in table A.1, appendix A). Figures 3.12(a) and (b) show the top-view SEM images of the samples grown on bare Si and thin AlN layer, respectively. We note that the NWs have similar morphology in the two cases; the NW density in LED1 and LED2 is $7.3 \times 10^9 \text{ cm}^{-2}$ and $6.1 \times 10^9 \text{ cm}^{-2}$, respectively. The lower NW density in the sample grown on thin AlN is reflected in a slightly lower coalescence degree of the NWs. The devices were produced following the processing scheme described in section 3.1, in both cases the ITO top contact was employed.

As the first step to compare the performance of NW-LEDs grown on AlN-buffered and bare Si, we acquired electroluminescence maps of the samples fabricated on these two

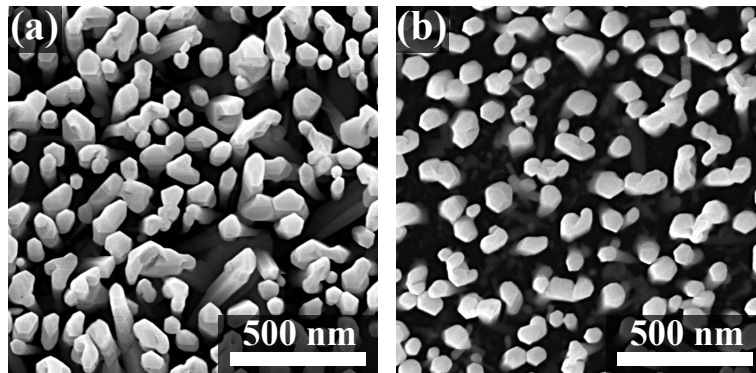


Figure 3.12: Top-view SEM micrograph of the unprocessed NW-LEDs grown on (a) bare and (b) AlN-buffered Si substrate.

3.3. Comparison of NW-LEDs on AlN-buffered and bare Si

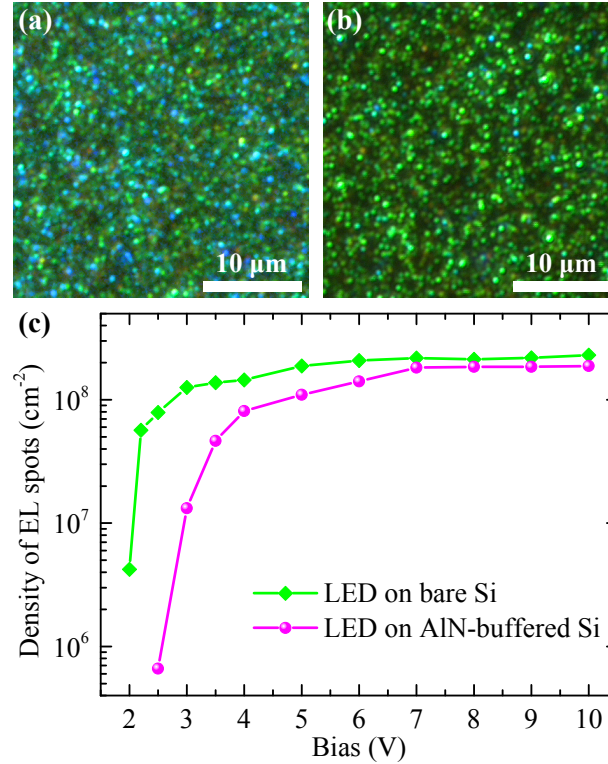


Figure 3.13: EL maps of the NW-LEDs grown (a) directly on Si and (b) on 4-nm-thick AlN, acquired under a forward bias of 6 V through an optical microscope. (c) Dependence of the number density of EL spots on the forward bias for the two different types of NW-LED.

types of substrates. Figures 3.13(a) and (b) show the maps of the resulting EL acquired through an optical microscope on devices with an area of 0.19 mm², under an applied forward bias equal to 6 V. Both the NW-LEDs grown on AlN and on bare Si exhibit spotty emission patterns, with a comparable density of emitting spots. The emission of EL from the sample grown on the 4-nm-thick AlN layer clearly proves that an electric current can flow across the barrier formed by this layer. Figure 3.13(c) shows the density of EL spots extracted from the EL maps as a function of the applied forward bias. The turn-on of the first individual NW-LEDs occurs in both the samples at similar bias (about +2 V), then the number density of emitting NWs rises faster in the sample grown on bare Si than in the one grown on thin AlN. Beyond +6 V the density of EL spots saturates at about $2 \times 10^8 \text{ cm}^{-2}$ regardless of the presence of the thin AlN layer. These outcomes suggest that some of the NWs grown on the thin AlN require slightly higher bias to turn on, but beyond +6 V the actual number of working NW-LEDs is almost identical in the two devices. The small difference in density of EL spots at high bias might be due to the slightly lower NW density in the sample grown on the AlN buffer layer.

Next, we compare the opto-electronic characteristics of the NW-LEDs grown on the two different substrates. The EL spectra were acquired at room temperature ($T=303 \text{ K}$) applying a direct current (DC), the light was collected by means of an optical microscope and analysed through a grating spectrometer (groove density equal to 600 mm^{-1}) connected to a cooled CCD camera. Figures 3.14(a) and (b) depict the EL spectra acquired at different injected currents for the samples grown on AlN-buffered and bare Si, respec-

3. Fabrication of (In,Ga)N/GaN NW-LEDs

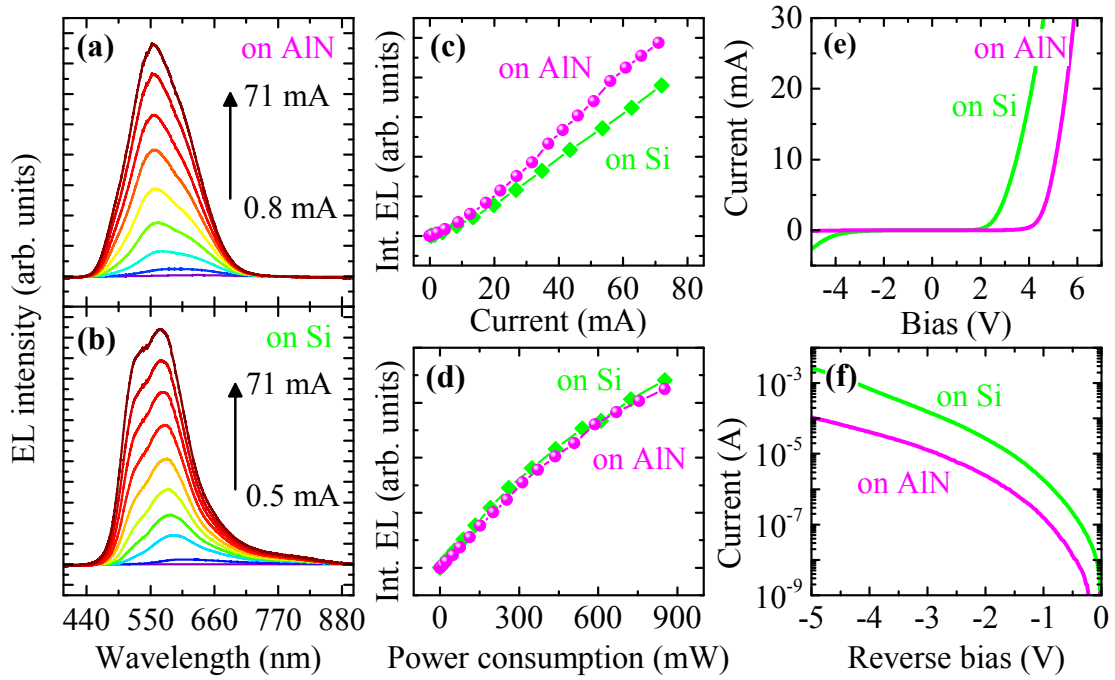


Figure 3.14: Optoelectronic characteristics of the NW-LEDs with area of 0.19 mm^2 fabricated on the two types of substrates. (a)–(b) Room temperature ($T=303 \text{ K}$) EL spectra acquired at different injected currents for the NW-LEDs grown on (a) 4-nm-thick AlN and (b) bare Si. (c)–(d) Integrated EL intensity plotted versus (c) the injected current and (d) the power consumption. (e) I-V characteristics of the two studied samples on a linear scale. (f) Same I-V curves in reverse bias regime plotted on a logarithmic scale.

tively. In all spectra, broad peaks centred in the green spectral range around 560 nm are observed. There are slight differences in the width and in the shape of the EL peaks between the two samples. These differences are not surprising for two different growth runs involving self-organization phenomena, and taking into account that NWs grown on AlN have a slightly lower density and thus coalescence degree (see figure 3.12). In any case, the evolution of the EL spectra with the current is comparable. Figure 3.14(c) shows the EL intensity integrated over the entire spectral range as a function of the injected current. Surprisingly, the EL intensity emitted by the devices grown on thin AlN and on bare Si is comparable, and for currents higher than 20 mA the NW-LED grown on AlN is even brighter. This result is also confirmed by figure 3.14(d), where the integrated EL intensity is plotted as a function of the power consumption, namely the product of injected current and applied voltage. It is clearly visible that the devices grown on thin AlN and on bare Si emit the same EL intensity in the entire range of considered powers.

In order to further understand the effect of the 4-nm-thick AlN layer on the flow of an electric current, we analysed the current-voltage characteristics of the samples fabricated on the two types of substrates. Figure 3.14(e) depicts the I-V characteristics of the two studied samples on a linear scale. The sample grown on bare Si exhibits a turn-on voltage that is about 2 V lower than the one observed for the device grown on the thin AlN layer. The lower turn-on voltage of the sample grown on bare Si might be due to several factors. Firstly, the number of individual NW-LEDs in operation for bias lower than +6 V differs, and hence the total current conducted is lower in the device grown on the AlN

3.3. Comparison of NW-LEDs on AlN-buffered and bare Si

layer than in the one grown on bare Si, as clearly visible in figure 3.13(c). Therefore, for small biases, the device on bare Si could conduct a higher total current simply because more NWs are contributing to the charge carrier conduction. Secondly, an early turn-on voltage might be caused by the presence of leakage current. Indeed, figure 3.14(f) reveals that in reverse bias regime the sample grown on bare Si has a leakage current about one order of magnitude higher than the one found in the sample with the AlN layer. Assuming that a similar leakage current occurs also for positive biases, for equal injected current the device grown on bare Si would emit EL less efficiently. These arguments might explain the very similar opto-electronic performance observed in the two devices, *i. e.* comparable efficiencies at a given current and power consumption, despite the higher turn-on voltage of the sample grown on AlN layer.

In section 3.1.2 it was shown that part of the leakage current conducted by the NW-LEDs seems to flow on the sidewalls of the NWs. The lower leakage current observed in the device grown on thin AlN buffer might be understood imagining that the leakage current flowing on the sidewalls of the NWs is blocked by the AlN buffer. In fact, the C-AFM analysis presented in section 2.3.3 suggests that the electrons can flow across the AlN buffer mainly through protrusions directly in touch with the Si substrate. Because of the small sizes of these protrusions, the portion of NW sidewall electrically connected with them is likely very small, and thus the surface leakage current able to flow across the AlN layer is little.

It is worth mentioning that the thin AlN buffer has also another important advantage. In fact, we found that for measurements at cryogenic temperatures (discussed in the next chapter), the thin AlN layer prevents the formation of cracks in the LED samples. Comparable devices grown without AlN buffer were always damaged during the measurements at low temperatures (below 100 K).

In conclusion, we have demonstrated that an AlN buffer layer that is only 4 nm thick both enables the SAG of GaN NWs on Si substrates and permits the operation of NW-LEDs. Furthermore, a careful characterization of the opto-electronic properties of comparable devices fabricated either on AlN-buffered or on bare Si has shown that the performance of NW-LEDs fabricated on the two types of substrates is similar.

Summary

In this chapter important optimizations of the various processing steps required to fabricate a functional NW-LEDs have been discussed. With regard to the top contact, we have found that exclusively employing ITO instead of Ni/Au significantly improves many of the factors that have so far limited device performance; such as low number density of emitting NWs, poor hole injection efficiency, and high turn-on voltage. The discussed outcomes definitely prove that the low density of emitting NWs reported so far can be explained by a poor p-type top contact and is thus not caused by limitations intrinsic to (In,Ga)N/GaN NWs grown on Si, such as the presence of Si_xN_y at the interface to the Si substrate or fluctuations in NW sizes. In addition, we have demonstrated that NW-LEDs grown on bare Si or on 4-nm-thick AlN layers have comparable performance. This outcome, together with the successful growth of ordered arrays of GaN NWs presented in section 2.4.2 of the previous chapter, demonstrates the compatibility of SAG on AlN-buffered Si substrates with device operation, thus paving the way for a new generation of LEDs based on homogeneous NW ensembles produced on cost-effective substrates.

Investigation of the opto-electronic characteristics of NW-LEDs

In this chapter an accurate analysis of the opto-electronic and transport properties of a NW-LED sample will be presented. The main goal of this study is to achieve a deeper understanding of the charge carrier recombination and transport phenomena present in (In,Ga)N/GaN LEDs based on NWs, and possibly describe them by means of quantitative physical models. In fact, despite the great effort invested by the scientific community in the fabrication of NW-LEDs, very little has been reported concerning the analysis of shallow traps and deep levels as well as their role for the opto-electronic properties of these devices^[50,172,177,178]. For this reason, many fundamental aspects of the (In,Ga)N/GaN NW-LEDs remain still obscure.

In this work, one and the same device was characterized by means of a wide spectrum of different techniques including: capacitance measurements (C-V), deep level transient spectroscopy (DLTS), temperature dependent current voltage measurements (I-V-T), as well as photoluminescence (PL) and electroluminescence (EL) acquired at different currents and temperatures. The DLTS and the I-V-T analyses on NW-LEDs presented in this chapter are original studies so far not reported in literature. In order to check the device-to-device variability of the opto-electronic properties, the same set of measurements was repeated on three different NW-LEDs produced from a dice of the same wafer. Although device-to-device fluctuations were observed, the same characteristic behaviour was found in all the analysed devices. For this reason, in the following sections, only the data relating to one device are discussed in detail; for further details about structure and growth parameters of this NW-LED refer to LED3 in appendix A, table A.1.

In the first sections of the chapter the emission properties of the NW-LED are carefully analysed, and possible explanations of the observed features are discussed. In the second section a novel interpretation of the I-V characteristics in forward bias regime is proposed. The classical Shockley model of the LED is revised so as to take into account the multi-element nature of a NW-based LED, which has to be considered as an ensemble of millions of nano-devices contacted in parallel. The third part of the chapter intends to elucidate the transport mechanisms in reverse bias regime, in which leakage processes dominate the current conduction. To this end, the presence of electrically active deep level states in the active region of the NW-LED was probed by means of DLTS measurements. Next, a physical model was developed to explain the peculiarities of the I-V-T curves in reverse bias regime.

4.1. Emission properties of NW-LEDs

In this section the emission properties of the NW-LEDs are investigated in-depth. We first discuss the current dependence of the opto-electronic characteristics; then temperature dependent EL and PL measurements are presented.

4.1.1. Evolution of the electroluminescence with the current

Figure 4.1(a) shows the evolution of the EL spectra emitted by the NW-LED ensemble when the current is increased from 0.001 mA up to 50 mA, from the blue to the yellow curves, respectively. The EL measurements were performed at room temperature ($T=303$ K) by means of a probe-station held in a dark ambient; the light was collected through an optical microscope and analysed by an array spectrometer, model CAS 140CT, with a cooled CCD camera.

The EL spectra emitted by the (In,Ga)N QWs are characterized by a broad peak consisting of two main lines, which exhibit a blue shift with increasing injection current, as marked by the magenta dashed arrows. Interestingly, similar asymmetric peaks with low energy tails have already been observed in the spectra presented in section 3.2.4, and also in other green NW-LEDs reported in literature with structures comparable to the one employed in this work^[131,133,179]. Nevertheless, in all these cases only the integrated EL or the position of the most intense peak was considered. Now we aim at studying in more detail the evolution of the different lines constituting the peaks. To this end, the EL spectra have been fitted by means of two Gaussian peaks. The resulting fits for three different currents are plotted in figures 4.1(b)–(d); we note that the cumulative fits, depicted by the cyan dashed lines, perfectly overlap the data points. The evolution of the relative intensity of the two peaks, labelled “Peak1” and “Peak2”, has a peculiar behaviour. At very low current ($I=0.01$ mA) the low energy line (Peak1) is much more intense than the high energy line (Peak2), but the latter increases faster, and for $I=0.1$ mA has already an intensity comparable with the one of Peak1; at higher current the high energy line overtakes the low energy one and dominates the spectrum. This behaviour is clearly visible in figures 4.1(b), (c), and (d) for injected currents equal to 0.01, 0.1, and 10 mA, respectively.

It is important to understand whether the observed effect is characteristic of each single NW or is due to a cumulative effect of the NW ensemble. In other words, whether the two peaks are emitted by every individual nano-LED or some NWs emit the line at low energy while others the line at high energy, and then the sum of the two produces the observed spectral shape. To this end spectrally resolved EL top-view maps of the same NW-LED were acquired by means of an electrically tunable liquid crystal filter (model CRI Inc. Varispec) with a bandwidth smaller than 7 nm. The spatial resolution of this technique is given by the magnification of the objective and by the density of pixels of the CCD camera employed to record the EL maps. An objective with 100x magnification was chosen so that each EL spot, whose size is limited by the diffraction of the lens to about $0.2\text{ }\mu\text{m}$, is recorded simultaneously by several pixels of the CCD camera. The resulting monochromatic false-colour top-view EL maps of the NW-LED acquired under an injected current of 20 mA at the emission energies corresponding to the two main peaks observed in the EL spectra, namely 2.29 and 2.38 eV, are shown in figures 4.2(a) and (b), respectively. A comparison of the two EL maps shows that almost each spot, which likely correspond to the emission of a single nano-LED or a cluster of few NWs, is present at both emission energies. This fact strongly suggests that the two peaks observed in the EL spectra of the NW ensemble are actually related to properties of the individual NW

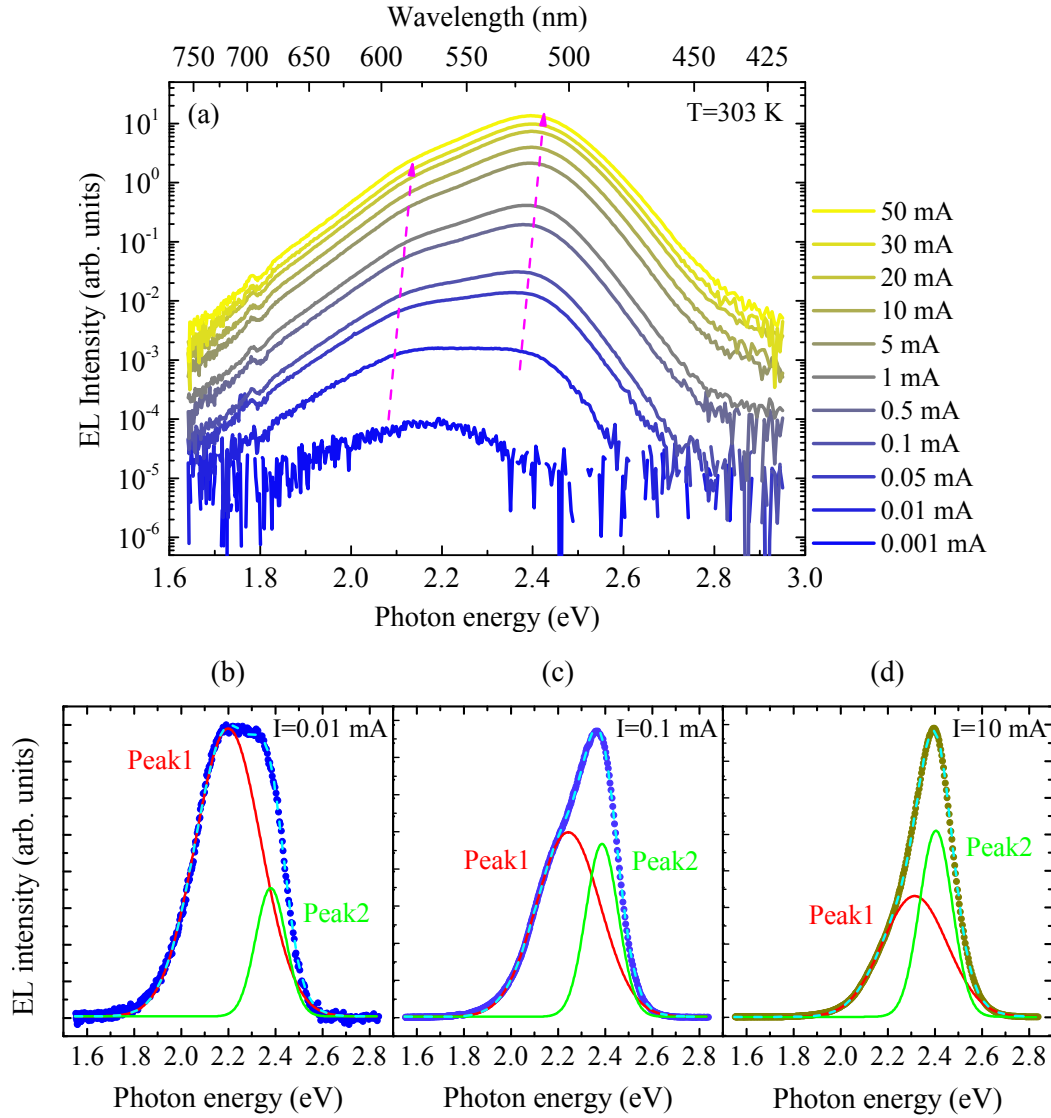


Figure 4.1: (a) EL spectra acquired at room temperature ($T=303$ K) varying the injection current from 0.001 up to 50 mA, the data are plotted on semi-logarithmic scale. The magenta arrows are lines to the eye which sketch the evolution of the two main peaks. (b)–(d) Fits of the data points obtained by means of two Gaussian peaks labelled “Peak1” and “Peak2”, red and green solid curves, respectively. The cyan dashed lines depict the cumulative fits, namely the algebraic sum of the two peaks. The data are plotted on linear scale and are related to measurements acquired with injection currents equal to (b) 0.001 mA, (c) 0.1 mA, and (d) 10 mA.

rather than cumulative effects of the ensemble.

The EL maps were acquired for several injected currents in the spectral range [1.8–2.8] eV. The EL spectra coming from different spots on the map were analysed in more detail. Several points were checked but for sake of clarity only the spectra related to two of them, from here on named NW1 and NW2, are plotted in figures 4.2(c)–(d). Although the EL intensity exhibits significant fluctuations from spot to spot, the spectra are always characterized by two main peaks; the energy position of these lines is slightly different in different NWs. This outcome confirms the presence of fluctuations in the emission

4. Investigation of the opto-electronic characteristics of NW-LEDs

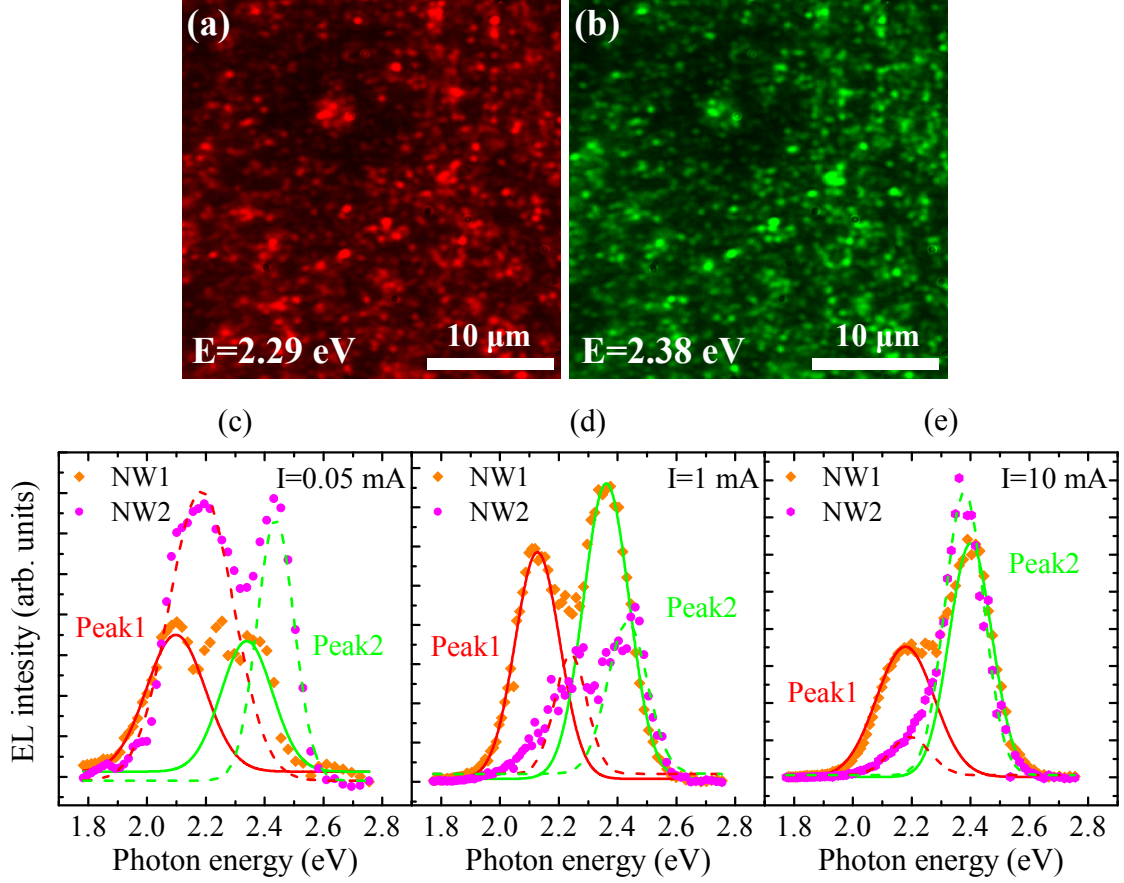


Figure 4.2: (a)–(b) Monochromatic false-colour top-view EL maps of the NW-LED acquired under an injected current of 20 mA at the emission energies corresponding to the two main peaks observed in the EL spectra, (a) 2.29 and (b) 2.38 eV. (b)–(d) The orange and magenta symbols depict the spectra extracted from two different spots of the EL maps, likely corresponding to single NWs. The solid and dashed lines represent the two Gaussian peaks used to fit the data points of NW1 and NW2, respectively. The three graphs are related to measurements acquired with total injection currents equal to (c) 0.05 mA, (d) 1 mA, and (e) 10 mA.

properties of single NWs already observed by different groups^[133,180]. The spectra were fitted by means of two Gaussian peaks (Peak1 and Peak2). Figures 4.2(c)–(d) show the spectra acquired at three different total currents (0.05, 1, and 10 mA.); the same peculiar evolution of the EL intensity with increasing current observed for the ensemble measurements is visible also in the spectra from single spots. For small currents [see figure 4.2(c)] the low energy line has higher or similar intensity than the high energy one. Increasing the current Peak2 rises faster than Peak1 and eventually dominates the spectra [see figures 4.2(d) and (e)]. Similar behaviour was observed in all analysed EL spots, which confirms that the emission of each individual NW is characterized by two main lines.

The evolution of the EL intensity emitted by the NW ensemble with the injection current for the two observed peaks is summarized in figure 4.3(a); in order to better compare the relative behaviour of the two peaks, the data were normalized to the weakest intensity obtained for Peak2 at 0.01 mA. We observe that Peak1 appears earlier than Peak2 at very low injection current ($I=0.001$ mA), but its intensity rises more slowly than that of the

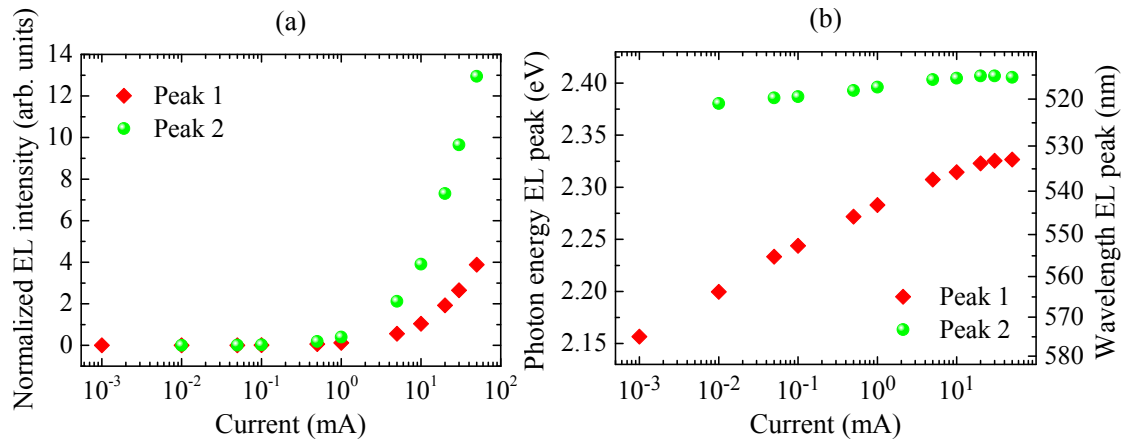


Figure 4.3: (a) Evolution of the EL intensity with the injection current for the two peaks observed in figure 4.1, red diamond and green circle points. The data were normalized to the weakest intensity obtained for Peak2 at 0.01 mA. (b) Evolution of the position of the EL peaks as a function of the current. To achieve a better view of the discussed effect, the abscissa axis is plotted on a logarithmic scale.

other peak. Figure 4.3(b) shows the evolution of the line position for the two observed EL peaks. A blue shift occurs in both lines as the injected current increases from 0.001 to 10 mA, but it is more pronounced for Peak1 than for Peak2: about 110 and 20 meV, respectively. In this semi-logarithmic plot, it is clear that the dependence of the peak position with current is logarithmic up to 10 mA and then saturates. This behaviour is comparable to the one predicted by Kuroda and Tackeuchi^[181] and by Pinos et al.^[182] for free-carrier screening of the internal electric field, namely the quantum-confined stark effect (QCSE)^[183]. The saturation of the peak shift at high current arises from the fact that the carrier lifetime decreases once screening is effective, thus requiring higher and higher currents to further increase the carrier concentrations in the QWs. For currents higher than 10 mA the peak positions of Peak1 and Peak2 saturate to values of about 2.33 and 2.41 eV, respectively. Simulations of the investigated structure performed by Sacconi and co-authors with a multiscale parametric approach found that these emission energies correspond to an average In-content inside the QWs of about 25 and 27 %^[30]. These values are in good agreement with the one obtained from XRD measurements in section 2.2.3. The same simulations also show a comparable blue shift of the emission energy with increasing current.

The observation of two main peaks with different energies in all the NW-LEDs investigated in this thesis and also in other green NW-LEDs reported in literature^[131,133,179] suggests that this effect is due to some peculiarity of the NW-LEDs, likely related to the 3D morphology of the wires or to the particular LED structure used. To elucidate this issue our collaborators at the university of Tor Vergata in Rome simulated the investigated NW-LED structure by means of a multiscale parametric approach implemented with the *Tiberlab* software^[184]. In particular, strain calculations of the 3D NW structure indicate that the (Al,Ga)N EBL placed directly in contact with the last QW induces compressive strain in the (In,Ga)N insertion. This strain makes the band gap of the QW close to the EBL wider, thus shifting its emission several tens of meV towards higher energies in comparison to the other QWs. The inhomogeneous strain produced by the EBL induces also an higher piezoelectric polarization at the interface, and thus a different electric field in-

4. Investigation of the opto-electronic characteristics of NW-LEDs

side the various QWs. Therefore, in this picture of the system, the two peaks observed in the EL spectra might be emitted by different QWs; particularly, the high energy Peak2 should be related to the strained QW in contact with the EBL, whereas Peak1 should be due to the other QWs. The strain induced by the EBL could even alter the shape of the last QW, thus changing the confinement properties of the (In,Ga)N insertion and its emission energy^[185,186]. Different energy lines coming from various (In,Ga)N QWs stacked along the NW axis has already been observed through spatially resolved cathodoluminescence by different groups^[180,186]. They have attributed the red shift of the emission energy observed along the QWs pile to compositional pulling. This effect should induce different incorporation of In in each QW, thus resulting in more than two lines when four QWs are present. For this reason, compositional pulling is unlikely the cause of the effect observed in our NW-LEDs.

The hypothesis that the high energy Peak2 is emitted by the strained QW in contact with the EBL could also explain the peculiar evolution of the peak intensity with current. Usually, in a LED with multiple QWs the charge carrier distribution in the active region varies with the total amount of injected current. In particular, for high current levels the charge concentration in the QW closer to the p-type EBL is higher than in the other wells^[19]; this effect is due to the higher mobility of electrons in comparison with the one of holes. Because of the progressive carrier accumulation, the EL emitted at high injected currents by the QW closer to the EBL is more intense than that coming from the other QWs. This is in agreement with the current dependence of the intensity of the two EL peaks shown in figure 4.3(a). Again, we are assuming that the brighter Peak2 is emitted by the QW closer to the EBL.

In conclusion, the systematic observation of two lines in the EL spectra emitted by each single NW can be explained by asymmetric strain distribution in the active region of the NW-LEDs due to the presence of the EBL.

4.1.2. External quantum efficiency and ABC model

We first analyse the relative EQE of the two main peaks observed in the EL spectra. Since these features are related to the emission coming from each single nano-LED, likely from different QWs, it makes sense to plot their relative EQE *vs.* the average current density injected into each NW (J_{NW}). As already discussed in section 3.2, this can be evaluated by means of the formula: $J_{NW} = J / A_{NW} D_{on}$, where A_{NW} is the average cross-sectional area of a single NW, and D_{on} represents the density of NWs that are actually conducting current. From top-view SEM images of the NW-LED under investigation we estimated $A_{NW} \approx 5.7 \times 10^{-11} \text{ cm}^2$; while from the analysis of the EL maps $D_{on} \approx 3 \times 10^8 \text{ cm}^{-2}$ was extrapolated. Figure 4.4(a) shows the relative EQE obtained by dividing the spectrally integrated EL intensity of Peak1 and Peak2 by the corresponding average current density per NW. Note that if the diffraction limited size of the EL spots is considered the average current density per NW could also be about eight times lower [see discussion in section 3.2]. However, such inaccuracy in the current determination does not affect the validity of the comparison presented in figure 4.4(a). In fact, a new set of current densities would rescale the relative EQE of both peaks by the same factor, thus preserving their ratio. For both peaks, the characteristic behaviour typical of nitride based LEDs is visible: the relative EQE rises quickly for low injected currents, then reaches a maximum and decreases for high current densities. We note that Peak1 reaches its maximum efficiency at very low current density per NW (about 1.5 Acm^{-2}), whereas Peak2 exhibits a maximum at higher current density (roughly 100 Acm^{-2}). This means that the recombination pro-

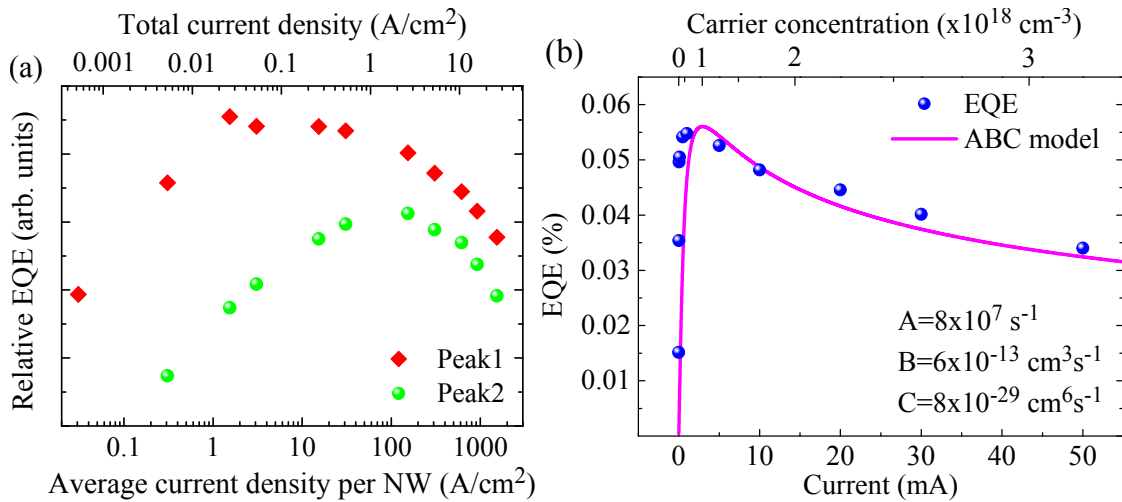


Figure 4.4: (a) Relative EQE plotted versus the logarithm of the average current density injected in each single NW, the top axis shows the corresponding total current density of the NW ensemble LED. The red diamond and green circle points are related to Peak1 and Peak2, respectively. (b) Estimated absolute EQE plotted versus the total injected current, the top axis shows the corresponding carrier concentration in the QWs. The solid line represents the fit of the data to the ABC model, the obtained coefficients are indicated in the lower right corner.

cess responsible for Peak1 saturates before the one producing Peak2. In the hypothesis that Peak2 is emitted by the QW closer to the EBL while Peak1 is due to the other QWs, the earlier efficiency saturation of Peak1 can be understood by imagining that, for high injected current, the carriers recombine more favourably in the QW closer to the EBL than in the others.

As already mentioned, the EL intensity was not integrated over the solid angle, therefore, only the relative EQE instead of the absolute one can be exactly calculate. In order to give an estimate, albeit approximate, of the absolute EQE and IQE of the NW-LED, the total emitted power was measured for few different currents, and then the relative EL data were accordingly rescaled. To this end, a calibrated 1.5-mm^2 -large Si sensor was placed very close to the emitting surface of the NW-LED under investigation, which has an area of only 0.19 mm^2 , so as to capture most of the emitted light. For instance, an emitted power of about $40\text{ }\mu\text{W}$ was measured at an injected current of 50 mA. Rescaling all the EL data, we obtained an estimation of the absolute EL intensity (L); the corresponding EQE was then calculated by means of equation 1.16. The data points are plotted in figure 4.4(b) as a function of the total current injected in the device. A peak EQE of 0.055 % was observed at about 1 mA. This value is about 20 times smaller than the one of the state-of-the-art green NW-LEDs grown by SAG on GaN template and passivated by means of Al_2O_3 shell^[179]; in this case a peak EQE of 1.1% occurring at a current of about 2 mA was reported. The relatively low EQE of the investigated device is likely due to the much simpler structure of our NW-LEDs and the light absorption at the Si substrate. In particular, the presence of a passivation shell around the nanostructures has been found to improve significantly the performance of the devices^[170]. The EQE decreases with increasing injected currents; a droop of about 37 % is observed at 50 mA. Although smaller efficiency droop has been reported for NW-LEDs with more advanced structure^[179], the observed droop is small compared with that of green (In,Ga)N/GaN planar LEDs of 54%^[187,188].

4. Investigation of the opto-electronic characteristics of NW-LEDs

The radiative and non-radiative recombination dynamics in an LED under high injection current [charge carrier concentration much higher than the equilibrium one, $n \gg (n_0 + p_0)$] is commonly described by means of the so called ABC model^[189]. It provides an expression of the internal quantum efficiency (IQE) of the LED in terms of three parameters: the Shockley-Read-Hall (SRH) coefficient A , the bimolecular coefficient B , and the Auger coefficient C . They determine the relevance of the non-radiative SRH, radiative, and non-radiative Auger recombination, respectively. More specifically, the electron-hole radiative recombination rate (R_r) in a quantum well of width W_{QW} can be expressed as the product of B times the effective three-dimensional (3D) carrier concentration of electron and holes: $R_r = B(n_{2D}p_{2D}/W_{QW}^2) \approx B(n_{2D}/W_{QW})^2$. The SRH non-radiative recombination rate (R_{nr}) in a QW is proportional to the effective 3D electron concentration [$R_{nr} = A(n_{2D}/W_{QW})$], thus, it will be dominant at low carrier concentrations. The non-radiative recombination rate due to the three-particle Auger effect can be expressed as $R_{Auger} = C(n_{2D}^2p_{2D}/W_{QW}^3) \approx C(n_{2D}/W_{QW})^3$; it will be dominant at high carrier concentrations. Other effects different from the three mentioned, *e. g.* leakage currents, can be included in the ABC model simply by expanding them into a Taylor series [$f(n) = \alpha n + \beta n^2 + \gamma n^3 + \delta n^4 \dots$]. In this case the A , B , and C coefficients obtained from the fit of the data would exhibit values larger than those got without the additional term (namely, $A' = A + \alpha$, $B' = B + \beta$ etcetera)^[189].

Employing the ABC model, the external quantum efficiency (EQE) of an LED can be written as

$$EQE = \frac{\text{emitted power}}{\text{injected current}} = \eta_{ext} IQE = \eta_{ext} \frac{Bn^2}{An + Bn^2 + Cn^3} \quad (4.1)$$

where η_{ext} represents the extraction efficiency and $n = n_{2D}/W_{QW}$ is the 3D carrier concentration. Under steady state conditions ($dn/dt = 0$), n is related to the current (I) injected into the QW by the equation

$$\frac{I}{qW_{QW}A_{QW}} = An + Bn^2 + Cn^3 \quad (4.2)$$

where q represents the elementary charge and A_{QW} the area of the quantum well. This is a complete third order equation in n which has three roots, two complex and one real *. The real root of equation (4.2) provides a direct relation between the measured current and the carrier concentration in the QWs, thus allowing the application of the ABC model in practical cases. Note that the particular dependences of the recombination rates assumed by the ABC model are valid only for non-degenerate semiconductors and high carrier concentrations; furthermore, localization effects are not included in equation (4.1), and the same set of data can be fitted by different combinations of parameters. This considerations would limit the validity of the entire model to few particular cases; nevertheless, this approach is still commonly used to describe the efficiency of (In,Ga)N/GaN LEDs. In this work, we employ the ABC model just to compare the properties of our devices with the ones reported in literature.

To apply the ABC model we have to estimate the effective volume of the active region, we assumed that the electron-hole recombinations take place mainly inside the two QWs closest to the EBL. Since each QW has a width of about 3 nm, a total width of the active

*Further details on history, solution methods, and roots of a third order equation can be found here: http://en.wikipedia.org/wiki/Cubic_function.

Table 4.1: List of SRH, bimolecular, and Auger coefficients (A , B , and C , respectively) obtained at room temperature from (In,Ga)N/GaN heterostructures in this work and in literature.

Structure	Colour	Orientation	A (s^{-1})	B (cm^3s^{-1})	C (cm^6s^{-1})
NW-LED <i>This work</i>	Green	-C [000 $\bar{1}$]	8×10^7	6×10^{-13}	8×10^{-29}
NW-LED ^[50]	White	-C [000 $\bar{1}$]	7×10^8	3×10^{-10}	4.5×10^{-29}
NW-LED ^[172]	Red	-C [000 $\bar{1}$]	4.9×10^8	4.8×10^{-11}	4.7×10^{-33}
Planar LED ^[189]	Blue	+C [0001]	—	1×10^{-10}	8×10^{-29}
Planar LED ^[190]	Blue	+C [0001]	2.3×10^7	—	1×10^{-30}
Planar LED ^[191]	Blue	+C [0001]	5.2×10^6	—	—
Planar LED ^[192]	Blue	M [1 $\bar{1}$ 00]	—	—	2×10^{-30}

region (W_{QW}) equal to 6 nm was used. Clearly, in a NW-LED the QWs do not extend over the entire surface of the device, but only in the fraction of area where the NWs are; the ratio between the total area of the device and the one filled by NWs is called filling factor (FF). From SEM top-view micrographs of the planarized sample, $FF \approx 30\%$ was estimated. Furthermore, the analysis of the EL top-view maps indicates that in the investigated device not all the NW-LEDs are emitting light; we assumed that only the 30 % of the total number of NWs participates to the EL emission. The effective emitting volume was thus calculated as $V_{QW} = 0.3 W_{QW} FF A_{tot}$, where A_{tot} is the total area of the device.

The magenta solid line in figure 4.4(b) depicts the fit of the data to the ABC model; the evolution of the data points is well described by equation (4.1). The values of the ABC coefficients obtained from the fits are indicated in the lower right corner of figure 4.4(b) and in table 4.1. The obtained value of the bimolecular coefficient B (related to radiative recombinations) is significantly smaller than the ones reported for both NW-LEDs^[50,172] and planar devices^[189]. An inefficient radiative recombination in the QWs of the NW-LED could explain the low EQE measured in the investigated device. The coefficient A (related to SRH non-radiative recombinations) extracted from the fit of the data is significantly lower than the ones reported for other NW-LEDs^[50,172], but still higher than the ones obtained from planar devices^[190,191]. Also the coefficient C (related to non-radiative Auger recombinations) is considerably higher than the ones reported for LEDs based on both NW ensembles and planar films. As discussed before, the values of the ABC coefficients can appear larger than the expected ones when other recombination mechanisms different from the three ones considered by the model are present. The observed high values of C in NW-LEDs would suggest the presence of electron overflow or any other high order carrier loss mechanism. From the fit of the calculated EQE to equation 4.1 also the extraction efficiency of the device can be estimated. We obtain $\eta_{ext} = 15\%$ in case of the studied NW-LED.

In conclusion, we have estimated the EQE of the NW-LED structure investigated in this thesis; relatively low values smaller than 0.1 % has been obtained. To correctly judge this result one should consider that LEDs based on GaN NWs are a relatively new technology and only few groups in the world are working on this topic. In addition, we recall that the NW-LEDs investigated in this thesis are still prototypes with a rather simple structure, without any particular surface passivation, epoxy lens, or collimating mirrors, and that the Si substrate can absorb a significant amount of light. Therefore, the EQE presently

4. Investigation of the opto-electronic characteristics of NW-LEDs

obtained for NW-LEDs may still be significantly improved, and should not be taken as the basis for assessing their potential.

4.1.3. Colorimetric properties

Differently from planar LEDs, the light produced by NW-LEDs comes from millions of single NWs, which may emit at very different wavelengths. Therefore, it is interesting to study how the various wavelengths blend together, and which colour would be eventually perceived by a human eye looking at the NW-LED.

The discipline that identifies the colours and studies how they are perceived by the human eye is called colorimetry. It defines each perceptible colour (*i. e.*, each spectrum) as a combination of three primary stimuli, also known as colour matching functions. In simple terms, these are mathematical relations that describe how the human eye perceives the pure red, green and blue light^[19]. In 1931, the *Commission Internationale de l'Eclairage* (CIE) standardized the measurements of the colours by introducing the chromaticity diagram. In this plot each colour is univocally identified by two chromaticity coordinates, x and y .

Figure 4.5 shows the CIE 1931 chromaticity diagram. The monochromatic lights are located on the perimeter of the colourful region, the numbers represent the wavelength of the light in nanometres; in general, the closer a point is to the perimeter the purer the colour. The pure white light is placed roughly at the centre of the graph, whereas the upper, lower left and lower right parts contain all the greenish, blueish and reddish

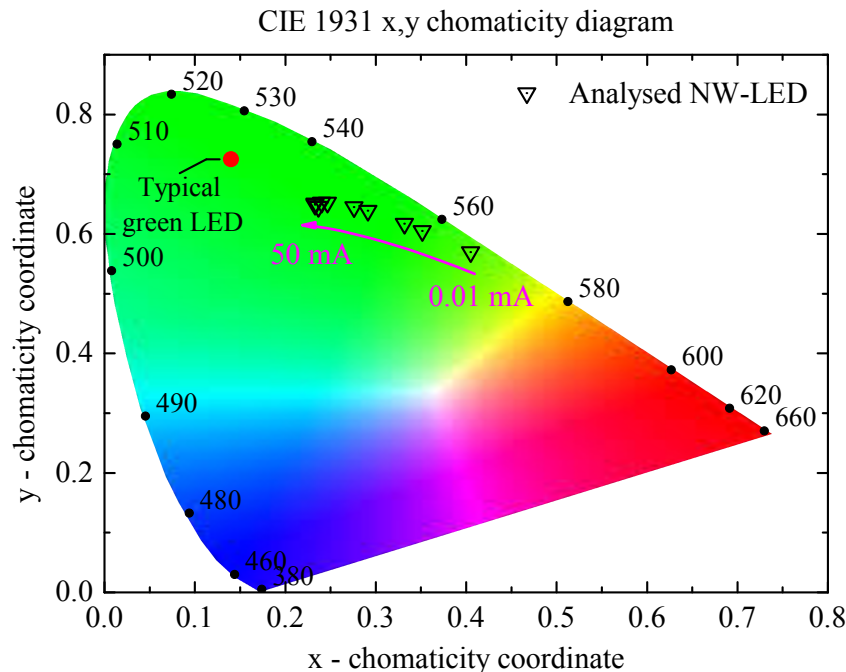


Figure 4.5: CIE 1931 (x,y) chromaticity diagram, which contains all the visible colours. The monochromatic light is located on the perimeter of the colourful region, the numbers represent the wavelength of the light in nanometres. The red point depicts the position in the chromaticity diagram of a typical green planar LED, while the triangular data points represent the variation of the chromaticity coordinates of the investigated NW-LED when the injected current is increased from 0.01 to 50 mA.

colours, respectively. All the other colours, and their shades, are located in the intermediate regions. From the analysis of the spectral-power distribution of the EL emitted by the NW-LED, we extracted the values of the chromaticity coordinates (x, y)^[19]. The triangular data points represent the variation of the chromaticity coordinates of the investigated NW-LED when the injected current is increased from 0.01 to 50 mA. At low currents the NW-LED exhibits a rather pure green-yellow emission. At higher injected currents, to which corresponds a higher density of emitting NWs, the perceived colour shifts towards the green region of the diagram, and its purity decreases. For comparison, the red point depicts the position in the chromaticity diagram of a typical green planar LED. At low current the NW-LED exhibits a colour rendering index (CRI) of about 36; this value is about 2.7 times smaller than the one reported for amber NW-LEDs with (Al,Ga)N shell^[170], suggesting that surface passivation can significantly improve also the CRI of the NW-LEDs. The corrected colour temperature (CCT) of the NW-LED can be varied by increasing the current from about 3000 K up to 7000 K.

4.1.4. Temperature dependence of PL and EL spectra

Temperature dependent PL spectroscopy was performed by Felix Feix at PDI. The measurements were carried out in a dark ambient by means of a cold finger cryostat in which liquid helium was let flow. The NWs were excited by a HeCd laser emitting at 325 nm; the resulting PL signal was collected by an optical microscope and analysed through a grating spectrometer (groove density equal to 600 mm⁻¹) connected to a cooled CCD camera. Two series of measurements were performed varying the temperature from 10 to 300 K, at different excitation powers: in one case an OD2.5 filter was used to reduce the intensity of the laser and obtain a final power of about 0.77 μ W, in the other case the NWs were excited with a power of 210 μ W (OD0 filter). Note that the employed experimental conditions produce a laser spot on the surface of the samples with a diameter of about 3 μ m, thus several hundreds of NWs are excited at the same time.

Figures 4.6(a) and (b) show the PL measurements acquired under the two different conditions. The spectra are dominated by three main series of peaks labelled (In,Ga)N, DAP, and GaN NBE, respectively. The peaks at high energy (3.47 eV) corresponds to the near-band-edge (NBE) emission coming from the GaN base of the LED; these peaks are barely visible at low excitation power because the laser beam is almost completely absorbed by the top part of the NWs, and because the excitons preferentially recombine in the quantum wells (QWs) or are trapped by doping impurities (Mg and Si). Indeed, the dopants can effectively capture electrons and holes and form donor-acceptor pairs (DAP); the decay of these quasiparticles in GaN is usually radiative and is the origin of the DAP peak present in the PL spectra at about 3.26 eV^[193]. Note that the other peaks present in the energy range 2.8–3.2 eV are replica due to interaction with longitudinal optical (LO) phonons.

The most interesting feature of the spectra is the luminescence related to the emission from the (In,Ga)N QWs. This is represented in figures 4.6(a) and (b) by the broad peaks centred in the green spectral range, between 2.2 and 2.5 eV. Note that the structure of the (In,Ga)N peak varies significantly with temperature and excitation power. In particular, at low temperatures and low excitation [see figures 4.6(a)] many different lines are recognizable in the PL spectra between 2.0 and 2.7 eV. The fine structure of the (In,Ga)N related peak is due to charge carrier localization caused by random fluctuations of the In content inside the QWs. Indeed, alloy disorder in ternary III-nitride semiconductors containing In has been recognized as one of the main causes of the high optical efficiency

4. Investigation of the opto-electronic characteristics of NW-LEDs

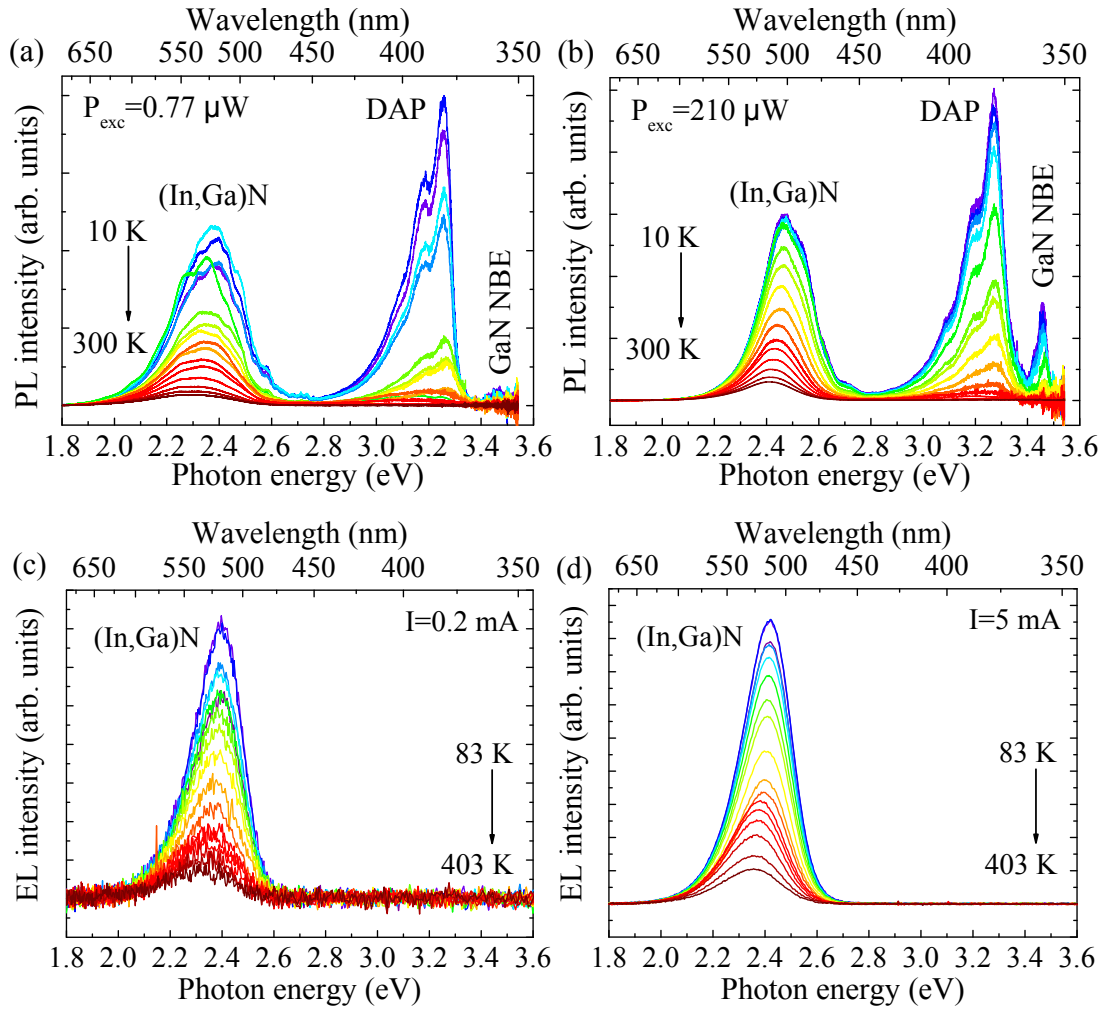


Figure 4.6: (c)–(b) PL spectra acquired varying the temperature from 10 to 300 K at different excitation powers of (a) $0.77 \mu\text{W}$ and (b) $210 \mu\text{W}$. Data acquired by Felix Feix at PDL. (c)–(d) EL spectra acquired varying the temperature from 83 to 403 K, with 20 K steps, at different constant driving currents of (c) 0.2 mA and (d) 5 mA. Data acquired by Laerte Scarpato and Carlo De Santi at the university of Padua, Italy.

in GaN-based LEDs^[194,195]. In fact, the potential fluctuations introduced by the alloy act as radiative recombination centres, thus preventing the decay of the exciton through non-radiative channels. The main drawback of localization phenomena in In-rich clusters is the presence of a big number of recombination centres with different energies, which in the end make the luminescence peaks broad. It is worth noting that the fine structure due to carrier localization vanishes at high temperature and/or high excitation. For example, the spectra shown in figure 4.6(b) exhibit (In,Ga)N peaks with rather uniform shapes, in which traces of carrier localization and multiple lines can only be inferred by the asymmetry of the peaks. This feature can be understood by imagining that at high temperature and/or excitation, the concentration of carriers with high energy in the QWs is high enough to flood all the localized states. In this case the carriers can recombine at many different energies, thus producing a smooth emission peak. It is important to note that the absence of fine structure in the PL spectra do not directly imply that the localiza-

tion effects are not present in the semiconductors. On the contrary, at high temperature and/or carrier concentration the localization effect can be simply dominated by other recombination processes.

In non-resonant PL measurements the electron-hole pairs are optically excited by means of a laser beam inside the entire volume of the NWs. Although much useful information can be obtained by the analysis of the PL data, in an LED device electron and holes are instead injected separately and they only coexist in the active region. In order to study the emission properties of a NW-LED under operation conditions, also the electroluminescence of the investigated sample was acquired. Temperature dependent EL spectroscopy was performed by Laerte Scarparo and Carlo De Santi at the department of information engineering (DEI) of the University of Padua in Italy. The measurements were carried out in a dark ambient by means of a cold finger cryostat filled with liquid nitrogen. The luminescence coming from the ensemble of NWs was collected through an optical fibre and analysed by an array spectrometer, model CAS 140CT, with a spectral resolution below 1 nm. Note that the EL signal was not collected by means of an integrating sphere, therefore we deal with relative EL intensities rather than absolute ones.

Three series of measurements were performed varying the temperature from 83 to 403 K, with 20 K steps, at different constant injected currents: 0.2, 1, and 5 mA. Figures 4.6(c) and (d) show the spectra acquired under a driving current of 0.2 mA and 5 mA, respectively. The spectra are dominated by an asymmetric peak centred in the green spectral range (about 2.4 eV), it is due to the recombination in the (In,Ga)N quantum wells. Although the EL peaks likely consist of more than one line, no clear fine structure is recognizable even at low temperature and injected current [see figure 4.6(c)]. This fact indicates that already at an injected current equal to only 0.2 mA the carrier concentration in the QWs is high enough to fill all the localized states. Therefore, electron-hole pairs can recombine through so many channels with different energies that the localization effects are masked. Interestingly, neither GaN NBE nor DAP emission is detected, suggesting that QWs and EBL effectively confine the electron-hole pair recombinations inside the intrinsic active region.

In all the spectra shown in figure 4.6, the (In,Ga)N related peaks exhibit an intensity drop, roughly by a factor of 8, and a red shift of the emission energy with increasing temperature. In the following paragraphs the emission properties of the NW-LEDs are analysed in a more quantitative way. Although the peaks often consist of more than one line, in the following discussion either the spectrally integrated intensity or the position of the dominant line is considered.

Figure 4.7(a) shows the position of the main (In,Ga)N related PL peak as a function of the temperature; the square and triangular points are related to the data acquired at low (0.77 μ W) and high (210 μ W) excitation power, respectively. Despite the fluctuations due to the fine structure of the PL peaks, especially at low excitation, a clear shift towards lower energies with increasing temperature is visible. In particular, rather constant emission energies are observed for $T \lesssim 60$ K, followed by a red shift of about 70 meV as the temperature is further increased from 60 to 300 K. The graph in figure 4.7(b) plots the energy position of the main EL peak for temperatures ranging from 83 to 403 K; the square, round and triangular points are related to the data acquired at 0.2, 1, and 5 mA, respectively. Also in this case, the EL peaks shift towards lower energies when the temperature is increased; in particular, a red shift of about 90, 60, and 66 meV is observed for driving current of 0.2, 1, and 5 mA, respectively. The peak position seems to saturate for temperatures lower than 83 K, in agreement with the PL data.

4. Investigation of the opto-electronic characteristics of NW-LEDs

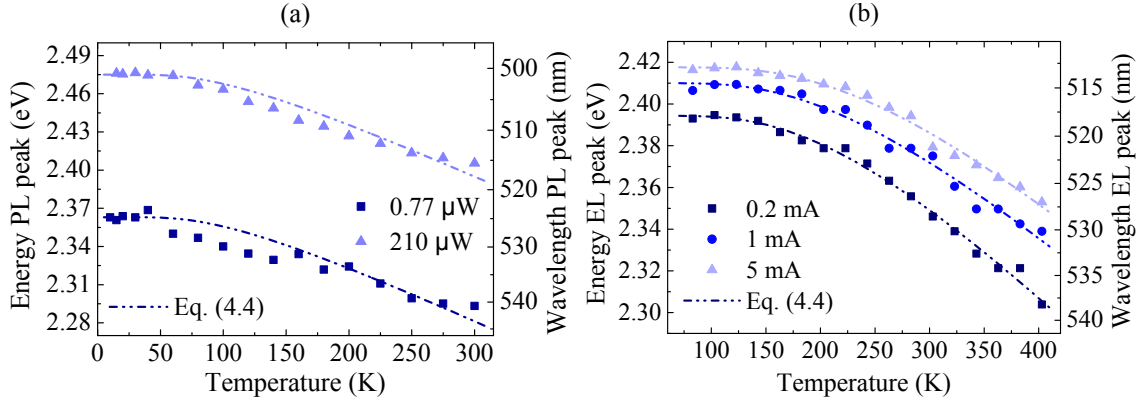


Figure 4.7: Evolution of the energy position of (a) PL and (b) EL peaks related to emission from the (In,Ga)N QWs as a function of the temperature. The dotted-dashed lines depict the fits of the data to equation (4.4).

The red shift of the emission energy is associated with the temperature-induced narrowing of the band gap, and it is commonly described by the empirical Varshni relation defined by the formula^[196]

$$E(T) = E_0 - \frac{\alpha T^2}{T + \beta} \quad (4.3)$$

where α and β are fitting parameters, while E_0 represents the value of the band gap at 0 K. However, Varshni model is purely empirical and has no physical meaning. Moreover, it has often been found inadequate to describe the emission energy shift observed in semiconductors with wide band gap^[197]. A physically motivated model taking into account the material-specific phonon dispersion has been proposed by Pässler^[198]. Another physical model able to describe the temperature dependence of the band gap in semiconductors was developed by Viña and co-authors. They obtained an expression based on the Bose-Einstein statistical factor which takes into account electron-phonon interactions^[199]

$$E(T) = a - b \left[1 + \frac{2}{\exp(\Theta/T) - 1} \right] = E_0 - \frac{A}{\exp(\Theta/T) - 1} \quad (4.4)$$

where $E_0 = a - b$ is the value of the band gap at 0 K, whereas $A = 2b$ represents the effective strength of the electron-phonon (optical and acoustical) interaction. In equation (4.4), $\Theta = E_{ph}^{avg}/k_B$ is the effective phonon temperature defined as the ratio between the average energy of the involved phonons (E_{ph}^{avg}) and the Boltzmann constant (k_B). Note that none of the introduced models takes into account the effects of carrier localization due to alloy fluctuations; nevertheless, we tried to fit the experimental data to equation (4.4). The resulted best fits are depicted by the dotted-dashed lines in figures 4.7(a) and (b). The parameters of the fits are listed in table 4.2. We note that the average phonon energy, E_{ph}^{avg} , obtained from the fits of PL and EL data, respectively, is about 1.3 and 3 times lower than the one reported for longitudinal optical phonons $E_{LO} = 91 \text{ meV}$ ^[200]. This would indicate the presence of a not negligible interaction with acoustical and transverse-optical (TO) phonons. Figure 4.7(a) shows that, although equation (4.4) can qualitatively de-

scribe the energy shift of PL peaks with temperature, a notable discrepancy is observed between fits and experimental data. This deviation is likely due to localization effects not included in the model developed by Viña.

Interestingly, equation (4.4) can describe the EL peak position very well for all the studied temperatures and currents. Furthermore, neither a blue shift at low temperature nor a pronounced “S-shaped” (red-blue-red shift) dependence of the peak position with increasing temperature was observed in the EL from the NW-LED. These effects have often been revealed by means of temperature dependent PL and EL measurements performed on UV and blue (In,Ga)N/GaN planar LEDs, whereas they are usually less pronounced in green LEDs^[201–203]. They are commonly attributed to alloy disorder and carrier localization phenomena occurring in the (In,Ga)N quantum wells. Note that the absence of an “S-shaped” temperature dependence of the EL does not imply that localization effects are negligible. As already discussed, we have indeed found evidence for localization states in the fine structure of the (In,Ga)N related PL peak at low temperature and excitation [see figures 4.6(a)]. This outcomes are also supported by other studies performed by means of cathodoluminescence (CL) and PL spectroscopy on similar NWs containing (In,Ga)N QWs^[180,204]. Nevertheless, the peculiar “S-shaped” dependence may not be observed in the EL characteristics of NW-LEDs, even when the QWs have high In content^[172]. This effect might be explained assuming a much higher carrier concentration in the QWs during EL measurements than that produced by PL or CL analysis. In fact, a high carrier density in the QWs would quickly saturate all the localization centres produced by the potential fluctuations in the (In,Ga)N alloy. Therefore, the effect of alloy disorder would be masked. The lack of blue shift at low temperature in green LEDs might also be explained imagining that the relatively high In content causes a strong spatial localization of the carriers, which thus cannot escape the potential wells and recombine in centres at higher energies^[203].

The temperature dependence of the linewidth, $\Gamma(T)$, of the PL and EL peaks is shown in figures 4.8(a) and (b), respectively. In both cases, the values of the full width at half maximum (FWHM) of the peaks increase with temperature, rather slowly for $T \lesssim 160$ K and then faster. The temperature dependence of the linewidth of radiative transitions in semiconductors can be expressed as^[205,206]

$$\Gamma(T) = \Gamma_0 + \gamma_A T + \frac{\Gamma_{LO}}{\exp(E_{LO}/k_B T) - 1} \quad (4.5)$$

where Γ_0 represents an inhomogeneous broadening arising from temperature indepen-

Table 4.2: List of parameters obtained from the fits of PL and EL peak positions shown in figures 4.7(a) and (b) by means of equation (4.4).

PL		EL			
P_{exc} (μ W)	I (mA)	E_0 (eV)	A (meV)	Θ (K)	E_{ph}^{avg} (meV)
0.77	210	2.363 ± 0.003	140 ± 70	300 ± 80	30 ± 8
		2.475 ± 0.003	140 ± 50	300 ± 60	30 ± 6
	0.2	2.394 ± 0.003	390 ± 70	680 ± 60	60 ± 5
	1	2.410 ± 0.003	350 ± 80	690 ± 80	60 ± 7
	5	2.418 ± 0.003	410 ± 80	800 ± 80	68 ± 7

4. Investigation of the opto-electronic characteristics of NW-LEDs

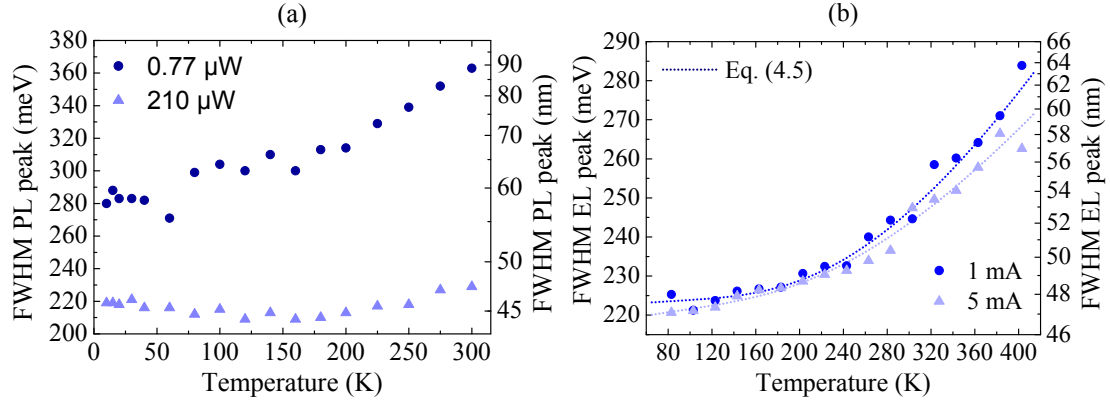


Figure 4.8: Evolution of the FWHM of (a) PL and (b) EL peaks related to emission from the (In,Ga)N QWs as a function of the temperature. The dotted lines in graph (b) are the fits of the data to equation (4.5).

dent mechanisms, such as impurities, point and extended defects, surface scattering, and electron–electron interactions; the second term corresponds to lifetime broadening arising from the electron–acoustical phonon interaction, and γ_A represents the electron–acoustical phonon coupling constant. The third term is caused by electron–LO phonon (Fröhlich) interaction; Γ_{LO} represents the strength of the electron–LO phonon coupling while E_{LO} is the LO phonon energy. The dotted lines in figure 4.8(b) depict the fits of the data obtained from EL measurements to equation (4.5), for injection currents equal to 1 and 5 mA; the agreement with the experimental data is fairly good. The parameters obtained from the fits are listed in table 4.3. We note that the contribution of the acoustical phonons is visible only at low temperatures; in other words, fixing $\gamma_A = 0$ would change the fits only for $T \lesssim 160$ K. The values of the electron–LO phonon coupling constants and of the LO phonon energies obtained from the fits are in relatively good agreement with the ones reported in literature for similar materials, namely $\Gamma_{LO} \approx 540$ meV^[207] and $E_{LO} = 91$ meV^[200].

Figure 4.9 shows the temperature evolution of the spectrally integrated luminescence intensity (L) of the peaks related to the QWs, obtained from (a) PL and (b) EL measurements, respectively. In both cases, a monotonic decrease of the emitted intensity with increasing temperature is observed, this trend is similar to the one reported for green planar LEDs by Cao *et al.*^[202]. In the considered temperature ranges, a drop by a factor roughly equal to 9 and 7 is observed in the PL and EL intensities, respectively. This decrease in luminescence intensity is mainly due to an enhancement of the non-radiative recombination rate. The evolution of L with T reflects the temperature dependence of radiative and non-radiative processes in localized and delocalized states. The temperature

Table 4.3: List of the parameters obtained from the fits of the FWHM of the EL peaks shown in figure 4.8(b) by means of equation (4.5).

I (mA)	Γ_0 (meV)	γ_A ($\mu\text{eV K}^{-1}$)	Γ_{LO} (meV)	E_{LO} (meV)
1	222 ± 6	20 ± 10	600 ± 200	90 ± 10
5	217 ± 6	40 ± 20	400 ± 200	90 ± 15

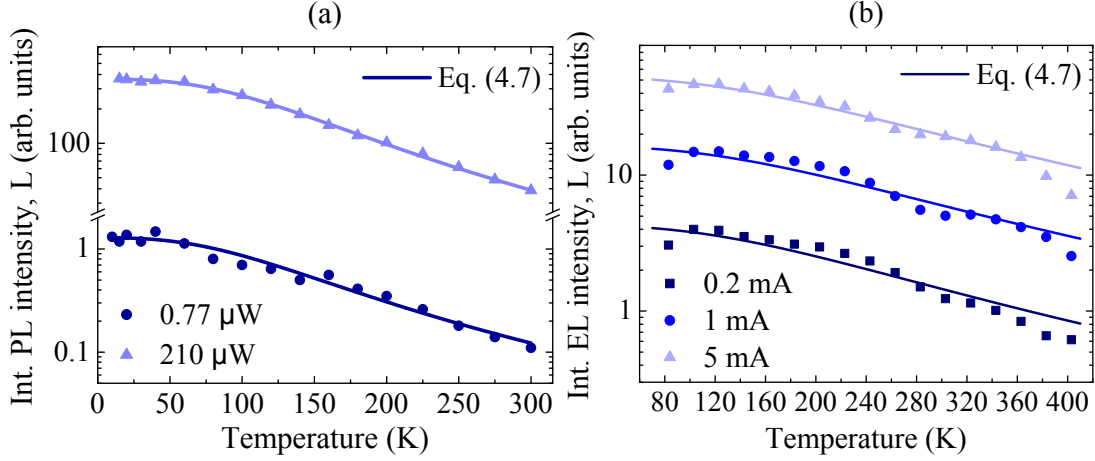


Figure 4.9: Evolution of the integrated luminescence intensity (L) of the peak related to (In,Ga)N as a function of the temperature plotted on semi-logarithmic scale. The data were obtained from (a) PL and (b) EL measurements. The solid lines depict the fits of the data to equation (4.7).

dependence of the luminescence intensity can be written as^[197]

$$L(T) = IQE L_0 = \frac{L_0}{1 + \tau_r(T)/\tau_{nr}(T)} \quad (4.6)$$

where IQE represents the internal quantum efficiency of the active region and L_0 the luminescence intensity at 0 K. The variation of the internal quantum efficiency with T is given by the characteristic temperature dependences of the lifetimes of radiative and non-radiative recombination processes, τ_r and τ_{nr} , respectively: $IQE = \tau_{nr}(T)/[\tau_r(T) + \tau_{nr}(T)]$, hence results the term on the right-hand side of equation (4.6). The radiative lifetime of an electron-hole recombination process in a n -dimensional system is proportional to $T^{n/3}$. Since the (In,Ga)N QW, where the radiative recombination takes place, can be considered to a first approximation as a two-dimensional (2D) system, one obtains $\tau_r \propto T$. With regard to this point, it is worth mentioning that the diameter of the NWs is much larger than the exciton Bohr radius and thus radial confinement is not expected and the QW should behave as a 2D system rather than a 1D one. At the same time, In-segregation and compositional fluctuations in the (In,Ga)N QW could cause a strong localization of the electron-hole pairs, which would thus recombine in a 0D-like system^[180]. However, we recall that the EL data analysed so far do not show significant evidences of localization phenomena, and also in the PL data they are very pronounced only for low temperature and excitation. Therefore, it was assumed that, at least to a first approximation, the QW behaves as a 2D system ($\tau_r \propto T$).

The ratio $\tau_r(T)/\tau_{nr}(T)$ is commonly approximated as a power law at high temperatures. Hence, equation (4.6) becomes

$$L(T) = \frac{L_0}{1 + a T^{1+b}} \quad (4.7)$$

where L_0 , a , and b are fitting parameters. The pre-factor a is a proportionality term in units of inverse temperature, whereas b describes the temperature dependence of the

4. Investigation of the opto-electronic characteristics of NW-LEDs

Table 4.4: List of the parameters obtained from the fits of the integrated luminescence intensity shown in figures 4.9 (a) and (b) to equation (4.7).

PL		EL		
P_{exc} (μ W)	I (mA)	L_0 (arb. units)	a ($\times 10^{-6}$)	b
0.77 210		1.28 ± 0.06	(2 ± 1)	1.7 ± 0.5
		365 ± 3	(1.1 ± 0.6)	1.8 ± 0.1
	0.2	4.3 ± 0.6	(1 ± 2)	1.5 ± 0.7
	1	16 ± 2	(1 ± 2)	1.5 ± 0.7
	5	52 ± 4	(1 ± 2)	1.5 ± 0.4

non-radiative recombination processes. The solid lines in figure 4.9 are the best fits of the data to equation (4.7). The parameters extracted from the fits are listed in table 4.4. Note that the parameters a and b are comparable in case of PL and EL measurements. Equation (4.7) well describes the drop of the PL intensity for both the employed excitation powers. In contrast, a systematic deviation from the fits is observable in case of EL intensity for all the three injected currents. In particular, a plateau followed by a decay with different slope is observed for $T \gtrsim 260$ K. This effect could be due to the activation of a different recombination channel at high temperature, but it could also be explained by imagining that the charge carriers injection into the active region varies with temperature. For instance, variations of the contact properties and/or electron traps present along the current path can affect the injection of carriers into the QWs, thus influencing also the emission characteristics. The absence of this particular behaviour in the evolution of the PL intensity would support the hypothesis of an electronic origin for this phenomenon. In any case, to elucidate the origin of this effect further experiments are needed.

At this point we would like to compare the IQE of our NW-LEDs with the one reported in literature for other LEDs. A popular method to estimate the IQE of optical devices is to calculate the ratio of the integrated PL intensity measured at 300 and 10 K: namely, $IQE_{PL} \approx L(300)/L(10)$. This method is based on the assumption that the IQE at low temperature ($T=10$ K) is equal to 1. Unfortunately, this assumption is not only unfounded but also wrong, and has created great confusion in literature. However, we will employ this method to estimate the IQE of our samples and obtain a comparison with the values reported by other groups. In case of the investigated NW-LEDs we obtained an $IQE_{PL} \approx 10\%$. Although higher values of the IQE_{PL} have been reported for white NW-LEDs with optimized active region^[129], the IQE_{PL} is already relatively good. In fact, its value is comparable with the one recently reported by Jeong *et. al.* for green LEDs based on planar (In,Ga)N QWs grown on GaN substrates, namely 12 %^[195].

In conclusion, The discussion presented in this section provides important insights necessary for a better understanding of the recombination mechanisms in (In,Ga)N/GaN NW-LEDs. In particular, the analysis of the temperature dependence of PL and EL spectra indicates that, although carrier localization phenomena have been identified at low temperature and excitation power, they do not dominate the EL emission properties of the NW-LED.

4.2. Effect of the multi-element nature of the NW-LEDs on the forward I-V characteristics

The I-V characteristics of a forward biased LED contain much useful information about the charge carrier transport dynamics and the recombination mechanisms in the device. Nevertheless, the analysis of the forward I-V characteristics is often tricky and not devoid of unclear points. This is particularly true for III-nitride based devices. In fact, the large band gap of these semiconductors together with a high density of point and extended defects in the material make the generation-recombination model developed by Sah, Noyce and Shockley for silicon p-n junctions^[208] inadequate to describe all the characteristics of the experimental data. In addition, the GaN based LEDs suffer from the difficulty of obtaining a good p-type doping, and consequently the p-type contact is often a not negligible issue. Therefore, further deviations from the expected behaviour may also come from the contact instead of the main p-n junction of the LED^[175]. All these issues are exacerbated in complex devices such as NW-LEDs, for which the three-dimensional nature together with a lack of appropriate characterization tools results in not trivial technological challenges. In addition, the LEDs based on NW ensembles are intrinsically different from the planar LEDs as they are composed of millions of nano-devices contacted in parallel. Although this intrinsic aspect of the NW-LED might play an important role in the transport properties of the devices, it is rarely taken into account^[10,173,174,209]. Indeed, the forward I-V characteristics of NW-LEDs are often barely commented in literature and frequently shown only on linear scale^[46,126,129,158,167].

In this section the I-V characteristics of forward biased NW-LEDs are discussed. In particular, the role of the multi-element nature of these devices is carefully investigated by means of an original model which takes into account the bias dependent peculiarities of a NW ensemble. This novel interpretation of the I-V characteristics provides a deeper understanding of the operation of NW-LEDs.

4.2.1. The limits of the Shockley model

As already introduced in section 1.2, the I-V characteristics of a real LED can usually be described by the Shockley equation

$$I_{LED} = I_S \left\{ \exp \left[\frac{q(V - IR_S)}{\eta k_B T} \right] - 1 \right\} + \frac{(V - IR_S)}{R_P} \quad (4.8)$$

where IR_S defines the voltage drop produced by the series resistance of the parts of the device with Ohmic-like properties, mainly contacts and the neutral region of the semiconductor; its effect is dominant only at high currents. The term on the right-hand side of the equation describes parallel leakage channels with Ohmic-like behaviour. R_P is an empirical parameter which takes into account one or more unknown conduction mechanisms usually responsible for the leakage current at low or negative biases. The value of the ideality factor, η , defines the slope of the I-V characteristics for values higher than the threshold voltage. It varies between 1 and 2 in silicon or germanium p-n junctions^[208], and between 2.5 and 7 in (In,Ga)N/GaN planar LEDs^[210–212]. The origin of $\eta \gg 2$ is commonly attributed to different effects: the formation of rectifying heterojunctions at the contact-semiconductor interface or between two layers with different composition^[175], the poor carrier transport properties of the (In,Ga)N/GaN heterostructure inside the active region^[212], asymmetry of the p-n junction^[213], and the deep-level-assisted tunnelling

4. Investigation of the opto-electronic characteristics of NW-LEDs

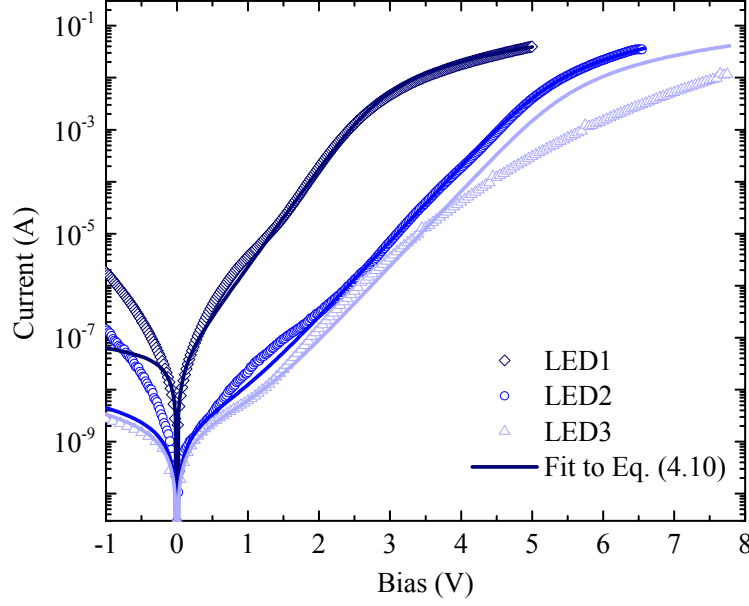


Figure 4.10: Fits (solid lines) of the experimental I-V characteristics of three different NW-LEDs (data points) to the Shockley model [Eq. (4.8)]. The data are plotted on logarithmic scale.

occurring at low biases^[210,211]. Note that these effects are not necessarily unrelated. In NW-based (In,Ga)N/GaN LEDs, the values of the ideality factor extracted from the I-V curves are significantly higher than the ones obtained for the planar counterparts: η as high as 16 and 25 were found^[115,173,174]. As discussed in section 3.2, these high values of η are partially due to a poor p-type contact; employing an ITO top contact we were able to reduce the ideality factor of NW-LEDs down to 9^[68].

In this subsection we aim at verifying whether the I-V characteristics of different NW-LEDs follow the behaviour defined by the Shockley model. Equation (4.8) was numerically solved by means of the Newton-Raphson method; to this end a *MATLAB* program was developed by David van Treck at the PDI^[176]. Three different NW-LEDs with area equal to 0.19 cm² are compared: LED1, LED2, and LED3. The former two are the same devices discussed in section 3.3, they are grown on bare and AlN-buffered Si, respectively. LED3 is also grown on a thin AlN layer and its structure is nominally identical to LED2. Further details about structure and growth parameters of the samples can be found in table A.1, appendix A. All the three devices were processed as discussed in section 3.1 employing an ITO top contact.

The data points in figure 4.10 depict the experimental I-V curves of the three NW-LEDs acquired at room temperature ($T=303$ K), while the solid lines are the fits of the data to equation (4.8). The parameters used to fit the data are listed in table 4.5; they were obtained by minimizing the variance between the experimental and modelled curves. Note that the four fitting parameters (R_p , R_s , I_s , and η) are independent, namely their variation produces discernible effects on different parts of the I-V curve; therefore, they can be uniquely determined. The Shockley model describes quite well the I-V characteristics of LED1 and LED2 in forward bias regime. For negative biases the I-V curves of the NW-LEDs significantly deviate from the theoretical model, a detailed analysis of the current conduction in reverse bias regime is presented in section 4.4. A relatively small discrepancy between experimental data and Shockley model is also present for low positive

4.2. Effect of the multi-element nature of the NW-LEDs on the forward I-V characteristics

biases ($V \lesssim 2$ V). Such a deviation from the expected behaviour has often been observed in planar (In,Ga)N/GaN LEDs^[214–217] and has been explained by means of trap-assisted tunnelling of charge carriers from the valence to the conduction band^[217–219]. Most likely, the same mechanism is responsible for the excess current measured in our NW-LEDs at low biases. The main differences between the I-V curves of LED1 and LED2 (lower R_P and larger I_S in the sample grown on bare Si) are due to the presence of the thin AlN buffer layer and are discussed in section 3.3.

More interesting are the differences between the I-V characteristics of LED2 and LED3. In fact, although the nominal structure of these two samples is identical (both devices are grown on AlN-buffered Si, have the same structure, and are contacted with ITO), LED2 can be described by the Shockley equation, whereas LED3 significantly deviates from the theoretical model. In particular, for biases higher than about 3.5 V the measured current of LED3 is smaller than the expected one.

In order to elucidate this puzzling issue, the actual density of NWs conducting current in the three LEDs was estimated by analysing the EL top-view maps as a function of the applied bias. Figures 4.11 (a)–(c) show the panchromatic EL maps acquired at 6 V from the samples LED1, LED2, and LED3, respectively. The EL spots of the former two samples cover the whole surface of the devices leaving almost no dark areas. The density of EL spots at 6 V is equal to about $2.08 \times 10^8 \text{ cm}^{-2}$ and $1.41 \times 10^8 \text{ cm}^{-2}$ in LED1 and LED2, respectively. This observation suggests that the majority of the nano-LEDs are contacted and emit EL. In contrast, figure 4.11 (c) clearly shows that several dark regions are present in the EL map of LED3, revealing that many nano-LEDs are still not under operation at the applied bias of 6 V. The density of EL spots in LED3 (about $3.1 \times 10^7 \text{ cm}^{-2}$) is roughly 6 times lower than in the other two samples. Analogous EL maps of the three devices were acquired at different applied biases; the density of EL spots extracted from the various images is plotted in figures 4.11 (d) and (e), on semi-logarithmic and linear scale, respectively.

Although in the two LEDs grown on AlN (LED2 and LED3) the first nano-devices turn on at exactly the same bias (≈ 2.5 V), the density of spots is about six times lower in LED3 than in LED2. With increasing bias the number density of spots rises with different rates in the two devices grown on AlN, and eventually saturates for voltages higher than 7 V. The saturation value is more than three times higher in LED2 than in LED3. Note that the number of NWs emitting EL in LED3 increases almost linearly in the entire bias range, as stressed by the linear fit (dotted line) shown in figure 4.11 (e). In other words, the analysis of the EL maps proves that the two devices grown on AlN behave differently; a higher number of nano-LEDs is conducting current in LED2, and they are distributed more uniformly on the sample surface. This observation indicates that a better top contact was formed in LED2 than in LED3. In order to verify whether the different quality of the top contact is actually responsible for the discrepancy observed in the I-V curves of LED2

Table 4.5: List of the parameters obtained from the fits of the I-V characteristics of the three different devices shown in figure 4.10 to equation (4.8).

Sample	Substrate	R_P (M Ω)	R_S (Ω)	I_S (A)	η
LED1	Si	30	45	3×10^{-8}	8.8
LED2	AlN/Si	240	28	3×10^{-10}	11.4
LED3	AlN/Si	310	45	1.1×10^{-10}	11.5

4. Investigation of the opto-electronic characteristics of NW-LEDs

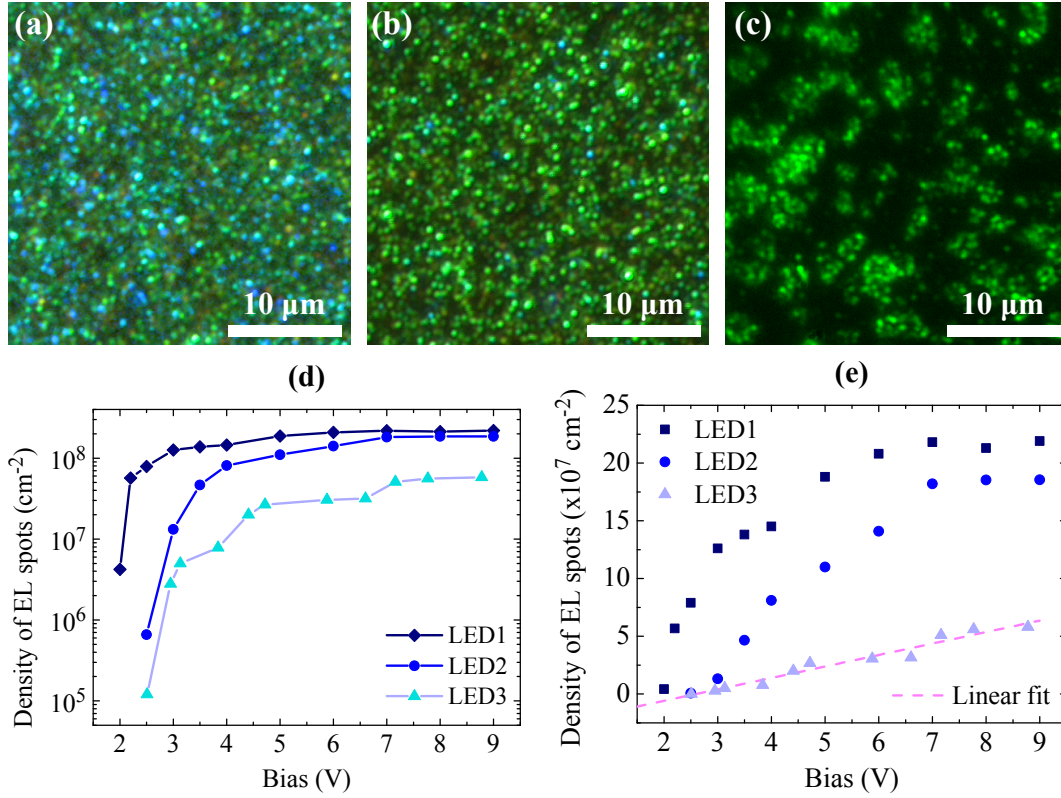


Figure 4.11: Panchromatic false-colour top-view EL maps of (a) LED1, (b) LED2, and (c) LED3 acquired under an applied bias of 6 V through an optical microscope. (d)–(e) Dependence of the number density of EL spots on the forward bias for the three different NW-LEDs, plotted on (d) semi-logarithmic and (e) linear scale.

and LED3 at high biases, an original model was developed.

4.2.2. Interpretation of the I-V curves

The correlation between density of nano-LEDs in operation and shape of the I-V characteristic was already introduced in section 3.2 by means of a “*Gedankenexperiment*”. Now we discuss this topic in more details.

Differently from a planar LED where the opto-electronic properties are roughly uniform over the device surface, the opto-electronic characteristics of a NW-based LED might strongly fluctuate on the local scale. In fact, a NW-LED has to be considered as an ensemble of millions of nano-devices contacted together (in a rough approximation they may be considered as connected in parallel). Size inhomogeneities of the NWs in the ensemble can cause variation of both In content and thickness of the QWs, different doping levels, and thus fluctuations in the resistance of the various NWs^[131]. Moreover, inhomogeneities in diameter and length of the nano structures can vary the contact area with the ITO thus producing various contact resistances (see section 3.2.1). In addition to these features intrinsic to NW ensembles obtained by means of self-induced processes, also the processing of the device might add further irregularities. For example, a not perfect etching of the resist employed to planarize the sample might result in residual Si_xO_y surrounding the tips of some of the NWs. The presence of a thin shell of insulating material can affect the current injection into the nano-LEDs, impeding it or

4.2. Effect of the multi-element nature of the NW-LEDs on the forward I-V characteristics

promoting non-Ohmic conduction mechanisms, which would cause an increase of the ideality factor of the device^[175,209]. Taking into account all the mentioned effects, it is easy to understand that the opto-electronic properties of the individual nano-devices in the ensemble can significantly fluctuate. In the formalism of the Shockley model, each nano-LED may have different I_S , R_S , R_P , and η . Therefore, the I-V characteristics of a NW-LED can only provide the mean value of these parameters averaged over the entire ensemble of nano-LEDs.

In a NW-LED with inhomogeneous electrical properties, the electrons preferentially flow through the paths with lower resistance, namely the nano-LEDs with small R_S and η . Once the applied voltage is high enough, the current might be injected also into the more resistive nano-devices, characterized by high R_S and η . Due to this effect, the average values of the ideality factor of the entire ensemble would increase with bias. In contrast, if the majority of the NWs had similar electrical properties, the mean values of the parameters would remain roughly constant and the nano-LEDs in the ensemble would turn on together. In the latter case the I-V characteristics of the NW-LED could be fitted by equation (4.8), which assumes constant values of the parameters. The proposed argument could explain why the Shockley equation can model the I-V characteristics of LED1 and LED2 but fails to fit the data related to LED3, which has less uniform electrical properties than the other two devices.

In order to verify this idea, we fitted the experimental data by means of a modified version of the Shockley model. In particular, we assumed that the mean value of the ideality factor linearly increases with bias: $\langle \eta \rangle = \eta_0 + s V$, where η_0 represents the initial ideality factor at low bias, when only few NWs are conducting, while the fitting parameter s defines the slope of the line. The simple linear approximation employed to describe the voltage dependence of the ideality factor can be seen as a Taylor series expansion of η_V stopped at the first order. Hence, the Shockley model becomes

$$I_{LED} = I_S \left\{ \exp \left[\frac{q(V - IR_S)}{(\eta_0 + s V) k_B T} \right] - 1 \right\} + \frac{(V - IR_S)}{R_P} \quad (4.9)$$

The solid lines in figure 4.12 represent the fits of the experimental data to equation (4.9); the obtained fitting parameters are listed in table 4.6. The modified Shockley model describes very well the I-V characteristics in forward bias of all the three investigated LEDs, thus corroborating the validity of the assumption made as well as of our model. From the comparison of tables 4.5 and 4.6, we note that the parameters R_P , R_S , and I_S remain almost the same when the data are fitted to equation (4.8) or (4.9). The obtained values of the series resistance are similar to the ones reported in literature for (In,Ga)N/GaN NW-LEDs^[171,172]. It is worth noting that, since the I-V characteristic *in case of LED3* does

Table 4.6: List of the parameters obtained from the fits of the I-V characteristics of the three different devices shown in figure 4.12 to equation (4.9). In the fifth column η_0 is the initial value of the ideality factor (for $V = 0$ V) whereas η_{max} represents its maximum value in the investigated bias range.

Sample	R_P (M Ω)	R_S (Ω)	I_S (A)	$\eta_0 - \eta_{max}$	s (V ⁻¹)
LED1	30	40	2.5×10^{-8}	8–9.3	0.26
LED2	240	22	2.4×10^{-10}	10.5–11.7	0.18
LED3	310	42	7.5×10^{-11}	9.2–15.5	0.72

4. Investigation of the opto-electronic characteristics of NW-LEDs

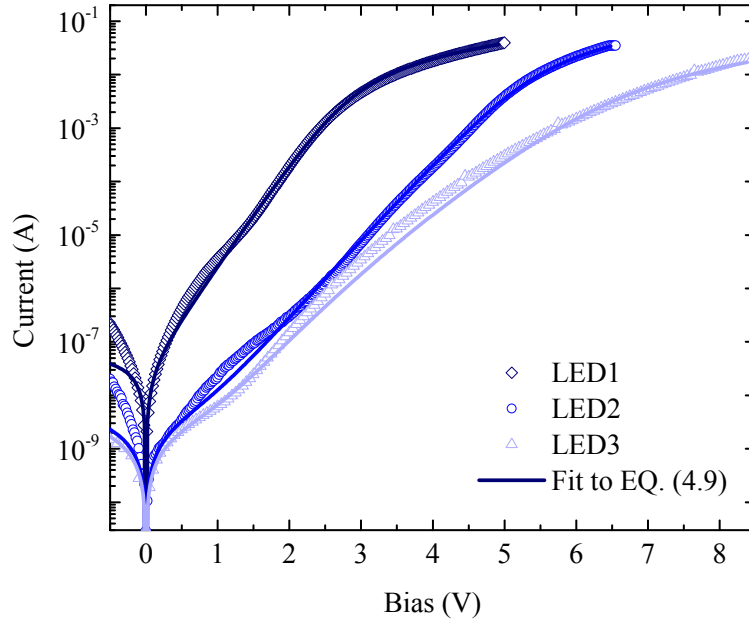


Figure 4.12: Fits (solid lines) of the experimental I-V characteristics of three different NW-LEDs (data points, as in figure 4.10) to equation (4.9). The data are plotted on logarithmic scale.

not exhibit the typical linear behaviour at high biases, the value of R_s obtained from the fit is just a rough estimation. As expected, the ideality factor of the devices LED1 and LED2 varies little in the considered bias range; this results in small values of the parameter s . The small variation of η is likely due to the turn on of nano-LEDs with ideality factors slightly higher than the average one. Interestingly, the values of η reported in table 4.5 for LED1 and LED2 roughly coincide with the mean value of the ideality factors obtained using the modified Shockley model [$\eta \approx (\eta_0 + \eta_{max})/2$]. Note that the values of η obtained in our NW-LEDs are lower than the ones previously reported for similar devices^[173,174]. As already mentioned, ideality factors much higher than 2 have also been reported for GaN-based planar LEDs^[175,210–213].

The ideality factor used to fit the I-V curve of LED3 exhibits a larger variation in the considered bias range, also visible from the higher value of s . As already explained, the large increase of the apparent ideality factor in LED3 is likely due to the turn-on of nano-devices with not optimal contact interface with the ITO, probably because of the presence of thin a Si_xO_y shell on the tip of NWs. Such nano-devices would be characterized by high ideality factors, thus causing an increase of the average value of η .

In conclusion, the proposed model provides a deeper understanding of the operation principles of LEDs based on NW ensembles. This novel interpretation of the forward bias I-V characteristics might be very useful to correctly analyse the electrical measurements of NW-LEDs, particularly in case of devices with very pronounced inhomogeneity of the electrical properties. It is important to underline that the basic considerations discussed in this section remain valid also for different types of electrical devices with multi-element nature, regardless of the material system employed.

4.3. Deep level transient spectroscopy on NW-LEDs

Shallow traps and deep level states inside the band gap determine often the charge carrier transport properties of many wide band gap semiconductors and play also an important role in the opto-electronic characteristics acting, for instance, as radiative or non-radiative recombination centres^[197]. An effective technique capable of probing the properties of electrically active states in the band gap of these materials is deep level transient spectroscopy (DLTS). We applied for the first time this technique to (In,Ga)N/GaN LEDs based on an ensemble of NWs to achieve a deeper understanding of electrically active defects in these structures. This study was presented at the SPIE Photonics West 2015 conference held in San Francisco (USA) and can be found in ref.^[220].

In this section capacitance-voltage (C-V) and DLTS measurements carried out on the same NW-LED are discussed, when necessary the physical basics of the techniques are briefly introduced. From the analysis of the DLTS signal we deduce the properties of the main deep level traps present in the NW-LEDs, and the possible nature of these traps is further discussed.

4.3.1. Capacitance-voltage measurements

Preliminary C-V measurements were carried out on a complete NW-LED sample with the aim to extract some useful parameters needed as basis for more advanced studies presented in the next sections. In particular, the net charge concentration and the average electric field in the depletion region of the p-i-n junction were extrapolated from the C-V measurements. The former is useful to estimate the density of traps probed by means of DLTS measurements (see section 4.3.4); whereas the latter will be employed to evaluate the leakage current in reverse bias regime (see section 4.4).

The C-V measurements were performed in the dark at room temperature ($T = 303$ K) by means of a capacitance meter, model SULA DDS-12. The C-V data were acquired at 1 MHz for voltages ranging between -8 and +3 V; the raw data are plotted as blue left-pointing triangles in figure 4.13(a). We analysed the C-V measurements taking advantage of the equations derived for planar capacitors^[221]. Under particular conditions, these equations are valid also for a p-n junction based on an ensemble of NWs. Specifically, we assume that only the very top of the NW tips is contacted, so that the single NW can be seen as a nano-planar capacitor rather than a cylindrical one. As discussed in section 3.1.1, the employed planarization process enables to contact only the last few tens of nanometres of the NW tips. In addition, we suppose that the NWs of the ensemble are connected in parallel, so that the equivalent capacitance of the ensemble is equal to the sum of the capacitances of the single NWs. Under these conditions, the relation between capacitance (C) and width of the depletion region (W) is given by

$$W = \frac{\epsilon_r \epsilon_0 A}{C} \quad (4.10)$$

where ϵ_r is the relative permittivity of GaN (equal to 5.35 at high frequency), ϵ_0 is the vacuum permittivity and A is the area of the capacitor, which is assumed to coincide with the area of the device (about 0.19 mm^2). In fact, the total contact area, namely the area of the top facet plus the one of the exposed sidewalls, coincides roughly with the surface of the device; in other words, the empty area between the NWs approximately equals the area of the exposed sidewalls. The dependence of the depletion region width on applied bias is depicted by the magenta right-pointing triangles in figure 4.13(a). In

4. Investigation of the opto-electronic characteristics of NW-LEDs

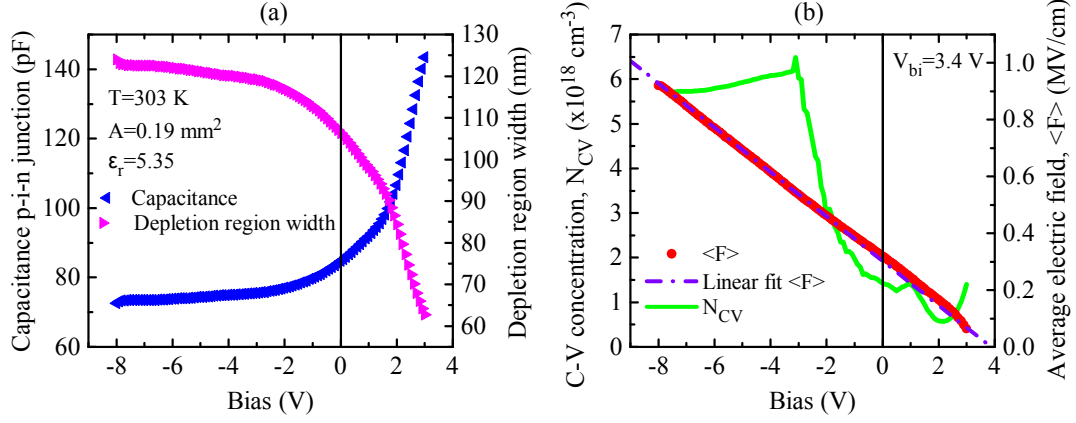


Figure 4.13: (a) C-V data acquired at $T = 303\text{ K}$ (blue left-pointing triangles) and corresponding width of the depletion region (magenta right-pointing triangles). (b) Net charge density (N_{CV} , green solid line) and average electric field ($\langle F \rangle$ red points) in the active region extrapolated by means of C-V measurements. The violet dashed-dotted line depicts the linear interpolation of the data used to approximate the average electric field in the depletion region.

the bias range employed for DLTS measurements, *i. e.* $[-2; +1]\text{ V}$, the width of the depletion region shrinks from 117 to 97 nm, see figure 4.13(a).

The C-V measurements provide also a direct estimation of the net charge stored in the depletion region. The C-V carrier concentration (N_{CV}) is given by the equation

$$N_{CV} = (N_D - N_A) = \frac{C^3}{q\epsilon_r\epsilon_0 A^3} \frac{dV}{d(C/A)}. \quad (4.11)$$

In equation (4.11) N_D and N_A represent the density of donors and acceptors in the depletion region, respectively; q is the elementary charge, and $dV/d(C/A)$ is the derivative of the voltage with respect to the capacitance per unit area. The net charge concentration estimated by means of equation (4.11) is depicted by the green solid line in figure 4.13(b). It will be used to estimate the density of traps probed by the DLTS technique (see section 4.3.4).

The C-V measurements are useful also to establish a relation between the applied voltage, V , and the average electric field, $\langle F \rangle$, present in the depletion region. In fact, the two quantities are linked by the equation

$$\langle F \rangle = \frac{(V_{bi} - V)}{W} \quad (4.12)$$

where V_{bi} is the built-in potential of the GaN p-i-n junction, assumed to be equal to 3.4 V. As is clear from the linear interpolation in figure 4.13(b) (violet dashed-dotted line), a good agreement between the experimental data (red points) and the linear behaviour predicted by equation (4.12) is found. The relation between bias and electric field extracted from the linear interpolation of the data (namely, $F = a + bV$ with $a = 302454\text{ Vcm}^{-1}$ and $b = -78289\text{ cm}^{-1}$) will be used as approximation of the average electric field in the analysis of the I-V curves carried out in section 4.4.3.

4.3.2. DLTS basics

The DLTS technique was developed by David Vern Lang in the seventies of the last century as a tool for studying electrically active defects in semiconductors^[222]. It can provide fundamental parameters of the traps, such as energy and capture cross-section, and can estimate their concentration in the material. This technique measures the capacitance transients occurring in the space charge (depletion) region of a p-n or Schottky junction when the charge carriers trapped by deep levels are released by means of thermally stimulated emission. In practice the junction is reverse-biased by applying a quiescent negative voltage, V_R , as depicted in figure 4.14(a) for a n^+p junction under equilibrium condition. The steady-state polarization is disturbed by a filling voltage pulse, $V_F > V_R$ (usually positive), applied for an interval of time Δt_F . The voltage pulse causes a narrowing of the depletion region, thus allowing free carriers from the semiconductor neutral region to populate (be trapped by) the defects, see figure 4.14(b). After the pulse, when the bias returns to the quiescent value V_R , the defects start to emit trapped carriers due to thermal emission processes, see figure 4.14(c). The emission of charge carriers from the traps in the depletion region causes a variation of both junction capacitance and width of the space charge region; the process lasts until the equilibrium condition is reached again. Traps of minority carriers produce a capacitance transient with positive initial peak which decreases with time; whereas traps of majority carriers give rise to a transient with negative initial peak and upward evolution. It is important to note that the traps probed by the DLTS technique are only those located inside the depletion region of the junction; deep level traps located elsewhere in the device cannot be detected with this method.

The temperature dependence of the electron emission rate of a trap state with thermal activation energy E_a measured from the conduction band edge (E_{CB}) can be written as

$$e_n = \frac{\sigma \langle v_{th} \rangle N_C}{g} \exp \left(\frac{E_a - E_{CB}}{k_B T} \right) = T^2 \sigma \gamma \exp \left(\frac{E_a - E_{CB}}{k_B T} \right) \quad (4.13)$$

$$\text{with } \gamma = \left(\frac{\langle v_{th} \rangle}{T^{1/2}} \right) \left(\frac{N_C}{T^{3/2}} \right) = \frac{2\sqrt{3}(2\pi)^{3/2} k_B^2 m_e^*}{h^3} \quad (4.14)$$

where σ is the capture cross-section of the trap, $\langle v_{th} \rangle$ is the mean thermal velocity of the carriers, N_C is the effective density of states of the trap level band, g is the degeneracy of the trap level (equal to 2 for electrons and to 6 for holes in GaN), k_B is the Boltzmann constant, and T is the temperature. The parameter γ takes into account the temperature dependence of the thermal velocity, *i.e.* $\langle v_{th} \rangle = (3k_B T / m_e^*)^{1/2}$, and of the effective density of states, *i.e.* $N_C = [g(2\pi)^{3/2} (k_B T)^{3/2} m_e^{*3/2}] / h^3$; in the expression of γ , h is the Planck constant, whereas m_e^* is the effective electron mass. Assuming $m_e^* = 0.2m_e$ ^[223], we obtained $\gamma \approx 6.513 \times 10^{24} \text{ cm}^{-2} \text{ K}^{-2} \text{ s}^{-1}$. A similar equation holds also for hole emission from trap states located above the valence band edge (E_{VB}), with all quantities referring to holes instead of electrons. The inverse of the emission rate defines the time constant of the capacitance transient, $\tau_n = 1/e_n$; it varies exponentially with the temperature. Equation (4.13) can also be written as

$$\ln \left(\frac{T^2}{e_n} \right) = \ln (\tau_n T^2) = \frac{E_{CB} - E_a}{k_B T} - \ln (\sigma \gamma) \quad (4.15)$$

This formula has the form of the Arrhenius equation, thus the energy of the trap ($E_t \approx$

4. Investigation of the opto-electronic characteristics of NW-LEDs

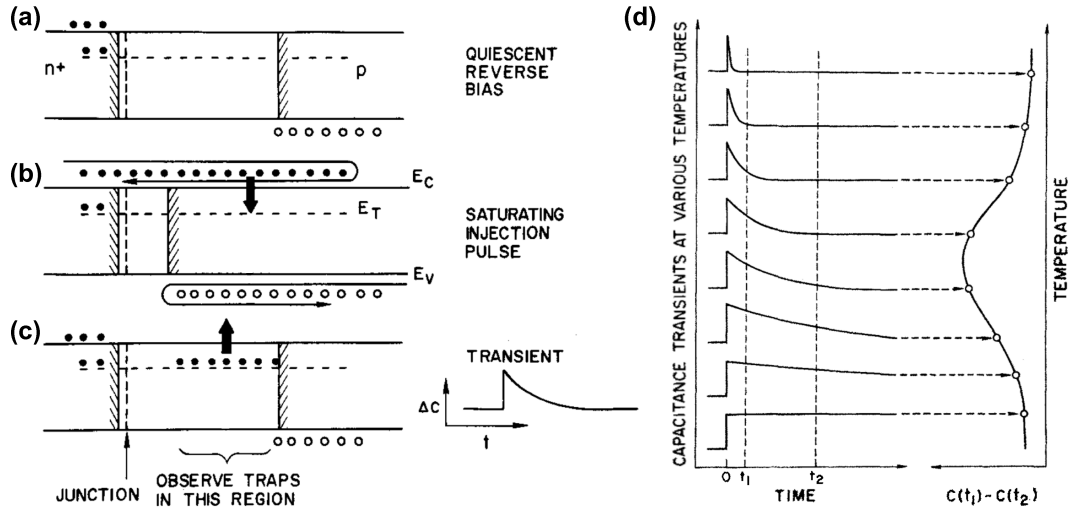


Figure 4.14: Illustration of DLTS basis. (a–c) Energy-*vs.*-position diagrams (with band banding omitted for simplicity) show the n^+p junction depletion region (edge denoted by shaded lines) as well as the trap occupation (a) before, (b) during, and (c) after the filling pulse. (d) The left-hand side shows capacitance transients at various temperatures, while the right-hand side depicts the corresponding DLTS signal obtained using a double boxcar to measure the capacitance difference at time t_1 and t_2 as a function of the temperature. Figure reproduced from Ref. [222].

$E_{CB} - E_a$) and its apparent capture cross-section (σ), *i.e.* the signature of the trap, can be extrapolated using an Arrhenius plot of $\ln(T^2/e_n)$ *vs.* $1/k_B T$. The DLTS technique provides a direct relation between the time constant of the capacitance transient and the temperature. In practice, the DLTS apparatus makes use of a dual-gated signal averager, also known as double boxcar, to measure the capacitance difference of the sample at two time instants (t_1 and t_2). Figure 4.14(d) illustrates the operation of this device; the left-hand side shows capacitance transients at various temperatures, while the right-hand side depicts the corresponding DLTS signal obtained using a double boxcar. The DLTS signal has a peak only when the time constant of the capacitance transient is equal to the chosen time interval ($t_2 - t_1$). Repeating the measurement for different time intervals, one obtains several peaks, also known as DLTS spectra, which provide a direct relation between the time constant of the capacitance transients (τ_n) and the temperature.

The ratio between the difference in capacitance sampled at the time instants t_1 and t_2 and the initial capacitance of the system at the time t_0 when the filling pulse ends defines the normalized DLTS signal: $S = [C(t_1) - C(t_2)] / C(t_0)$. The reciprocal of the time interval between two subsequent samplings is called emission rate window: $e_n^* = 1/(t_2 - t_1)$.

4.3.3. Analysis of the DLTS measurements

The DLTS measurements were performed in a dark ambient by means of a cold finger cryostat filled with liquid nitrogen. The DLTS signal was acquired through a capacitance meter, model SULA DDS-12, working at 1 MHz. A series of measurements was performed varying the emission rate window (e_n^*) from 2.4 to 2381 s^{-1} , while the sample temperature was swept from 83 up to 360 K. A quiescent reverse bias of -2 V was employed; to ensure an adequate filling of the traps, filling pulses with amplitude of +1 V

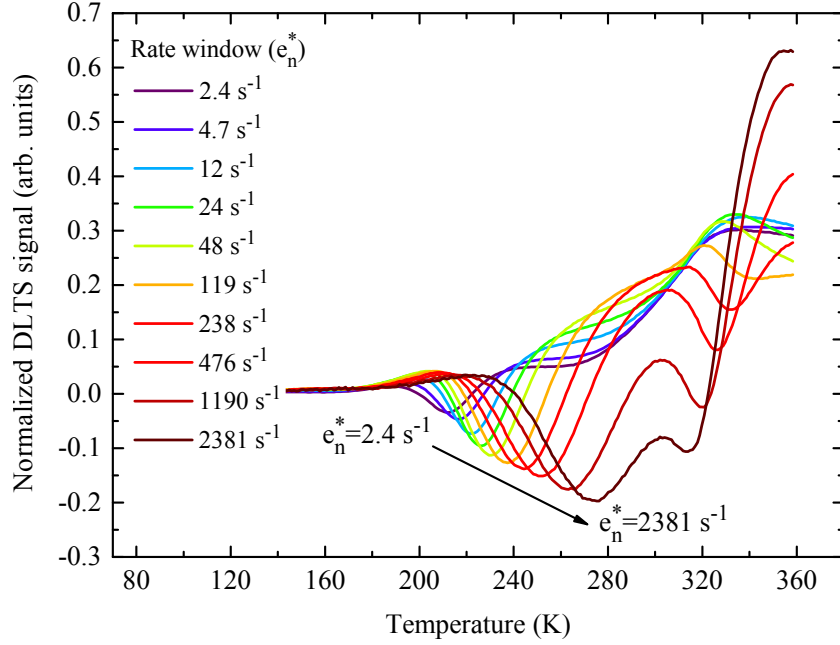


Figure 4.15: DLTS spectra measured with a quiescent bias of -2 V, filling pulses of +1 V and width of 100 ms for ten different rate windows ranging from 2.4 to 2381 s^{-1} . The black arrow highlights the evolution of the main negative peak.

and duration of 100 ms were chosen.

Figure 4.15 shows the normalized DLTS signal as a function of the temperature for ten different rate windows. For temperatures lower than 180 K the capacitance of the system does not change, indicating that in this temperature range the traps are not active, and therefore do not emit charge carriers. For temperatures higher than about 215 K negative peaks appear. The position of these peaks increases for increasing rate window; more specifically the peak position varies from 215 to 275 K when the rate window increases from 2.4 to 2381 s^{-1} . As discussed in subsection 4.3.2, this behaviour is typical for thermally assisted emission of charge carriers from trap levels. In fact, in this case higher temperatures produce higher emission rates, which correspond to larger rate windows. The negative sign of these peaks indicates that they are related to traps of majority carriers, *i. e.* electrons in our system^[222].

For temperatures higher than 260 K several peaks of different nature appear; some of them are positive and others negative. It is difficult to distinguish the various components and identify the peculiar evolution of the peaks simply by looking at the graph of figure 4.15; for this reason a fit of the DLTS data is required. We decided to fit the DLTS curves by means of four different Gaussian peaks. The best fit of the data is achieved when two negative and two positive peaks are employed. Figures 4.16(a) and (b) show the fits of the data corresponding to emission rate windows equal to 2.4 and to 48 s^{-1} , respectively; similar analysis was carried out for all the employed rate windows. The solid lines in the graphs represent the raw DLTS data, while the dashed ones are the cumulative fits; we note that the cumulative fits perfectly overlap the raw data ($R^2 > 0.999$) for all the considered rate windows. The single peaks are depicted by the dotted lines and named E_1 , E_2 , P_3 and P_4 , respectively. The negative peak E_1 corresponds to the electron trap level already identified in figure 4.15. The fits of the data reveal the presence of a second negative peak (E_2) which appears for temperatures close to 300 K. In the raw

4. Investigation of the opto-electronic characteristics of NW-LEDs

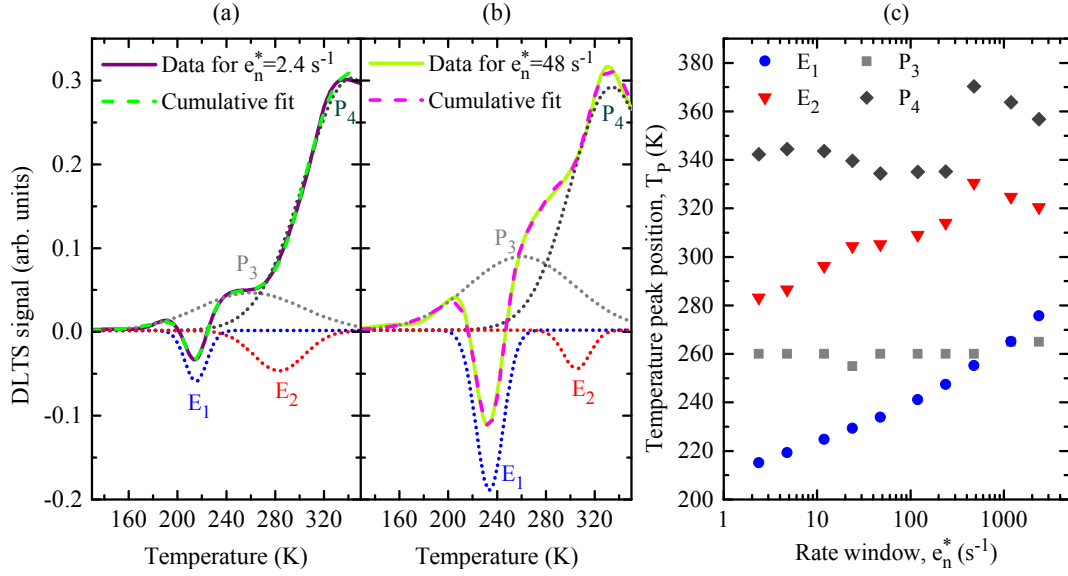


Figure 4.16: (a)–(b) DLTS spectra (solid lines) acquired with rate windows of (a) 2.4 s^{-1} and (b) 48 s^{-1} . The data are fitted by means of four Gaussian peaks, depicted by the dotted lines and named E_1 , E_2 , P_3 and P_4 , respectively. The dashed curves are the cumulative fits, *i. e.* the algebraic sum of the four single peaks. (c) The graph summarizes the temperature peak position (T_p) extracted from the fits as a function of the rate windows employed; the four series of points correspond to the four different peaks used for the fits.

DLTS data, peak E_2 is hidden by the appearance of one or more positive peaks at high temperatures ($T \gtrsim 260 \text{ K}$). These peaks might be caused either by traps of minority carriers (holes) or by leakage currents that disturb the capacitance measurements. Indeed, the capacitance of the depletion region can be accurately determined only if the diode under analysis exhibits low leakage current, *i. e.* its parallel resistance is high.

The presence of artefacts in the DLTS spectra can be discovered by looking at the evolution of the temperature peak position (T_p) as a function of the rate window. This quantity is plotted in figure 4.16(c) for all the four considered peaks. While the position of the negative peak E_1 increases monotonically with the rate window, as expected for charge emission from thermally activated traps, both the positive peaks P_3 and P_4 do not follow this characteristic behaviour. On the contrary, their positions seem to remain rather constant in a large range of rate windows, suggesting that these two features are artefacts due to disturbances of the capacitance measurements. The second negative peak E_2 shifts also towards higher temperature as the rate window increases, more specifically the peak position varies from 283 to 314 K when the rate window increases from 2.4 to 238 s^{-1} . Thus, in this range peak E_2 follows the behaviour typical for a thermally activated charge emitter. For higher emission rates peak E_2 suddenly reverses its trend, afterwards evolving in a way similar to peak P_4 . This fact would suggest that the real behaviour of the trap E_2 is masked by the presence of peak P_4 , which is likely related to leakage currents.

4.3.4. The signature of the main deep level traps in NW-LEDs

In order to extrapolate the characteristic parameters of the traps from the DLTS data we make use of the Arrhenius plot $\ln(T^2/e_n)$ *vs.* $1/k_B T$. Figure 4.17 shows the plot obtained

for the traps E_1 and E_2 ; the ratio (T^2/e_n) was calculated using the information extracted from the fits and plotted in figure 4.16(c). From the slope of the linear interpolation of the data we obtained the energy of the traps measured from the conduction band edge, $E_t \approx (E_{CB} - E_a)$, while from the intercept the apparent cross section of the traps (σ) was estimated. For trap E_1 we obtained $E_{t1} = (570 \pm 20)$ meV and $\sigma_{t1} = (2 \pm 1) \times 10^{-16}$ cm²; whereas for trap E_2 the extracted energy and cross section are $E_{t2} = (840 \pm 30)$ meV and $\sigma_{t2} = (5 \pm 3) \times 10^{-15}$ cm², respectively. Trap E_1 is depicted in figure 4.17 by the blue circles while trap E_2 by the red triangles. It is worth mentioning that DLTS measurements based on thermal activation of traps can only probe band gap states located in the vicinity of the conduction (valence) band edge. Conventional DLTS techniques can excite charge carriers from band gap states located within about 1 eV from the conduction band minimum (valence band maximum). In fact, trap levels located deeper in the band gap would require unrealistically high temperatures to be activated. This means that other deep levels, beyond those identified, might be present in the sample. Such mid-gap states can be detected by means of more advanced deep level optical spectroscopy (DLOS) measurements not performed in this work.

To achieve a better understanding of the physical origin of the traps E_1 and E_2 , we compared the obtained DLTS signatures with the ones reported in literature for deep levels in GaN based devices. We found that the trap level E_1 may correspond to the most prominent electron trap often revealed by DLTS measurements in n-type GaN layers grown by different techniques. Although several energy values are reported in literature for this level (ranging from 520 to 600 meV)^[224–230], its origin has often been attributed to nitrogen antisite defects (N_{Ga}). This conclusion is based on tight binding calculations performed by Jenkins and Dow for several point defects in III-N semiconductors^[231]; for a nitrogen atom substituting on a Ga site they determined an energy of the associated deep level equal to 540 meV. The DLTS signature of the trap E_1 is in good agreement with the ones reported in literature; for instance, the cyan symbols shown in figure 4.17 refer to the trap level found by Hierro *et. al*^[227] ($E \approx 590$ meV and $\sigma \approx 2 \times 10^{-15}$ cm²). Trap E_1 exhibits also a relatively good agreement with the signature of a different kind of defect recently reported by Jahangir *et. al*^[172] and depicted by the orange symbols in figure 4.17 ($E \approx 607$ meV and $\sigma \approx 3.3 \times 10^{-15}$ cm²). This trap level was found in GaN n⁺-p junctions obtained from NW ensembles with different densities. Interestingly, the trap concentration seemed to increase with the density of NWs, suggesting that this deep level could originate from the coalescence of multiple NWs. Hence, this trap state has been attributed to the formation of chains of boundary dislocations (BDs) at the sidewalls of coalescing NWs^[231].

Both the deep levels reported by Hierro and Jahangir may be likely present in the investigated NW-LED. In fact, the formation of Ga vacancies (V_{Ga}) as well as nitrogen antisite defects (N_{Ga}) could be promoted by the highly N-rich ambient employed for the growth of NWs, while dislocations at the boundary of coalesced NWs are certainly present in the studied sample^[100,159,233]. Hence, it seems to be rather plausible that the trap level E_1 originates from the coexistence of these two types of defects in the NW-LED, namely N_{Ga} and chains of BDs. The former are likely located in the core of the NWs, whereas the latter form on the sidewalls. Both the N_{Ga} defects in the bulk and chains of BDs on the sidewalls of the NWs can act as non-radiative recombination centres, thus affecting the optical^[100,172] and the transport properties^[228] of the NW-LEDs.

The signature of trap level E_2 is in very good agreement with the ones already found in GaN planar layers grown by MBE ($E_t \approx 890$ meV^[230] and $E_t \approx 910$ meV^[227]), by

4. Investigation of the opto-electronic characteristics of NW-LEDs

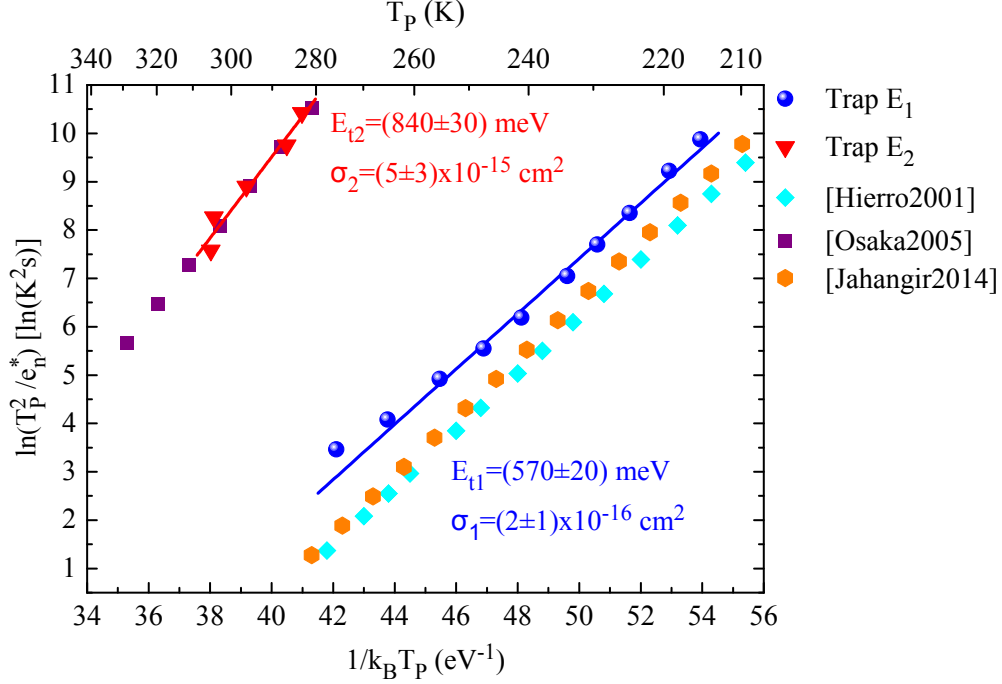


Figure 4.17: Arrhenius plot for the deep levels E_1 and E_2 [220]. T_p is the temperature at which the DLTS peaks occur, while e_n^* is the corresponding emission rate window. The slope and the intercept of the linear interpolations of the data (solid lines) yield the energy and the cross section of the traps. For comparison, we plot also the signatures of three traps found by Hierro *et al.* [227], Jahangir *et al.* [172], and by Osaka *et al.* [232], see the cyan, orange and purple symbols.

metalorganic vapor phase epitaxy ($E_t \approx 800$ meV [229]), and also by hydride vapor-phase epitaxy ($E_t \approx 808$ meV [232]). As an example, in figure 4.17 we report the signature of the trap found by Osaka *et al.* [232] (purple squares). This trap level was found to be related to interacting point defects arranged along lines, which are presumed to be threading dislocations (TDs) [227, 229]. Also Peta *et al.* [230] ascribed this trap level to defect complexes located along dislocation sites. Our NW-LEDs are free of extended defects such as TDs; nevertheless, dangling bonds similar to those present in threading dislocations might exist on the surface of the NWs. Therefore, we tentatively assign the trap level E_2 to defect complexes (likely dangling bonds) located on the sidewalls of the NWs.

Next, we aim at estimating the concentration of these traps. Assuming that the defects are uniformly distributed inside the volume of the depletion region, the concentration of traps can be extrapolated by means of the formula [222]

$$N_t = 2 (N_D - N_A) \frac{\Delta C}{C} . \quad (4.16)$$

In this equation, $(N_D - N_A)$ is the net charge density in the active region, which can be extrapolated by means of capacitance-voltage measurements (see section 4.3.1); for the reverse bias $V = -2$ V, that corresponds to the quiescent voltage used for the DLTS measurements, $N_{CV} \approx 3 \times 10^{18} \text{ cm}^{-3}$ was found. The ratio $\Delta C/C$ corresponds to the normalized DLTS signal (S) defined in section 4.3.2. The obtained trap concentrations are $N_{t1} \approx 5 \times 10^{16} \text{ cm}^{-3}$ and $N_{t2} \approx 1 \times 10^{16} \text{ cm}^{-3}$ for trap E_1 and E_2 , respectively. The trap concentrations obtained in this work for NW-LEDs are between one and two orders of

4.4. A physical model for the reverse bias regime

magnitude higher than the ones reported in literature for similar defects observed in GaN planar layers^[226] and in (In,Ga)N/GaN blue LEDs^[234] grown by MBE.

Such high values of the defect density might be partially due to the coexistence in NW-LEDs of different defects with very similar signatures, see for instance the previous discussion on trap E_1 . In fact, in this case the estimated concentration would coincide with the sum of the densities of the various trap states with similar signatures. However, this explanation cannot justify by itself a difference in defect concentration of two orders of magnitude between similar (In,Ga)N/GaN heterostructures based on planar layers and on NWs. The cause should rather be sought in the particular growth conditions used for the formation of NWs, in their three-dimensional shape, and in the less mature technology of the NW-LEDs compared to that achieved for planar LEDs in about 30 years of development and optimization.

In conclusion, the main deep states observed in NW-LEDs seem to originate from native point defects (N_{Ga}) present in the bulk material, from chains of boundary dislocations (BDs) at the edge of coalescing NWs, and from dangling bonds present on the free sidewalls. In the next generation of NW-LEDs, the detrimental effect of these trap states could be suppressed by optimizing the growth conditions and the structure of the device. For example, less N-rich conditions and higher temperatures than the ones commonly used for the growth of the (In,Ga)N/GaN active region might reduce the density of N_{Ga} defects. In addition, an improved alignment of the NWs and high growth temperatures can reduce the coalescence degree^[159], thus suppressing the formation of BDs. Moreover, the dangling bonds on the free sidewalls of the NWs could be passivated by the deposition of a semi-amorphous shell. Indeed, it was recently demonstrated that the deposition of (Al,Ga)N^[170] or Al_2O_3 ^[179] shells on the sidewalls can improve significantly the opto-electronic performance of the NW-LEDs.

4.4. A physical model for the reverse bias regime

The I-V characteristics of a rectifying diode in the reverse bias regime provide often much useful information about the charge carrier transport dynamics in the semiconductor. In fact, when a p-n junction is inversely polarized its depletion region widens, thus making the semiconductor highly resistive, similarly to a semi-insulating material. At the same time, the electric field strength inside the space charge region rises up to very high levels, thus promoting the activation of trap-assisted conduction mechanisms. The field-enhanced charge carrier transport mediated by traps should be significant in those semiconductors with high density of defects and wide band gap, for which the drift-diffusion and the Sah-Noyce-Shockley generation-recombination current is negligible. In fact, the I-V characteristics of reverse biased LEDs based on (In,Ga)N/GaN planar heterostructures significantly deviate from the ideal behaviour described by the Shockley model^[175,235]. The occurrence of a sizeable reverse leakage current is even more pronounced in NW-based LEDs^[46,125,173,236]. Despite the important implications that a high leakage current could have on the performance of the NW-LEDs, the reverse current is rarely analysed^[173], and often the part of the I-V characteristic related to negative biases is completely omitted^[10,167]. Also for this reason, the physical origin of the high reverse leakage current in NW-LEDs is still unclear.

In this section a comprehensive physical model able to describe quantitatively the current conduction properties of a reverse biased NW-LED as a function of the temperature is developed. A study on the temperature dependence of the reverse current is presented;

4. Investigation of the opto-electronic characteristics of NW-LEDs

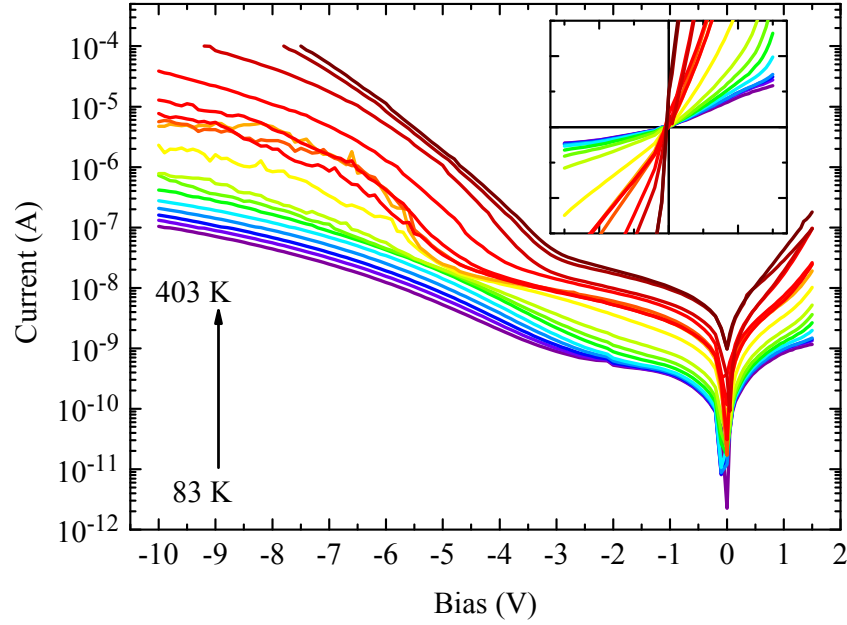


Figure 4.18: I-V characteristics in semi-logarithmic scale of the analysed NW-LED acquired under reverse bias regime for temperatures ranging from 83 to 403 K with increments of 20 K. The inset reproduces the same data in linear scale in the bias range [-1.5;+1.5] V.

it helps to reveal the nature of the involved conduction mechanisms. The robustness of the assumptions made and the coherence of the employed parameters are discussed. This model provides an enhanced insight into the causes of the sizeable leakage current observed in NW-LEDs.

4.4.1. Experimental data and introduction to conduction mechanisms

Figure 4.18 shows the temperature-dependent current-voltage (I-V-T) characteristics in semi-logarithmic scale acquired for temperatures ranging from 83 to 403 K. The data were acquired in a dark ambient by means of a cold finger cryostat filled with liquid nitrogen and a semiconductor parameter analyser, model HP 4155.

The curves exhibit a peculiar hump-like shape. For small reverse voltages (approximately between 0 and -3 V) a nearly Ohmic-like behaviour is observed, this trend is better recognizable on linear scale in the inset of figure 4.18. On the contrary, for higher reverse biases the evolution of the current with the applied bias is certainly not Ohmic. In particular, for temperatures higher than 243 K (yellow curve in figure 4.18), the current increases much faster as the reverse voltage is swept from -4 to -6 V, thus suggesting the activation of a further conduction process which is not present in the low temperature range. Therefore, the I-V-T curves suggest the presence of at least two different current conduction channels, one of which is thermally activated.

In the following part the relevant conduction mechanisms are introduced, as basis for later fitting of the experimental data. To further elucidate the nature of the involved current conduction processes, we have to make some assumptions. First, the contribution of the drift-diffusion and Sah-Noyce-Shockley generation-recombination process to the reverse current is negligible; this is plausible in wide band gap semiconductors such as GaN^[20]. Second, the ITO/p-GaN heterojunction at the top-contact does not limit the

4.4. A physical model for the reverse bias regime

current injection; indeed, this n^+p junction is under direct polarization when a negative bias is applied at the ITO surface, and thus it should easily let the charge carriers flow. Third, the insulating Si_xO_y matrix used to planarize the NW ensemble does not provide further leakage paths. This is proved by conductivity measurements performed on a separate sample with a roughly 500-nm-thick Si_xO_y layer deposited on Si without any NWs; the current observed across the Si_xO_y layer was negligible, namely few pico-amps. Under these assumptions, it seems reasonable to say that the leakage paths are located along the p-i-n junction of the NW-LEDs or along the side-walls of the NWs. This idea is also supported by the conductive AFM measurements presented in section 3.1.2, which show the presence of leakage current close to both the sidewalls and the centre of the NWs.

In reverse bias, the space charge region along the axis of the NW-LEDs can be imagined as a semi-insulating segment under a strong electric field. In addition, the DLTS measurements detected a high density of electron traps in the depletion region. As discussed in section 4.3.4, the trap states are likely due to point defects such as N antisites, boundary dislocations and dangling bonds on the surface of the NWs, or also to alloy disorder inside the (In,Ga)N quantum wells. A current conduction model for disordered semi-insulating material was proposed in the late sixties by N. F. Mott^[237] and R. M. Hill^[238] for amorphous germanium and carbon. According to this theory, the current conduction process is due to hopping of electrons from one trap state to another one. More recently, this model was also successfully applied to GaN layers and to (In,Ga)N/GaN planar LEDs by Look *et al.*^[239] and Shan *et al.*^[235], respectively. A schematic description of this conduction process is depicted in figure 4.19(a). The model assumes that many trap states are present at different energies (E_t) inside the band gap of the semiconductor, and that these traps are characterized by a specific density of states (DOS). The electrons could hop from a supply trap [labelled A in figure 4.19(a)], to an empty one located at a distance R [for instance trap B or C in figure 4.19(a)]. At low temperatures the charge carriers have a narrow energy distribution, and thus only hops towards states with energy close to E_t are possible; this usually results in longer hop distances (*i. e.*, to trap C). On the contrary, high temperatures cause a broader energy distribution of the charge carriers, which can thus hop towards traps located at energies higher than E_t ; this usually results in shorter hop distances (*i. e.*, to trap B). The hopping mechanism is enhanced by the presence of an electric field, which can facilitate the tunnelling from one trap state to the next one.

Considering electric-field-enhanced hopping conduction with a non-uniform energy distribution of trap states, hereafter named variable range hopping (VRH), Hill obtained the following expression for the current^[238]

$$I_{VRH} = I_0^{VRH} \exp \left[-1.76 \left(\frac{T_0}{T} \right)^{1/4} + 4.626 \times 10^{-3} \left(\frac{T_0}{T} \right)^{3/4} \left(\frac{qFa}{U} \right)^2 \right]. \quad (4.17)$$

In this equation, the pre-exponential term I_0^{VRH} converts the emission rate of the trap state into current; it is proportional to the density of traps (N_t) which are actually contributing to the conduction process. T_0 is a characteristic temperature parameter defined as

$$T_0 \approx \frac{18}{k_B D_t a^3} \quad (4.18)$$

where a is the localization radius of the wave function describing the trapped electron

4. Investigation of the opto-electronic characteristics of NW-LEDs

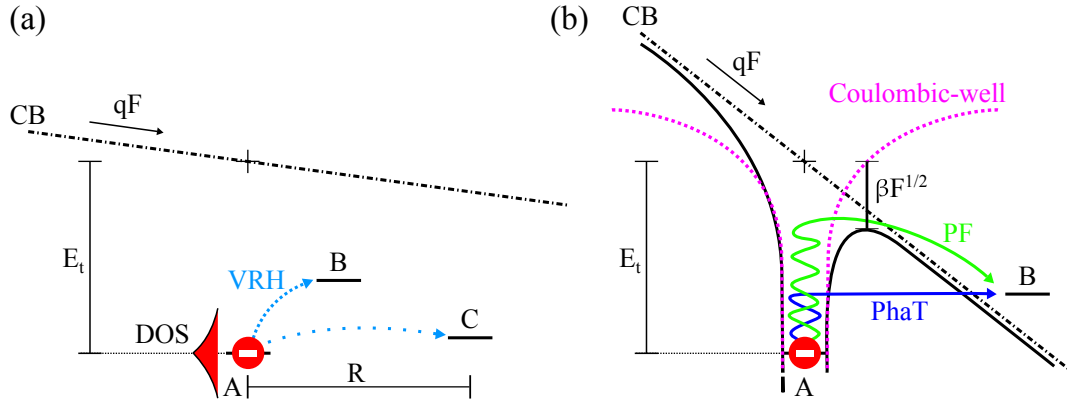


Figure 4.19: Energy diagram of localized trap states in the band gap with a schematic description of the conduction mechanisms. The trap A located at the energy E_t below the conduction band (CB) is the supply centre and is negatively charged. (a) At moderate electric fields (F) VRH should be the dominant conduction process. The electrons could hop from a trap A to an empty state located at a distance R (*i. e.*, B or C). (b) At high electric fields the PF effect (green) and PhaT (blue) dominate the current conduction. The trap state is described as a Coulombic-well, and the height of the barrier is decreased by a factor $\beta F^{1/2}$.

(it can also be written as $a = 2.62/\alpha$, where α represents the decay constant of the wave function), and D_t is the trap density of states at the energy of the supply trap (E_t) in units of $\text{volume}^{-1} \text{energy}^{-1}$. In fact, one of the assumptions of the VRH model is that the trap density of states (DOS) varies with the energy following an exponential distribution:

$$DOS = \frac{\partial N_t}{\partial E} = D_t \exp\left(-\frac{|E - E_t|}{U}\right) \quad (4.19)$$

where U is the characteristic energy or scale parameter of the exponential distribution; it may also be seen as the standard deviation of the distribution, so that almost all the available states are distributed inside an energy range equal to $2.62 \times U$. In equation (4.17) the product (qFa) defines the electrical energy (or work) required to move an electron over a characteristic hop distance R , we assume $R \equiv a$; as usual, q represents the elementary charge and F the electric field. Sometimes, it is convenient to group together some of the constants in equation (4.17) introducing the quantity

$$C_{VRH} = 4.626 \times 10^{-3} (qa/U)^2. \quad (4.20)$$

Equation (4.17) is valid for moderate electric fields, namely $qFa \lesssim 5k_B T$. For $T=300$ K and assuming a localization radius of the wave function equal to the Bohr radius of an electron bound to an oxygen donor in GaN, namely $a = 2.8 \text{ nm}^{[240]}$, we obtain $F \lesssim 5 \times 10^5 \text{ V/cm}$. For electric fields higher than this value hopping should not be the dominant current conduction mechanism any longer.

At high electric fields the potential surrounding the trap state, which is usually assumed to be Coulombic, is strongly deformed; the height of the Coulomb barrier is lowered and the dominant emission processes are well described by the Poole-Frenkel (PF) effect and by phonon-assisted tunnelling (PhaT). Figure 4.19(b) shows a graphical representation of the charge carrier emission from a Coulomb state in the high-field case. At zero temperature (0 K) only direct tunnelling into the conduction band at the energy level

4.4. A physical model for the reverse bias regime

of the Coulomb centre is possible. With increasing temperature, due to electron-phonon coupling, the electrons gain energy and can thus tunnel through the potential barrier also towards states at higher energy (*i. e.*, state B). The electrons can either tunnel through the barrier (blue arrow) or overpass it (green arrow), the former case is called PhaT whereas the latter PF effect. At high temperatures and strong electric field the PF effect should dominate over PhaT.

The PF effect describes the emission of charge carriers resulting from the lowering of the Coulomb potential barrier. The electron emission rate e_{PF} from donor states located at the energy E_t below the conduction band edge is described by the formula^[241,242]

$$e_{PF} \propto \exp\left(-\frac{E_t - \beta F^{1/2}}{k_B T}\right) \quad \text{with} \quad \beta = \left(\frac{Zq^3}{\pi\epsilon_r\epsilon_0}\right)^{1/2}. \quad (4.21)$$

The energy E_t corresponds to the potential barrier at zero electric field that the electron has to overcome to escape from the trap, it coincides with the thermal activation energy of the trap. The term $\beta F^{1/2}$ describes the lowering of the Coulomb barrier, where β is called Poole-Frenkel coefficient. In equation (4.21), Z is the charge state of the Coulomb centre, ϵ_r is the relative permittivity of GaN, while ϵ_0 is the permittivity of the vacuum. It is worth noting that equation (4.21) was derived by J. Frenkel^[241] in the one-dimensional case. A more complete three-dimensional calculation, carried out by J. L. Hartke^[243], gives a qualitatively similar result but with a pre-exponential factor [not shown in equation (4.21)] that slightly decreases with the field.

The PF effect does not take into account the tunnelling through the thinned potential barrier; in fact, a high electric field not only lowers the height of the barrier but also makes it thinner. This effect is well described by the phonon-assisted tunnelling. Vincent *et al.*^[244] found that the electron emission rate e_{PhaT} due to PhaT through the whole depth of the Coulombic well has the form

$$e_{PhaT} \propto \exp\left(-\frac{E_t}{k_B T}\right) \times \int_{\beta F^{1/2}/k_B T}^{E_t/k_B T} \exp\left\{z - z^{3/2} \left(\frac{4}{3} \frac{(m_e^*)^{1/2} (k_B T)^{3/2}}{q\hbar F}\right) \left[1 - \left(\frac{\beta F^{1/2}}{zk_B T}\right)\right]\right\} dz \quad (4.22)$$

where m_e^* is the effective mass of the electron and \hbar the Planck constant divided by 2π ; the variable z represents the depth of the well. The total current emitted by the Coulombic trap states (I_{CT}) has to take into account both contribution, it is thus proportional to the sum of e_{PF} and e_{PhaT} ^[244]:

$$I_{CT} = I_0^{CT} (e_{PF} + e_{PhaT}) \quad (4.23)$$

where the factor I_0^{CT} converts the emission rate into current, it is proportional to the density of traps (N_t) which are actually contributing to the conduction process. According to the calculation carried out by Hill^[242], I_0^{CT} would also have a residual dependence on the temperature and on the electric field, namely: $I_0^{CT} \propto qN_t(k_B T)^2 F$.

In the next sections we try to fit the experimental I-V-T curves to the equations (4.17) and (4.23) in order to verify whether the discussed conduction mechanisms can describe the transport properties of the NW-LEDs.

4. Investigation of the opto-electronic characteristics of NW-LEDs

4.4.2. Temperature dependence of the reverse current

As first step to investigate the current conduction mechanisms in reverse bias regime the temperature dependence of the leakage current was analysed. Such a study helps to reveal the nature of the involved conduction mechanisms, which often are characterized by different temperature dependences.

From the temperature dependent I-V characteristics presented in figure 4.18, we extracted the reverse currents measured at each applied bias, and then we plotted them *vs.* the reciprocal temperature, $1/T$. The resulting curves, for five different reverse biases, are plotted as data points in figure 4.20. In the graph two main regions are clearly identifiable. For temperatures lower than approximately 240 K (namely, $1/T > 4.16 \times 10^{-3} \text{ K}^{-1}$), the current varies slowly with temperature, while above 240 K a rather fast change in the slopes of the curves is visible. This behaviour suggests the presence of at least two different conduction channels, one of which is activated at temperatures higher than 240 K.

The data were fitted by means of equation (4.17), using as fitting parameters I_0^{VRH} and T_0 . The quantity T_0 varies the slope of the curves, whereas a variation of I_0^{VRH} produces an almost rigid vertical shift of the curves. The electric field (F) as a function of the applied reverse bias was estimated by using the average electric field ($\langle F \rangle$) in the depletion region obtained from C-V measurements, see section 4.3.1. The parameter C_{VRH} was kept constant and equal to $2 \times 10^{-18} \text{ C}^2 \text{ m}^2 \text{ eV}^{-2}$; by means of a process of iterative optimization, David van Treeck found that this value gives the best fit of the data in a wide range of temperatures^[176]. Assuming a localization radius of the wave function equal to the Bohr radius of an electron bound to an oxygen donor in GaN^[240], namely $a \equiv a_B = \hbar / (2E_b m^*)^{1/2} = 2.8 \text{ nm}$ (binding energy $E_b = 33 \text{ meV}$), we obtain $U \approx 135 \text{ meV}$, which is a reasonable value for the scale factor of the DOS distribution.

The VRH model, depicted by the dashed-dotted lines in figure 4.20, can well describe the temperature dependence of the reverse current only for $T \lesssim 240 \text{ K}$ and biases ranging from -0.5 to -5 V. For higher negative biases the discrepancy between experimental points and VRH model becomes larger and larger; only in a very small temperature range, between 80 and 120 K the data seem to follow the VRH model. The chosen fitting parameters are listed in table 4.7. Shan *et al.*^[235] and Jung *et al.*^[245] performed a similar analysis on planar (In,Ga)N/GaN LEDs but they considered only a bias of -5 V. The value of T_0 obtained from the fit of the data related to this voltage is about one order of magnitude lower than the ones reported by Shan and Jung. This would indicate the presence of a higher trap DOS in the NW-LEDs than in the planar counterparts. Both fitting parameters, I_0^{VRH} and T_0 , decrease strongly when the reverse voltage is swept from 0 to -5 V. Such a strong dependence on the applied bias could be due to either a strong variation of the density of traps actually contributing to the current transport or an overestimation of the F dependence in equation (4.17).

Above 243 K a rapid increase of the current with temperature is observed. This behaviour seems to suggest the appearance of a thermally activated emission process. As discussed in section 4.3.2, the temperature dependence of the current emitted by trap states with thermal activation energy E_a can be written as

$$I_{CT} = AT^2 \exp\left(-\frac{E_a}{k_B T}\right) \quad (4.24)$$

where A is a proportionality factor which contains all the residual dependences. A variation of this quantity produces an almost rigid vertical shift of the curves, whereas E_a de-

4.4. A physical model for the reverse bias regime

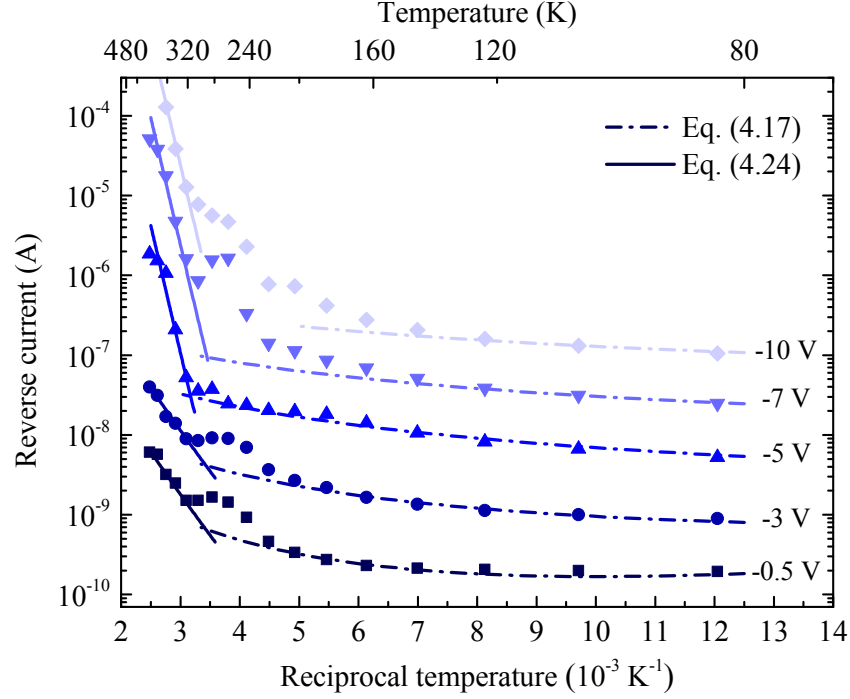


Figure 4.20: I-T characteristics of the NW-LED measured at five different reverse biases for temperatures ranging from 83 to 403 K (symbols). The data were fitted using equations (4.17) and (4.24), indicated by the dashed-dotted and solid lines, respectively.

defines the slope of the curves. It is worth noting that the temperature dependence defined by equation (4.24) coincides also with the one expected for the PF effect^[242]; moreover, it describes the main temperature dependence of the current emitted by Coulombic traps. The fit of the data is represented by the solid lines in figure 4.20; the evolution of the current is qualitatively described by equation (4.24) for temperatures higher than 300 K. Two different slopes of the curves are obtained, corresponding to two different activation energies: $E_a \approx 150$ meV for $|V| \lesssim -3$ V and $E_a \approx 570$ meV for higher reverse biases, see table 4.7. Interestingly, the activation energy for negative voltages higher than -5 V, $E_a \approx 570$ meV, is identical to the one obtained from DLTS measurements in section 4.3.4. Therefore, the trap states probed by means of DLTS measurements are most likely responsible for the current conduction properties of the NW-LEDs at temperatures and absolute

Table 4.7: List of the parameters used to fit the I-T curves with the equations (4.17) and (4.24) at five different reverse biases for temperatures ranging from 83 to 403 K. The parameter C_{VRH} was kept constant and equal to $2 \times 10^{-18} \text{ C}^2 \text{ m}^2 \text{ eV}^{-2}$.

Bias (V)	I_0^{VRH} (A)	T_0 (K)	A (A K^{-2})	E_a (meV)
-0.5	1×10^{-2}	5.6×10^6	3×10^{-12}	150
-3	1×10^{-4}	6×10^5	1.9×10^{-11}	150
-5	2.5×10^{-5}	1×10^5	4×10^{-4}	570
-7	2.2×10^{-5}	4×10^4	9×10^{-3}	570
-10	1.6×10^{-5}	1×10^4	9×10^{-2}	570

4. Investigation of the opto-electronic characteristics of NW-LEDs

biases higher than 240 K and -5 V, respectively. Indeed, deep states in bulk GaN (with $E_t \approx 555$ meV)^[228] as well as dangling bonds located on the surface of NWs^[246] were found to influence the charge carrier transport properties of the semiconductor. The energy $E_a \approx 150$ meV observed at low biases might be related to the activation of shallow Mg acceptors in p-type GaN, which have an ionization energy ranging between 150 and 220 meV^[17,193].

The analysis of the I-T curves together with the DLTS measurements seem thus to suggest that the current conduction is dominated by VRH at low temperatures and small reverse biases ($T \lesssim 240$ K and $|V| \lesssim 5$ V). At high temperatures and biases ($T \gtrsim 300$ K and $|V| \gtrsim 5$ V) the dominant conduction mechanism is due to the thermally activated emission from deep states located 570 meV below the conduction band edge in the depletion region of the NW-LED.

4.4.3. Fitting the I-V curves in the temperature range 83–403 K

The analysis of the I-T curves suggests that band gap states located 570 meV below the conduction band edge in the depletion region of the NW-LED are contributing to the reverse current conduction. A puzzling issue is to understand how these traps are fed. More specifically, how can the electrons overcome the energy gap present between the valence band maximum and the deep states located 570 meV below the CB edge. A possible explanation could be obtained by imagining that electrons from the valence band of p-type GaN can hop into shallow states close to the VB maximum, and then move towards the other side of the band gap by multiple hops. This model has already been successfully applied to describe the reverse leakage current in planar (In,Ga)N/GaN LEDs^[235]. Once the electrons reach the vicinity of the conduction band minimum, they could hop directly into the CB or, if temperature and electric field are high enough, be emitted by means of a thermally activated process. We assume that the electron hopping from the VB up to the states located 570 meV below the CB edge is well described by the VRH model [*i. e.*, equation (4.17)]; whereas the last part of the electron motion is modelled by emission from Coulomb states [*i. e.*, equation (4.23)]. Figure 4.21 shows a schematic of the assumed model; in this picture of the system, the VRH mechanism acts as charge carrier supplier of the Coulombic traps (CT) close to the CB minimum. Therefore, the VRH conduction channel can be considered in series to the CT system described by PF and PhaT processes. The total electron current from the VB to the CB (I_{tot}) can be expressed by the analytical relation

$$I_{tot} \approx \frac{I_{VRH} I_{CT}}{I_{VRH} + I_{CT}} \quad (4.25)$$

where I_{VRH} and I_{CT} are defined by equations (4.17) and (4.23), respectively. This formula describes the competition between two mechanisms that limit each other, so that the slower process governs the faster one. Shockley and Read found that a similar relation defines the generation-recombination processes in trap states when the mechanism that fills the traps is in competition with the one that empties them^[247].

In order to fit the data points for low negative biases, ranging from 0 to roughly -3 V or -4.5 V, depending on the temperature, another term with linear dependence on the voltage (called I_{Rp}) was added to equation (4.25). In fact, neither the VRH [defined by equation (4.17)] nor the emission from the Coulombic traps [namely equations (4.23)] can describe the Ohmic-like behaviour observed in the experimental data at low biases.

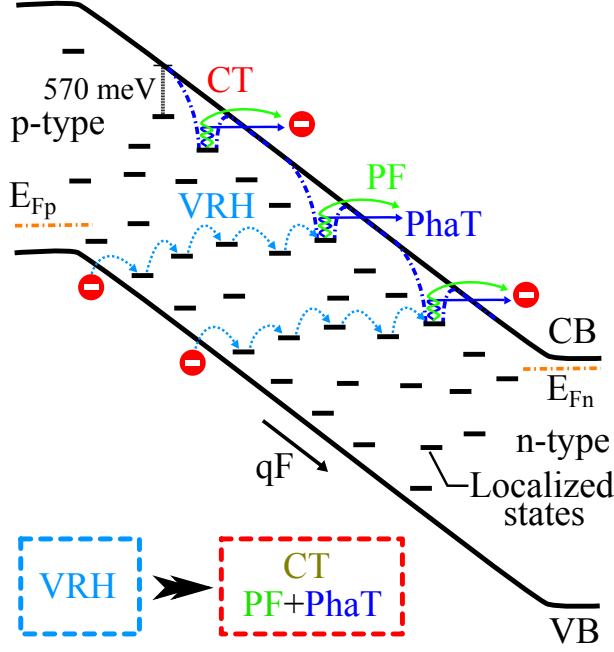


Figure 4.21: The schematic depicts the depletion region of the p-n junction under reverse bias, for sake of simplicity the (In,Ga)N QWs are omitted. The electrons hop (VRH) from the valence band (VB) up to the Coulombic traps (CT) located 570 meV below the conduction band (CB). Then, they are emitted by means of the PF effect and PhaT processes into the CB. The other localized states might be due to the second electron trap revealed by DLTS measurements ($E_{t2} = 840$ meV), mid-gap states often reported in (In,Ga)N/GaN LEDs^[218,219], and Mg acceptors. E_{Fp} and E_{Fn} represent the position of the Fermi level in the p- and n-type material, respectively.

Hence, the total reverse current becomes

$$I_{tot} = \frac{I_{VRH}I_{CT}}{I_{VRH} + I_{CT}} + I_{Rp} = \frac{I_{VRH}I_{CT}}{I_{VRH} + I_{CT}} + \frac{V}{R_p} \quad (4.26)$$

where R_p , named parallel resistance, is an empirical parameter that takes into account further parallel leakage mechanisms not included in our model. The physical origin of this Ohmic-like leakage current is unclear. It might be related to other types of band-to-band tunnelling not considered in this study; for example, similar to the one responsible for the low forward bias current conduction in (In,Ga)N/GaN LEDs found by Auf der Maur *et al.*^[218]. Other possible explanations could be a different field dependence of the VRH at low electric fields, as predicted by Hill^[238], or also short circuits between the ITO top contact and the n-type base of the NW-LEDs.

To verify the validity of our model, we fit the I-V-T data by implementing equation (4.26) in a *MATLAB* program developed by David van Treeck at the PDI^[176]. The electric field (F) present in the equations (4.17), (4.21) and (4.22) was replaced by the average electric field in the depletion region ($\langle F \rangle$) estimated by C-V measurements in section 4.3.1. The choice of the fitting parameters and their meaning are discussed in subsection 4.4.4. The resulting fits of the data to equation (4.26) are shown by the solid lines in figure 4.22(a). We note that the agreement with the data points is excellent in the entire bias range and for all the temperatures up to 323 K. For higher temperatures some discrepancy occurs,

4. Investigation of the opto-electronic characteristics of NW-LEDs

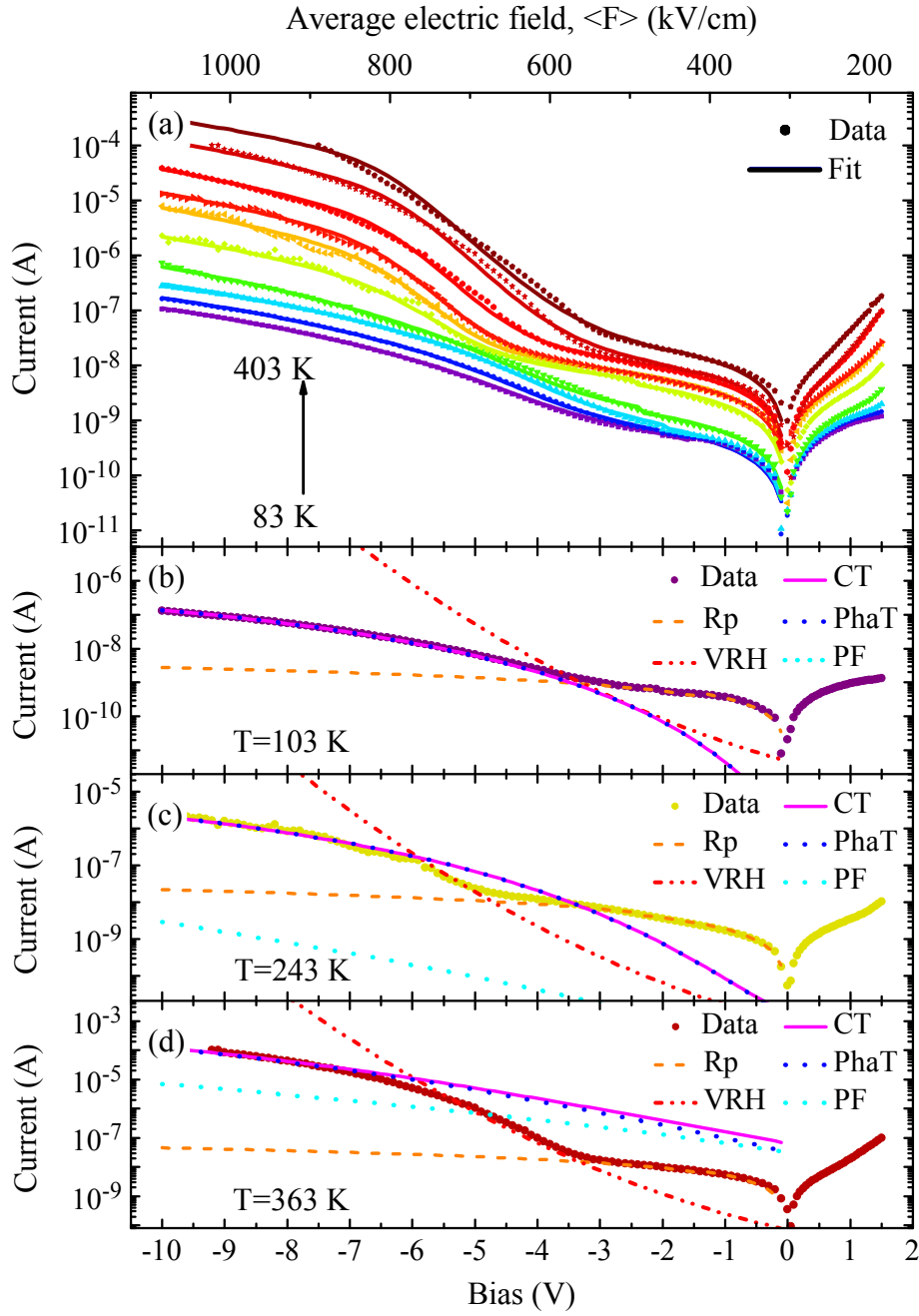


Figure 4.22: (a) Experimental I-V curves in reverse bias (data points) and fits (solid lines) to equation (4.26) plotted in semi-logarithmic scale for temperatures increasing from 83 to 403 K. The curves correspond to temperatures of 83, 123, 163, 203, 243, 303, 323, 343, 363, and 403 K (from bottom to top). (b)–(d) Contributions of each conduction channel to the total current plotted for three different temperatures: (b) 103 K, (c) 243 K, and (d) 363 K.

but the qualitative behaviour is still well described by the employed model.

The contribution of each conduction mechanism is shown in figures 4.22(b)–(d) for three different temperatures: 103, 243 and 363 K. The red dotted-dashed lines and the magenta solid lines depict the current obtained by VRH and emission from Coulombic traps (CT) as defined by equations (4.17) and (4.23), respectively. For completeness, the

4.4. A physical model for the reverse bias regime

two components constituting the CT emission, namely PF and PhaT processes, are plotted in figures 4.22(b)–(d) as dotted blue and cyan lines, respectively. At low temperature ($T=103$ K), the VRH would potentially supply much more current than the one that the CT states are able to emit (compare red and magenta curves). The total current is thus limited by the low emission rate of the CT states. For negative biases higher than about -4 V, the data are perfectly fitted by I_{CT} , which for such a low temperature coincides with the PhaT contribution (the current due to the PF effect is not visible on this scale). For negative biases lower than about -4 V the data points are well described by the linear dependence defined by R_p .

At intermediate temperature ($T=243$ K), the emission rate of the CT states significantly increases, and the charge carriers supplied by VRH for negative biases up to -6 V are not able to follow the fast emission rate of the CT states any longer. In this bias range ($[-6;0]$ V), the low emission rate of the VRH process limits the current emitted by the CT states, which would thus coincide with the VRH current. Between 0 and -4.5 V, the current provided by VRH is lower than the measured one (compare red curve and data points); in this bias range the total charge carrier flow is dominated by the contribution coming from R_p . In contrast, for reverse voltages higher than -6 V the emission rate of the VRH process overtakes the one of the CT, and the total current is again limited by the emission from CT states. We note that, despite a remarkable increase of the PF current, I_{CT} still coincides with the PhaT contribution.

At high temperature ($T=363$ K), the situation is similar to the one observed at $T=243$ K, with the difference that the contribution to I_{CT} coming from the PF process increased quite a lot. The data are well fitted by the mutual interaction of VHR and CT for negative biases higher than -3 V; for lower voltages the total current is dominated by the contribution coming from R_p . From the analysis of the data we can thus conclude that the peculiar hump-like shape observed in the I-V curves in reverse bias is likely due to the fast increase of the emission rate of the CT states with temperature.

4.4.4. Discussion of the fitting parameters

In this section, we discuss the validity of the parameters used to fit the data, and consequently also the one of the whole model.

Looking at equation (4.17), it is clear that the VRH process is characterized by six quantities: I_0^{VRH} , T_0 , U , a , T , and F . The latter two (T and F) are defined by the measurement conditions. U and a are unknown constants, which describe physical properties related to the intimate nature of the trap states; for this reason we assume that they depend more on the type of involved defects than on the temperature. Since both of them are unknown, it can be convenient to group them in the quantity C_{VRH} , defined by equation (4.20). As already discussed in section 4.4.2, we found that the best fit of the data is obtained for $C_{VRH} \approx 2 \times 10^{-18} \text{ C}^2\text{m}^2\text{eV}^{-2}$ ^[176] in a wide range of temperatures. The value of C_{VRH} is thus kept constant for all the fits. Assuming a localization radius of the wave function equal to the Bohr radius of an electron bound to an oxygen donor in GaN^[240], namely $a \equiv a_B = \hbar/(2E_b m^*)^{1/2} = 2.8 \text{ nm}$ (binding energy $E_b = 33 \text{ meV}$), we obtain $U \approx 135 \text{ meV}$, which is a reasonable value for the scale factor of the DOS distribution. The two remaining parameters, I_0^{VRH} and T_0 , were used to fit the experimental data; T_0 controls the slope of the curves, whereas a variation of I_0^{VRH} produces an almost rigid vertical shift. Since these parameters are independent from each other, the values obtained from the fits are unique within a certain inaccuracy, which we estimate to be smaller than few percent of the reported values. The values employed to fit the I-V

4. Investigation of the opto-electronic characteristics of NW-LEDs

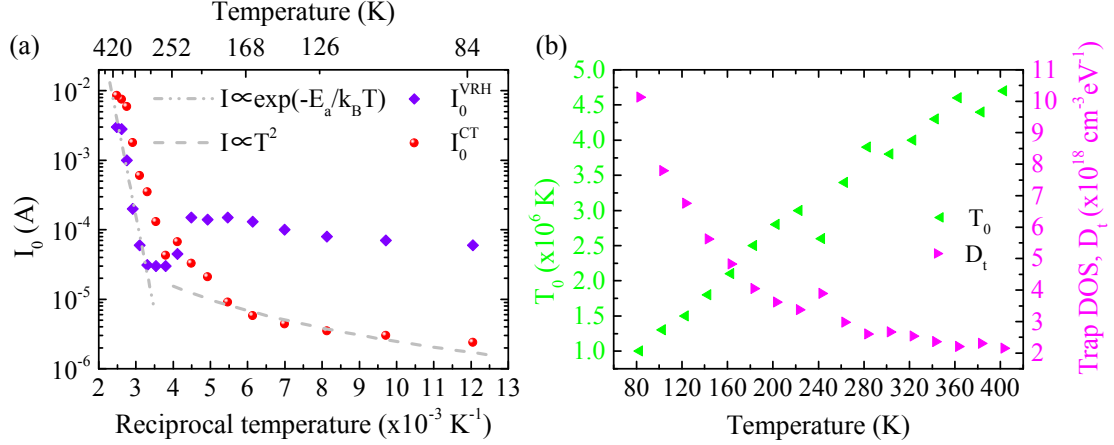


Figure 4.23: (a) Arrhenius plot of the pre-exponential terms; the violet diamond and the red circle points represent the parameters I_0^{VRH} and I_0^{CT} , respectively. The grey dotted-dashed line is a linear interpolation of the data at high temperatures, whereas the grey dashed curve depicts a hypothetical quadratic temperature dependence of the current ($I \sim T^2$). (b) The axis on the left-hand side depicts the variation of the parameter T_0 with the temperature, while the right-hand side axis shows the corresponding trap density of states D_t .

curves in the temperature range [83; 403] K are listed in table 4.8.

The violet diamond points in figure 4.23(a) show the variation of I_0^{VRH} with the reciprocal temperature. This parameter exhibits small fluctuations for temperatures ranging from 83 up to 323 K, but not a well defined behaviour. Indeed, no particular temperature dependence of the pre-exponential factor is expected from the VRH model^[238]. For temperatures higher than 343 K an exponential increase of I_0^{VRH} is observed. The slope of the Arrhenius plot (see grey dotted-dashed line) indicates a thermal activation energy of this process equal to $E_a \approx 540$ meV; interestingly, this value is very close to the energy of the Coulomb traps obtained from the DLTS measurements. Such a strong temperature dependence of the pre-exponential factors would suggest that for temperatures higher than about 300 K the charge carriers transport between deep level states is no longer described by VRH [*i.e.*, equation (4.17)]. Indeed, this conduction mechanism is supposed to dominate only at low temperatures, when the hop into remote trap states with energy close to E_T is more favourable than the hop into neighbouring states with energies very different than that of the supply trap. On the contrary, at high temperatures the hopping into close states with energies higher than E_T is favoured; this transport mechanism is usually referred to as nearest-neighbour hopping, and is characterized by a temperature dependence stronger than that of VRH^[248]. It is also important to understand that the equations used in our model describe the single conduction mechanisms without considering possible mutual interference between different processes. In a more complex system, where several conduction channels act at the same time, the actual behaviour of each process might be slightly different than the expected one.

The left-pointing green triangles in figure 4.23(b) show the variation of the parameter T_0 ; it increases monotonously with temperature. The right-pointing magenta triangles in the same graph depict the trap density of states, D_t , calculated from T_0 using equation (4.18) with $a = 2.8$ nm. D_t decreases with increasing temperature, nevertheless, its variation is relatively small (less than a factor 5). This variation might be explained imagining that at high temperature the electrons can be promoted to states with higher

4.4. A physical model for the reverse bias regime

Table 4.8: List of the parameters obtained by fitting the I-V curves for temperatures ranging from 83 to 403 K.

Variable range hopping			Coulombic traps		
T (K)	$I_0^{VRH} (\times 10^{-4} \text{ A})$	$T_0 (\times 10^6 \text{ K})$	$I_0^{CT} (\text{A})$	m_e^*/m_e	$R_p (\text{G}\Omega)$
83	0.06	1.0	2.4×10^{-6}	0.10	3.40
103	0.07	1.3	3.0×10^{-6}	0.10	3.25
123	0.08	1.5	3.5×10^{-6}	0.10	3.25
143	0.10	1.8	4.4×10^{-6}	0.10	2.95
163	0.13	2.1	5.8×10^{-6}	0.10	2.70
183	0.15	2.5	9.1×10^{-6}	0.11	2.15
203	0.14	2.8	2.1×10^{-5}	0.17	1.60
223	0.15	3.0	3.3×10^{-5}	0.17	1.15
243	0.05	2.6	6.7×10^{-5}	0.15	0.50
263	0.03	3.4	4.3×10^{-5}	0.05	0.37
283	0.03	3.9	1.3×10^{-4}	0.12	0.32
303	0.03	3.8	3.5×10^{-4}	0.22	0.35
323	0.06	4.0	6.0×10^{-4}	0.22	0.36
343	0.20	4.3	1.8×10^{-3}	0.25	0.23
363	1.00	4.6	5.9×10^{-3}	0.26	0.21
383	2.80	4.4	7.5×10^{-3}	0.20	0.13
403	3.00	4.7	8.5×10^{-3}	0.20	0.12

energy, thus making the distribution of the trap DOS broader and consequently the density of state per unit energy smaller. The average value of the temperature parameter is $T_0^{avg} \approx 3 \times 10^6 \text{ K}$; this value is similar to the one obtained by Shan *et. al* [235] analysing the I-T curve of planar (In,Ga)N/GaN LEDs at -5 V (namely, $1.3 \times 10^6 \text{ K}$). From the average value of the trap DOS ($D_t^{avg} \approx 4 \times 10^{18} \text{ cm}^{-3} \text{ eV}^{-1}$) we estimated the density of traps involved in the VRH conduction: $N_t^{avg} = 2 U D_t^{avg} \approx 8 \times 10^{17} \text{ cm}^{-3}$, for the calculation we took $U = 135 \text{ meV}$. This value is more than one order of magnitude higher than the one estimated from DLTS measurements for the deep states E_1 (see section 4.3.4), probably because the VRH involves more traps distributed over a wide range of energies in the band gap. Unfortunately, the lack of experimentally determined values for the parameters a and U casts some doubt on the validity of this estimate. In particular, because of the strong (cubic) dependence of N_T on a , the value of the density of traps can be arbitrary adjusted by choosing different values of a (which is unknown). Furthermore, from the analysis of the I-V curves it was not possible to determine the exact nature of the traps responsible for the VRH conduction.

The emission from the Coulomb traps described by equation (4.23) is characterized by six quantities: I_0^{CT} , E_t , β , m_e^* , T , and F . Again, the latter two (T and F) are defined by the measurement conditions. In our model we assumed that the CT states have the same nature as the trap E_1 observed by DLTS, namely nitrogen antisite defects inside the NWs and boundary dislocations at the edge of coalescing NWs; therefore, the parameter E_t was chosen equal to $E_{t1} = 570 \text{ meV}$. This assumption is further corroborated by the analysis of the temperature dependence of the reverse current. In fact, at high temperatures and biases ($T \gtrsim 300 \text{ K}$ and $|V| \gtrsim 3 \text{ V}$) the leakage current is dominated by a conduction process characterized by a thermal activation energy equal to 570 meV,

4. Investigation of the opto-electronic characteristics of NW-LEDs

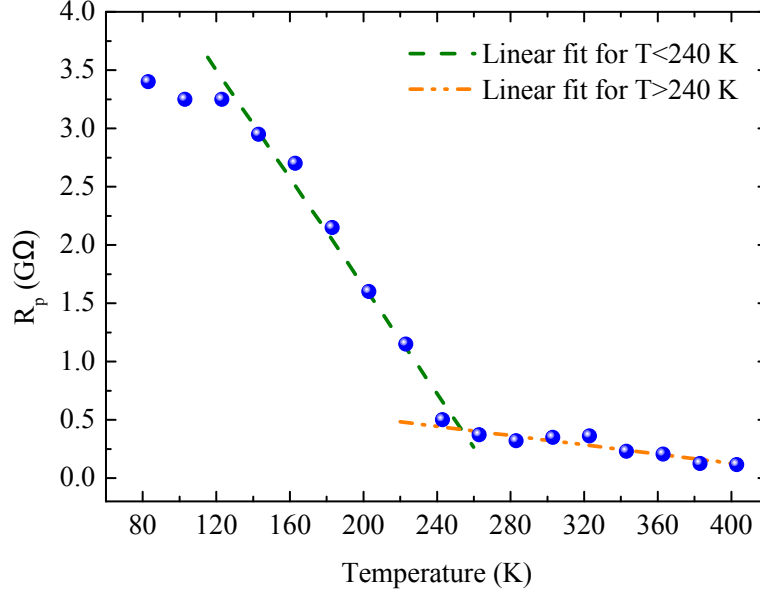


Figure 4.24: Variation of the parallel resistance with temperature. The green dashed and orange dotted-dashed lines are linear interpolations of the data for low and high temperature, respectively.

see section 4.4.2. The Poole-Frenkel coefficient $\beta = (Zq^3/\pi\epsilon_r\epsilon_0)$ was estimated to be $3.45 \times 10^{-5} \text{ eV V}^{-1/2} \text{ m}^{1/2}$; for the calculation we used a charge state of the CT $Z = 2$, as expected for N_{Ga} defects in GaN^[249], and the static relative permittivity of GaN $\epsilon_r = 9.7$. The two remaining parameters, I_0^{CT} and m_e^* , were used to fit the experimental data; m_e^* changes the slope of the curves, whereas a variation of I_0^{CT} produces an almost rigid vertical shift. Since these parameters are independent from each other, they can be univocally determined. The values employed to fit the I-V curves are listed in table 4.8. The red data points in figure 4.23(a) show the evolution of I_0^{CT} with the temperature. The increase of this parameter for $T < 200 \text{ K}$ can be explain by the residual temperature dependence of I_0^{CT} predicted by Hill^[242], $I_0^{CT} \propto qN_t F(k_B T)^2$, as shown by the grey dashed curve in figure 4.23(a). For higher temperatures the rise becomes much faster than the expected T^2 behaviour and I_0^{CT} increases almost exponentially. As already discussed, the slope of the Arrhenius plot indicates a thermal activation energy of this process equal to about 540 meV, which indeed is very closed to the activation energy of the Coulomb traps.

The second parameter used to model the current from CT states is the effective electron mass (m_e^*). As seen in table 4.8, its value slightly increases between $0.1 m_e$ and $0.25 m_e$ for temperatures ranging from 83 to 403 K. The employed effective electron masses agree very well with the ones obtained from theoretical^[250] ($m_e^* = 0.13 - 0.2 m_e$) and experimental^[223] ($m_e^* = 0.22 m_e$ at $T=300 \text{ K}$) studies for GaN. An increase of the effective electron mass with temperature was also observed by Hofmann and co-authors^[251] in (Al,Ga)N/GaN heterojunctions; this effect was attributed to a decreased spatial confinement of the electron wave function at high temperatures.

The reverse current at low negative biases was described by means of an empirical linear relation, as shown by equation (4.26). Figure 4.24 shows the variation of the parallel resistance with temperature extracted from the fits of the I-V curves at small voltages. R_p decreases monotonically; more precisely, two intervals where R_p follows an almost linear behaviour are distinguishable. For temperatures ranging from 83 up to 243 K, the

4.4. A physical model for the reverse bias regime

parallel resistance drops faster than for $T > 243$ K. This observation would suggest the activation of a second conduction mechanism not present for $T < 243$ K. Without a physical model it is not possible to learn more about the involved conduction processes. We can just observe that the transition between the two mechanisms roughly occurs at $T = 243$ K; the analysis of the I-T curves for low biases (see section 4.4.2) reveals that at this temperature a thermally activated process appears, its activation energy is $E_a = 150$ meV. As already discussed this effect might be related to the activation of shallow acceptors. We remark that the values of all the parameters employed in our model are comparable to the ones reported in literature, and provide a rather good description of the experimental measurements. Therefore, it seems fair to conclude that the developed model provides a reasonable and compelling description of the physical origin of the reverse leakage current in NW-LEDs.

In summary, a physical model able to describe the peculiar I-V-T characteristics of (In,Ga)N/GaN NW-LEDs in reverse bias regime was developed. A careful analysis of the data reveals that the leakage current in reverse bias is due to trap levels present in the band gap of the semiconductor. At moderate and high reverse biases (from -3 to -10 V), the current conduction can be described by the interaction of two competing mechanisms: variable range hopping (VRH) and emission from Coulomb centres (CT) located in the vicinity of the conduction band edge. The latter is described as the sum of two contributions defined by phonon-assisted tunnelling (PhaT) and the Poole-Frenkel effect (PF). Furthermore, the developed model indicates that the peculiar hump-like shape observed in the I-V curves in reverse bias is likely due to the fast increase of the emission rate of the CT states with temperature.

The obtained results suggest that the leakage current in NW-LEDs is due to the presence of a spectrum of different band gap states with high density. The analysis of the DLTS measurements indicates that these trap states originate from nitrogen antisite point defects inside the NWs, boundary dislocations at the edge of coalescing NWs, and dangling bonds present on the free sidewalls. It was recently demonstrated that the latter issue can be significantly mitigated by an adequate surface passivation, for instance by means of an (Al,Ga)N^[170] or Al₂O₃^[179] shells. Differently, the other points still require further technological improvements to be overcome. For example, it is well known that the III/V flux ratio plays an important role in the formation of point defects during the MBE growth^[252]; in particular, a high N flux could promote the formation of Ga vacancies and nitrogen antisite defects. We could thus speculate that lower N fluxes, possibly also characterized by a smaller amount of ions, could reduce the density of defects. A similar result could also be achieved by growing the NWs at higher temperatures. In addition, an improved alignment of the NWs would decrease their coalescence degree and consequently also the formation of the related boundary dislocations. Many other optimizations might result in better performance of the NW-LEDs. For instance, it was shown that a moderate Mg doping of the GaN barrier in the active region of the NW-LED can improve the IQE^[129]. Anyway, it is clear that more studies are required to further improve the quality of the MBE grown NW-LEDs.

Summary

In this chapter both opto-electronic and transport properties of the NW-LEDs have been carefully studied.

A peculiar double-line structure has been observed in the EL spectra emitted by the

4. Investigation of the opto-electronic characteristics of NW-LEDs

NWs. An accurate analysis of the data, supported by simulations of the strain distribution inside the active region of the NW-LEDs, would suggest that the fine structure of the EL peaks is related to the emission from different QWs. In particular, the compressive strain caused by the (Al,Ga)N EBL in the neighbouring (In,Ga)N QW could shift its emission towards higher energies. The prototype NW-LEDs investigated in this chapter exhibit a relatively low EQE smaller than 0.1 %. Although, more advanced structures can provide EQE as high as 1.1 %, the limited performance of the NW-LEDs so far obtained would suggest that still significant improvements has to be achieved to make this type of technology competitive on the market. Furthermore, the analysis of the temperature dependent PL and EL measurements indicates that, although carrier localization phenomena are present, they do not dominate the EL emission properties of the device, at least at the temperatures and injected current densities used for normal device operation.

The forward bias I-V characteristics of different NW-LEDs have been modelled by means of a modified version of the classical Shockley equation. The proposed model takes into account the multi-element nature of LEDs based on NW ensembles by assuming a linear dependence of the ideality factor on applied bias. Therefore, this study provides a deeper understanding of the operation principles of this type of devices. It might be particularly useful to correctly analyse the I-V characteristics of devices with inhomogeneous electrical properties, regardless the material system employed.

The transport mechanisms in reverse bias regime have been carefully studied by means of DLTS and temperature dependent I-V measurements. Two main deep states have been observed in the active region of NW-LEDs at energies of $E_{t1} \approx 570$ meV and $E_{t2} \approx 840$ meV below the conduction band minimum. These defects exhibit relatively high concentration: the values $N_{t1} \approx 5 \times 10^{16} \text{ cm}^{-3}$ and $N_{t2} \approx 1 \times 10^{16} \text{ cm}^{-3}$ have been estimated by DLTS measurements for the two types of traps. The comparison of the signatures of the observed electron traps with the ones reported in literature has indicated that the deep states might originate from native point defects (namely, nitrogen antisites) present in the bulk material, from chains of boundary dislocations (BDs) at the edge of coalescing NWs, and from dangling bonds present on the free sidewalls. Several strategies to limit the density of these unwanted defects have been suggested, in summary: less N-rich conditions and higher temperatures than the ones commonly used for the growth of the (In,Ga)N/GaN active region might reduce the density of point defects; an improved alignment of the NWs can reduce the coalescence degree of the NWs thus suppressing the formation of BDs; dangling bonds on the free sidewalls could be passivated by the deposition of a semi-amorphous shell around the NWs.

The deep levels observed via DLTS measurements have been used to develop a physical model able to describe quantitatively the peculiar I-V-T characteristics of NW-LEDs in reverse bias regime. We have found that at moderate and high reverse biases (from -3 to -10 V), the current conduction can be described by the interaction of two competing mechanisms: variable range hopping (VRH) and emission from Coulomb centres (CT) located in the vicinity of the conduction band edge. The latter has been described as the sum of two contributions defined by phonon-assisted tunnelling (PhaT) and the Poole-Frenkel effect (PF). Furthermore, the developed model indicates that the peculiar hump-like shape observed in the I-V curves in reverse bias is likely due to the fast increase of the emission rate of the CT states with temperature.

Conclusion and outlook

Different topics have been covered in this thesis, from the epitaxial growth of the NW-LED structures to the technological processing steps required to fabricate working devices, ending with an in-depth investigation of the opto-electronic properties of the obtained NW-LEDs. This chapter briefly summarizes the most important results of the entire work and provides an outlook where possible solutions to the main issues still open are suggested.

In the second and third chapter of this thesis new or optimized strategies to fabricate NW-LEDs with improved performance have been discussed. In particular, in the second chapter the growth of NW-LEDs by means of MBE have been addressed.

- We have found that the PL intensity emitted from the QWs can be increased by about ten times by suppressing the coalescence of the nanostructures. To this end, the Mg flux has been adjusted so as to supply the amount of atoms necessary to obtain a good doping of the material, avoiding at the same time the coalescence of the NWs.
- A three-step growth procedure for the deposition of very thin (less than 10 nm), smooth, and closed AlN layers on Si substrate has been developed.
- We have demonstrated that an AlN buffer layer that is only 4 nm thick both enables the SAG of GaN NWs on Si substrates and permits the current conduction required for the operation of NW-LEDs.
- Ordered arrays of ultrathin NWs have been successfully obtained by combining SAG and *in situ* post-growth thermal decomposition.

These results represent a fundamental step towards the fabrication via SAG of ordered arrays of nano-LEDs with different emission colours on the same Si substrate, which could enable the production of NW-LEDs on large scale and low cost substrates, and the integration with the Si-based technology. In addition, the presented study paves the way to the realization of vertically aligned ultrathin GaN NWs. In the third chapter important optimizations of the various processing steps required to fabricate a functional NW-LEDs have been discussed.

- We have found that exclusively employing ITO instead of Ni/Au as top contact significantly improves many of the factors that have so far limited device performance; such as low number density of emitting NWs, poor hole injection efficiency, and high turn-on voltage.

4. Investigation of the opto-electronic characteristics of NW-LEDs

- We have demonstrated that NW-LEDs grown on bare Si or on 4-nm-thick AlN layers have comparable performance.

The presented experiments definitely prove that the low density of emitting NWs often reported in literature can be explained by a poor p-type top contact and is thus not caused by limitations intrinsic to (In,Ga)N/GaN NWs grown on Si, such as the presence of Si_xN_y at the interface to the Si substrate or fluctuations in NW sizes. Furthermore, these outcomes, together with the successful growth of ordered arrays of GaN NWs, demonstrates the compatibility of SAG on AlN-buffered Si substrates with device operation. Therefore, this study paves the way for a new generation of LEDs based on homogeneous NW ensembles grown on large size and low cost Si substrates.

In the fourth chapter an in-depth characterization of both opto-electronic and transport properties of the obtained NW-LEDs have been carried out.

- A peculiar double-line structure has been observed in the EL spectra emitted by the NWs. An accurate analysis of the data, supported by simulations of the strain distribution inside the active region of the NW-LEDs, would suggest that the fine structure of the EL peaks is related to the emission from different QWs. More precisely, the compressive strain caused by the (Al,Ga)N EBL in the neighbouring (In,Ga)N QW could shift the emission of this particular QW towards higher energies.
- The prototype NW-LEDs investigated in this thesis exhibit a relatively low EQE smaller than 0.1 %. Although, more advanced structures can provide EQE as high as 1.1 %, the limited performance of the NW-LEDs so far obtained would suggest that still significant improvements has to be achieved to make this type of technology competitive on the market.
- The efficiency droop at high injected current is smaller than that observed in green (In,Ga)N/GaN planar LEDs.
- The analysis of the temperature dependent PL and EL measurements indicates that, although carrier localization phenomena are present, they do not dominate the EL emission properties of the NW-LEDs, at least for normal operation conditions.

It is worth recalling that film-based LEDs look back on at least 20 years of technological development more than the NW-based counterpart. In addition, we remind that the NW-LEDs investigated in this thesis are still prototypes with a rather simple structure, without any particular surface passivation, epoxy lens, or collimating mirrors. Therefore, the EQE presently obtained for NW-LEDs may still be significantly improved, and should not be taken as the basis for assessing their potential.

The forward bias I-V characteristics of different NW-LEDs have been analysed.

- An original model based on a modified version of the classical Shockley equation has been developed.
- The multi-element nature of LEDs based on NW ensembles has been taken into account by assuming a linear dependence of the ideality factor on applied bias.

This novel interpretation of the forward bias I-V characteristics might be very useful to correctly analyse the electrical measurements of NW-LEDs, particularly in case of devices with very pronounced inhomogeneity of the electrical properties. We underline that the

4.4. A physical model for the reverse bias regime

main considerations at the base of the model remain valid also for different types of electrical devices with multi-element nature, regardless the material system employed.

The transport mechanisms in reverse bias regime have been carefully studied by means of DLTS and temperature dependent I-V measurements.

- Two main deep states have been observed in the active region of NW-LEDs at energies of about $E_{t1} \approx 570 \text{ meV}$ and $E_{t2} \approx 840 \text{ meV}$ below the conduction band minimum. These defects exhibit relatively high concentration: the values $N_{t1} \approx 5 \times 10^{16} \text{ cm}^{-3}$ and $N_{t2} \approx 1 \times 10^{16} \text{ cm}^{-3}$ have been estimated by DLTS measurements for the two types of traps.
- The comparison of the signatures of the observed electron traps with the ones reported in literature has indicated that the deep states might originate from native point defects (namely, nitrogen antisites) present in the bulk material, from chains of boundary dislocations at the edge of coalescing NWs, and from dangling bonds present on the free sidewalls.
- A physical model able to describe quantitatively the peculiar I-V-T characteristics of NW-LEDs in reverse bias regime has been developed.
- At moderate and high reverse biases (from -3 to -10 V), the current conduction can be described by the interaction of two competing mechanisms: variable range hopping and emission from Coulomb centres located in the vicinity of the conduction band edge. The latter has been described as the sum of two contributions defined by phonon-assisted tunnelling and the Poole-Frenkel effect.

Several strategies to limit the density of the unwanted defects have been suggested, in summary: less N-rich conditions and higher temperatures than the ones commonly used for the growth of the (In,Ga)N/GaN active region might reduce the density of point defects; an improved alignment of the NWs can reduce the coalescence degree of the NWs thus suppressing the formation of boundary dislocations; dangling bonds on the free sidewalls could be passivated by the deposition of a semi-amorphous shell around the NWs.

In conclusion, it seems fair to say that despite the important improvements achieved in the last years the NW-LED technology has not yet reached its full maturity. Several developments are still possible in terms of both basic research, to better understand the fundamental phenomena, and engineering optimization, to improve the performance of the devices. Nevertheless, it seems plausible to predict a bright future for the NW-LEDs as one of the possible next generation light sources.

Sample list

The growth parameters for all samples presented in this work are listed in Table A.1. The values of the substrate temperatures (T_{sub}) were measured by means of an optical pyrometer if higher than 400 °C and by a thermocouple in the case of lower values. The effective nitrogen flux (Φ_N) and the ones of the metals ($\Phi_{Ga/Al/In}$) are expressed in growth rate units (nm/min); whereas for the Mg flux only the BEP is given. The Si flux was too low to be measured; for all the Si doped samples a cell temperature (T_{Si}) of 1100 °C was used.

Table A.1: List of all samples presented in this work. All samples were grown by MBE at PDI, they are sorted by type. The columns "Sample" and "Lab ID" report the names of the samples as used in this thesis and as labelled in the lab book, respectively.

Sample	Lab ID	Struct.	Sub.	Base NWs (Layer)				Active region + Cap							
				Φ_{N} ($\frac{\text{nm}}{\text{min}}$)	T_{sub} ($^{\circ}\text{C}$)	t_{growth} (min)	$\Phi_{\text{Ga(Al)}}$ ($\frac{\text{nm}}{\text{min}}$)	QW + barrier				EBL + Cap			
								T_{sub} ($^{\circ}\text{C}$)	$t_{\text{QW/bar}}$ (min)	Φ_{Ga} ($\frac{\text{nm}}{\text{min}}$)	Φ_{In} ($\frac{\text{nm}}{\text{min}}$)	T_{Sub} ($^{\circ}\text{C}$)	$t_{\text{EBL/cap}}$ (min)	Φ_{Al} ($\frac{\text{nm}}{\text{min}}$)	BEP_{Mg} (mbar)
AlN layers on Si(111)															
AlN1	M1245	AlN 2 nm	Si(111)	6	680	0.25	(7)								
AlN2	M1279	AlN 4 nm	Si(111)	6	680	0.75	(5.7)								
AlN3	M1251	AlN 8 nm	Si(111)	6	680	1.5	(6)								
AlN4	M1254	AlN 14 nm	Si(111)	6	680	3	(5.7)								
GaN NWs on AlN-buffered Si(111)															
NW1	M1218	GaN NWs	Si(111)	11	805	180	4								
NW2	M1247	GaN NWs 2 nm	AlN	11	805	150	4								
NW3	M1257	GaN NWs 4 nm	AlN	11	805	150	4								
NW4	M1252	GaN NWs 8 nm	AlN	11	805	150	4								
NW5	M1246	GaN NWs 14 nm	AlN	11	805	150	4								

continued on next page

Table A.1 – continued from previous page

Sample	Lab ID	Struct.	Sub.	Base NWs (Layer)				Active region + Cap								
				Φ_{N} ($\frac{\text{nm}}{\text{min}}$)	T_{sub} (°C)	t_{growth} (min)	$\Phi_{\text{Ga(Al)}}$ ($\frac{\text{nm}}{\text{min}}$)	QW + barrier				EBL + Cap				
								T_{sub} (°C)	$t_{\text{QW/bar}}$ (min)	Φ_{Ga} ($\frac{\text{nm}}{\text{min}}$)	Φ_{In} ($\frac{\text{nm}}{\text{min}}$)	T_{Sub} (°C)	$t_{\text{EBL/cap}}$ (min)	Φ_{Al} ($\frac{\text{nm}}{\text{min}}$)	BEP_{Mg} (mbar)	
<i>SAG samples</i>																
SAG1	M81494	GaN NWs	M1314	10	813	180	3									
SAG2	M91096	GaN QWR	M1429	8	846	180	3									
SAG3	M91099	GaN NWs	M1497	8	846	180	3									
<i>Si doped GaN NWs ($T_{\text{Si}} = 1100^\circ\text{C}$)</i>																
NW:Si	M81375	GaN:Si NWs	Si(111)	10	780	90	3									
<i>NW-LED samples</i>																
LED1	M81379	LED 4×QW	Si(111)	10	780	90	3	603	2/8	0.95	0.8	↗ 750	15/120	0.28	3×10^{-10}	
LED2	M81391	LED 4×QW	M1306	10	780	90	3	600	2/8	0.95	0.8	↗ 750	15/120	0.28	3×10^{-10}	
LED3	M81485	LED 4×QW	M1334	10	780	90	3	600	2/8	0.95	0.8	↗ 750	15/120	0.28	3×10^{-10}	
LEDref	M81146	LED 4×QW	Si(111)	10	780	90	3	600	2/8	0.95	0.8	↗ 750	16/110	0.28	1×10^{-8}	
QWref	M81400	NWs+ 8×QW	Si(111)	10	780	90	3	600	2/8	0.95	0.8					

Bibliography

- [1] International Energy Agency. *Light's Labour's Lost: Policies for Energy-efficient Lighting*. OECD in support of the G8 meeting, Paris, 2006.
- [2] C. J. Humphreys. Solid-State Lighting. *MRS Bulletin*, 33(4):459, January 2011.
- [3] S. Pimputkar, J. S. Speck, S. P. DenBaars, and S. Nakamura. Prospects for LED lighting. *Nat. Photon.*, 3(4):180, April 2009.
- [4] S. Li and A. Waag. GaN based nanorods for solid state lighting. *J. Appl. Phys.*, 111(7):071101, 2012.
- [5] N. P. Dasgupta, J. Sun, C. Liu, S. Brittman, S. C. Andrews, J. Lim, H. Gao, R. Yan, and P. Yang. 25th anniversary article: semiconductor nanowires—synthesis, characterization, and applications. *Adv. Mater.*, 26(14):2137, April 2014.
- [6] J. Piprek. Efficiency droop in nitride-based light-emitting diodes. *Phys. Status Solidi A*, 207(10):2217, October 2010.
- [7] J. Cho, E. F. Schubert, and J. K. Kim. Efficiency droop in light-emitting diodes: Challenges and countermeasures. *Laser Photon. Rev.*, 7(3):408, May 2013.
- [8] Frank Glas. Critical dimensions for the plastic relaxation of strained axial heterostructures in free-standing nanowires. *Phys. Rev. B*, 74(12):121302, September 2006.
- [9] S. D. Hersee, A. K. Rishinaramangalam, M. N. Fairchild, L. Zhang, and P. Varangis. Threading defect elimination in GaN nanowires. *J. Mater. Res.*, 26(17):2293, June 2011.
- [10] H.-M. Kim, Y.-H. Cho, H. Lee, S. I. Kim, S. R. Ryu, D. Y. Kim, T. W. Kang, and K. S. Chung. High-Brightness Light Emitting Diodes Using Dislocation-Free Indium Gallium Nitride/Gallium Nitride Multiquantum-Well Nanorod Arrays. *Nano Lett.*, 4(6):1059, June 2004.
- [11] C. Kölper, M. Sabathil, F. Römer, M. Mandl, M. Strassburg, and B. Witzigmann. Core-shell InGaN nanorod light emitting diodes: Electronic and optical device properties. *Phys. Status Solidi A*, 209(11):2304, November 2012.

Bibliography

- [12] E. Calleja, M. Sánchez-García, F. Sánchez, F. Calle, F. Naranjo, E. Muñoz, U. Jahn, and K. H. Ploog. Luminescence properties and defects in GaN nanocolumns grown by molecular beam epitaxy. *Phys. Rev. B*, 62(24):16826, December 2000.
- [13] L. Cerutti, J. Ristić, S. Fernández-Garrido, E. Calleja, A. Trampert, K. H. Ploog, S. Lazić, and J. M. Calleja. Wurtzite GaN nanocolumns grown on Si(001) by molecular beam epitaxy. *Appl. Phys. Lett.*, 88(21):213114, 2006.
- [14] T. Stoica, E. Sutter, R. J. Meijers, R. K. Debnath, R. Calarco, H. Lüth, and D. Grützmacher. Interface and wetting layer effect on the catalyst-free nucleation and growth of GaN nanowires. *Small*, 4(6):751, June 2008.
- [15] What's The Best Business Model For Nanowire LEDs? *Compound Semiconductor - News*, December 2014. URL <http://www.compoundsemiconductor.net/article/95856-whats-the-best-business-model-for-nanowire-leds.html>.
- [16] Nanowire LED developer Aledia raises €28M. *SPIE Optics.org*, June 2015. URL <http://optics.org/news/6/6/35>.
- [17] Hadis Morkoç. *Handbook of Nitride Semiconductors and Devices - Volume 1. Materials Properties, Physics and Growth*. Wiley, 2008. ISBN 978-3-527-40837-5.
- [18] Hadis Morkoç. *Handbook of Nitride Semiconductors and Devices - Volume 3. GaN-based Optical and Electronic Devices*. Wiley, 2008. ISBN 978-3-527-40839-9.
- [19] E. Fred Schubert. *Light-Emitting diodes*. Wiley, 2006. ISBN 978-0-521-86538-8.
- [20] S. M. Sze and Kwok K. Ng. *Physics of Semiconductor Devices, 3rd Edition*. Wiley, 2006. ISBN 978-0-471-14323-9.
- [21] O. Ambacher. Growth and applications of Group III-nitrides. *J. Phys. D: Appl. Phys.*, 31(20):2653, October 1998.
- [22] W. Walukiewicz, J. W. Ager, K. M. Yu, Z. Liliental-Weber, J. Wu, S. X. Li, R. E. Jones, and J. D. Denlinger. Structure and electronic properties of InN and In-rich group III-nitride alloys. *J. Phys. D: Appl. Phys.*, 39(5):R83, March 2006.
- [23] I. Vurgaftman and J. R. Meyer. Band parameters for nitrogen-containing semiconductors. *J. Appl. Phys.*, 94(6):3675, 2003.
- [24] A. Krost and A. Dadgar. GaN-Based Devices on Si. *Phys. Status Solidi A*, 194(2):361, December 2002.
- [25] F. Bernardini, V. Fiorentini, and D. Vanderbilt. Spontaneous polarization and piezoelectric constants of III-V nitrides. *Phys. Rev. B*, 56(16):R10024, October 1997.
- [26] J. Lähnemann, O. Brandt, U. Jahn, C. Pfüller, C. Roder, P. Dogan, F. Grosse, A. Be-labbes, F. Bechstedt, A. Trampert, and L. Geelhaar. Direct experimental determination of the spontaneous polarization of GaN. *Phys. Rev. B*, 86(8):081302, January 2012.
- [27] V. Fiorentini, F. Bernardini, and O. Ambacher. Evidence for nonlinear macroscopic polarization in III-V nitride alloy heterostructures. *Appl. Phys. Lett.*, 80(7):1204, 2002.

- [28] F. Bloch. Ueber die Quantenmechanik der Elektronen in Kristallgittern. *Zeitschrift für Physik*, 52(7):555, July 1929.
- [29] Miguel Ángel Caro Bayo. Theory of elasticity and electric polarization effects in the group-III-nitrides. *Ph.D. Thesis, University College Cork*, 2013.
- [30] F. Sacconi, F. Panetta, M. {Auf der Maur}, A. {Di Carlo}, A. Pecchia, M. Musolino, A. Tahraoui, L. Geelhaar, and H. Riechert. Multiscale approach for the study of optoelectronic properties of InGaN / GaN nanowire light-emitting diodes. *Proc. IEEE*, 978:8156, 2015.
- [31] D. Zhu, D. J. Wallis, and C. J. Humphreys. Prospects of III-nitride optoelectronics grown on Si. *Rep. Prog. Phys.*, 76(10):106501, October 2013.
- [32] C. A. Hurni, A. David, M. J. Cich, R. I. Aldaz, B. Ellis, K. Huang, A. Tyagi, R. A. DeLille, M. D. Craven, F. M. Steranka, and M. R. Krames. Bulk GaN flip-chip violet light-emitting diodes with optimized efficiency for high-power operation. *Appl. Phys. Lett.*, 106(3):031101, January 2015.
- [33] H. J. Round. A note on carborundum. *Electrical World*, 19:309, February 1907.
- [34] R. M. Potter. Silicon Carbide Light-Emitting Diodes. *J. Appl. Phys.*, 40(5):2253, November 1969.
- [35] R. Hall, G. Fenner, J. Kingsley, T. Soltys, and R. Carlson. Coherent Light Emission From GaAs Junctions. *Phys. Rev. Lett.*, 9(9):366, November 1962.
- [36] J. I. Pankove, E. A. Miller, D. Richman, and J. E. Berkeyheiser. Electroluminescence in GaN. *J. Lumin.*, 4(1):63, 1971.
- [37] H. Amano, M. Kito, K. Hiramatsu, and I. Akasaki. P-Type Conduction in Mg-Doped GaN Treated with Low-Energy Electron Beam Irradiation (LEEBI). *Jpn. J. Appl. Phys.*, 28:L2112, December 1989.
- [38] S. Nakamura, M. Senoh, N. Iwasa, and S.-I. Nagahama. High-Brightness InGaN Blue, Green and Yellow Light-Emitting Diodes with Quantum Well Structures. *Jpn. J. Appl. Phys.*, 34:L797, July 1995.
- [39] S. Nakamura, M. Senoh, S.-I. Nagahama, N. Iwasa, T. Yamada, T. Matsushita, Y. Sugimoto, and H. Kiyoku. Room-temperature continuous-wave operation of InGaN multi-quantum-well structure laser diodes. *Appl. Phys. Lett.*, 69(26):4056, December 1996.
- [40] William Shockley. *Electrons and holes in semiconductors: With applications to transistor electronics*. Krieger, 1950. ISBN 0-88275-382-7.
- [41] M. Peter, A. Laubsch, W. Bergbauer, T. Meyer, M. Sabathil, J. Baur, and B. Hahn. New developments in green LEDs. *Phys. Status Solidi A*, 206(6):1125, June 2009.
- [42] T. D. Stanescu and S. Tewari. Majorana fermions in semiconductor nanowires: fundamentals, modeling, and experiment. *J. Phys. Condens. Matter*, 25(23):233201, June 2013.

Bibliography

- [43] H. Sekiguchi, K. Kishino, and A. Kikuchi. GaN/AlGaN nanocolumn ultraviolet light-emitting diodes grown on n-(111) Si by RF-plasma-assisted molecular beam epitaxy. *Electron. Lett.*, 44(2):151, 2008.
- [44] H. Sekiguchi, K. Kishino, and A. Kikuchi. Emission color control from blue to red with nanocolumn diameter of InGaN/GaN nanocolumn arrays grown on same substrate. *Appl. Phys. Lett.*, 96(23):231104, 2010.
- [45] M. Wölz, J. Lähnemann, O. Brandt, V. M. Kaganer, M. Ramsteiner, C. Pfüller, C. Hauswald, C. N. Huang, L. Geelhaar, and H. Riechert. Correlation between In content and emission wavelength of InGaN/GaN nanowire heterostructures. *Nanotechnology*, 23(45):455203, October 2012.
- [46] K. Kishino, J. Kamimura, and K. Kamiyama. Near-Infrared InGaN Nanocolumn Light-Emitting Diodes Operated at 1.46 μ m. *Appl. Phys. Express*, 5:2, 2012.
- [47] S. Albert, A. Bengoechea-Encabo, M. A. Sánchez-García, X. Kong, A. Trampert, and E. Calleja. Selective area growth of In(Ga)N/GaN nanocolumns by molecular beam epitaxy on GaN-buffered Si(111): from ultraviolet to infrared emission. *Nanotechnology*, 24(17):175303, April 2013.
- [48] H.-W. Lin, Y.-J. Lu, H.-Y. Chen, H.-M. Lee, and S. Gwo. InGaN/GaN nanorod array white light-emitting diode. *Appl. Phys. Lett.*, 97(7):073101, 2010.
- [49] C. Kölper, M. Sabathil, M. Mandl, M. Strassburg, and B. Witzigmann. All-InGaN Phosphorless White Light Emitting Diodes : An Efficiency Estimation. *J. Lightwave Technol.*, 30(17):2853, 2012.
- [50] H. P. T. Nguyen, K. Cui, S. Zhang, M. Djavid, A. Korinek, G. a Botton, and Z. Mi. Controlling Electron Overflow in Phosphor-Free InGaN/GaN Nanowire White Light-Emitting Diodes. *Nano Lett.*, 12(3):1317, March 2012.
- [51] Martin Wölz. Control of the emission wavelength of gallium nitride-based nanowire light-emitting diodes. *Ph.D. thesis, Humboldt-Universität zu Berlin*, 2013.
- [52] M. Wölz, M. Ramsteiner, V. M. Kaganer, O. Brandt, L. Geelhaar, and H. Riechert. Strain engineering of nanowire multi-quantum well demonstrated by Raman spectroscopy. *Nano Lett.*, 13(9):4053, September 2013.
- [53] M. Musolino, A. Tahraoui, S. Fernández-Garrido, O. Brandt, A. Trampert, L. Geelhaar, and H. Riechert. Compatibility of the selective area growth of GaN nanowires on AlN-buffered Si substrates with the operation of light emitting diodes. *Nanotechnology*, 26(8):085605, February 2015.
- [54] M. A. Herman and H. Sitter. *Molecular beam epitaxy: Fundamentals and current status*. Springer-Verlag, 1996. ISBN 978-3-642-97098-6.
- [55] E. H. C. Parker. *The Technology and physics of molecular beam epitaxy*. Plenum Press, 1985. ISBN 978-1-4899-5366-7.
- [56] W. E. Hoke, P. J. Lemonias, and D. G. Weir. Evaluation of a new plasma source for molecular beam epitaxial growth of InN and GaN films. *J. Cryst. Growth*, 111:1024, May 1991.

- [57] W. Braun. *Applied RHEED: Reflection High-energy Electron Diffraction During Crystal Growth*. Springer, 1999. ISBN 9783540651994.
- [58] A. Ichimiya and P. I. Cohen. *Reflection High-Energy Electron Diffraction*. Cambridge University Press, 2004. ISBN 978-0-5214-5373-8.
- [59] J. H. Batey. Quadropole gas analysers. *Vacuum*, 37:659, 1987.
- [60] N. J. C. Ingle, A. Yuskas, R. Wicks, M. Paul, and S. Leung. The structural analysis possibilities of reflection high energy electron diffraction. *J. Phys. D: Appl. Phys.*, 43(13):133001, April 2010.
- [61] S. W. King, R. F. Davis, and R. J. Nemanich. Kinetics of Ga and In desorption from (7×7) Si(111) and (3×3) 6H-SiC(0001) surfaces. *Surf. Sci.*, 602(2):405, January 2008.
- [62] C. Hu. Hysteresis in the (1×1)-(7×7) first-order phase transition on the Si(111) surface. *Surf. Sci.*, 487(1):191, July 2001.
- [63] J. S. Brown, G. Koblmüller, F. Wu, R. Averbeck, H. Riechert, and J. S. Speck. Ga adsorbate on (0001) GaN: In situ characterization with quadrupole mass spectrometry and reflection high-energy electron diffraction. *J. Appl. Phys.*, 99(7):074902, 2006.
- [64] G. Koblmüller, S. Fernández-Garrido, E. Calleja, and J. S. Speck. In situ investigation of growth modes during plasma-assisted molecular beam epitaxy of (0001) GaN. *Appl. Phys. Lett.*, 91(16):161904, 2007.
- [65] S. Fernández-Garrido, G. Koblmüller, E. Calleja, and J. S. Speck. In situ GaN decomposition analysis by quadrupole mass spectrometry and reflection high-energy electron diffraction. *J. Appl. Phys.*, 104(3):33541, 2008.
- [66] C. Chèze, L. Geelhaar, A. Trampert, and H. Riechert. In situ investigation of self-induced GaN nanowire nucleation on Si. *Appl. Phys. Lett.*, 97(4):43101, 2010.
- [67] F. Limbach, R. Caterino, T. Gotschke, T. Stoica, R. Calarco, L. Geelhaar, and H. Riechert. The influence of Mg doping on the nucleation of self-induced GaN nanowires. *AIP Advances*, 2(1):012157, 2012.
- [68] M. Musolino, A. Tahraoui, F. Limbach, J. Lähnemann, U. Jahn, O. Brandt, L. Geelhaar, and H. Riechert. Understanding peculiarities in the optoelectronic characteristics of light emitting diodes based on (In,Ga)N/GaN nanowires. *Appl. Phys. Lett.*, 105:083505, 2014.
- [69] S. Fernández-Garrido, J. K. Zettler, L. Geelhaar, and O. Brandt. Monitoring the Formation of Nanowires by Line-of-Sight Quadrupole Mass Spectrometry: A Comprehensive Description of the Temporal Evolution of GaN Nanowire Ensembles. *Nano Lett.*, 15(3):1930, February 2015.
- [70] G. Koblmüller. *Studies of Nucleation and Surfaces Kinetics in Molecular Beam Epitaxy*. Ph.D. thesis, T. U. Wien, 2005.
- [71] B. Heying, R. Averbeck, L. F. Chen, E. Haus, H. Riechert, and J. S. Speck. Control of GaN surface morphologies using plasma-assisted molecular beam epitaxy. *J. Appl. Phys.*, 88(4):1855, 2000.

Bibliography

- [72] M. Musolino. *Growth and investigation of AlGaIn/GaN heterostructures for applications in solid state electronics*. Master thesis, Università degli studi di Roma Tor Vergata, 2011.
- [73] S. Fernández-Garrido, G. Koblmüller, H. Riechert, and J. S. Speck. In situ GaN decomposition analysis by quadrupole mass spectrometry and reflection high-energy electron diffraction. *J. Appl. Phys.*, 104(3):33541, 2008.
- [74] Y. R. Wu, C. H. Chiu, C. Y. Chang, P. C. Yu, and H. C. Kuo. Size-Dependent Strain Relaxation and Optical Characteristics of InGaIn/GaN Nanorod LEDs. *IEEE J. Sel. Topics Quantum Electron.*, 15(4):1226, July 2009.
- [75] Toma Stoica, Anna Haab, David Griesche, Martin Mikulics, Friederich Limbach, Timo Schumann, Tobias Gotschke, Eli Sutter, Raffaella Calarco, Hilde Hardtdegen, and Detlev Grützmacher. Photoluminescence and Raman scattering studies of GaN nanowires obtained by top-down and bottom-up approaches. *Proc. MRS*, 1408:29, February 2012.
- [76] E. Ertekin, P. A. Greaney, D. C. Chrzan, and T. D. Sands. Equilibrium limits of coherency in strained nanowire heterostructures. *J. Appl. Phys.*, 97(11):114325, 2005.
- [77] S. Albert, A. Bengoechea-Encabo, M. Sabido-Siller, M. Müller, G. Schmidt, S. Metzner, P. Veit, F. Bertram, M. A. Sánchez-García, Jürgen Christen, and E. Calleja. Growth of InGaIn/GaN core-shell structures on selectively etched GaN rods by molecular beam epitaxy. *J. Cryst. Growth*, 392:5, April 2014.
- [78] R. S. Wagner and W. C. Ellis. Vapor-Solid-Liquid mechanism of single crystal growth. *Appl. Phys. Lett.*, 4(5):89, 1964.
- [79] H. J. Joyce, Q. Gao, H. Hoe-Tan, C. Jagadish, Y. Kim, J. Zou, L. M. Smith, H. E. Jackson, J. M. Yarrison-Rice, P. Parkinson, and M. B. Johnston. III-V semiconductor nanowires for optoelectronic device applications. *Prog. Quantum Electron.*, 35:23, March 2011. ISSN 00796727.
- [80] M. C. Putnam, M. A. Filler, B. M. Kayes, M. D. Kelzenberg, Y. Guan, N. S. Lewis, J. M. Eiler, and H. A. Atwater. Secondary Ion Mass Spectrometry of Vapor-Liquid-Solid Grown, Au-Catalyzed, Si Wires. *Nano Lett.*, 8(10):3109, 2008.
- [81] J. E. Allen, E. R. Hemesath, D. E. Perea, J. L. Lensch-Falk, Z. Y. Li, F. Yin, M. H. Gass, P. Wang, A. L. Bleloch, R. E. Palmer, and L. J. Lauhon. High-resolution detection of Au catalyst atoms in Si nanowires. *Nat. Nanotechnol.*, 3(3):168, 2008.
- [82] C. Chèze, L. Geelhaar, O. Brandt, W. Weber, H. Riechert, S. Münch, R. Rothemund, S. Reitzenstein, A. Forchel, T. Kehagias, P. Komninou, G. Dimitrakopoulos, and T. Karakostas. Direct comparison of catalyst-free and catalyst-induced GaIn nanowires. *Nano Res.*, 3(7):528, 2010.
- [83] C. Chèze, L. Geelhaar, B. Jenichen, and H. Riechert. Different growth rates for catalyst-induced and self-induced GaIn nanowires. *Appl. Phys. Lett.*, 97(15):153105, 2010.
- [84] C. Chèze. *Investigation and comparison of GaIn nanowire nucleation and growth by the catalyst-assisted and self-induced approaches*. Ph.D. thesis, Humboldt-Universität zu Berlin, 2010.

- [85] M. Yoshizawa, A. Kikuchi, M. Mori, N. Fujita, and K. Kishino. Growth of Self-Organized GaN Nanostructures on Al₂O₃ (0001) by RF-Radical Source Molecular Beam Epitaxy. *Jpn. J. Appl. Phys.*, 36(4B):L459, April 1997.
- [86] M. A. Sanchez-García, E. Calleja, E. Monroy, F. J. Sanchez, F. Calle, E. Muñoz, and R. Beresford. The effect of the III/V ratio and substrate temperature on the morphology and properties of GaN- and AlN-layers grown by molecular beam epitaxy on Si(1 1 1). *J. Cryst. Growth*, 183:23, January 1998.
- [87] S. Fernández-Garrido, E. Grandal, J. Calleja, M. A. Sanchez-García, and D. Lopez-Romero. A growth diagram for plasma-assisted molecular beam epitaxy of GaN nanocolumns on Si(111). *J. Appl. Phys.*, 106(12):126102, 2009.
- [88] J. Ristić, E. Calleja, S. Fernández-Garrido, L. Cerutti, A. Trampert, U. Jahn, and K. H. Ploog. On the mechanisms of spontaneous growth of III-nitride nanocolumns by plasma-assisted molecular beam epitaxy. *J. Cryst. Growth*, 310(18):4035, August 2008.
- [89] V. Consonni, M. Hanke, M. Knelangen, L. Geelhaar, A. Trampert, and H. Riechert. Nucleation mechanisms of self-induced GaN nanowires grown on an amorphous interlayer. *Phys. Rev. B*, 83(3):035310, January 2011.
- [90] V. G. Dubrovskii, V. Consonni, A. Trampert, L. Geelhaar, and H. Riechert. Scaling thermodynamic model for the self-induced nucleation of GaN nanowires. *Phys. Rev. B*, 85(16):165317, April 2012.
- [91] V. Consonni. Self-induced growth of GaN nanowires by molecular beam epitaxy: A critical review of the formation mechanisms. *Phys. Status Solidi RRL*, 7(10):699, October 2013.
- [92] R. Calarco, R. J. Meijers, R. K. Debnath, T. Stoica, E. Sutter, and H. Lüth. Nucleation and growth of GaN nanowires on Si(111) performed by molecular beam epitaxy. *Nano Lett.*, 7(8):2248, August 2007.
- [93] V. Consonni, V. G. Dubrovskii, A. Trampert, L. Geelhaar, and H. Riechert. Quantitative description for the growth rate of self-induced GaN nanowires. *Phys. Rev. B*, 85(15):155313, April 2012.
- [94] S. Fernández-Garrido, V. M. Kaganer, K. K. Sabelfeld, T. Gotschke, J. Grandal, E. Calleja, L. Geelhaar, and O. Brandt. Self-Regulated Radius of Spontaneously Formed GaN Nanowires in Molecular Beam Epitaxy. *Nano Lett.*, 13(7):3274, June 2013.
- [95] M. Tchernycheva, C. Sartel, G. E. Cirlin, L. Travers, G. Patriarche, J.-C. Harmand, L. S. Dang, J. Renard, B. Gayral, L. Nevou, and F. Julien. Growth of GaN free-standing nanowires by plasma-assisted molecular beam epitaxy: structural and optical characterization. *Nanotechnology*, 18(38):385306, September 2007.
- [96] R. Songmuang, O. Landré, and B. Daudin. From nucleation to growth of catalyst-free GaN nanowires on thin AlN buffer layer. *Appl. Phys. Lett.*, 91(25):251902, 2007.
- [97] K. A. Bertness, A. Roshko, L. M. Mansfield, T. E. Harvey, and N. A. Sanford. Mechanism for spontaneous growth of GaN nanowires with molecular beam epitaxy. *J. Cryst. Growth*, 310(13):3154, June 2008.

Bibliography

- [98] R. K. Debnath, R. J. Meijers, T. Richter, T. Stoica, R. Calarco, and H. Lüth. Mechanism of molecular beam epitaxy growth of GaN nanowires on Si(111). *Appl. Phys. Lett.*, 90(12):123117, 2007.
- [99] B. Jenichen, O. Brandt, C. Pfüller, P. Dogan, M. Knelangen, and A. Trampert. Macro- and micro-strain in GaN nanowires on Si(111). *Nanotechnology*, 22(29):295714, July 2011.
- [100] V. Consonni, M. Knelangen, U. Jahn, A. Trampert, L. Geelhaar, and H. Riechert. Effects of nanowire coalescence on their structural and optical properties on a local scale. *Appl. Phys. Lett.*, 95(24):241910, 2009.
- [101] S. Fernández-Garrido, V. M. Kaganer, C. Hauswald, B. Jenichen, M. Ramsteiner, V. Consonni, L. Geelhaar, and O. Brandt. Correlation between the structural and optical properties of spontaneously formed GaN nanowires: a quantitative evaluation of the impact of nanowire coalescence. *Nanotechnology*, 25(45):455702, November 2014.
- [102] S. Fernández-Garrido, X. Kong, T. Gotschke, R. Calarco, L. Geelhaar, A. Trampert, and O. Brandt. Spontaneous Nucleation and Growth of GaN Nanowires: The Fundamental Role of Crystal Polarity. *Nano Lett.*, 12(12):6119, November 2012.
- [103] A. Feduniewicz, C. Skierbiszewski, M. Siekacz, Z. R. Wasilewski, I. Sproule, S. Grzanka, R. Jakiela, J. Borysiuk, G. Kamler, E. Litwin-Staszewska, R. Czernecki, M. Boćkowski, and S. Porowski. Control of Mg doping of GaN in RF-plasma molecular beam epitaxy. *J. Cryst. Growth*, 278:443, May 2005.
- [104] S. F. Chichibu, A. Setoguchi, A. Uedono, K. Yoshimura, and M. Sumiya. Impact of growth polar direction on the optical properties of GaN grown by metalorganic vapor phase epitaxy. *Appl. Phys. Lett.*, 78(1):28, January 2001.
- [105] A. J. Ptak, L. J. Holbert, L. Ting, C. H. Swartz, M. Moldovan, N. C. Giles, T. H. Myers, P. Van Lierde, C. Tian, R. A. Hockett, S. Mitha, A. E. Wickenden, D. D. Koleske, and R. L. Henry. Controlled oxygen doping of GaN using plasma assisted molecular-beam epitaxy. *Appl. Phys. Lett.*, 79(17):2740, October 2001.
- [106] K. Xu and A. Yoshikawa. Effects of film polarities on InN growth by molecular-beam epitaxy. *Appl. Phys. Lett.*, 83(2):251, 2003.
- [107] D. N. Nath, E. Guer, S. A. Ringel, and S. Rajan. Molecular beam epitaxy of N-polar InGaN. *Appl. Phys. Lett.*, 97(7):071903, 2010.
- [108] X. Kong, J. Ristić, M. A. Sánchez-García, E. Calleja, and A. Trampert. Polarity determination by electron energy-loss spectroscopy: application to ultra-small III-nitride semiconductor nanocolumns. *Nanotechnology*, 22(41):415701, October 2011.
- [109] K. Hestroffer, C. Leclerc, C. Bougerol, H. Renevier, and B. Daudin. Polarity of GaN nanowires grown by plasma-assisted molecular beam epitaxy on Si(111). *Phys. Rev. B*, 84(24):245302, December 2011.
- [110] M. I. den Hertog, F. Gonzalez-Posada, R. Songmuang, J. L. Rouviere, T. Fournier, B. Fernandez, and E. Monroy. Correlation of Polarity and Crystal Structure with Optoelectronic and Transport Properties of GaN/AlN/GaN Nanowire Sensors. *Nano Lett.*, 12(11):5691, November 2012.

- [111] S. Wright and H. Kroemer. Reduction of oxides on silicon by heating in a gallium molecular beam at 800°C. *Appl. Phys. Lett.*, 36(3):210, 1980.
- [112] A. Wierzbicka, Z. R. Zytkeiwicz, S. Kret, J. Borysiuk, P. Dluzewski, M. Sobanska, K. Klosek, A. Reszka, G. Tchutchulashvili, A. Cabaj, and E. Lusakowska. Influence of substrate nitridation temperature on epitaxial alignment of GaN nanowires to Si(111) substrate. *Nanotechnology*, 24(3):035703, December 2012.
- [113] K. Hestroffer, C. Leclere, V. Cantelli, C. Bougerol, H. Renevier, and B. Daudin. In situ study of self-assembled GaN nanowires nucleation on Si(111) by plasma-assisted molecular beam epitaxy. *Appl. Phys. Lett.*, 100(21):212107, 2012.
- [114] S. Gangopadhyay, T. Schmidt, and J. Falta. Initial stage of silicon nitride nucleation on Si(111) by rf plasma-assisted growth. *e-J. Surf. Sci. Nanotech.*, 4:84, January 2006.
- [115] Friederich Limbach. Steps towards a gan nanowire based light emitting diode and its integration with si-mos technology. *Ph.D. thesis, Humboldt-Universität zu Berlin*, 2012.
- [116] A. C. E. Chia, J. P. Boulanger, and R. R. LaPierre. Unlocking doping and compositional profiles of nanowire ensembles using SIMS. *Nanotechnology*, 24(4):045701, February 2013.
- [117] K. K. Sabelfeld, V. M. Kaganer, F. Limbach, P. Dogan, O. Brandt, L. Geelhaar, and H. Riechert. Height self-equilibration during the growth of dense nanowire ensembles: Order emerging from disorder. *Appl. Phys. Lett.*, 103(13):133105, 2013.
- [118] Robert Averbeck and Henning Riechert. Quantitative Model for the MBE-Growth of Ternary Nitrides. *Phys. Status Solidi A*, 176(1):301, November 1999.
- [119] C. S. Gallinat, G. Koblmüller, J. S. Brown, and J. S. Speck. A growth diagram for plasma-assisted molecular beam epitaxy of In-face InN. *J. Appl. Phys.*, 102(6):064907, 2007.
- [120] C. Denker, J. Malindretos, F. Werner, F. Limbach, H. Schuhmann, T. Niermann, M. Seibt, and A. Rizzi. Self-organized growth of InN-nanocolumns on p-Si(111) by MBE. *Phys. Status Solidi C*, 5(6):1706, May 2008.
- [121] M. Wölz, S. Fernández-Garrido, C. Hauswald, O. Brandt, F. Limbach, L. Geelhaar, and H. Riechert. Indium incorporation in InGaN/GaN nanowire heterostructures investigated by line-of-sight quadrupole mass spectrometry. *Cryst. Growth Des.*, 12:5686, 2012.
- [122] M. Wölz, V. M. Kaganer, O. Brandt, L. Geelhaar, and H. Riechert. Analyzing the growth of $\text{In}_x\text{Ga}_{1-x}\text{N}/\text{GaN}$ superlattices in self-induced GaN nanowires by x-ray diffraction. *Appl. Phys. Lett.*, 98:261907, 2011.
- [123] M. D. Brubaker, P. T. Blanchard, J. B. Schlager, A. W. Sanders, A. M. Herrero, A. Roshko, S. M. Duff, T. E. Harvey, V. M. Bright, N. A. Sanford, and K. A. Bertness. Toward Discrete Axial p–n Junction Nanowire Light-Emitting Diodes Grown by Plasma-Assisted Molecular Beam Epitaxy. *J. Electron. Mater.*, 42(5):868, March 2013.

Bibliography

- [124] L. T. Romano, J. E. Northrup, A. J. Ptak, and T. H. Myers. Faceted inversion domain boundary in GaN films doped with Mg. *Appl. Phys. Lett.*, 77(16):2479, October 2000.
- [125] A. Kikuchi, M. Kawai, M. Tada, and K. Kishino. InGaN/GaN Multiple Quantum Disk Nanocolumn Light-Emitting Diodes Grown on (111) Si Substrate. *Jpn. J. Appl. Phys.*, 43(No. 12A):L1524, November 2004.
- [126] W. Guo, M. Zhang, A. Banerjee, and P. Bhattacharya. Catalyst-free InGaN/GaN nanowire light emitting diodes grown on (001) silicon by molecular beam epitaxy. *Nano Lett.*, 10(9):3355, September 2010.
- [127] A.-L. Bavecove, G. Tourbot, E. Pougéoise, J. Garcia, P. Gilet, F. Levy, B. André, G. Feuillet, B. Gayral, B. Daudin, and L. S. Dang. GaN-based nanowires: From nanometric-scale characterization to light emitting diodes. *Phys. Status Solidi A*, 207(6):1425, May 2010.
- [128] R. Armitage and K. Tsubaki. Multicolour luminescence from InGaN quantum wells grown over GaN nanowire arrays by molecular-beam epitaxy. *Nanotechnology*, 21(19):195202, May 2010.
- [129] H. P. T. Nguyen, S. Zhang, K. Cui, X. Han, S. Fatholouloumi, M. Couillard, G. Botton, and Z. Mi. p-Type modulation doped InGaN/GaN dot-in-a-wire white-light-emitting diodes monolithically grown on Si(111). *Nano Lett.*, 11(5):1919, May 2011.
- [130] A.-L. Bavecove, D. Salomon, M. Lafossas, B. Martin, A. Dussaigne, F. Levy, B. André, P. Ferret, C. Durand, J. Eymery, L. S. Dang, and P. Gilet. Light emitting diodes based on GaN core/shell wires grown by MOVPE on n-type Si substrate. *Electron. Lett.*, 47(13):765, 2011.
- [131] F. Limbach, C. Hauswald, J. Lähnemann, M. Wölz, O. Brandt, A. Trampert, M. Hanke, U. Jahn, R. Calarco, L. Geelhaar, and H. Riechert. Current path in light emitting diodes based on nanowire ensembles. *Nanotechnology*, 23(46):465301, November 2012.
- [132] D. Salomon, A. Dussaigne, M. Lafossas, C. Durand, C. Bougerol, P. Ferret, and J. Eymery. Metal organic vapour-phase epitaxy growth of GaN wires on Si (111) for light-emitting diode applications. *Nanoscale Res. Lett.*, 8(1):61, January 2013.
- [133] A.-L. Bavecove, G. Tourbot, J. Garcia, Y. Désières, P. Gilet, F. Levy, B. André, B. Gayral, B. Daudin, and L. S. Dang. Submicrometre resolved optical characterization of green nanowire-based light emitting diodes. *Nanotechnology*, 22(34):345705, August 2011.
- [134] K. Kishino, K. Nagashima, and K. Yamano. Monolithic Integration of InGaN-Based Nanocolumn Light-Emitting Diodes with Different Emission Colors. *Appl. Phys. Express*, 6:012101, 2012.
- [135] S. D. Hersee, X. Sun, and X. Wang. The controlled growth of GaN nanowires. *Nano Lett.*, 6(8):1808, August 2006.
- [136] W. Bergbauer, M. Strassburg, C. Kölper, N. Linder, C. Roder, J. Lähnemann, A. Trampert, S. Fündling, S. F. Li, H.-H. Wehmann, and A. Waag. Continuous-flux MOVPE growth of position-controlled N-face GaN nanorods and embedded InGaN quantum wells. *Nanotechnology*, 21(30):305201, July 2010.

- [137] K. Choi, M. Arita, and Y. Arakawa. Selective-area growth of thin GaN nanowires by MOCVD. *J. Cryst. Growth*, 357:58, October 2012.
- [138] H. Sekiguchi, K. Kishino, and A. Kikuchi. Ti-mask Selective-Area Growth of GaN by RF-Plasma-Assisted Molecular-Beam Epitaxy for Fabricating Regularly Arranged InGaN/GaN Nanocolumns. *Appl. Phys. Express*, 1:124002, December 2008.
- [139] K. Kishino, H. Sekiguchi, and A. Kikuchi. Improved Ti-mask selective-area growth (SAG) by rf-plasma-assisted molecular beam epitaxy demonstrating extremely uniform GaN nanocolumn arrays. *J. Cryst. Growth*, 311(7):2063, March 2009.
- [140] C. Denker, J. Malindretos, B. Landgraf, and A. Rizzi. Catalyst-free selective area growth of InN nanocolumns by MBE. *ArXiv e-prints*, 0905:3133, May 2009.
- [141] S. Ishizawa, K. Kishino, and A. Kikuchi. Selective-Area Growth of GaN Nanocolumns on Si(111) Substrates Using Nitrided Al Nanopatterns by RF-Plasma-Assisted Molecular-Beam Epitaxy. *Appl. Phys. Express*, 1(1):015006, January 2008.
- [142] K. A. Bertness, A. W. Sanders, D. M. Rourke, T. E. Harvey, A. Roshko, J. B. Schlager, and N. A. Sanford. Controlled Nucleation of GaN Nanowires Grown with Molecular Beam Epitaxy. *Adv. Funct. Mater.*, 20(17):2911, September 2010.
- [143] T. Schumann, T. Gotschke, F. Limbach, T. Stoica, and R. Calarco. Selective-area catalyst-free MBE growth of GaN nanowires using a patterned oxide layer. *Nanotechnology*, 22(9):095603, March 2011.
- [144] Tobias Gotschke. Untersuchungen zum geordneten wachstum von iii-nitrid nanodrähten. *Ph.D. thesis, Humboldt-Universität zu Berlin*, 2011.
- [145] V. Consonni, A. Trampert, L. Geelhaar, and H. Riechert. Physical origin of the incubation time of self-induced GaN nanowires. *Appl. Phys. Lett.*, 99(3):033102, 2011.
- [146] H. P. D. Schenk, G. D. Kipshidze, U. Kaiser, A. Fissel, J. Kräulich, J. Schulze, and W. Richter. Investigation of two-dimensional growth of AlN(0001) on Si(111) by plasma-assisted molecular beam epitaxy. *J. Cryst. Growth*, 200(45):1059, April 1999.
- [147] A. Madan, I. Kim, S. Cheng, P. Yashar, V. Dravid, and S. Barnett. Stabilization of Cubic AlN in Epitaxial AlN/TiN Superlattices. *Phys. Rev. Lett.*, 78(9):1743, March 1997.
- [148] W. Lin, L. Meng, G. Chen, and H. Liu. Epitaxial growth of cubic AlN films on (100) and (111) silicon by pulsed laser ablation. *Appl. Phys. Lett.*, 66(16):2066, April 1995.
- [149] S. Okubo, N. Shibata, T. Saito, and Y. Ikuhara. Formation of cubic-AlN layer on MgO(100) substrate. *J. Cryst. Growth*, 189:452, 1998.
- [150] O. Bierwagen, L. Geelhaar, X. Gay, M. Piešiš, H. Riechert, B. Jobst, and A. Rucki. Leakage currents at crystallites in ZrAl_xO_y thin films measured by conductive atomic-force microscopy. *Appl. Phys. Lett.*, 90(23):232901, June 2007.

Bibliography

- [151] L. Brockway, C. Pendyala, J. Jasinski, M. K. Sunkara, and S. Vaddiraju. A postsynthesis decomposition strategy for group III-nitride quantum wires. *Cryst. Growth Des.*, 11:4559, 2011.
- [152] T. Gotschke, T. Schumann, F. Limbach, T. Stoica, and R. Calarco. Influence of the adatom diffusion on selective growth of GaN nanowire regular arrays. *Appl. Phys. Lett.*, 98(10):103102, 2011.
- [153] L. V. Keldysh. Coulomb interaction in thin semiconductor and semimetal films. *JETP Lett.*, 29(11):658, 1979.
- [154] M. Diarra, Y.-M. Niquet, C. Delerue, and G. Allan. Ionization energy of donor and acceptor impurities in semiconductor devices: Importance of dielectric confinement. *Phys. Rev. B*, 75(4):45301, January 2007.
- [155] E. A. Muljarov, E. A. Zhukov, V. S. Dneprovskii, and Y. Masumoto. Dielectrically enhanced excitons in semiconductor-insulator quantum wires: Theory and experiment. *Phys. Rev. B*, 62(11):7420, 2000.
- [156] X. Fu, C. Su, Q. Fu, X. Zhu, R. Zhu, C. Liu, Z. Liao, J. Xu, W. Guo, J. Feng, J. Li, and D. Yu. Tailoring exciton dynamics by elastic strain-gradient in semiconductors. *Adv. Mater.*, 26(16):2572, April 2014.
- [157] S. D. Hersee, M. Fairchild, A. K. Rishinaramangalam, M. S. Ferdous, L. Zhang, P. M. Varangis, B. S. Swartzentruber, and A. A. Talin. GaN nanowire light emitting diodes based on templated and scalable nanowire growth. *Electron. Lett.*, 45(1):75, 2009.
- [158] W. Guo, A. Banerjee, P. Bhattacharya, and B. S. Ooi. InGaN/GaN disk-in-nanowire white light emitting diodes on (001) silicon. *Appl. Phys. Lett.*, 98(19):193102, 2011.
- [159] V. Consonni, M. Knelangen, A. Trampert, L. Geelhaar, and H. Riechert. Nucleation and coalescence effects on the density of self-induced GaN nanowires grown by molecular beam epitaxy. *Appl. Phys. Lett.*, 98(7):071913, 2011.
- [160] A. C. E. Chia and R. R. LaPierre. Contact planarization of ensemble nanowires. *Nanotechnology*, 22(24):245304, June 2011.
- [161] Dow Corning Corporation. Dow Corning XR-1541 E-Beam Resist. <http://www.dowcorning.com/content/publishedlit/11-1547e-01.pdf>, 2008.
- [162] Dow Corning Corporation. Dow Corning FOx-1x and FOx-2x Flowable Oxides. <http://www.dowcorning.com/DataFiles/090276fe801e1020.pdf>, 2015.
- [163] X. Guo and E. F. Schubert. Current crowding and optical saturation effects in GaInN/GaN light-emitting diodes grown on insulating substrates. *Appl. Phys. Lett.*, 78(21):3337, May 2001.
- [164] F. Akyol, D. N. Nath, S. Krishnamoorthy, P. S. Park, and S. Rajan. Suppression of electron overflow and efficiency droop in N-polar GaN green light emitting diodes. *Appl. Phys. Lett.*, 100(11):111118, 2012.

- [165] C.-Y. Wang, L.-Y. Chen, C.-P. Chen, Y.-W. Cheng, M.-Y. Ke, M.-Y. Hsieh, H.-M. Wu, L.-H. Peng, and J.-J. Huang. GaN nanorod light emitting diode arrays with a nearly constant electroluminescent peak wavelength. *Optics express*, 16(14):10549, July 2008.
- [166] Y.C. Lin, S.J. Chang, Y.K. Su, T.Y. Tsai, C.S. Chang, S.C. Shei, C.W. Kuo, and S.C. Chen. InGaN/GaN light emitting diodes with Ni/Au, Ni/ITO and ITO p-type contacts. *Solid-State Electron.*, 47(5):849, 2003.
- [167] Y.-H. Ra, R. Navamathavan, J.-H. Park, and C.-R. Lee. High-quality uniaxial $\text{In}_x\text{Ga}_{1-x}\text{N}$ /GaN multiple quantum well (MQW) nanowires (NWs) on Si(111) grown by metal-organic chemical vapor deposition (MOCVD) and light-emitting diode (LED) fabrication. *ACS applied materials & interfaces*, 5(6):2111, March 2013.
- [168] A. M Herrero, P. T. Blanchard, A. Sanders, M. D. Brubaker, N. Sanford, A. Roshko, and K. A. Bertness. Microstructure evolution and development of annealed Ni/Au contacts to GaN nanowires. *Nanotechnology*, 23(36):365203, September 2012.
- [169] O. Brandt, S. Fernández-Garrido, J. K. Zettler, E. Luna, U. Jahn, C. Chèze, and V. M. Kaganer. Statistical Analysis of the Shape of One-Dimensional Nanostructures: Determining the Coalescence Degree of Spontaneously Formed GaN Nanowires. *Cryst. Growth Des.*, 14(5):2246, May 2014.
- [170] H. P. T. Nguyen, S. Zhang, A. T. Connie, M. G. Kibria, Q. Wang, I. Shih, and Z. Mi. Breaking the carrier injection bottleneck of phosphor-free nanowire white light-emitting diodes. *Nano Lett.*, 13(11):5437, November 2013.
- [171] Q. Wang, A. T. Connie, H. P. T. Nguyen, M. G. Kibria, S. Zhao, S. Sharif, I. Shih, and Z. Mi. Highly efficient, spectrally pure 340 nm ultraviolet emission from $\text{Al}_x\text{Ga}_{1-x}\text{N}$ nanowire based light emitting diodes. *Nanotechnology*, 24(34):345201, August 2013.
- [172] S. Jahangir, T. Schimpke, M. Strassburg, K. A. Grossklaus, J. M. Millunchick, and P. Bhattacharya. Red-Emitting ($\lambda = 610$ nm) $\text{In}_{0.51}\text{Ga}_{0.49}\text{N}$ /GaN Disk-in-Nanowire Light Emitting Diodes on Silicon. *IEEE J. Quantum Electron.*, 50(7):530, July 2014.
- [173] Y.-J. Lee, C.-J. Lee, C.-H. Chen, T.-C. Lu, and H.-C. Kuo. Elucidating the Physical Property of the InGaN Nanorod Light-Emitting Diode: Large Tunneling Effect. *IEEE J. Sel. Topics Quantum Electron.*, 17(4):985, July 2011.
- [174] C.-H. Wang, Y.-W. Huang, S.-E. Wu, and C.-P. Liu. Is it viable to improve light output efficiency by nano-light-emitting diodes? *Appl. Phys. Lett.*, 103(23):233113, 2013.
- [175] J. M. Shah, Y.-L. Li, T. Gessmann, and E. F. Schubert. Experimental analysis and theoretical model for anomalously high ideality factors ($n > 2.0$) in AlGaIn/GaN p-n junction diodes. *J. Appl. Phys.*, 94(4):2627, August 2003.
- [176] D. van Treeck. *Analysis of (In,Ga)N/GaN nanowire LEDs: From the ensemble to single nanowires*. Master thesis, Technische Universität Berlin, 2015.

Bibliography

- [177] H. P. T. Nguyen, M. Djavid, K. Cui, and Z. Mi. Temperature-dependent nonradiative recombination processes in GaN-based nanowire white-light-emitting diodes on silicon. *Nanotechnology*, 23(19):194012, May 2012.
- [178] S. Zhang, A. T. Connie, D. A. Laleyan, H. P. T. Nguyen, Q. Wang, J. Song, I. Shih, and Z. Mi. On the Carrier Injection Efficiency and Thermal Property of InGaN / GaN Axial Nanowire Light Emitting Diodes. *IEEE J. Quantum Electron.*, 50(6):483, 2014.
- [179] K. Kishino and K. Yamano. Green-Light Nanocolumn Light Emitting Diodes with Triangular-Lattice Uniform Arrays of InGaN-Based Nanocolumns. *IEEE J. Quantum Electron.*, 50(7):538, 2014.
- [180] J. Lähnemann, C. Hauswald, M. Wölz, U. Jahn, M. Hanke, L. Geelhaar, and O. Brandt. Localization and defects in axial (In,Ga)N/GaN nanowire heterostructures investigated by spatially resolved luminescence spectroscopy. *J. Phys. D: Appl. Phys.*, 47(39):394010, October 2014.
- [181] T. Kuroda and A. Tackeuchi. Influence of free carrier screening on the luminescence energy shift and carrier lifetime of InGaN quantum wells. *J. Appl. Phys.*, 92(6):3071, 2002.
- [182] A. Pinos, S. Marcinkevicius, K. Liu, M. S. Shur, E. Kuokstis, G. Tamulaitis, R. Gaska, J. Yang, and W. Sun. Screening dynamics of intrinsic electric field in AlGaIn quantum wells. *Appl. Phys. Lett.*, 92(6):61907, 2008.
- [183] P. Lefebvre, S. Kalliakos, T. Bretagnon, P. Valvin, T. Taliercio, B. Gil, N. Grandjean, and J. Massies. Observation and modeling of the time-dependent descreening of internal electric field in a wurtzite GaN/Al_{0.15}Ga_{0.85}N quantum well after high photoexcitation. *Phys. Rev. B*, 69(3):35307, January 2004.
- [184] {Auf der Maur}, G. Penazzi, G. Romano, F. Sacconi, A. Pecchia, and A. {Di Carlo}. The multiscale paradigm in electronic device simulation. *IEEE Transact.*, 58(5):1425, 2011. URL www.tiberlab.com.
- [185] M. Knelangen, M. Hanke, E. Luna, L. Schrottke, O. Brandt, and A. Trampert. Monodisperse (In, Ga)N insertions in catalyst-free-grown GaN(0001) nanowires. *Nanotechnology*, 22(46):469501, November 2011.
- [186] G. Tourbot, C. Bougerol, F. Glas, L. F. Zagonel, Z. Mahfoud, S. Meuret, P. Gilet, M. Kociak, B. Gayral, and B. Daudin. Growth mechanism and properties of InGaIn insertions in GaN nanowires. *Nanotechnology*, 23(13):135703, April 2012.
- [187] Y. Yang, X. A. Cao, and C. H. Yan. Electrical and optical characteristics of green light-emitting diodes grown on bulk gan substrates. In K. P. Streubel, H. Jeon, and L.-W. Tu, editors, *Proc. SPIE*, pages 72310W–6, February 2009.
- [188] J. Cho, E. F. Schubert, and J. K. Kim. Efficiency droop in light-emitting diodes: Challenges and countermeasures. *Laser Photon. Rev.*, 7(3):408, May 2013.
- [189] Q. Dai, Q. Shan, J. Wang, S. Chhajed, J. Cho, E. F. Schubert, M. H. Crawford, D. D. Koleske, M.-H. Kim, and Y. Park. Carrier recombination mechanisms and efficiency droop in GaInN/GaN light-emitting diodes. *Appl. Phys. Lett.*, 97(13):133507, September 2010.

- [190] M. Meneghini, N. Trivellin, G. Meneghesso, E. Zanoni, U. Zehnder, and B. Hahn. A combined electro-optical method for the determination of the recombination parameters in InGaN-based light-emitting diodes. *J. Appl. Phys.*, 106(11):114508, December 2009.
- [191] D. S. Meyaard, Q. Shan, Q. Dai, J. Cho, E. F. Schubert, M.-H. Kim, and C. Sone. On the temperature dependence of electron leakage from the active region of GaInN/GaN light-emitting diodes. *Appl. Phys. Lett.*, 99(4):041112, July 2011.
- [192] S.-C. Ling, T.-C. Lu, S.-P. Chang, J.-R. Chen, H.-C. Kuo, and S.-C. Wang. Low efficiency droop in blue-green m-plane InGaN/GaN light emitting diodes. *Appl. Phys. Lett.*, 96(23):231101, June 2010. doi: 10.1063/1.3449557.
- [193] Michael A. Reshchikov and Hadis Morkoç. Luminescence properties of defects in GaN. *J. Appl. Phys.*, 97(6):061301, March 2005.
- [194] O. Brandt and K. H. Ploog. Solid-state lighting: the benefit of disorder. *Nat. Mater.*, 5(10):769, October 2006.
- [195] H. Jeong, H. J. Jeong, H. M. Oh, C.-H. Hong, E.-K. Suh, G. Lerondel, and M. S. Jeong. Carrier localization in In-rich InGaN/GaN multiple quantum wells for green light-emitting diodes. *Sci. Rep.*, 5:9373, 2015.
- [196] Y. P. Varshni. Temperature dependence of the energy gap in semiconductors. *Physica*, 34(1):149, January 1967.
- [197] Hadis Morkoç. *Handbook of Nitride Semiconductors and Devices - Volume 2. Electronic and Optical Processes in Nitrides*. Wiley, 2008. ISBN 978-3-527-40838-2.
- [198] R. Paessler. Basic Model Relations for Temperature Dependencies of Fundamental Energy Gaps in Semiconductors. *Phys. Status Solidi B*, 200(1):155, March 1997.
- [199] L. Viña, S. Logothetidis, and M. Cardona. Temperature dependence of the dielectric function of germanium. *Phys. Rev. B*, 30(4):1979, August 1984.
- [200] M. E. Levinshtein, S. L. Rumyantsev, and M. S. Shur. *Properties of Advanced Semiconductor Materials: GaN, AlN, InN, BN, SiC, SiGe*. Wiley, 2001. ISBN 978-0-471-35827-5.
- [201] Y.-H. Cho, G. H. Gainer, J. Fischer, J. J. Song, S. Keller, U. K. Mishra, and S. P. DenBaars. “S-shaped” temperature-dependent emission shift and carrier dynamics in InGaN/GaN multiple quantum wells. *Appl. Phys. Lett.*, 73(10):1370, 1998.
- [202] X. A. Cao, S. F. LeBoeuf, L. B. Rowland, C. H. Yan, and H. Liu. Temperature-dependent emission intensity and energy shift in InGaN/GaN multiple-quantum-well light-emitting diodes. *Appl. Phys. Lett.*, 82(21):3614, May 2003.
- [203] X. A. Cao, S. F. Leboeuf, L. B. Rowland, and H. Liu. Temperature-dependent electroluminescence in InGaN/GaN multiple-quantum-well light-emitting diodes. *J. Electron. Mater.*, 32(5):316, May 2003.
- [204] C.-C. Hong, H. Ahn, C.-Y. Wu, and S. Gwo. Strong green photoluminescence from In_xGa_{1-x}N/GaN nanorod arrays. *Optics express*, 17(20):17227, September 2009.

Bibliography

- [205] J. Lee, E. S. Koteles, and M. O. Vassell. Luminescence linewidths of excitons in GaAs quantum wells below 150 K. *Phys. Rev. B*, 33(8):5512, April 1986.
- [206] K. P. Korona, A. Wyszomolek, K. Pakula, R. Stępniewski, J. M. Baranowski, I. Grzegory, B. Lucznik, M. Wróblewski, and S. Porowski. Exciton region reflectance of homoepitaxial GaN layers. *Appl. Phys. Lett.*, 69(6):788, August 1996.
- [207] G. Franssen, E. Litwin-Staszewska, R. Piotrkowski, T. Suski, and P. Perlin. Optical and electrical properties of homoepitaxially grown multiquantum well In-GaN/GaN light-emitting diodes. *J. Appl. Phys.*, 94(9):6122, October 2003.
- [208] C.-T. Sah, R. Noyce, and W. Shockley. Carrier Generation and Recombination in P-N Junctions and P-N Junction Characteristics. *Proc. IRE*, 45(9):1228, September 1957.
- [209] S. N. Mohammad. Contact mechanisms and design principles for (Schottky and Ohmic) metal contacts to semiconductor nanowires. *J. Appl. Phys.*, 108(3):034311, 2010.
- [210] H. C. Casey, J. Muth, S. Krishnankutty, and J. M. Zavada. Dominance of tunneling current and band filling in InGaN/AlGaN double heterostructure blue light-emitting diodes. *Appl. Phys. Lett.*, 68(20):2867, May 1996.
- [211] P. Perlin, M. Osiński, P. G. Eliseev, V. A. Smagley, J. Mu, M. I. Banas, and P. Sartori. Low-temperature study of current and electroluminescence in In-GaN/AlGaN/GaN double-heterostructure blue light-emitting diodes. *Appl. Phys. Lett.*, 69(12):1680, September 1996.
- [212] D. Zhu, J. Xu, A. N. Noemaun, J. K. Kim, E. F. Schubert, M. H. Crawford, and D. D. Koleske. The origin of the high diode-ideality factors in GaInN/GaN multiple quantum well light-emitting diodes. *Appl. Phys. Lett.*, 94(8):081113, February 2009.
- [213] H. Masui. Diode ideality factor in modern light-emitting diodes. *Semicond. Sci. Technol.*, 26(7):075011, July 2011.
- [214] J. B. Fedison, T. P. Chow, H. Lu, and I. B. Bhat. Electrical characteristics of magnesium-doped gallium nitride junction diodes. *Appl Phys. Lett.*, 72(22):2841, June 1998.
- [215] L. Hirsch and A. S. Barrière. Electrical characterization of InGaN/GaN light emitting diodes grown by molecular beam epitaxy. *J. Appl. Phys.*, 94(8):5014, September 2003.
- [216] X. A. Cao, J. M. Teetsov, M. P. D'Evelyn, D. W. Merfeld, and C. H. Yan. Electrical characteristics of InGaN/GaN light-emitting diodes grown on GaN and sapphire substrates. *Appl Phys. Lett.*, 85(1):7, June 2004.
- [217] D. Yan, H. Lu, D. Chen, R. Zhang, and Y. Zheng. Forward tunneling current in GaN-based blue light-emitting diodes. *Appl Phys. Lett.*, 96(8):083504, February 2010.
- [218] M. Auf der Maur, B. Galler, I. Pietzonka, M. Strassburg, H. Lugauer, and A. Di Carlo. Trap-assisted tunneling in InGaN/GaN single-quantum-well light-emitting diodes. *Appl. Phys. Lett.*, 105(13):133504, September 2014.

- [219] M. Mandurrino, G. Verzellesi, M. Goano, M. Vallone, F. Bertazzi, G. Ghione, M. Meneghini, G. Meneghesso, and E. Zanoni. Physics-based modeling and experimental implications of trap-assisted tunneling in InGaN/GaN light-emitting diodes. *Phys. Status Solidi A*, page 1, January 2015.
- [220] M. Musolino, M. Meneghini, L. Scarparo, C. De Santi, A. Tahraoui, L. Geelhaar, E. Zanoni, and H. Riechert. Deep level transient spectroscopy on light-emitting diodes based on (In,Ga)N/GaN nanowire ensembles. *Proc. SPIE*, 9363:936325, March 2015.
- [221] E. F. Schubert, J. M. Kuo, and R. F. Kopf. Theory and experiment of capacitance-voltage profiling on semiconductors with quantum-confinement. *J. Electron. Mater.*, 19(6):521, June 1990.
- [222] D. V. Lang. Deep-level transient spectroscopy: A new method to characterize traps in semiconductors. *J. Appl. Phys.*, 45(7):3023, October 1974.
- [223] A. M. Witowski, K. Pakuła, J. M. Baranowski, M. L. Sadowski, and P. Wyder. Electron effective mass in hexagonal GaN. *Appl. Phys. Lett.*, 75(26):4154, December 1999.
- [224] P. Hacke, T. Detchprohm, K. Hiramatsu, N. Sawaki, K. Tadatomo, and K. Miyake. Analysis of deep levels in n-type GaN by transient capacitance methods. *J. Appl. Phys.*, 76(1):304, July 1994.
- [225] D. Haase, M. Schmid, W. Kürner, A. Dörnen, V. Härle, F. Scholz, M. Burkard, and H. Schweizer. Deep-level defects and n-type-carrier concentration in nitrogen implanted GaN. *Appl. Phys. Lett.*, 69(17):2525, October 1996.
- [226] C. D. Wang, L. S. Yu, S. S. Lau, E. T. Yu, W. Kim, A. E. Botchkarev, and H. Morkoç. Deep level defects in n-type GaN grown by molecular beam epitaxy. *Appl. Phys. Lett.*, 72(10):1211, March 1998.
- [227] A. Hierro, A.R. Arehart, B. Heying, M. Hansen, J.S. Speck, U.K. Mishra, S.P. DenBaars, and S.A. Ringel. Capture Kinetics of Electron Traps in MBE-Grown n-GaN. *Phys. Status Solidi B*, 228(1):309, November 2001.
- [228] G. A. Umana-Membreno, G. Parish, N. Fichtenbaum, S. Keller, U. K. Mishra, and B. D. Nener. Electrically Active Defects in GaN Layers Grown With and Without Fe-doped Buffers by Metal-organic Chemical Vapor Deposition. *J. Electron. Mater.*, 37(5):569, October 2007.
- [229] D. Kindl, P. Hubík, J. Krištofik, J. J. Marevs, Z. Výborný, M. R. Leys, and S. Boeykens. Deep defects in GaN/AlGaIn/SiC heterostructures. *J. Appl. Phys.*, 105(9):093706, May 2009.
- [230] K. R. Peta, S.-T. Lee, K. Moon-Deock, J.-E. Oh, S.-G. Kim, and T.-G. Kim. Deep level defects in Ga- and N-polarity GaN grown by molecular beam epitaxy on si(111). *J. Cryst. Growth*, 378:299, September 2013.
- [231] D. Jenkins and J. Dow. Electronic structures and doping of InN, In_xGa_{1-x}N, and In_xAl_{1-x}N. *Phys. Rev. B*, 39(5):3317, February 1989.

Bibliography

- [232] J. Osaka, Y. Ohno, S. Kishimoto, K. Maezawa, and T. Mizutani. Deep levels in n-type AlGaIn grown by hydride vapor-phase epitaxy on sapphire characterized by deep-level transient spectroscopy. *Appl. Phys. Lett.*, 87(22):222112, November 2005.
- [233] K. A. Grossklaus, A. Banerjee, S. Jahangir, P. Bhattacharya, and J. M. Millunchick. Misorientation defects in coalesced self-catalyzed GaN nanowires. *J. Cryst. Growth*, 371:142, May 2013.
- [234] M. Meneghini, M. la Grassa, S. Vaccari, B. Galler, R. Zeisel, P. Drechsel, B. Hahn, G. Meneghesso, and E. Zanoni. Characterization of the deep levels responsible for non-radiative recombination in InGaIn/GaN light-emitting diodes. *Appl. Phys. Lett.*, 104(11):113505, March 2014.
- [235] Q. Shan, D. S. Meyaard, Q. Dai, J. Cho, F. E. Schubert, K. J. Son, and C. Sone. Transport-mechanism analysis of the reverse leakage current in GaInN light-emitting diodes. *Appl. Phys. Lett.*, 99(25):253506, December 2011.
- [236] M. Tchernycheva, P. Lavenus, H. Zhang, A. V. Babichev, G. Jacopin, M. Shahmohammadi, F. H. Julien, R. Ciechonski, G. Vescovi, and O. Kryliouk. InGaIn/GaN core-shell single nanowire light emitting diodes with graphene-based p-contact. *Nano Lett.*, 14(5):2456, April 2014.
- [237] N. F. Mott. Conduction in non-crystalline materials. *Philos. Mag.*, 19(160):835, April 1969.
- [238] R. M. Hill. Hopping conduction in amorphous solids. *Philos. Mag.*, 24(192):1307, 1971.
- [239] D. C. Look, D. C. Reynolds, W. Kim, Ö. Aktas, A. Botchkarev, A. Salvador, and H. Morkoç. Deep-center hopping conduction in GaN. *J. Appl. Phys.*, 80(5):2960, September 1996.
- [240] C. Echeverría-Arrondo, J. Pérez-Conde, and A. K. Bhattacharjee. Acceptor and donor impurities in GaN nanocrystals. *J. Appl. Phys.*, 104(4):044308, August 2008.
- [241] J. Frenkel. On Pre-Breakdown Phenomena in Insulators and Electronic Semiconductors. *Phys. Rev.*, 54(8):647, October 1938.
- [242] R. M. Hill. Poole-Frenkel conduction in amorphous solids. *Philos. Mag.*, 23(181):59, January 1971.
- [243] J. L. Hartke. The Three-Dimensional Poole-Frenkel Effect. *J. Appl. Phys.*, 39(10):4871, November 1968.
- [244] G. Vincent, A. Chantre, and D. Bois. Electric field effect on the thermal emission of traps in semiconductor junctions. *J. Appl. Phys.*, 50(8):5484, July 1979.
- [245] E. Jung and H. Kim. Analysis of GaN-based light-emitting diodes degraded by generation of deep-level states. *Phys. Status Solidi A*, 211(8):1764, August 2014.
- [246] M. Choueib, R. Martel, C. S. Cojocaru, A. Ayari, P. Vincent, and S. T. Purcell. Current saturation in field emission from H-passivated Si nanowires. *ACS nano*, 6(8):7463, August 2012.

- [247] W. Shockley and W. Read. Statistics of the Recombinations of Holes and Electrons. *Phys. Rev.*, 87(5):835, September 1952.
- [248] B. I. Shklovskii and A. L. Efros. *Electronic Properties of Doped Semiconductors*.
- [249] T. Mattila, A. Seitsonen, and R. Nieminen. Large atomic displacements associated with the nitrogen antisite in GaN. *Phys. Rev. B*, 54(3):1474, July 1996.
- [250] D. I. Fritsch, H. Schmidt, and M. Grundmann. Band-structure pseudopotential calculation of zinc-blende and wurtzite AlN, GaN, and InN. *Phys. Rev. B*, 67(23):1, June 2003.
- [251] T. Hofmann, P. Kühne, S. Schöche, Jr-Tai Chen, U. Forsberg, E. Janzén, N. Ben Sedrine, C. M. Herzinger, J. A. Woollam, M. Schubert, and V. Darakchieva. Temperature dependent effective mass in AlGaN/GaN high electron mobility transistor structures. *Appl. Phys. Lett.*, 101(19):192102, November 2012.
- [252] A. Hierro, A. R. Arehart, B. Heying, M. Hansen, U. K. Mishra, S. P. DenBaars, J. S. Speck, and S. A. Ringel. Impact of Ga/N flux ratio on trap states in n-GaN grown by plasma-assisted molecular-beam epitaxy. *Appl. Phys. Lett.*, 80(5):805, February 2002.

Acknowledgements

*"We are like dwarfs sitting on the shoulders of giants.
We see more, and things that are more distant, than they did,
not because our sight is superior or because we are taller than they,
but because they raise us up, and by their great stature add to ours."*

Bernardus Carnotensis quoted by John of Salisbury
Metalogicon, III, 4

Wise are the words of the philosopher Bernard of Chartres (Bernardus Carnotensis) and particularly appropriate for the present work. In fact, the writing of this PhD thesis would not have been possible without the continuous support by a number of people at, but not restricted to, the Paul-Drude-Institut (PDI). This institute has provided me the calm and fruitful environment needed for my work; I have greatly benefited from the possibilities for cooperation between the different departments and with external partners. In the following, I will try to acknowledge all the people who have provided a direct contribution to the realization of this thesis, but my gratitude extends also to other colleagues and friends not mentioned explicitly.

First of all, I would like to thank Prof. Dr. Henning Riechert for accepting me as a PhD student, securing the financial support, and being open for discussion and suggestions. This work has also been partially supported by the European Commission through the DEEPEN project (FP7-NMP-2013-SMALL-7, grant Agreement No. 604416). Furthermore, I am very grateful to Prof. Dr. Ted W. Masselink and Prof. Dr. Bruno Daudin for reviewing this thesis.

Special thanks go to Lutz Geelhaar as head of the epitaxy department for his constant supervision of my work and the precious feedback he has provided.

It has also been a very stimulating experience to work in the framework of the nanowire group at PDI. For the countless suggestions and scientific discussion, I am especially grateful to Dr. Oliver Brandt, Dr. Sergio Fernández-Garrido, Dr. Friederich Limbach, Dr. Martin Wölz, Dr. Tobias Gotschke, Dr. Javier Grandal-Quintana, Dr. Johannes K. Zettler, and Dr. Pinar Dogan. Particularly fruitful has also been the collaboration with David van Treeck, with whom I have closely worked during his master thesis. For support with the optical measurements at PDI, I thank Dr. Christian Hauswald, Felix Feix, Dr. Uwe Jahn, and Dr. Jonas Lähnemann. For the fabrication of the presented devices the contribution of the colleagues working in the clean room has been essential; I particularly acknowl-

Acknowledgements

edge the help of Walid Anders, Sander Rauwerdink, Bernd Drescher, and Werner Seidel supervised by Dr. Abbas Tahraoui. I am also grateful to Dr. Bernd Jenichen for his help with XRD measurements, as well as to Dr. Achim Trampert and Anne-Kathrin Bluhm for providing me high quality transmission electron and scanning electron micrographs, respectively. Very important has also been the maintenance of the MBE systems carried out by Claudia Herrmann, Hans-Peter Schönherr, and Michael Höricke.

In addition to the indispensable collaboration with the other departments internal to PDI, this thesis has also taken advantage of other external partners. In particular, most of the measurements presented in chapter 4 have been acquired in the framework of a fruitful collaboration with the research group headed by Prof. Dr. Matteo Meneghini and Prof. Dr. Enrico Zanoni at the department of information engineering (DEI) of the University of Padua in Italy. I gratefully acknowledge Prof. Dr. Matteo Meneghini as well as Dr. Carlo De Santi and Laerte Scarparo for their help during the data acquisition and for the beneficial scientific discussions. The C-AFM measurements presented in chapter 2 and 3 have been performed at the Suzhou Institute of Nano-Tech and Nano-Bionics (SINANO) in China under the supervision of Dr. Xu Gengzhao and Dr. Haijian Zhong. Moreover, the patterned substrates used for the SAG experiments presented in chapter 2 have been prepared by Namil Koo and Jungwuk Kim at the *AMO GmbH* in Aachen, and by Mathias Matalla at the Ferdinand-Braun-Institut in Berlin. I gratefully acknowledge their help.

There are also many other colleagues and friends, whose names I do not even start mentioning for sake of brevity and fear of omissions. I am sure that the people who shared with me many adventures in the last years will feel my affection reading these lines, even without seeing their names written down on paper. I thank you all for your support and for the scientific and non-scientific discussions.

Last, but not least, all this would not have been possible without my family. The greatest thanks go to my mummy, my daddy, my sister and my great love Emanuela, who have always inspired and supported me.

Selbständigkeitserklärung

Ich erkläre, dass ich die vorliegende Arbeit selbständig und nur unter Verwendung der angegebenen Literatur und Hilfsmittel angefertigt habe.

Berlin, den 21.07.2015

Mattia Musolino